

**Uncertainty in the Prediction of Overtopping  
Parameters in Numerical and Physical Models due to  
Offshore Spectral Boundary Conditions**

**Hannah Elizabeth Williams**

A thesis submitted to the University of Nottingham  
for the degree of Doctor of Philosophy

September 2015



## **Abstract**

The accurate prediction of wave overtopping is one of the most important aspects in the design of coastal defence structures. This can be achieved by using three different approaches: by physical modelling using laboratory tests, by empirical formulae available in literature derived from physical modelling and field tests, or by numerical simulation of the hydraulic response of the structure.

All of these prediction methods are subject to a certain level of uncertainty. One source of this is the requirement of a defined free surface elevation and velocity time series seaward boundary condition in any model. Often, these are not available but the modeller is instead provided with an incident energy density spectrum. A time series will then be reconstructed from this spectrum to be used as boundary conditions. Since the energy density spectrum provides only information on the amplitude of the components, it is usually assumed that the phases of these components are randomly distributed. To create the randomly generated phases, an initial seed value is required to generate a population of uniformly distributed random phases. By varying this value for each simulation a different time series will be produced. The overall objective of this research is to quantify the uncertainty in the prediction of overtopping due to this process.

This research involved carrying out two sets of laboratory experiments. Firstly, those carried out in the 2D wave flume at HR Wallingford, which provided a reference case for the validation of a numerical model, as well as a measured incident wave spectra for the generation of the population of reconstructed offshore boundary time series. The second set of experiments was carried out in the smaller 2D flume at the University of Nottingham to investigate the effect of random seeding to generate the time series at the wave paddle on the resulting overtopping parameters. This was also carried out to allow a comparison in the variability between the physical and numerical results.

It was found in the work, that when a measured free surface elevation is used as the input, good agreement between the numerical solver prediction and the overtopping measurements was observed. Subsequently, when a Monte Carlo approach was used to generate the population of reconstructed offshore boundary time series from the measured incident spectra the statistical analysis of the results showed that the variability was higher for the small numbers of overtopping waves and decreases as overtopping becomes more frequent.

To allow for more generalised conclusions on the uncertainty, further numerical tests were then

carried out with synthetic spectra allowing different hydraulic and structural parameters to be considered. These showed good agreement with the findings of the initial statistical analysis. Finally, the results from the physical model tests carried out at the University of Nottingham were analysed. The influence of laboratory effects were studied and analysis was carried out to establish the magnitude and sources of variability in these results. As with the numerical results, the characteristics of the distribution of the predicted overtopping parameters were also studied.

## **Acknowledgements**

I am firstly grateful to my supervisors, Dr Riccardo Briganti and Professor Nicholas Dodd, whose guidance, enthusiasm and advice has been useful throughout this work. I appreciate all the time and help they have both given to me.

I would also like to thank my colleagues within the Department of Civil Engineering at the University of Nottingham including all of the helpful technical staff in the fluid dynamics laboratory, in particular Steve Gange. An additional thanks should go out to the other members of the Coastal Dynamics and Engineering Group, as well as Alessandro Romano who were always available for helpful and informative discussions, be it in person or via email. The help provided by Marco Matteucci in carrying out the experiments at the University of Nottingham is also greatly appreciated.

I would also like to extend my thanks to Dr Tim Pullen, Dr Stephen Richardson, Professor William Allsop and Dr Giovanni Cuomo at HR Wallingford for allowing me access to both their facilities and their expertise. I would also like to thank all the staff at HR Wallingford for making me feel welcome, in particular Daniel Carter for his help carrying out the overtopping experiments.

I am also grateful to the Engineering and Physical Sciences Research Council (EPSRC) for generously funding my PhD research along with the University of Nottingham.

Finally, I would also like to thank my family and friends for all their help and support throughout the last 3.5 years.



## **List of Publications**

Williams, H.E. and Briganti, R. and Pullen, T., 2013. Analysis of the uncertainty in the prediction of overtopping in coastal numerical models. Peer Reviewed Proceedings of ICE Coasts, Marine Structures and Breakwaters, Edinburgh.

Williams, H.E.; Briganti, R., and Pullen, T., 2014. The role of offshore boundary conditions in the uncertainty of numerical prediction of wave overtopping using non-linear shallow water equations. Coastal Engineering, 89, 30-44.

Williams, H.E; Briganti, R., Pullen, T., and Dodd, N., 2015. The uncertainty in the prediction of the distribution of individual wave overtopping volumes using a non-linear shallow water equation solver. Accepted for publication in Journal of Coastal Research.



# Contents

<b>1</b>	<b>Introduction</b>	<b>1</b>
1.1	Motivations . . . . .	1
1.2	Research Objectives . . . . .	5
1.3	Thesis Outline . . . . .	5
<b>2</b>	<b>Background</b>	<b>7</b>
2.1	Introduction . . . . .	7
2.2	Wave Characteristics . . . . .	7
2.2.1	Small Amplitude Wave Theory . . . . .	8
2.2.2	Shallow Water Approximation . . . . .	9
2.2.3	Wave Breaking . . . . .	9
2.3	Irregular Waves . . . . .	10
2.3.1	Analysis in the Time Domain . . . . .	11
2.3.2	Analysis in the Frequency Domain . . . . .	12
2.3.3	Spectral Shape . . . . .	14
2.4	Types of Structures . . . . .	15
2.4.1	Smooth Slopes . . . . .	16
2.4.2	Vertical Walls . . . . .	16
2.5	Prediction of Overtopping . . . . .	17
2.5.1	Empirical Methods . . . . .	17
2.5.2	Numerical Models . . . . .	24
2.5.3	Physical Models . . . . .	30
2.6	Uncertainty . . . . .	32
2.6.1	Types of Uncertainty . . . . .	32
2.6.2	Sources of Uncertainty in Numerical Models . . . . .	33
2.6.3	Identifying Uncertainty . . . . .	35
2.6.4	Monte Carlo Simulation . . . . .	37
<b>3</b>	<b>Model Validation and Measured Offshore Boundary Conditions</b>	<b>39</b>
3.1	Introduction . . . . .	39
3.2	Physical Model . . . . .	39
3.2.1	Experimental set-up . . . . .	40
3.2.2	Wave Conditions and Measurement . . . . .	40
3.2.3	Overtopping Measurement . . . . .	43
3.3	Numerical Model . . . . .	45
3.3.1	Numerical set-up . . . . .	45
3.4	Model Validation . . . . .	46
3.4.1	Physical Model Results . . . . .	46
3.4.2	Run-Up Comparison . . . . .	48
3.4.3	Overtopping Time Series Comparison . . . . .	48
3.4.4	Mean Overtopping Discharge . . . . .	49

3.4.5	Maximum Individual Overtopping Volume . . . . .	51
3.4.6	Probability of Overtopping . . . . .	53
3.5	Summary . . . . .	55
<b>4</b>	<b>Model Uncertainty due to Spectral Boundary Conditions</b>	<b>57</b>
4.1	Introduction . . . . .	57
4.2	Reconstructed Offshore Boundary Conditions . . . . .	58
4.2.1	Incident Spectra . . . . .	58
4.2.2	Spectral Energy Density Estimation . . . . .	58
4.2.3	Definition of the Monte Carlo Population Size . . . . .	60
4.2.4	Definition of Test Length . . . . .	60
4.3	Comparison with the Validation Tests . . . . .	62
4.3.1	Overtopping Time Series . . . . .	62
4.3.2	Overtopping parameters . . . . .	64
4.4	Variability due to ROBC . . . . .	65
4.4.1	Probability distribution of the overtopping parameters . . . . .	72
4.5	Summary . . . . .	84
<b>5</b>	<b>Distribution of Individual Overtopping Volumes</b>	<b>87</b>
5.1	Introduction . . . . .	87
5.2	Incoming Waves . . . . .	87
5.2.1	Wave Height Distribution . . . . .	88
5.2.2	Measured Spectra . . . . .	92
5.2.3	Time Series Comparison . . . . .	95
5.3	Individual Overtopping Volumes . . . . .	95
5.3.1	Comparison of MOBC results . . . . .	97
5.3.2	Comparison of ROBC results . . . . .	99
5.4	Summary . . . . .	104
<b>6</b>	<b>Effect of Hydraulic and Structural Parameters on Uncertainty</b>	<b>107</b>
6.1	Introduction . . . . .	107
6.2	Synthetic Spectra . . . . .	107
6.3	Influence of Spectral Shape . . . . .	108
6.4	Influence of Surf Similarity Parameter . . . . .	109
6.4.1	Variability . . . . .	111
6.4.2	Comparison with Empirical Methods . . . . .	114
6.4.3	Distributions . . . . .	117
6.5	Influence of Surface Roughness . . . . .	123
6.5.1	Influence on Magnitude of Run-up . . . . .	124
6.5.2	Variability . . . . .	129
6.5.3	Distributions . . . . .	129
6.6	Summary . . . . .	134
<b>7</b>	<b>Uncertainty in Physical Modelling</b>	<b>135</b>
7.1	Introduction . . . . .	135
7.2	Experimental set-up . . . . .	135
7.2.1	Wave Conditions . . . . .	136
7.2.2	Measurement . . . . .	138
7.3	Influence of Laboratory Effects . . . . .	139
7.3.1	Wave Height Distribution . . . . .	139
7.3.2	Presence of Long Waves . . . . .	142
7.4	Tests with Same Seeding . . . . .	147

7.4.1	Still Water Level Control . . . . .	147
7.4.2	Overtopping Measurement . . . . .	148
7.4.3	Wave Heights . . . . .	150
7.5	Tests with Different Seeding . . . . .	151
7.5.1	Overtopping Time Series . . . . .	151
7.5.2	Distributions . . . . .	159
7.5.3	Comparison with Same Seeding Results . . . . .	165
7.6	Summary . . . . .	168
<b>8</b>	<b>Conclusions</b>	<b>169</b>
8.1	Summary of this Work . . . . .	169
8.2	Recommendations for Future Work . . . . .	172



# List of Figures

1.1	a. Example of overtopping at Dawlish, UK in Feb 2014. b. Subsequent damage to the railway line. c. Overtopping causing flooding at Ilfracombe, UK in Jan 2014. d. Overtopping causing flooding on The Wirral, UK in Feb 2014. e. Overtopping causing flooding in Pembrokeshire, UK in Feb 2014. f. Overtopping causing flooding in Aberystwyth, UK in Feb 2014. . . . .	2
2.1	Wave definition sketch based on a regular sine wave . . . . .	8
2.2	Water particle motion at different water depths . . . . .	10
2.3	Classification of Breaker Types . . . . .	11
2.4	Random waves shown in the time domain . . . . .	12
2.5	Example of a wave spectrum . . . . .	13
2.6	a. Grass covered dyke. b. Asphalt covered dyke. . . . .	16
2.7	a. Modern concrete caisson. b. Stone block-work wall. . . . .	17
2.8	Definition of run-up and overtopping parameters on smooth slope structure . . . . .	19
2.9	Definition of wave impact and overtopping parameters on vertical wall structure . . . . .	20
3.1	a. layout of the physical model. b. Detail of the tested structure and overtopping measurement system together with the numerical model set-up. c. Photograph of physical model . . . . .	41
3.2	Excerpt of measured and post-processed time series of water depth in tank 2 for test 006. Blue line:raw signal. Red line: filtered signal. Black dots: visually detected overtopping events. . . . .	44
3.3	Comparison of water elevation at the same point on the slope. Black solid line: $\eta$ for Test 006 from experimental data measured at <i>WG8</i> . Red solid line: $\eta$ for Test 006 from MOBC results. . . . .	48
3.4	Cumulative overtopping volumes. a. Test 003. b. Test 006. c. Test 007. Black solid line: Measurement in tank for each test from experimental data. Red solid line: Volumes calculated for each test from MOBC results. . . . .	50
3.5	Comparison of $q$ measured in physical model versus $q$ calculated with the numerical model. Grey dashed line represents perfect fit. . . . .	51
3.6	Comparison of $q$ measured in physical model versus $q$ calculated with the numerical model and predicted using empirical formulae. Grey dashed line represents perfect fit. . . . .	52
3.7	Comparison of $V_{max}$ measured in physical model versus $V_{max}$ calculated with the numerical model. Grey dashed line represents perfect fit. . . . .	53
3.8	Comparison of $V_{max}$ measured in physical model versus $V_{max}$ calculated with the numerical model and predicted using empirical formulae. Grey dashed line represents perfect fit. . . . .	54
3.9	Comparison of $P_{ov}$ measured in physical model versus $P_{ov}$ calculated with the numerical model. Grey dashed line represents perfect fit. . . . .	54
3.10	Comparison of $P_{ov}$ measured in physical model versus modified $P_{ov}$ calculated with the numerical model. Grey dashed line represents perfect fit. . . . .	55

3.11	Comparison of $P_{ov}$ measured in physical model versus modified $P_{ov}$ calculated with the numerical model and $P_{ov}$ predicted using empirical formulae. Grey dashed line represents perfect fit. . . . .	56
4.1	Relative error for $q$ due to the spectral estimate and spectral components used for test 006. Red line: $N_{FFT} = 512$ , Green line: $N_{FFT} = 1024$ and Blue line: $N_{FFT} = 2048$ . . . . .	60
4.2	Relative error. a. $q$ . b. $P_{ov}$ . c. $V_{max}$ due to the number of ROBC tests. Green line: test 003 for low overtopping. Red line: test 006 for moderate overtopping and Blue line: test 007 for high overtopping. . . . .	61
4.3	Overtopping time series for three tests. a. Test 003 (Low Overtopping). b. Test 006 (Moderate Overtopping). c. Test 007 (High Overtopping). Black line: experimental data, Red line: MOBC. Grey lines: 15 randomly selected ROBC tests. . . . .	63
4.4	Comparison of $P_{ov}$ measured in physical model versus both a. $P_{ov}$ and b. modified $P_{ov}$ calculated with the numerical model for MOBC and ROBC tests. Grey dashed line represents perfect fit. . . . .	66
4.5	Comparison of $q$ measured in physical model versus $q$ calculated with the numerical model for MOBC and ROBC tests. Grey dashed line represents perfect fit. . . . .	67
4.6	Comparison of $V_{max}$ measured in physical model versus modified $V_{max}$ calculated with the numerical model for MOBC and ROBC tests. Grey dashed line represents perfect fit. . . . .	67
4.7	Logarithmic scatter graph showing the correlation between $P_{ov}$ and $q$ . Grey horizontal dashed lines: overtopping limits for $q$ from Pullen et al. (2007). Solid black line: trend line of the average $q$ . Black dash lines: 95% confidence interval for $q$ . . . . .	69
4.8	Logarithmic scatter graph showing correlation between $P_{ov}$ and $V_{max}$ . Grey horizontal dashed lines: overtopping limits from Pullen et al. (2007). . . . .	70
4.9	Logarithmic scatter graph showing correlation between $R^*$ and $P_{ov}$ . . . . .	71
4.10	Logarithmic graph showing correlation between $R^*$ and $q$ . . . . .	73
4.11	Logarithmic scatter graph showing correlation between $R^*$ and $Q^*$ . . . . .	74
4.12	Relative histograms comparing distribution of $q$ for different levels of overtopping. a. Test 003 (Low Overtopping). b. Test 006 (Moderate Overtopping). c. Test 007 (High Overtopping). . . . .	76
4.13	Empirical frequency curves for $q$ from ROBC tests (black solid lines) compared with known distributions. a. Test 003 (Low Overtopping). b. Test 006 (Moderate Overtopping). c. Test 007 (High Overtopping). . . . .	77
4.14	Histograms comparing distribution of $P_{ov}$ for different levels of overtopping. a. Test 003 (Low Overtopping). b. Test 006 (Moderate Overtopping). c. Test 007 (High Overtopping). . . . .	79
4.15	Empirical frequency curves for $P_{ov}$ from ROBC (black solid lines) compared with known distributions. a. Test 003 (Low Overtopping). b. Test 006 (Moderate Overtopping). c. Test 007 (High Overtopping). . . . .	80
4.16	Relative histograms comparing distribution of $V_{max}$ for different levels of overtopping. a. Test 003 (Low Overtopping). b. Test 006 (Moderate Overtopping). c. Test 007 (High Overtopping). . . . .	82
4.17	Empirical frequency curves for $V_{max}$ from ROBC (black solid lines) compared with known distributions. a. Test 003 (Low Overtopping). b. Test 006 (Moderate Overtopping). c. Test 007 (High Overtopping). . . . .	83
5.1	Distributions of the measured incident wave heights and the wave heights of 10 randomly selected reconstructed time series at the location of the structure toe for Test 003 (Low Overtopping). Rayleigh and Battjes and Groenendijk (2000) distributions are also shown. . . . .	90

5.2	Distributions of the measured incident wave heights and the wave heights of 10 randomly selected reconstructed time series at the location of the structure toe for Test 006 (Moderate Overtopping). Rayleigh and Battjes and Groenendijk (2000) distributions are also shown. . . . .	91
5.3	Distributions of the measured incident wave heights and the wave heights of 10 randomly selected reconstructed time series at the location of the structure toe for Test 007 (High Overtopping). Rayleigh and Battjes and Groenendijk (2000) distributions are also shown. . . . .	92
5.4	Measured incident spectrum from Test 003 ( $H_{m0}/d_t = 0.40$ ). . . . .	93
5.5	Measured incident spectra from Test 006 ( $H_{m0}/d_t = 0.29$ ). . . . .	94
5.6	Measured incident spectra from Test 007 ( $H_{m0}/d_t = 0.84$ ). . . . .	94
5.7	Excerpt of measured and one reconstructed time series. a. Test 003 ( $H_{m0}/d_t = 0.40$ ). b. Test 006 ( $H_{m0}/d_t = 0.29$ ). c. Test 007 ( $H_{m0}/d_t = 0.84$ ). . . . .	96
5.8	Comparison of the distribution of $V_{ov}$ from the MOBC test of 006 with the empirical methods and the physical model . . . . .	98
5.9	Comparison of the distribution of $V_{ov}$ from the MOBC test of 007 with the empirical methods and the physical model . . . . .	99
5.10	Comparison of the distribution of $V_{ov}$ at moderate levels of overtopping from the ROBC tests and the empirical formulae. a. Test 004. b. Test 005. c. Test 006 . . . . .	101
5.11	Comparison of the distribution of $V_{ov}$ from the randomly selected ROBC tests and the empirical formulae for Test 006. . . . .	102
5.12	Comparison of the distribution of $V_{ov}$ at high levels of overtopping from the ROBC tests and the empirical formulae. a. Test 001. b. Test 007. c. Test 008. . . . .	103
5.13	Comparison of the distribution of $V_{ov}$ from the randomly selected ROBC tests and the empirical formulae for Test 007. . . . .	105
6.1	Energy density spectra used for analysis of the effect of spectral shape. Red line: JONSWAP. Blue line: Pierson-Moskovitz. . . . .	108
6.2	Empirical CDFs for each of the overtopping parameters for the two spectral shapes. Red line: JONSWAP and blue line: PiersonMoskovitz. a. $q$ . b. $P_{ov}$ . c. $V_{max}$ . . . . .	110
6.3	Numerical domain showing the different structural geometries. Dimensions can be found in Table 6.4 . . . . .	112
6.4	Logarithmic scatter graph showing $q$ plotted against $P_{ov}$ classified in terms of slope angle. Solid lines represent the mean values of $q$ . Dashed lines represent the 95% confidence limits of $q$ . . . . .	114
6.5	Logarithmic scatter graph showing $q$ plotted against $P_{ov}$ classified in terms of wave steepness. Solid lines represent the mean values of $q$ . Dashed lines represent the 95% confidence limits of $q$ . . . . .	115
6.6	Logarithmic scatter graph showing $q$ plotted against $P_{ov}$ classified in terms of surf similarity. Solid lines represent the mean values of $q$ . Dashed lines represent the 95% confidence limits of $q$ . . . . .	116
6.7	Scatter graph showing $\xi_{m-1,0}$ plotted against $Q^*$ classified in terms of slope angle. Solid lines represent the empirical predictions based on each $R_c/H_{m0}$ present. . . . .	117
6.8	Scatter graph showing $\xi_{m-1,0}$ plotted against $Q^*$ classified in terms of wave steepness. Solid lines represent the empirical predictions based on each $R_c/H_{m0}$ present. . . . .	118
6.9	Scatter graphs showing $R^*$ plotted against $Q^*$ classified in terms of $\xi_{m-1,0}$ . Solid lines represent empirical predictions. . . . .	119
6.10	Empirical frequency curves for $q$ from ROBC (black solid lines) compared with expected distributions for different levels of overtopping. a. $\xi_{m-1,0} = 0.44$ . b. $\xi_{m-1,0} = 1.21$ . c. $\xi_{m-1,0} = 1.94$ . d. $\xi_{m-1,0} = 3.04$ . . . . .	120

6.11	Empirical frequency curves for $P_{ov}$ from ROBC (black solid lines) compared with expected distributions for different levels of overtopping. a. $\xi_{m-1,0} = 0.44$ . b. $\xi_{m-1,0} = 1.21$ . c. $\xi_{m-1,0} = 1.94$ . d. $\xi_{m-1,0} = 3.04$ . . . . .	121
6.12	Empirical frequency curves for $V_{max}$ from ROBC (black solid lines) compared with expected distributions for different levels of overtopping. a. $\xi_{m-1,0} = 0.44$ . b. $\xi_{m-1,0} = 1.21$ . c. $\xi_{m-1,0} = 1.94$ . d. $\xi_{m-1,0} = 3.04$ . . . . .	122
6.13	Water depth detected at various points in numerical domain of 1:2.55 slope for different surface roughness. a. Toe. b. Still water level. c. Front slope. d. Structure crest. . . . .	125
6.14	Water depth detected at various points in numerical domain of 1:4 slope for different surface roughness. a. Toe. b. Still water level. c. Front slope. d. Structure crest . . . . .	127
6.15	Water depth detected at various points in numerical domain of 1:7 slope for different surface roughness. a. Toe. b. Still water level. c. Front slope. d. Structure crest . . . . .	128
6.16	Logarithmic scatter graph showing the correlation between $P_{ov}$ and $q$ for different slope angles and values of $K_n$ . . . . .	130
6.17	Empirical frequency curves for $q$ from ROBC (black solid lines) compared with expected distributions for different levels of overtopping. a. $K_n=0.001m$ . b. $K_n=0.030m$ . c. $K_n=0.070m$ . d. $K_n=0.200m$ . . . . .	131
6.18	Empirical frequency curves for $P_{ov}$ from ROBC (black solid lines) compared with expected distributions for different levels of overtopping. a. $K_n=0.001m$ . b. $K_n=0.030m$ . c. $K_n=0.070m$ . d. $K_n=0.200m$ . . . . .	132
6.19	Empirical frequency curves for $V_{max}$ from ROBC (black solid lines) compared with expected distributions for different levels of overtopping. a. $K_n=0.001m$ . b. $K_n=0.030m$ . c. $K_n=0.070m$ . d. $K_n=0.200m$ . . . . .	133
7.1	a. Layout of the physical model with smooth sloped structure. b. Layout of the physical model with vertical wall structure . . . . .	137
7.2	Photographs of University of Nottingham experimental set-up. a. Smooth Impermeable Slope. b. Vertical Wall. . . . .	138
7.3	Distributions of the measured incident wave heights at paddle compared with expected Rayleigh distributions. a. TS01. b. TS02. c. TS03. d. TS05. e. TS07. . . . .	141
7.4	Measured spectra at different locations in the wave flume for smooth slope tests. a. TS01. b. TS02. c. TS03. d. TS05 . . . . .	144
7.5	Measured spectra at different locations in the wave flume for vertical wall tests. a. TS01. b. TS02. c. TS05. d. TS07 . . . . .	146
7.6	Graph showing $R^*$ plotted against $Q^*$ for tests with the same offshore wave time series for each condition . . . . .	149
7.7	Comparison of Relative error of $H_{m0}$ versus $q$ for same seeding tests. Grey dashed line represents the perfect fit. . . . .	151
7.8	Measured filtered overtopping time series for all tests in each condition for smooth slope. Black lines: Minimum and Maximum measurements. a. TS01. b. TS02. c. TS03. d. TS05. . . . .	153
7.9	Measured filtered overtopping time series for all tests in each condition for vertical wall. Black lines: Minimum and Maximum measurements. a. TS01. b. TS02. c. TS05. d. TS07. . . . .	154
7.10	Graph showing $R^*$ plotted against $Q^*$ for random seeding test with smooth slope structure. Solid line: Empirical prediction. Dash line: 95% confidence interval. . . . .	155
7.11	Graph showing $R^*$ plotted against $Q^*$ for random seeding test with vertical wall structure. Solid line: Empirical prediction. Dash line: 95% confidence interval. . . . .	156
7.12	Graph showing $P_{ov}$ plotted against $q$ for random seeding test with both structures. . . . .	157
7.13	Graph showing $P_{ov}$ plotted against $V_{max}$ for random seeding test with both structures. . . . .	158

7.14	Empirical frequency curves for $q$ from physical model tests (black solid lines) compared with expected distributions for different levels of overtopping. a. TS01. b. TS02. c. TS03. d. TS05 . . . . .	159
7.15	Empirical frequency curves for $q$ from physical model tests (black solid lines) compared with expected distributions for different levels of overtopping. a. TS01. b. TS02. c. TS05. d. TS07 . . . . .	161
7.16	Empirical frequency curves for $P_{ov}$ from physical model tests (black solid lines) compared with expected distributions for different levels of overtopping. a. TS01. b. TS02. c. TS03. d. TS05 . . . . .	162
7.17	Empirical frequency curves for $P_{ov}$ from physical model tests (black solid lines) compared with expected distributions for different levels of overtopping. a. TS01. b. TS02. c. TS05. d. TS07 . . . . .	163
7.18	Empirical frequency curves for $V_{max}$ from physical model tests (black solid lines) compared with expected distributions for different levels of overtopping. a. TS01. b. TS02. c. TS03. d. TS05 . . . . .	164
7.19	Empirical frequency curves for $V_{max}$ from physical model tests (black solid lines) compared with expected distributions for different levels of overtopping. a. TS01. b. TS02. c. TS05. d. TS07 . . . . .	166
7.20	Relative error of $q$ for Random Seeding and Same Seeding tests. a. Smooth Slope. b. Vertical Wall. . . . .	167



# List of Tables

2.1	Breaking classification according to surf similarity parameter . . . . .	10
3.1	Incident wave conditions prescribed at the paddle for the JONSWAP spectra random wave laboratory tests . . . . .	42
3.2	Measured incident wave conditions at structure toe for the JONSWAP spectra random wave laboratory tests . . . . .	42
3.3	Overtopping parameters measured during laboratory wave tests . . . . .	47
4.1	Overtopping parameters for tests with varying number of waves . . . . .	62
4.2	CDF parameters for $q$ . . . . .	75
4.3	Results of the one sample K-S test for $q$ . . . . .	78
4.4	CDF parameters for $P_{ov}$ . . . . .	78
4.5	Results of the one sample K-S test for $P_{ov}$ . . . . .	81
4.6	CDF parameters for $V_{max}$ . . . . .	84
4.7	Results of the one sample K-S test for $V_{max}$ . . . . .	84
5.1	Incident wave conditions for the JONSWAP spectra random wave laboratory tests, and measured overtopping . . . . .	88
5.2	Results of the K-S test for distribution of $V_{ov}$ comparing physical model with MOBC tests and empirical formulae. . . . .	98
5.3	Results showing the percentage of the K-S tests that achieved the null hypothesis by comparing empirical formulae with distribution of $V_{ov}$ from ROBC tests. The shape factor ( $b_t$ ) of each test is also compared with the shape factor ( $b_w$ ) for each empirical method to show the percentage of over and under prediction. . . . .	100
5.4	Results of the K-S test for distribution of $V_{ov}$ comparing empirical formulae with 10 randomly selected ROBC tests. . . . .	104
6.1	Distribution parameters and results of K-S test for $q$ using a JONSWAP and PM spectra with $H_{m0} = 0.04\text{m}$ , $T_p = 1.32\text{s}$ and $R_c = 0.17\text{m}$ . . . . .	109
6.2	Distribution Parameters and results of K-S test for $P_{ov}$ using a JONSWAP and PM spectra with $H_{m0} = 0.04\text{m}$ , $T_p = 1.32\text{s}$ and $R_c = 0.17\text{m}$ . . . . .	109
6.3	Distribution Parameters and results of K-S test for $V_{max}$ using a JONSWAP and PM spectra with $H_{m0} = 0.04\text{m}$ , $T_p = 1.32\text{s}$ and $R_c = 0.17\text{m}$ . . . . .	109
6.4	Structural geometry in the numerical domain . . . . .	112
6.5	Incident wave conditions for the JONSWAP spectra random wave numerical tests . . .	112
6.6	Results of the one sample K-S test based on $q$ for various values of $\xi_{m-1,0}$ . . . . .	118
6.7	Results of the one sample K-S test based on $P_{ov}$ for various values of $\xi_{m-1,0}$ . . . . .	119
6.8	Results of the one sample K-S test based on $V_{max}$ for various values of $\xi_{m-1,0}$ . . . . .	123
6.9	Incident wave conditions for the JONSWAP spectra random wave numerical tests based on $K_n$ . . . . .	124
6.10	Results of the one sample K-S test based on $q$ for various values of $K_n$ . . . . .	131
6.11	Results of the one sample K-S test based on $P_{ov}$ for various values of $K_n$ . . . . .	133

6.12	Results of the one sample K-S test based on $V_{max}$ for various values of $K_n$ . . . . .	133
7.1	Incident wave conditions prescribed at the paddle for the JONSWAP spectra random wave laboratory tests . . . . .	136
7.2	Incident wave conditions measured at the toe for the JONSWAP spectra random wave laboratory tests . . . . .	139
7.3	Relative depths at the paddle . . . . .	140
7.4	Natural Periods of the Experimental Setup . . . . .	143
7.5	Percentage variation in $Q^*$ for same seeding tests . . . . .	149
7.6	Percentage variation in $H_{m0}$ for same seeding tests . . . . .	150
7.7	Distribution parameters and results of the one sample K-S test for $q$ for smooth slope .	160
7.8	Results of the one sample K-S test for $q$ for vertical wall . . . . .	161
7.9	Distribution parameters and results of the one sample K-S test for $P_{ov}$ on smooth slope	163
7.10	Results of the one sample K-S test for $P_{ov}$ on vertical wall . . . . .	163
7.11	Results of the one sample K-S test for $V_{max}$ on smooth slope . . . . .	165
7.12	Results of the one sample K-S test for $V_{max}$ on vertical wall . . . . .	165

## Nomenclature

$a$	[ $m$ ]	Amplitude
$a_w$	[-]	Weibull distribution scale factor
$a'$	[-]	Weibull scale factor correction coefficient
$b_w$	[-]	Weibull distribution shape factor
$C$	[ $m/s$ ]	Wave celerity
$C2 \left( \frac{H_{m0}}{H_{1/10}} \right)$	[-]	Nørgaard et al. (2014) formula correction term
$D_n$	[-]	Absolute maximum difference for K-S test
$d$	[ $m$ ]	Water depth
$d_p$	[ $m$ ]	Water depth at paddle
$d_t$	[ $m$ ]	Water depth at structure toe
$d_{tb}$	[ $m$ ]	Water depth at breaking
$d'$	[-]	Relative depth ratio
$g$	[ $m/s^2$ ]	Gravitational acceleration
$Fr$	[-]	Froude Number
$f$	[ $Hz$ ]	Frequency
$f_p$	[ $Hz$ ]	Peak frequency
$H$	[ $m$ ]	Individual wave height
$H_b$	[ $m$ ]	Wave height of breaking wave
$H_m$	[ $m$ ]	Mean wave height
$H_{m0}$	[ $m$ ]	Spectral significant wave height
$H_{m0b}$	[ $m$ ]	Spectral significant wave height at breaking
$H_{rms}$	[ $m$ ]	Root mean square wave height
$H_s$	[ $m$ ]	Significant wave height
$H_{tr}$	[ $m$ ]	Transition wave height
$H_{1/3}$	[ $m$ ]	Mean height of largest third of waves
$H_{1/10}$	[ $m$ ]	Mean height of largest 10% of waves
$h$	[ $m$ ]	Total water depth = $d_t + \eta$
$h^*$	[-]	Wave breaking parameter
$K_n$	[ $m$ ]	Roughness coefficient
$k$	[-]	Weibull distribution shape factor
$k_w$	[-]	Wave number
$L$	[ $m$ ]	Wave length
$L_b$	[ $m$ ]	Wave length of breaking wave
$L_{m-1,0}$	[ $m$ ]	Deep water spectral wave length
$m$	[-]	Foreshore Slope
$m0$	[ $m^2s$ ]	Total wave energy
$N_{comp}$	[-]	Number of components for FFT
$N_{FFT}$	[-]	Number of samples for FFT
$N_{Fr}$	[-]	Froude Number
$N_{ov}$	[-]	Number of overtopping events
$N_w$	[-]	Number of incoming waves
$n$	[-]	Number of points in dataset for RMSE
$P_{ov}$	[-]	Probability of overtopping
$P_v$	[-]	Exceedance probability of each overtopping volume
$Q$	[ $m^3$ ]	Flow discharge
$Q^*$	[-]	Dimensionless discharge
$q$	[ $m^3/s/m$ ]	Mean overtopping discharge
$R_c$	[ $m$ ]	Crest freeboard
$R_{u2\%}$	[ $m$ ]	2% Run-up height

$R^*$	[-]	Dimensionless freeboard
$S(\omega)$	$[m^2s]$	Energy density
$s_{m-1,0}$	[-]	Spectral wave steepness
$s_n$	[-]	Starting phase
$s_o$	[-]	Wave steepness
$s_{op}$	[-]	Peak wave steepness
$T$	[s]	Longest natural period
$T_m$	[s]	Mean wave period
$T_{m-1,0}$	[s]	Mean spectral wave period
$T_p$	[s]	Peak wave period
$T_{1/3}$	[s]	Significant period
$t$	[s]	Time
$U$	$[m/s]$	Depth-averaged flow horizontal velocity
$u$	$[m/s]$	Wind speed at an elevation of 19.5m
$V$	$[m/s]$	Velocity
$V_{max}$	$[m^3/m]$	Maximum individual overtopping volume
$V_{min}$	$[m^3/m]$	Minimum identifiable individual overtopping volume
$V_{ov}$	$[m^3/m]$	Individual overtopping volume
$x$	[m]	Horizontal abscissa
$z_B$	[m]	Bed level
$z_\varphi$	[-]	Standard Score
<b>Greek Symbols</b>		
$\alpha$	[°]	Angle of structure slope
$\alpha_p$	[-]	Phillips constant
$\beta$	[-]	Pierson-Moskovitz constant
$\eta$	[m]	Free surface elevation
$\Gamma$	[-]	Test decision for K-S test
$\gamma$	[-]	Peak enhancement factor of the JONSWAP spectra
$\lambda$	[-]	Weibull distribution scale factor
$\mu$	[-]	Mean
$\mu_x$	[-]	GEV distribution location factor
$\omega$	$[Hz]$	Angular frequency
$\rho$	$[kg/m^3]$	Water density
$\sigma$	[-]	Standard Deviation
$\sigma_x$	[-]	GEV distribution scale factor
$\sigma'$	[-]	Relative Error
$\tau_b$	$[Pa]$	Bottom shear stress
$\varphi$	[-]	Parameter of interest
$\xi_x$	[-]	GEV distribution shape factor
$\xi_b$	[-]	Surf similarity parameter of breaking wave
$\xi_{m-1,0}$	[-]	Spectral surf similarity parameter

## Abbreviations

BG	Battjes and Groenendijk (2000)
CDF	Cumulative Distribution Function
CLASH	Crest Level Assessment of coastal Structures by full scale monitoring, neural network prediction and Hazard analysis on permissible wave overtopping
FFT	Fast Fourier Transform
GEV	Generalised Extreme Value
JONSWAP	Joint North Sea Wave Project
K-S	Kolmogorov-Smirnov Test
MOBC	Measured Offshore Boundary Conditions
MWL	Mean Water Level
NLSWE	Non-Linear Shallow Water Equations
PDF	Probability Density Function
RANS	Reynolds-averaged Navier-Stokes Equations
ROBC	Reconstructed Offshore Boundary Conditions
SPH	Smooth Particle Hydrodynamics
SS	Smooth Slope
SWL	Still Water Level
VOF	Volume of Fluids
VW	Vertical Wall
WG	Wave Gauge



# Chapter 1

## Introduction

### 1.1 Motivations

It is estimated by the United Nations that more than 75% of the World's population live within the coastal zone (Reeve et al., 2004). It is due to the significant economic and social importance of these regions that coastal structures have been constructed throughout the World to shield harbours, ships and boats in port, as well as communities, habitats and beaches from the effect of wave action and currents.

These type of coastal structures are subjected to a variety of hydraulic phenomena, one of which is overtopping. This occurs when waves are sufficiently large that they run-up the structure and pass over the crest. This results in a breach of the coastal defence, which can result in flooding and damage to the area being protected.

There are a variety of issues that arise from overtopping, which fall into three general categories as shown below;

- It is a hazard to people occupying the area behind the seawall, which can result in serious injury and even fatalities, the risk of which is increased due to the lack of understanding of the dangers.
- It can cause damage to the property and infrastructure being defended which could result in large economic losses.
- It can cause damage to the structure itself rendering it ineffective and hence no longer acting as protection to the area in question (Allsop et al., 2005).

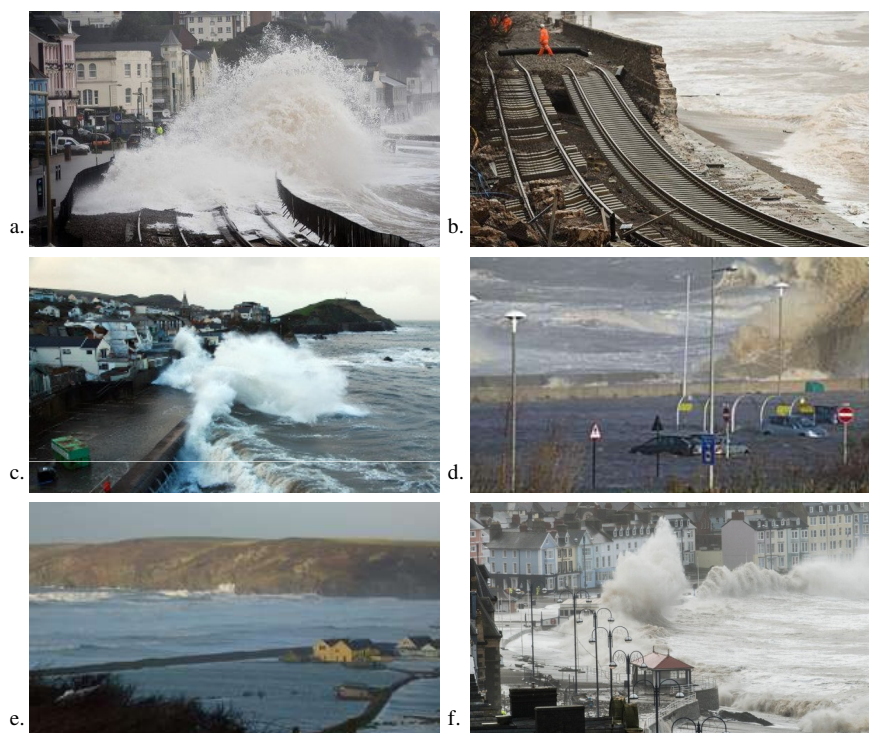


Figure 1.1: a. Example of overtopping at Dawlish, UK in Feb 2014. b. Subsequent damage to the railway line. c. Overtopping causing flooding at Ilfracombe, UK in Jan 2014. d. Overtopping causing flooding on The Wirral, UK in Feb 2014. e. Overtopping causing flooding in Pembrokeshire, UK in Feb 2014. f. Overtopping causing flooding in Aberystwyth, UK in Feb 2014.

To illustrate the destructive power of overtopping waves some examples are shown in Fig. 1.1. They all occurred throughout the winter of 2014, when the west coast of the United Kingdom experienced a number of severe storms which led to a large number of occurrences of overtopping resulting in both flooding and significant damage to structures.

Photos a and b, show the damage caused to the main railway line to Cornwall at Dawlish in Devon, where the overtopped water caused parts of the structure to be washed away (Network Rail, 2014). This damage resulted in repairs of £35m, and an estimated economic impact of upto £1.2bn (BBC, 2014a). The other photos (c.BBC (2014b), d.BBC (2014c), e.WalesOnline (2014) and f.Guardian (2014)) show flooding that occurred during the same period at various locations around the coast of Britain, resulting in damage of upto £135m across the country.

It is clear that the ability to accurately predict the probability of wave overtopping is of great importance and in the future, the continued increase in the population living in coastal areas, as well as the expected rise in sea levels and increase in extreme weather events, means that improved overtopping prediction is needed for effective coastal structures to be designed for the

future.

Overtopping has been studied in depth over the last 60 years, during this time the prediction methods for typical sea defence structures have been continuously developed. The three primary prediction methods available are empirical formulae, physical modelling and numerical modelling.

Empirical formulae were developed from field measurements, and physical models and are frequently used by engineers. Recently two artificial neural networks tools have been developed during the EU-programme CLASH (**C**rest **L**evel **A**ssessment of coastal **S**tructures by full scale monitoring, neural network prediction and **H**azard analysis on permissible wave overtopping). The official neural network was developed by Delft Hydraulics, with a second developed as part of the Ph.D work of Verhaeghe (2005) at Gent University. Both have been trained using a large database of laboratory tests and are able to take into account complex structural geometries. The Delft Hydraulics neural network is more user friendly, however a major advantage of the Gent neural network is the inclusion of tests which resulted in zero overtopping, making it the most comprehensive and accurate empirical predictive tool to date. Pullen et al. (2007) provides extensive guidelines on the applications of these predictive tools, including their associated uncertainties.

Numerical modelling is also frequently used to predict wave overtopping. Phase resolving models are particularly suitable as they can simulate individual overtopping events. Within this class of models, depth integrated ones are very popular, particularly when sloping structures are considered, due to their simplicity and low computational requirements. A number of models based on the Non-Linear Shallow Water Equations (NLSWE) have been proposed for wave overtopping prediction.

When this type of phase resolving model is used, free surface elevation and velocity time series are required at the seaward boundary, which should be prescribed close to the structure to maximise accuracy. In design applications, these might not be available. Frequently the modeller is provided with the incident energy density spectrum retrieved by a wave buoy or computed by a large scale spectral model such as SWAN (Booij et al., 1999). A time series will then be reconstructed from this spectrum to be used as boundary conditions. Since the energy density spectrum provides only information on the amplitude of the components, and generally a phase spectrum is not recorded for wave analysis, it is usually assumed that the phases of these components are randomly distributed. To create the randomly generated phases, an initial seed value is

required to generate a population of uniformly distributed random phases. By varying this value for each simulation a different time series will be produced.

There are two issues related to this procedure. First, this assumption implies a linear superposition of wave components that is strictly valid only for linear waves, an approximation typically valid in deep water. Despite this, the superposition is used in many existing intermediate and shallow water models proposed in the literature. Recent examples of such an assumption in the computation of run-up and overtopping are given in Zijlema et al. (2011), Shi et al. (2012), McCabe et al. (2011) and McCabe et al. (2013).

Second, from every energy density spectrum an infinite number of different wave series can be generated by changing the seeding of the random phase distribution. Evidence that this process plays an important role in the variability of the results is given in McCabe et al. (2011) for the run-up prediction and McCabe et al. (2013) for overtopping, in which a small number of tests with a very limited number of waves were conducted. The authors compared the different run-up heights and overtopping volumes resulting from different free surface time series at the boundary, all obtained by the same spectrum, and therefore the same energy. These initial results showed that the parameters under study significantly vary with the random seeding used, however due to the limitations of the results, a full analysis was not carried out.

Physical modelling is generally considered to be a reliable approach to predict overtopping at coastal structures, above all when complex layouts and wave conditions are considered. During CLASH, model and scale effects have been analysed (Franco et al., 2009, Geeraerts et al., 2009). However, similarly to numerical models a wave time series is required at the wave paddle. Again, this is usually unavailable, so a deep water incident energy density spectrum is provided. This introduces the issue that an infinite number of wave time series are possible in the same way as the numerical model. Although, Pullen et al. (2007) describes some of the uncertainty in laboratory experiments, based on several studies, this particularly phenomenon has never been investigated.

Overall the uncertainty in the overtopping prediction introduced by the coupling of both numerical models and physical models with spectral data is under-studied. In particular, in numerical modelling, the lack of specific study on the uncertainty in numerical models is one of the reasons why, in Pullen et al. (2007) this approach is not considered as reliable as the other two approaches.

The purpose of this study is therefore to examine and quantify the variability of the overtop-

ping parameters in coastal numerical and physical models due to the reconstruction of boundary conditions from spectral data.

## **1.2 Research Objectives**

The aim of this research is to investigate the uncertainty in overtopping prediction due to the reconstruction of wave time series created from offshore spectral boundary conditions. This will be done in the following way:

1. The performance of the overtopping prediction of a NLSWE model will be validated using measured offshore boundary conditions obtained from physical modelling.
2. Monte Carlo simulations will be carried out to assess the uncertainty in the overtopping prediction of the NLSWE model when reconstructed offshore boundary conditions are used.
3. Further physical modelling will be carried out to investigate the effect on overtopping of the random seeding of the wave time series at the wave paddle.

The outcome of this research will be recommendations for the improvement of standard procedures when predicting overtopping of random waves using these methods.

## **1.3 Thesis Outline**

The subsequent chapters of this thesis are divided as follows:

Chapter 2 will present a background to waves including a description of the principles of small amplitude wave theory, the shallow water approximation, and irregular wave theory. It will then examine the principle of overtopping, and the available prediction methods. Finally, it will present the principles of uncertainty and the methods to allow its quantification which will be utilised in the rest of the work.

Chapter 3 will describe the first set of physical model experiments carried out at HR Wallingford. The results from which are then used to examine the ability of a NLSWE model to replicate these, and allow a validation of the model for this work.

Chapter 4 will introduce and quantify variability in the commonly used overtopping parameters due to the use of offshore spectral boundary conditions in the NLSWE model based on the wave

conditions and single structure used in the physical model tests.

Chapter 5 will investigate the reconstruction of the wave height distribution due to the offshore spectral boundary conditions in the numerical model, followed by the effect that this has on the distribution of individual volumes.

Chapter 6 will extend the work of the previous chapters by carrying out further numerical tests looking at the variability due to the offshore spectral boundary conditions, this time a range of different sloped structures and wave conditions will be modelled to examine if this has an additional effect, and allow more generalised conclusions to be made.

Chapter 7 will present a second set of laboratory experiments, this time carried out at the University of Nottingham, examining the uncertainty in the prediction of overtopping discharge due to the spectral boundary conditions used at the wave paddle in physical modelling.

Finally, Chapter 8 will summarise the main findings from this research and give some recommendations for further research in this area.

# Chapter 2

## Background

### 2.1 Introduction

This chapter will first examine the various theories and models that have been derived and developed by others previously to describe the propagation of waves in shallow water, and the prediction of wave overtopping of coastal structures. It will then present the principles of uncertainty, including providing relevant examples for this work. It will then describe available methodologies for quantifying these uncertainties that will be used in this work.

### 2.2 Wave Characteristics

Waves occur in the ocean when the water is acted on by an external force, usually wind, which causes a disturbance of the free surface. These then propagate due to the fluid properties of water. The simplest form is the sinusoidal wave, which can be seen in Fig. 2.1, and used here to define the basic properties of waves.

Firstly, MWL denotes the mean water level (also sometimes classified as SWL, or still water level), which is the average height of the water surface over a long period of time. The high water levels of the waves are known as crests, with the low water levels known as troughs. The total vertical distance between a crest and a trough is known as the wave height,  $H$ . The wave amplitude,  $a$ , is the height of the wave crest above the MWL. The water surface elevation is the distance between the MWL and any particular point of interest on the wave, and is denoted by  $\eta$ . The wavelength,  $L$ , is the horizontal distance from any point on one wave to the same

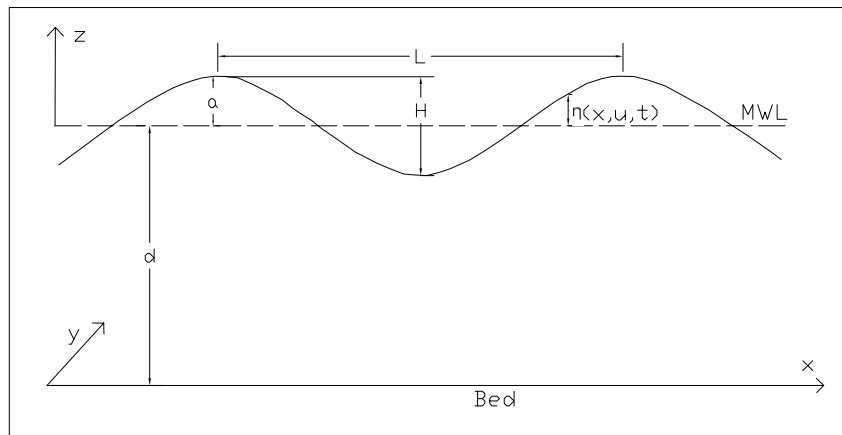


Figure 2.1: Wave definition sketch based on a regular sine wave

point on the next wave. The wave period,  $T$ , is the length of time between consecutive crests of waves as they pass a fixed point. The waves propagate with a velocity, or celerity,  $C$ . The inverse of the wave period is the wave frequency,  $f$ . The depth of the water to the MWL is denoted by  $d$ .

### 2.2.1 Small Amplitude Wave Theory

The simplest mathematical theory to describe ocean wave behaviour is the small amplitude wave theory formulated by Airy (1845). This theory describes the propagation of waves above a horizontal bottom where the wave amplitude is small in comparison to the wave length and the water depth, similar to that shown in Fig. 2.1. This relies on a number of assumptions including:

- Constant depth
- Water is incompressible
- Water is inviscid
- Irrotational motion
- 2 dimensional motion

The basis of this theory is the existence of a velocity potential that satisfies the Laplace equation. The surface elevation of the waves can be described by a sinusoidal curve, and is a function of the horizontal position,  $x$ , and of the time,  $t$ . This results in the surface elevation denoted as  $\eta$  being expressed.

$$\eta = (x, t) = a \cos(k_w x - \omega t), \quad (2.1)$$

where  $k_w$  is the wave number, defined as the measurements of repeating units of a propagating wave, and is determined by its relation with the wave length,  $L$ , and can be expressed as  $k_w = 2\pi/L$ .  $\omega$  is the angular frequency, and relates to the wave frequency by  $\omega = 2\pi f$ .

The relationship between  $k_w$  and  $\omega$  is represented by the dispersion relation.

$$\omega^2 = g k_w \tanh(k_w d). \quad (2.2)$$

This relationship is of particular importance to coastal engineers because it provides a link between wave period (which remains constant in any water depth), wavelength (which alters) and water depth; and can therefore be used for the basis of wave transformation across different water depths. The celerity,  $C$  of a travelling wave in deep water is represented by the ratio between  $L$  and  $T$ ,  $C = L/T = k_w/\omega$ .

### 2.2.2 Shallow Water Approximation

When considering the formation and propagation of waves it is common to classify the depth of the water present using three different terms; deep water, intermediate water and shallow water. The formal classification of these terms is given by the relative depth ratio

$$d' = \frac{d}{L}. \quad (2.3)$$

These classifications are based on the movement of water particles whose vertical and horizontal component of velocity are dependent on the water depth. In deep water, the motion of the particles is circular, and tends towards horizontal in vanishingly shallow waters. This is shown in Fig. 2.2.

### 2.2.3 Wave Breaking

As waves approach shallow water conditions, the transition from deep water causes the waves to shoal. The wave period remains constant, whilst the wavelength decreases and the wave height increases. This causes an asymmetry in the profile of the wave, and when the wave height becomes too large to sustain the shape of the wave, then breaking occurs.

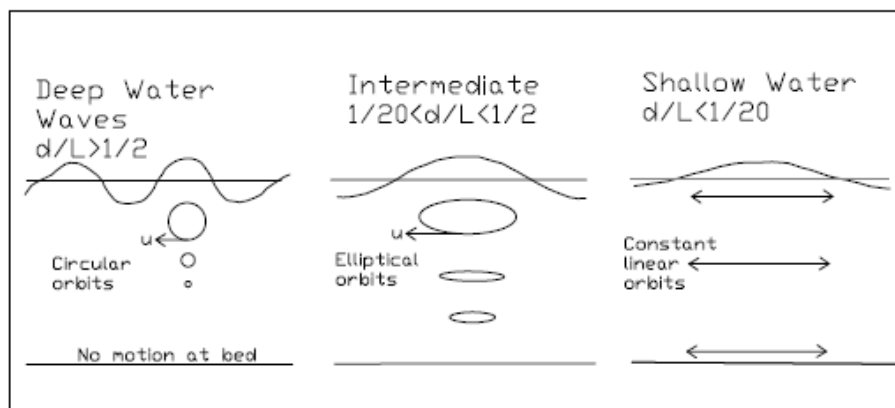


Figure 2.2: Water particle motion at different water depths

Table 2.1: Breaking classification according to surf similarity parameter

Surf Similarity Parameter	Type of Wave Breaking
$0.2 < \xi_b$	Spilling
$0.2 < \xi_b < 2 - 3$	Plunging
$\xi_b \pm 2 - 3$	Collapsing
$\xi_b > 2 - 3$	Surging

The combination of foreshore or structure slope and wave steepness produces certain types of breaking. These breaking waves can be classified into four different types: spilling breakers, plunging breakers, collapsing breakers and surging breakers, illustrated in Fig. 2.3 (USACE, 2002). The breaker type can be determined by the surf similarity number

$$\xi_b = \frac{\tan \alpha}{\sqrt{(H_b/L_b)}}, \quad (2.4)$$

where  $\alpha$  is the slope angle,  $H_b$  is the wave height of the breaking wave and  $L_b$  is the wavelength of the breaking wave. The waves can then be classified according to Table 2.1.

### 2.3 Irregular Waves

The wave characteristics discussed in section 2.2 were based on regular waves, which very rarely occur in reality. Real sea waves appear as random sequences, however, they can be analysed by assuming they consist of an infinite number of sinusoidal waves each with different amplitude, frequency and direction (Goda, 1985). They can be analysed using techniques in two domains;



Figure 2.3: Classification of Breaker Types

in the time domain or in the frequency domain.

It should be noted here that this work is concerned only with the short-term analysis of waves, which covers short periods of time such as during a storm, rather than long term over months, years or more.

### 2.3.1 Analysis in the Time Domain

In the time domain, wave analysis can be carried out using a zero-upcrossing or zero-downcrossing method. For both methods, firstly the mean water level of a random wave signal is deduced and defined as the zero line. For the upcrossing method, the first point at which the surface profile crosses the zero line in the upward direction is found. This point is taken as the start of one individual wave. The surface profile of the wave is then followed to find the next point where it passes the zero line going upwards. This point defines the end of this first wave and the beginning of the next. If the horizontal axis represents time, the distance between these two points is the wave period. The wave height can then be obtained by measuring the vertical distance between the highest and lowest point of the defined wave ignoring small bumps that do not cross the zero line. Fig. 2.4 shows a sequence of waves with the heights and periods being defined using this zero-upcrossing method.

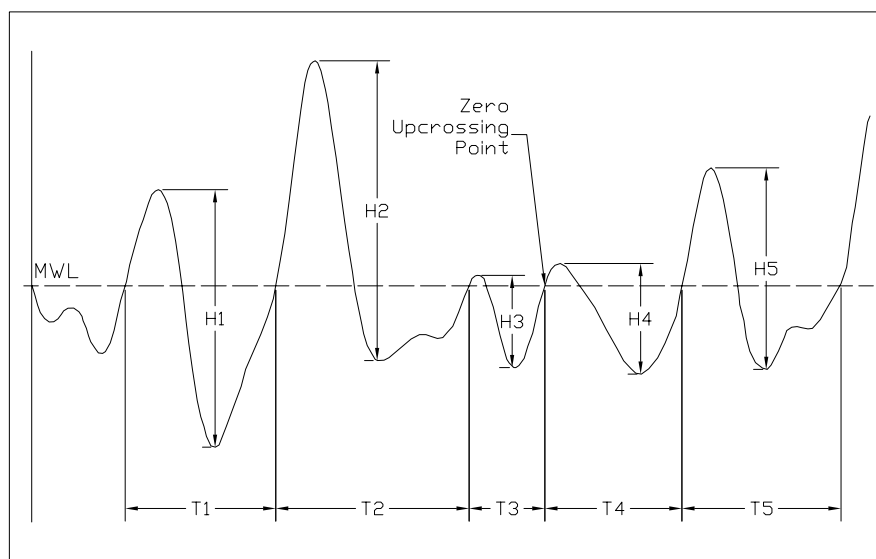


Figure 2.4: Random waves shown in the time domain

For the downcrossing method, the same procedure is followed but the initial point is taken as where the surface profile crosses the zero line downwards. The end of this wave is next point that this occurs. Both methods will yield the same statistical results, except in the surf zone where the zero-downcrossing will produce results with slightly shorter wave periods to those obtained using zero-upcrossing. This variation is caused by the ability of the zero-downcrossing method to reproduce the development of secondary water surface fluctuations which are a characteristic of shallow water. The wave height results however will not be affected by this.

It is useful to represent these waves of different heights and periods by some general parameters. For a coastal engineer, it is the larger waves that are of most importance. This led to the development of the concept of the significant wave height ( $H_s$ ), which is defined as the mean of the highest third of the waves present, noted as  $H_{1/3}$ . The wave period in this case is usually defined by the average period of all the waves ( $T_m$ ), or the significant period ( $T_{1/3}$ ) which is the mean period of the highest third of the waves used to obtain  $H_s$ .

### 2.3.2 Analysis in the Frequency Domain

In the frequency domain, a random wave signal can be split into the component sinusoidal waves of different frequencies. These provide an energy density spectrum

$$S(\omega) = \left| \int_{-\infty}^{\infty} \eta(t) e^{i\omega t} dt \right|^2, \quad (2.5)$$

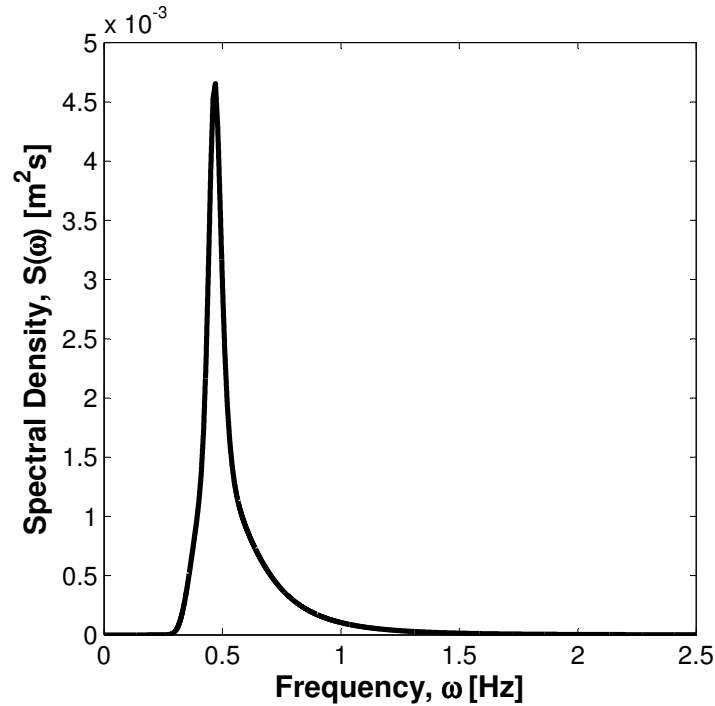


Figure 2.5: Example of a wave spectrum

where  $\omega = 2\pi/f$  is the angular frequency,  $f$  being the ordinary frequency and  $S(\omega)$  is the energy density function.

The free surface can be described as a sum of harmonic components

$$\eta(t) = \sum_{n=1}^{\infty} a_n \cos(\omega_n t + s_n), \quad (2.6)$$

where  $n$  is the index of the component,  $a_n$  is the amplitude of the  $n$ -th component and  $s_n$  is its starting phase. Using this decomposition it is possible to relate the spectral energy density of the  $n$ -th component to its amplitude,

$$S(\omega_n) = \frac{1}{2} \rho g a_n^2 / \Delta\omega_n. \quad (2.7)$$

Here  $\Delta\omega_n = \omega_{n+1} - \omega_n$  is the frequency interval.

An example of a wave spectrum is shown in Fig. 2.5. Longuet-Higgins (1952) showed that the approximately linear behaviour of waves in deep water allows for a theoretically sound statistical description of the wave characteristics, based on a Gaussian distribution of instantaneous values of surface elevation, resulting in a Rayleigh distribution of wave heights. This allows the estimation of heights and periods of representative waves from the wave spectra. Firstly, the

representative value of the total wave energy ( $m_0$ ) is obtained by integrating the full wave spectra (Goda, 1985). This integral, is by definition, equal to the variance of the surface elevation. The root-mean-square (rms) value of the surface elevation can be given by

$$\eta_{rms} = \sqrt{\bar{\eta}^2} = \sqrt{m_0} \quad (2.8)$$

where  $\bar{\eta}$  indicates the mean value of  $\eta$ . As mentioned, when the wave height follows the Rayleigh distribution, this rms value relates to the heights of representative waves. In particular the significant wave height can be obtained

$$H_{1/3} \simeq H_{m0} = 4.004\eta_{rms} = 4.004\sqrt{m_0}. \quad (2.9)$$

The notation  $H_{m0}$  is used to distinguish the significant wave height being estimated from the spectral information, rather than the zero-crossing method.

The wave period can be specified in a number of ways, firstly, the peak period ( $T_p$ ), which corresponds to the period at the peak of the spectra. The wave period used for some prediction formulae is the spectral period ( $T_{m-1,0} = m_{-1}/m_0$ ), which is more stable than  $T_p$  and gives more weight to the longer wave periods.

### 2.3.3 Spectral Shape

Equations 2.5 – 2.9 give certain statistical properties and parameters associated with wave energy spectra. However, they do not give a description of what type of spectrum is expected in the field. There are many forms of wave energy spectra available, which are based on one or more parameters such as wind speed, significant wave height, wave period and shape factors amongst other, and which one is most suitable depends on the individual conditions present.

An equation for the equilibrium range of the spectra for a fully developed sea, i.e. when energy input from the wind to the waves is equalled by the dissipation of wave energy in breaking, was developed by Phillips (1958), and is shown in equation Eq. 2.10.

$$S(\omega) = \alpha_p \frac{g^2}{\omega^5} \quad (2.10)$$

where  $\alpha_p$  is the Phillips constant,  $\simeq 8 \times 10^{-3}$ ,  $g$  is the gravitational acceleration and  $\omega$  is the angular frequency.

Pierson and Moskowitz (1964) proposed a spectrum, in which they assumed that if the wind blew steadily for a long time over a large area, then the waves will eventually reach the point of equilibrium. This was developed by analysing wind and wave data from these fully developed seas. It is given in terms of wind speed to determine wave growth

$$S(\omega) = \alpha_p \frac{g^2}{\omega^5} \exp \left[ \beta \left( \frac{g}{u\omega} \right)^4 \right]. \quad (2.11)$$

where  $\beta$  has the value of 0.74, and  $u$  is the wind speed at an elevation of 19.5m. As part of JONSWAP (**JO**int **N**orth **S**ea **WA**ve **O**bservation **P**roject) Hasselmann et al. (1973) analysed data collected and found that the wave spectrum is never fully developed. It continues to develop through non-linear, wave-wave interactions over very long times and distances. This resulted in the addition of an artificial factor added to the Pierson-Moskowitz spectrum in order to improve the fit to their measurements. The JONSWAP spectra is therefore a Pierson-Moskowitz spectrum multiplied by an extra peak enhancement factor ( $\gamma$ ) which controls the sharpness of the spectral peak.

These spectra includes the wind speed as the parameter for the purpose of wave forecasting, but they can be rewritten in approximate form in terms of the parameters of wave height and period as follows (Goda, 1985):

$$S(\omega) = \beta_j H_{1/3}^2 T_p^{-4} \omega^{-5} \exp[-1.25(T_p \omega)^{-4} \gamma \exp[-(T_p \omega - 1)^2 / 2\sigma^2]], \quad (2.12)$$

$$\beta_j = \frac{0.0624}{0.230 + 0.0336\gamma - 0.185(1.9 + \gamma)^{-1}} [1.094 - 0.01915 \ln \gamma], \quad (2.13)$$

$$T_p \simeq T_{1/3} / [1 - 0.132(\gamma + 0.2)^{-0.559}], \quad (2.14)$$

$$\sigma \simeq \begin{cases} 0.07 : & \omega \leq \omega_p \\ 0.09 : & \omega \geq \omega_p. \end{cases} \quad (2.15)$$

## 2.4 Types of Structures

Wave overtopping is of concern for structures that are constructed primarily to protect against flooding. Other structures where overtopping may be a concern are those built to protect areas

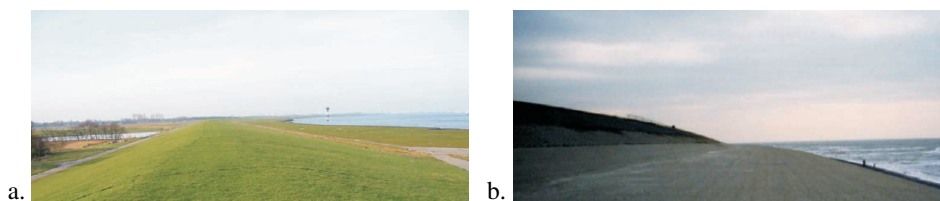


Figure 2.6: a. Grass covered dyke. b. Asphalt covered dyke.

of water for ship navigation, or mooring. This work is primarily concerned with two of the three principal types of sea defences; smooth sloping sea dykes and vertical walls.

### 2.4.1 Smooth Slopes

Smooth sloped structures, or sea dykes are usually onshore structures with the principal function of protecting low lying areas behind the structure from flooding. They are usually impermeable with a constant gradient slope, and are often constructed as a mound of fine materials, such as sand and clay. The seaward slope is often quite gentle to reduce the wave run-up, however this requires large areas of land which are not always available so steeper slopes may sometimes be more appropriate. The surface of the dyke is then armoured with grass, asphalt, stones or concrete slabs to protect from wave action and erosion. Some examples of dykes are shown in Fig. 2.6 (Pullen et al., 2007).

This type of structure is commonly found along the European coast, as they are structurally simple to design, and can offer good functionality and durability when designed and monitored properly.

### 2.4.2 Vertical Walls

Along urban frontages, or close to ports where space is at a premium, vertical seawalls are commonly used to protect areas from heavy wave action. Similarly to sea dykes, their principal function is to prevent or alleviate overtopping and therefore flooding of the land behind. They are usually constructed as massive concrete gravity walls, or tied walls using steel or concrete piling.

Historically, vertical seawalls have been built due to their simplicity to design and construction. They work well in exposed situations as they deflect wave energy away from the coast. Examples of vertical walls are shown in Fig. 2.7 (Pullen et al., 2007).

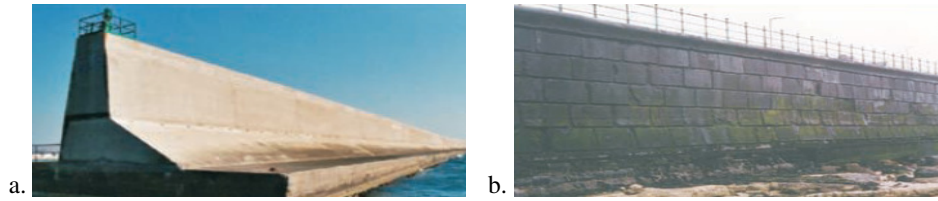


Figure 2.7: a. Modern concrete caisson. b. Stone block-work wall.

## 2.5 Prediction of Overtopping

Overtopping occurs when waves run-up the face of a seawall. If this run-up is large enough, the water will reach and pass over the crest of the wall. When this is a continuous sheet of water, this is known as "green water" overtopping. When a vertical structure is in place, this may also occur when a wave impacts the front of the wall and a vertical jet of water is carried over the crest.

Another form of overtopping occurs when waves break on the seaward face of a structure and produce significant quantities of splash. These droplets can then be carried over the structure crest (Pullen et al., 2007), referred to as "splash overtopping".

Throughout the last 60 years, numerous investigations have been carried out researching wave overtopping of coastal structures. During this time suitable methodologies for the prediction of overtopping have been continuously developed. This has resulted in the development of the three main approaches: physical modelling using laboratory tests, empirical formulae available in literature or numerical simulation of the hydraulic response of the structure.

### 2.5.1 Empirical Methods

Over the years, the overtopping performance of coastal structures under random waves has been studied extensively using physical models. These results, along with those collected from field measurements have been used to produce forms and coefficients of empirical formulae based on simplified representations of the physics present. In recent years further developments have been made to the empirical methods to increase the accuracy of their predictions, such as the EurOtop Manual (Pullen et al., 2007), which uses the results from research around Europe, including at existing breakwaters to predict overtopping based on the database of this information. The empirical methods developed predict both the green water and splash overtopping, since both were measured during model tests on which the prediction methods are based.

### Mean Overtopping Discharge

There are a number of response parameters of interest relating to overtopping, the most commonly used is the mean wave overtopping discharge. This is the mean discharge per linear metre of width. It is usually measured in  $\text{m}^3/\text{s}/\text{m}$ , although can also be measured in  $\text{l}/\text{s}/\text{m}$ , and is given the nomenclature,  $q$ . It is the easiest parameter to measure experimentally, and most of the other parameters are related in some way to this overtopping discharge.

As it is relatively straightforward to measure mean overtopping discharge, large numbers of tests have been performed all over the world, both for generic and site specific conditions. Some of these series of tests have been used to develop the empirical methods for the prediction of overtopping. Usually, the empirical formulae are applicable to typical structures only, such as; smooth slopes, rubble mound structures or vertical walls. The principal empirical formula describing wave overtopping is

$$\frac{q}{\sqrt{gH_{m0}^3}} = a \exp(-bR_c/H_{m0}). \quad (2.16)$$

It is an exponential function relating the dimensionless overtopping discharge  $Q^* = \frac{q}{\sqrt{gH_{m0}^3}}$  and the relative crest freeboard  $R^* = R_c/H_{m0}$ .

### Smooth Slopes

There are a large number of different empirical prediction methods for the overtopping discharge of smooth impermeable slopes designed to dissipate a large amount of wave energy by causing wave breaking. In this work, the formulae chosen to be used are those that provide a deterministic prediction in Pullen et al. (2007). It should also be noted that the original formulae include influence factors for a number of criteria such as berms, or oblique waves. These influences have not been assessed as part of this work, resulting in them all having a value of 1 and are therefore removed from the formulae in this case. These formulae will be used for validation of the numerical model as well a comparison with the physical model results. The formulae are based on a number of different parameters, which are defined in Fig. 2.8.

In assessing the overtopping on sloped structures, it is first necessary to distinguish whether the waves are likely to be plunging or surging up the structure. This results in two different

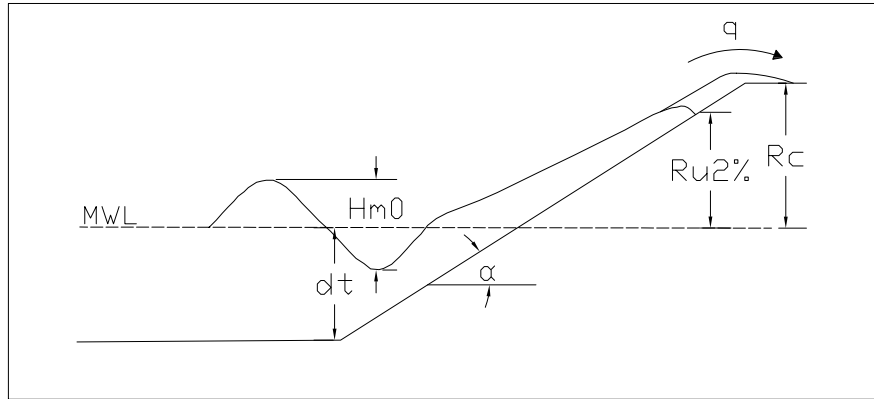


Figure 2.8: Definition of run-up and overtopping parameters on smooth slope structure

formulae depending on conditions. Firstly for  $\xi_{m-1,0} < 5$  the formula

$$\frac{q}{\sqrt{gH_{m0}^3}} = \frac{0.067}{\sqrt{\tan \alpha}} \xi_{m-1,0} \exp\left(-4.3 \frac{R_c}{\xi_{m-1,0} H_{m0}}\right) \quad (2.17)$$

can be used, with a maximum of

$$\frac{q}{\sqrt{gH_{m0}^3}} = 0.2 \exp\left(-2.3 \frac{R_c}{H_{m0}}\right). \quad (2.18)$$

When  $\xi_{m-1,0} > 7$ , then

$$\frac{q}{\sqrt{gH_{m0}^3}} = 0.21 \exp\left(-\frac{R_c}{H_{m0}(0.33 + 0.022\xi_{m-1,0})}\right) \quad (2.19)$$

For conditions where  $5 < \xi_{m-1,0} < 7$  then linear interpolation between the results of the two formulae should be used (Pullen et al., 2007).

### Vertical Walls

Again, there are a variety of different empirical prediction methods for the overtopping discharge of vertical walls. As before the formulae chosen to be used are those that provide a deterministic prediction in Pullen et al. (2007). These formulae will be used for comparison with the physical model results. The formulae are based on a number of different parameters, which are defined in Fig. 2.9.

For the assessment of overtopping at vertical walls, instead of identifying the breaker type, the wave-structure interaction must be identified. These can be divided into two separate categories;

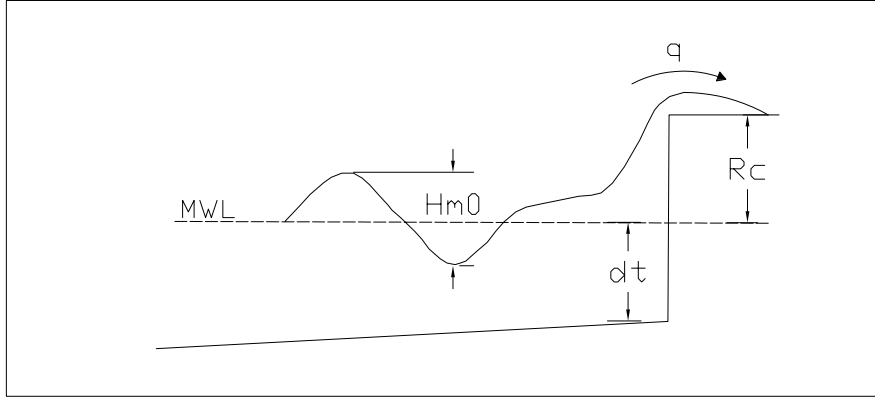


Figure 2.9: Definition of wave impact and overtopping parameters on vertical wall structure

non-impulsive or pulsating and impulsive conditions.

Non-impulsive conditions occur when the waves at the structure are relatively small in relation to the local water depth, or of low wave steepness. This type of wave overtops by running up and over the crest of the wall. Impulsive conditions occur when waves are large in relation to the water depth at the structure. In these cases, some of the waves will break violently against the wall, which results in a violent uprushing jet of water causing overtopping.

When the toe of the vertical wall is submerged, then the type of conditions can be established by the wave breaking parameter,  $h_*$ , where

$$h_* = 1.35 \frac{d_t}{H_{m0}} \frac{2\pi d_t}{gT_{m-1,0}^2}. \quad (2.20)$$

Non-impulsive waves dominate at the wall when  $h_* > 0.3$ , whereas impulsive waves dominate when  $h_* < 0.2$ . The transition between these conditions, where both breaking and non-breaking waves occur, lies between  $0.2 \leq h_* \leq 0.3$ . In this region, the overtopping should be predicted using both conditions and the worse value assumed. For non-impulsive conditions ( $h_* > 0.3$ ) then

$$\frac{q}{\sqrt{gH_{m0}^3}} = 0.04 \exp\left(-1.8 \frac{R_c}{H_{m0}}\right), \quad (2.21)$$

or for impulsive conditions ( $h_* < 0.2$ )

$$\frac{q}{h_* \sqrt{gd_t^3}} = 2.8 \times 10^{-4} \left(h_* \frac{R_c}{H_{m0}}\right)^{-3.1}. \quad (2.22)$$

### Overtopping Volumes

Due to the random nature of waves, there is no constant discharge over the crest of a structure during overtopping i.e. larger waves will push large amounts of water over a structure in a short period of time, whilst smaller waves will not produce any overtopping at all. When the safety of individuals or property to the direct impact of an overtopping wave is to be addressed, the distribution of the individual overtopping volumes ( $V_{ov}$ ) and, in particular, the maximum expected individual overtopping volume ( $V_{max}$ ), are used.

A significant amount of work based on physical modelling has been carried out by a number of researchers in order to describe the probability distribution of the overtopping volumes ( $V_{ov}$ ) for sloped structures. Initial work by van der Meer and Janssen (1994) found that the distribution of  $V_{ov}$  can be described by a two parameter Weibull distribution

$$P_v = P(\underline{V_{ov}} \leq V_{ov}) = 1 - \exp \left[ - \left( \frac{V_{ov}}{a} \right)^{b_w} \right], \quad (2.23)$$

where  $P_v$  is the exceedance probability of each overtopping volume. The shape of the distribution is determined by  $b_w$  known as the shape factor. In the case of smooth slopes an average value of  $b_w = 0.75$  was chosen. The scale factor,  $a_w$ , which describes the magnitude of the individual volumes and depends on the wave attack parameters and percentage of overtopping waves can be calculated using

$$a_w = 0.84 T_m \frac{q}{P_{ov}} \quad (2.24)$$

where  $q$  is the overtopping discharge,  $P_{ov}$  is the probability of overtopping and  $T_m$  is the mean wave period. A more detailed analysis by Besley (1999), considering a range of different structures, found fairly consistent behaviour for all structures tested, confirming the findings of van der Meer and Janssen (1994). The van der Meer and Janssen (1994) formulation for the scale and shape factors has been included in Pullen et al. (2007).

Recently further work looking at the individual overtopping volumes on smooth slopes has been carried out. Using laboratory tests of low crested, relatively steep slopes, Victor et al. (2012) found that the individual volumes still followed a Weibull distribution but with different values for the Weibull parameters. This was found to be dependant on the slope of the structure and

the relative freeboard following

$$b_w = \exp\left(-2.0\frac{R_c}{H_{m0}}\right) + (0.56 + 0.15 \cot \alpha), \quad (2.25)$$

where  $R_c$  is the crest freeboard,  $H_{m0}$  is the spectral significant wave height and  $\alpha$  is the angle of the sloped structure. In addition to the new formula for  $b_w$ , a modification to how  $a_w$  is calculated was also obtained. The value of 0.84 in the van der Meer and Janssen (1994) formula for  $a_w$ , is replaced with the coefficient  $a'$  that is defined

$$a' = 1.13 \tanh(1.32b_w). \quad (2.26)$$

Nørgaard et al. (2014) investigated depth-limited wave conditions and found that for non-Rayleigh distributed wave heights, the Victor et al. (2012) shape factor over-predicted the individual overtopping volumes, so a correction term was developed,

$$b_w = \exp\left(-2.0\frac{R_c}{H_{m0}}\right) + (0.56 + 0.15 \cot \alpha)C2 \left(\frac{H_{m0}}{H_{1/10}}\right) \quad (2.27)$$

where

$$C2 \left(\frac{H_{m0}}{H_{1/10}}\right) = \begin{cases} 1 & \text{for } H_{m0}/H_{1/10} \leq 0.848 \text{ or } H_{m0}/d_t \leq 0.2 \\ -10.8 + \frac{H_{m0}}{H_{1/10}} 13.9 & \text{for } H_{m0}/H_{1/10} \geq 0.848 \text{ and} \\ H_{m0}/d_t \geq 0.2 & \end{cases} \quad (2.28)$$

$H_{1/10}$  is the mean of the largest 10% of the waves and  $d_t$  is the water depth at the toe of the structure.

Based on the individual overtopping volume distributions, a method to calculate the maximum overtopping volume during a storm can be calculated

$$V_{max} = a_w [\ln N_{ov}]^{4/3}. \quad (2.29)$$

$N_{ov}$  is the number of overtopping waves, and the values of  $a_w$  is dependent on the conditions present. It should be noted that the prediction of  $V_{max}$  is subject to quite some uncertainty, which is always the case for a maximum in a distribution.

### Probability of Overtopping

The final parameter of interest is the probability of overtopping ( $P_{ov}$ ), which gives an indication of the likelihood of an overtopping event occurring. It is directly related to the number of overtopping waves ( $N_{ov}$ ) and the number of incoming waves ( $N_w$ ),

$$P_{ov} = \frac{N_{ov}}{N_w}. \quad (2.30)$$

This probability can be calculated by assuming a Rayleigh distribution of the wave run-up heights and taking the 2% run-up height ( $R_{u2\%}$ ) as the basis,

$$P_{ov} = \exp \left[ - \left( \sqrt{-\ln 0.02} \frac{R_c}{R_{u2\%}} \right)^2 \right]. \quad (2.31)$$

### Wave Run-up

In recent years, more focus in design has been placed on allowable overtopping instead of wave run-up, but the prediction of this value is still useful as seen previously, it is the basic input for predicting  $P_{ov}$  and therefore  $V_{max}$ . The wave run-up height is defined as the vertical difference between the highest point of wave run-up and the still water level on a slope (Pullen et al., 2007). Due to the irregular nature of incoming waves, each one will result in a different level of run-up. In general, structures are designed to a wave run-up height,  $R_{u2\%}$ . This is the wave run-up height that is exceeded by 2% of the incoming waves. The basic formula for  $R_{u2\%}$

$$\frac{R_{u2\%}}{H_{m0}} = 1.65 \xi_{m-1,0}, \quad (2.32)$$

where  $\xi_{m-1,0}$  is the surf similarity parameter based on spectral analysis, which relates the slope steepness to the wave steepness as in equation 2.4.  $H_{m0}$  is the spectral significant wave height.

### CLASH Database

As part of the CLASH (Crest Level Assessment of coastal Structures by full scale monitoring, neural network prediction and Hazard analysis on permissible wave overtopping) programme an extensive database was produced from the results of wave overtopping tests. The database contains information on more than 10,000 tests from more than 165 independent projects or test series, including both field and laboratory measurements. Each is described by means of

31 parameters (Verhaeghe et al., 2003). All coastal structures, including dykes, rubble mound breakwaters, berm breakwaters, caisson structures and combinations have been considered.

It can be used when a user would like to know the overtopping discharge of a similar structure to one already in the database. The information available includes wave heights and periods, model bathymetry and mean overtopping rates. It does not, however, contain detailed information about the wave spectrum, and cannot provide information on the distribution of overtopping events or number of waves modelled.

### **Neural Network**

From the CLASH database, a neural network was developed (van Gent et al., 2007). A neural network is based on the principle that each input parameter is entered at the first layer. Each input parameter is a different neuron. The last layer is the output, and each neuron in this layer is a output parameter to be predicted. The middle layer is a hidden layer where each neuron receives information from the neurons above through various connections. These neurons then carry out standard processes and produce the output.

A neural network can be used where a process is affected by a large number of input parameters, and a large volume of data is available for the network to calculate the influence of each parameter. The advantage of the neural network is that that due to the large amount of data contained in the CLASH database it can be used to calculate overtopping at almost every structural configuration (Pullen et al., 2007). It is also possible to calculate trends in results easily as it is simple to change parameters and therefore find an optimum design.

### **2.5.2 Numerical Models**

Many researchers have developed computational models to simulate wave overtopping at coastal structures. The success of the numerical model depends upon the equations and solution techniques used. They are less restrictive than the other prediction methods as they can be configured for any structure within an overall range. There are 2 main types of numerical model of interest in wave overtopping simulation; Depth-integrated, wave-resolving models and Navier-Stokes models detailed below.

### **Depth-Integrated Equations**

In general, there are two sets of equations that belong to this class of depth-integrated, wave-resolving models: Non-linear shallow water equations (NLSWE), including those that incorporate non-hydrostatic pressure (Zijlema et al., 2011), and Boussinesq type models (Brocchini and Dodd, 2008).

### **Non-Linear Shallow Water Equations**

A computational model often used for wave overtopping of structures uses the NLSWE. Hibberd and Peregrine (1979) first used the NLSWE to model surf and run-up on a beach. They established that as waves reached shallower water they developed short steep turbulent fronts causing these breaking waves to behave like bores. This means that waves in this area can be described by the conservative form of the NLSWE.

The use of the NLSWE was expanded by Kobayashi and Wurjanto (1989), to apply the principles to compute monochromatic wave overtopping of impermeable sloping coastal structures. They used the velocity and depth of the overtopping on the crest of the structure to compute the average overtopping rates. The resulting model was validated against laboratory data and was found to be capable of representing wave shoaling and reflection effects in the calculation of average wave overtopping rates.

Similar models have been developed based on the same principles of the NLSWE, such as Van Gent (1994); Dodd (1998), Hu et al. (2000), and the model used in this study, Briganti and Dodd (2009).

The Non-Linear Shallow Water Equations are derived from the Euler equations which provide a description of flow based on the conservation of mass and momentum. The NLSWE are suitable to describe the flow when the vertical velocity is much smaller than the horizontal velocity. Together these principles, along with a number of assumptions, as stated below, provide a complete set of equations for modelling flow with unknown velocity.

- Shallow water, i.e.  $d/L < 0.05$
- Hydrostatic pressure
- Incompressible fluid

- Impermeable and fixed bed
- Gentle slope
- Free slip condition at the bottom

The equations are integrated over the water column, and the Leibniz rule applied to the boundary conditions at the free surface and the bottom. When these assumptions are met, NLSWE models are shown to be computationally efficient. However, in order to satisfy the shallow water limit, the seaward boundary has to be placed near to the structure.

### **Non-hydrostatic Pressure Models**

Non-hydrostatic models consist of the NLSWE with the addition of a vertical momentum equation and non-hydrostatic pressure in horizontal momentum equations (Zijlema et al., 2011). They provide a general basis for describing the complex changes in the rapidly varied flows typically found in coastal flooding and wave transformation in both surf and swash zones due to non-linear wave-wave interactions, interaction of waves with currents, and wave breaking as well as run-up and overtopping at the shoreline. The most popular version of this type of model is SWASH (Simulating WAVes till SHore), which is publicly available and intended to be used for predicting transformation of surface waves and rapidly varied shallow water flows in coastal waters (Zijlema et al., 2011).

### **Boussinesq Equations**

Another type of model that can be used for wave overtopping studies are those based on the Boussinesq equations, all of which began from the work of Peregrine (1967). These equations are an extension of the NLSWE theory and make it possible to simulate the propagation of waves travelling from deep water to shallow water where frequency dispersion and non linearity are important (Brocchini and Dodd, 2008).

However, there are limitations to these types of models in the nearshore region. Firstly, the Boussinesq equations can not naturally simulate wave breaking, and secondly, these types of models can be computationally very demanding. These two weaknesses mean that as very shallow water is approached, numerical problems arise, because an already numerically demanding set of equations must now be modified to account for breaking yet numerical convergence and stability still be retained (Brocchini and Dodd, 2008).

However, Boussinesq models have been applied to wave run-up and overtopping. Chen et al. (2000) used this type of model with an additional term for energy dissipation due to wave breaking to investigate wave run-up and overtopping. Stansby (2003) used a Boussinesq model to simulate the wave run up and overtopping of solitary waves, which provided good agreement with experimental results without wave breaking. Also, Lynett et al. (2010) used a Boussinesq model to provide detailed prediction of wave run-up and overtopping of embankments in New Orleans during Hurricane Katrina. Work on these types of model is continuing.

### Finite-Volume Method

The principle technique for solving these types of equations is the Finite-Volume method. For example with the NLSWE, they are written in vector form and split into an ordinary differential equation and a partial differential equation.

$$\frac{\delta U_t}{\delta t} + \frac{\delta F(U)_x}{\delta x} = 0, \quad (2.33)$$

$$\frac{dU}{dt} = S, \quad (2.34)$$

where

$$U = \underbrace{\begin{bmatrix} h \\ hU \end{bmatrix}}_{\text{unknowns}} \quad (2.35)$$

where  $h$  is the depth and  $hU$  is the depth averaged velocity.

$$F = \underbrace{\begin{bmatrix} hU \\ hU^2 + \frac{1}{2}gh^2 \end{bmatrix}}_{\text{Fluxes Vector}} \quad (2.36)$$

$$S = \underbrace{[-gh \sin \alpha]}_{\text{Source Term}} + \underbrace{\begin{bmatrix} \tau_b \\ \rho \end{bmatrix}}_{\text{Bottom Friction}} \quad (2.37)$$

where  $g$  is the gravitational acceleration,  $\alpha$  is the angle of the slope,  $\tau_b$  is the bottom shear stress, and  $\rho$  is the water density. This finite volume method splits the model domain into a set of  $N$ , control volumes (cell of equal width  $\Delta x$ ). Each  $i$ -th cell (for  $i=1:N$ ) has its centre located at  $x_i$ , so at a generic time level,  $n$ , piecewise constant states in each cell are assumed (Briganti and

Dodd, 2009). The numerical solution of this homogeneous system is based on the solution of the following relationship,

$$U_i^{(n+1)} = U_i^n - \frac{\Delta t}{\Delta x} \underbrace{[F_{(i+1/2)} - F_{(i-1/2)}]}_{\text{Intercell Flux}} + \Delta t S. \quad (2.38)$$

The solution of the differential equation can then be carried out at each stage with a Runge-Kutta fourth order scheme, whilst the flux can be evaluated by making use of a weighted average flux technique.

### **Navier-Stokes Equations**

The two fundamental principles in fluid mechanics are the conservation of mass and the conservation of momentum. When Newton's second law is applied to a fluid the resulting equations are known as the Navier-Stokes equations (NSE). These equations allow the calculation of the velocity field in the whole computational domain for either rotational or irrotational flows. This allows for the calculation of flows in complex geometries providing information on the velocity, pressure and turbulence field are present.

Although the Navier-Stokes describe the governing equations for a wide range of flow motion, in the case of turbulent flows with high Reynolds number, they are difficult to use. This has led to the Reynolds-Averaged Navier-Stokes equations (RANS), where Reynolds averaging is used to remove the turbulent components over short time scales. These can then be averaged over the depth of the water column to get the depth-averaged Reynolds-Averaged Navier-Stokes equations (DARANS).

The fluid motion for models based on the NSE in the context of overtopping will generally be solved by one of two principal techniques: the Volume of Fluid; and the Smooth Particle Hydrodynamics method.

### **Smooth Particle Hydrodynamic Method**

To describe the complexities of flow that occur during wave overtopping, a model that makes no assumptions of the vertical flow structure is useful. This is true of the Smoothed Particle Hydrodynamics (SPH) model, which is a mesh-free Lagrangian method that has been successfully applied to wave overtopping of structures.

The method divides the flow into discrete particles, and the fluid flow is computed as the tra-

jectories of each particle, which interact according to the Navier Stokes equations. This means that the accuracy of the SPH method depends on the number of particles represented, and for increased number of particles the method becomes more computationally demanding.

These types of models have been developed to simulate overtopping by a number of researchers. Dalrymple and Rogers (2006) included several improvements to the basic models to handle turbulence, the fluid viscosity and density and a different time-stepping algorithm, resulting in a model capable of reproducing green water overtopping and wave-structure interaction. Shao et al. (2006) compared the results from a SPH model with those obtained using other models, and found it provided good estimations of random wave overtopping of a sloping structure. More recent work by Pu and Shao (2012) has allowed porous structures such as rubblemound breakwaters to be modelled, which cannot be modelled using NLSWE models, however St-Germain et al. (2014) has found that results from both SPH and NLSWE models are generally comparable, although further improvements in the computational efficiency of SPH are needed before it can be used for practical purposes.

### **Volume of Fluid Method**

An alternative to the SPH model, that also makes no assumptions of the vertical flow structure, is the Eulerian approach using a fixed mesh, based on the NSE. This type of model can provide a complete description of the flow. Numerous researchers have been working with this type of model, with applications that include wave breaking and overtopping.

In general this type of model takes less time to run than the SPH type, but remains computationally demanding in comparison with NLSWE models, and simulating more than a few irregular overtopping waves is not yet possible (Pullen et al., 2007).

Reeve et al. (2008) used a model developed by Lin and Liu (1998) for simulating breaking waves in surf zones, which was validated against published experimental observations for zero freeboard conditions, with empirical formulae for negative freeboard (weir flow) conditions, and with empirical design formulae for positive freeboard, and found to be well within the accepted ranges of uncertainty for overtopping formulae. Raosa et al. (2012) performed numerical simulations using the Reynolds-averaged Navier-Stokes equations, based on physical model tests with impermeable submerged or zero freeboard dykes, and found the numerical model could reproduce overtopping accurately when forced with the measured levels obtained in the physical modelling. Suzuki et al. (2014) also found that the Navier-Stokes equations provided good es-

timations of flow rates over coastal dykes, however due to the high computational requirements these were run for only 150-200 waves.

### **2.5.3 Physical Models**

Physical models are usually scale representations of a physical system carried out within a laboratory (Hughes, 1993). They are designed so that the major dominant forces are represented in the model at the correct proportion to the full size physical system. Physical models are commonly used as they are a reliable method for determining mean overtopping discharge (Pullen et al., 2007).

A major advantage of physical modelling is that it allows the assessment of overtopping due to multiple factors whose individual and combined influences are unknown, and difficult to predict, however, they are also expensive to run and are generally specific to a particular structure, meaning making small design changes can be difficult.

#### **Scaling**

When carrying out physical modelling it is important to replicate the physical behaviour of waves at a smaller scale, this means that it is essential that the main force and therefore physical processes are correctly simulated. This requires as many factors influencing the simulation to be proportional between model and prototype scales as possible (Hughes, 1993).

Different scaling laws can be used depending on the requirements of the modelling being carried out. Scaling laws are based on the similitude criteria of the physical parameters: Kinematic, gravity and viscous laws, among others. These laws have been developed to ensure that all major factors influencing reactions are in proportion between prototype and model, while those factors that are not in proportion throughout the modelled domain are so small that they are insignificant to the process.

In the case of coastal engineering, Hughes (1993) recommends that either the Froude scaling law when gravity is the predominant force, or the Reynolds scaling law when viscous forces are predominant, should be used. In this work surface tension, compressibility and viscosity are neglected as they are relatively small. Thus, gravity is the predominant force, so the Froude Number is the major scaling criterion to assure similarity between physical models and prototype.

The Froude number expresses the relative influence of the inertial and gravitational forces in a

hydraulic flow (Hughes, 1993)

$$Fr = \frac{V}{\sqrt{gL}}. \quad (2.39)$$

$V$  is velocity,  $g$  is gravitational acceleration and  $L$  is wavelength. This scaling law requires that the Froude number in the model and in the prototype should be the same, i.e.

$$\left(\frac{V}{\sqrt{gL}}\right)_p = \left(\frac{V}{\sqrt{gL}}\right)_m. \quad (2.40)$$

The subscripts  $p$  and  $m$  indicate respectively the Froude number at prototype (or full size) and model scale. This leads to

$$\frac{V_p}{V_m} = \sqrt{\left(\frac{g_p}{g_m}\right) \left(\frac{L_p}{L_m}\right)}. \quad (2.41)$$

Expressing in terms of scale ratios, and rearranging gives the Froude model criterion

$$N_{Fr} = \frac{N_V}{\sqrt{N_g N_L}} = 1. \quad (2.42)$$

It is important to remember when choosing the most appropriate scaling law, that scale effects will occur in the physical modelling due to the fact that it is not possible to replicate all of the relevant variables in the correct relationship to each other. When considering the Froude scale, viscous forces and surface tension effects are neglected which could cause inaccuracies in determining the response of the structure (Hughes, 1993). The influence of secondary forces has been shown to be more prominent at model scale, and the smaller is the scale the stronger these effects can be.

### Laboratory Effects

According to (Hughes, 1993), laboratory effects in short wave physical models can influence the processes being simulated resulting in incorrect approximation of the prototype values. Typical laboratory effects are mainly due to:

- The physical constraints of boundaries on the water flow
- The occurrence of unintentional non-linear effects due to the mechanical generation of waves
- The simplification of prototype forcing conditions

When using a two-dimensional wave flume, cross-waves can develop when energetic wave conditions are being generated by a mechanical wave paddle. Also, the mechanical wave generation can create unwanted non-linear effects. These can be higher harmonics in finite amplitude regular waves or spurious long waves (Hughes, 1993). In addition, a boundary effect for wave flumes can occur due to the re-reflecting of waves at the paddle. This occurs as waves reflected at the structure, travel back to the wave paddle. In reality, these waves would continue to travel out into the ocean, but this effect can be eliminated in physical modelling with the use of an active absorption system that is capable of absorbing these unwanted reflected waves.

## **2.6 Uncertainty**

A numerical model can contain uncertainties that effect the output, leading to physical processes being incorrectly modelled. It is important to be able to analyse this uncertainty to increase confidence in numerical model results. To fully analyse the uncertainty within a numerical model, then information on the type and sources of uncertainty is required. This will allow a better understanding when evaluating the model performance.

### **2.6.1 Types of Uncertainty**

#### **Aleatory Uncertainty**

Aleatory uncertainty (also known as irreducible uncertainty, stochastic uncertainty, intrinsic uncertainty or variability) is the uncertainty that arises due to the inherent randomness of natural processes (Roy and Oberkampf, 2011). It is impossible to remove, but it can be analysed and quantified using statistical methods. It is often characterised by a probability density function (PDF) or a cumulative distribution function (CDF).

A relevant example of an aleatory uncertainty are the waves in a fully developed sea. Although these can be expressed by an energy density spectrum over a range of frequencies, the individual waves themselves are random and irregular. If there are sufficient samples available then these can be characterised by probability functions, but the uncertainty of the individual wave properties will remain.

### **Epistemic Uncertainty**

Epistemic uncertainty (also known as reducible uncertainty or ignorance uncertainty) is caused by a lack of knowledge within the modelling and simulation. This uncertainty can be reduced, and even be removed, by improvements to the model through experimentation and improved numerical analysis, as well as gathering increased knowledge about the system.

An example of an epistemic uncertainty within this model, is the roughness factor assigned to the slope of the structure. This is a physically based parameter which depends on the material of the structure. As further information is collected about the structure then this value can be improved and hence provide a more accurate approximation of the roughness of the structure and the uncertainty around this value could then be eliminated altogether.

### **2.6.2 Sources of Uncertainty in Numerical Models**

It is important to understand the various sources of uncertainty within the numerical model. All the sources of uncertainty within the model must be identified, to ensure that the accurate quantification of the overall uncertainty of the model can be obtained. If a source of uncertainty is ignored then the confidence in the model output is low.

#### **Boundary and Initial Conditions**

The numerical model used in this work uses the Non-Linear Shallow Water Equations, together with a set of additional restraints known as the boundary conditions and the initial conditions. Initial conditions are a particular type of boundary condition and refer to the initial values of elements that vary with time. To produce the correct solution, the numerical model must satisfy both the differential equations as well as the boundary conditions.

In this work, the boundary conditions are the incoming waves at the toe of the structure. They are described by their wave height and period. A continuous train of waves enters the domain at the boundary. These waves are generated to realistically mimic the random nature of waves, and will therefore have varying wave heights and periods. This random natural process of the waves leads to an inherent variability in the boundary conditions. This is an aleatory uncertainty. If a measured time series of waves was available, then this uncertainty would not be present.

In addition to the natural variability of the incoming waves, it is also possible that further uncertainty will be present in the boundary conditions. This could be caused by a lack of data,

poor quality data or an inadequate method of parameter estimation. An example of this is the significant wave height, if only one measurement from reality was used to establish the value then a high level of uncertainty would remain. However if multiple samples were obtained, then the uncertainty surrounding this value would decrease. This is an epistemic uncertainty. It is therefore possible for the boundary conditions to consist of both types of uncertainty, although theoretically the epistemic uncertainty can be eliminated at the start of the modelling process.

### **Model Domain**

The model domain refers to the set-up of the model. It characterises the context and framing of the simulation, and is typically determined at the beginning of the model when the problem is identified. Information on all the relevant criteria should be gathered, to develop the conceptualised system. This includes information on spatial and temporal detail required by the model. Within the model there are a number of parameters that are specified as part of the initial set-up.

- Bathymetry, this includes the initial water depth, the slope of the bed, and the overall length of the domain.
- Geometry, this includes the dimensions of the structure, the slope of the structure and the location of the structure.
- Physical properties, this includes permeability and deformability of the structure.

All of these factors are either determined by measurement, or apportioned to suit the specific requirements of the simulation. There may be epistemic uncertainty relating to the sampling of the measured values, and to the suitability of the allocated values. Again, these uncertainties can in theory be eliminated with the addition of further information at the start of the modelling process.

### **Model Structure**

A numerical model is a description of a system using mathematical concepts. It usually describes a system by a set of variables and a set of equations that establish relationships between the variables. This can be a simplification of the process, and can therefore inadequately predict the output of the true process, even if all the inputs are known. This is known as model form, or

structural uncertainty, and gives the difference between the real process and the output from the numerical model, assuming all the input parameters are correct.

The mathematical concept behind this particular model are the Non-Linear Shallow Water Equations. It is known that the NLSWE work well in the inner surf zone where non linearity dominates. They have also previously been shown to work well in simulating wave run-up and overtopping at coastal structures (Kobayashi et al. (1987); Kobayashi and Wurjanto (1989); Shankar and Jayaratne (2003); Shiach et al. (2004)). The model being used meets all the criteria required for the NLSWE to work so minimal structural uncertainty should be present.

### **Model Assumptions**

The uncertainty due to model assumptions arises when there is a simplification of the modelled processes. It can be caused by making assumptions, conceptualisations, approximations and errors within the numerical model. Numerical approximations occur due to discretisation error and round-off errors. Discretisation errors occur due to the spatial and temporal domains being split up into a finite number of elements. In this numerical model, an example of this kind of discretisation error is the definition of the shoreline that occurs at the interface between the wet and dry cells. This is an approximation of the real one because the zero depth condition is never met in the model (Briganti and Dodd, 2009).

Round-off errors occur due to the fact that only a finite number of significant figures can be used to store values. This means that values are potentially rounded up or down, and lose accuracy. As these values are used throughout the model, then more round-off errors can occur, resulting in a larger error at the end of the simulation.

Mistakes and errors in the computer code can occur when implementing the mathematical concepts. These are unknown errors, which cannot be quantified. However, when these errors are identified they can be eliminated from the model.

As this work is interested in the uncertainty propagation due to the input parameters, it will concentrate on this particular source of uncertainty and the most suitable forms of analysis methods.

### **2.6.3 Identifying Uncertainty**

There are various different methods of analysis that need to be carried out to ensure all uncertainties are addressed, and the predictive capabilities of the numerical model can be fully quantified.

### **Model Validation**

The purpose of model validation is to assess how well a numerical model predicts reality. It is used to ensure that numerical outputs match those that are observed in experimentation. This addresses the model structure uncertainty by comparing the simulation results with the experimental measurements. Statistical methods are used to quantify the disagreement between the simulated results and the experimental results, assuming identical conditions are present (Roy and Oberkampf (2011); Trucano et al. (2006)).

Ideally validation experiments are carried out that are designed and executed to quantitatively estimate the ability of the numerical model to simulate a physical system or process. If the numerical experiment exactly matches the physical experiment then the other sources of uncertainty can be ignored during the validation process.

This method is used to address the uncertainty in the model structure, and can therefore eliminate this uncertainty at the start of the modelling process.

### **Uncertainty Analysis**

Uncertainty analysis aims to quantify the uncertainties in the numerical model output, caused by the uncertainties in the input. It involves the quantification of the model inputs, and their propagation through the model (Roy and Oberkampf, 2011). Uncertainty analysis is usually applied when inputs to the model are not known precisely, or are subject to inherent variability.

### **Sensitivity Analysis**

Sensitivity analysis concentrates on how the output is influenced by changes in the input, for example finding out how variation in the output can be apportioned to changes in the input. There are a number of reasons for carrying out sensitivity analysis (Ferson and Hajagos (2006); Hall et al. (2009)):

- To focus on the inputs that have the most significant influence on the outputs.
- To identify the inputs that have little effect on the output so they can be eliminated from further analysis.

Sensitivity analysis varies from uncertainty analysis, in that it can be used to analyse the allocated parameters, that are known within the model. It is useful to apply sensitivity analysis to these variables to identify their influence on the overall system performance.

#### **2.6.4 Monte Carlo Simulation**

For numerical models that can be run for a large number of different boundary conditions a Monte Carlo approach can be used to carry out uncertainty analysis. Monte Carlo method is a statistical technique for the analysis of stochastic models.

For each input in the model which is represented by a random variable, a probability distribution is specified. Random samples are simulated for each input distribution, and entered into the numerical model. The model then carries out the analysis as it would for any deterministic value. This process is then repeated until an appropriate number of model iterations have been completed. Instead of obtaining a single deterministic output from the model, a set of outputs are obtained. These can be represented as cumulative distribution functions, and quantified using statistics.

The drawback of the Monte Carlo method is that it only allows for the propagation of the aleatory uncertainty through the model, i.e. parameters still have to be specified.



## **Chapter 3**

# **Model Validation and Measured Offshore Boundary Conditions**

### **3.1 Introduction**

Before the uncertainty in the numerical model due to the spectral boundary conditions can be considered, it is important to confirm that the results produced are reliable. As a numerical model is essentially a combination of equations and boundary conditions, it can not be guaranteed to accurately predict physical processes unless it has been validated against physical model data. Therefore to allow a comprehensive study of the variability of the numerical model predictions a reference test case in which the hydraulic input and output conditions are known is required.

### **3.2 Physical Model**

For this work, the reference tests are provided by simulating random wave overtopping in a series of small scale (1:25) laboratory experiments carried out in a two dimensional (2D) wave flume at HR Wallingford. To avoid any issues due to the scaling of results it should be noted that all the results from the experiments are presented at model scale in this work, and not at prototype scale.

### 3.2.1 Experimental set-up

The flume is 40m long and 1.5m wide, and equipped with an absorbing piston-type wave generator situated at one end, that is electronically controlled. The bottom of the flume has a flat section directly in front of the paddle followed by a gentle slope of 1:50 which acts as a fore-shore to the structure. For these particular experiments, a simple concrete impermeable sloped structure was constructed near the other end of the flume. This simple configuration was chosen so that the permeability of an armour layer, which would introduce a further modelling uncertainty, could be neglected. The slope of the structure itself was 1:2.55, and remained constant throughout the experiments. The toe to crest height of the structure was 0.29m, with a varying crest freeboard ( $R_c$ ) being achieved by altering the water depth in the flume. The set-up of the experiment is shown in Fig. 3.1, along with a photograph showing the equipment used.

### 3.2.2 Wave Conditions and Measurement

A requirement of NLSWE solvers is that they must be in shallow water for the model assumptions to be met, and that the wave entering the numerical domain have or will break. This resulted in the wave conditions being chosen for the physical experiments as those that could be suitably modelled with a NLSWE solver.

A summary of the wave conditions that were prescribed at the paddle for these tests are shown in Table 3.1. Here  $H_{m0}$  is the spectral significant wave height,  $T_p$  is the peak period,  $d_p$  is the water depth at the paddle,  $s_{op}$  is the wave steepness defined as  $s_{op} = \frac{2\pi H_{m0}}{gT_p^2}$ ,  $T_p$  being the peak period of the energy density spectrum and  $g$  is the gravitational acceleration.  $\xi_{m-1,0}$  is the surf similarity parameter defined as  $\xi_{m-1,0} = \frac{\tan \alpha}{\sqrt{\frac{2\pi H_{m0}}{gT_{m-1,0}^2}}}$ . Where  $T_{m-1,0}$  is the mean spectral period, computed as  $\sqrt{\frac{m-1}{m_0}}$  and  $\alpha$  is the structure slope.

The water free surface ( $\eta$ ) was measured at various points along the flume using eight wave gauges ( $WG1 - 8$ , see Fig. 3.1 for their positions) including one at the toe of the structure ( $WG7$ ) and one ( $WG8$ ) close to the position of the shoreline at the structure at the beginning of the tests, which can be seen in Fig. 3.1.

The wave gauges used were resistance type wave gauges which work by passing a high frequency voltage through two parallel wires a fixed distance apart placed perpendicular to the wave direction. The conductance between the wires is recorded, which is proportional to the

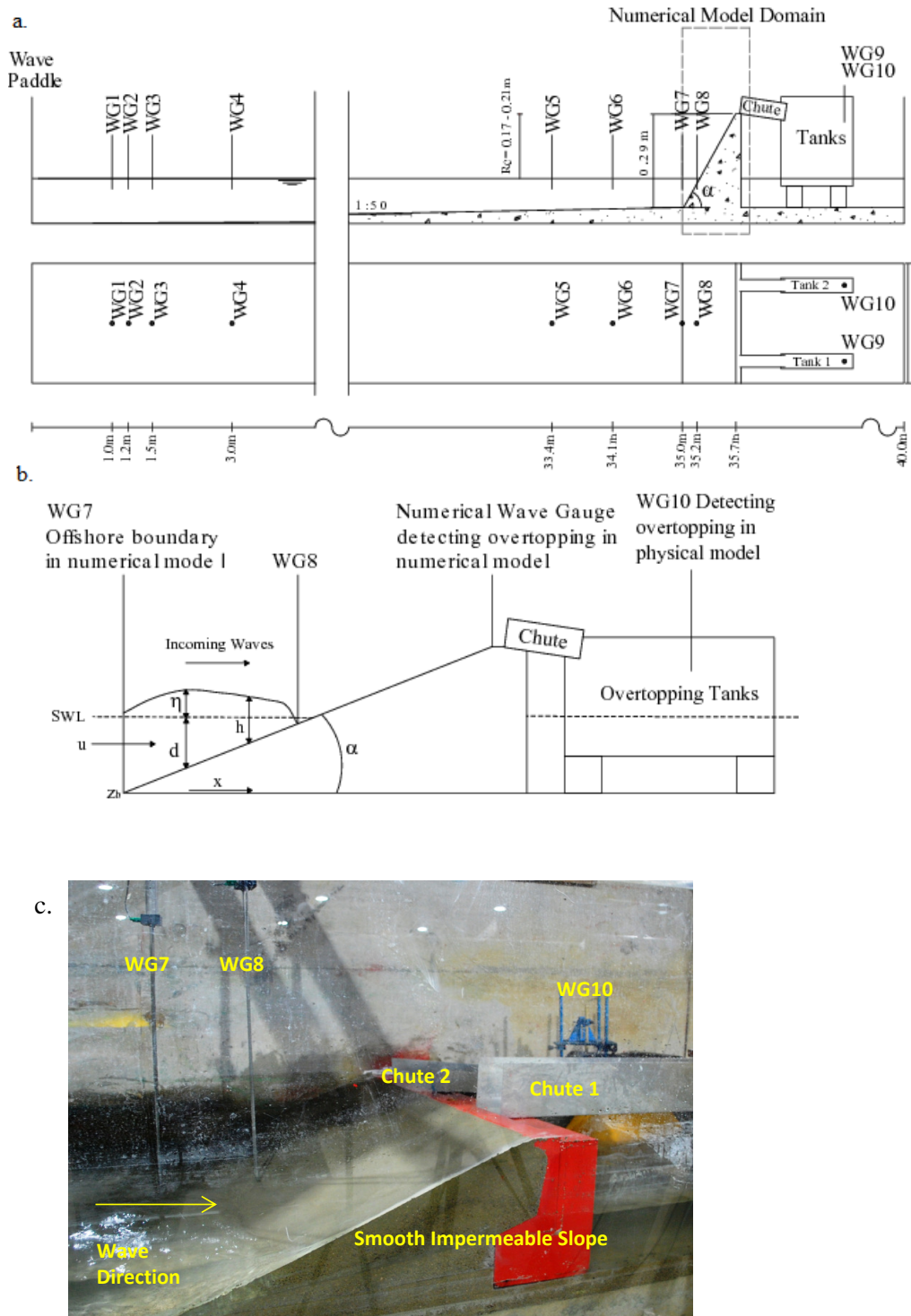


Figure 3.1: a. layout of the physical model. b. Detail of the tested structure and overtopping measurement system together with the numerical model set-up. c. Photograph of physical model

Table 3.1: Incident wave conditions prescribed at the paddle for the JONSWAP spectra random wave laboratory tests

Test	$H_{m0}$ (m)	$T_p$ (s)	$d_p$ (m)	$s_{op}$ (-)	$\xi_{m-1,0}$ (-)
001	0.08	1.30	0.694	0.030	2.29
002	0.02	1.76	0.694	0.004	6.22
003	0.02	2.20	0.694	0.003	7.78
004	0.02	1.32	0.734	0.007	4.66
005	0.02	1.76	0.734	0.004	6.22
006	0.02	2.20	0.734	0.003	7.78
007	0.04	1.76	0.694	0.008	4.40
008	0.08	1.20	0.694	0.036	2.12

Table 3.2: Measured incident wave conditions at structure toe for the JONSWAP spectra random wave laboratory tests

Test	$H_{m0}$ (m)	$d_t$ (m)	$R_c$ (m)	$H_{m0}/d_t$ (-)	$R_c/H_{m0}$ (-)
001	0.085	0.09	0.21	0.943	2.474
002	0.032	0.09	0.21	0.354	6.599
003	0.036	0.09	0.21	0.404	5.777
004	0.026	0.13	0.17	0.202	6.459
005	0.031	0.13	0.17	0.238	5.472
006	0.038	0.13	0.17	0.293	4.464
007	0.075	0.09	0.21	0.839	2.781
008	0.081	0.09	0.21	0.899	2.596

length of wire submerged and the conductivity of the water. The changes in sea surface elevation are converted from these changes in conductance. Due to the sensitivity of the wave gauges to changes in the water, these had to be calibrated at the beginning of each day before testing began.

To retrieve the incident wave conditions at the toe of the structure, the wave conditions tested were calibrated in the empty flume (i.e. without the structure in place) so that the reflection from the structure could be neglected. During the overtopping tests the paddle was operated with active absorption to absorb any reflected waves; in the calibration tests, the incident waves were absorbed by the presence of a porous beach at the end of the flume in place of the structure.

A summary of the incident wave conditions measured at the location of the toe of the structure is shown in Table 3.2. Here  $H_{m0}$  is the measured spectral significant wave height,  $H_{m0}/d_t$  is the local wave height to local water depth ratio, where  $d_t$  is the water depth at the structure toe and  $R_c/H_{m0}$  is relative freeboard, where  $R_c$  is the structure freeboard.

The results of the measured incident waves can now be used to confirm the suitability of the waves for being modelled by the NLSWE solver. This is achieved by considering the ra-

ratio  $H_{m0}/d_t$ , which from the values measured indicates that in some of the experiments waves may already be breaking at the toe of the structure. To identify the occurrence of depth limited breaking the simple criterion proposed by Kamphuis (1991) is used. The criterion establishes

$$\frac{H_{m0b}}{d_{tb}} = 0.56e^{3.5m}. \quad (3.1)$$

Here  $H_{m0b}$  is the value of the significant wave height at breaking and  $d_{tb}$  is the water depth at breaking,  $m$  is the foreshore slope, i.e.  $m = 1:50$ . According to Eq. 3.1,  $H_{m0b}/d_{t.b} = 0.6$  in the present tests. As seen in Table 3.2 tests 001, 007 and 008 this value is exceeded. Therefore these tests are characterised by a large portion of the waves breaking at the toe of the structure.

### 3.2.3 Overtopping Measurement

During the experiments the individual overtopping volumes were measured using a standard procedure implemented at HR Wallingford. The principle behind this is that the overtopped water is collected over a specific crest width and runs down a chute into a reservoir where the amount of accumulated overtopped water is continuously measured using a wave gauge during a test run. The output of the measurements then consists of a gradually increasing curve of water elevation as a function of time.

In this case this consisted of placing two chutes at the crest of the sloped structure, allowing water to flow into two separate overtopping tanks situated behind the structure. A false wall is situated inside each overtopping tank, this allows water to flow underneath but reduces the oscillations due to the incoming water in the back half of the tank. A gauge was then placed inside each rear section of the overtopping tank (*WG9* and *WG10*) to detect the change in depth of water. By knowing the dimensions of the collection tanks, chute width and the length of the test, this change in depth could then be converted into individual overtopping volumes, and overtopping discharge per unit width.

The individual overtopping volumes were computed following the procedure used in Briganti et al. (2005). According to this technique individual overtopping events are visually identified from a post-processed time series of levels in the overtopping tank. Large oscillations appear on the water surface as the water enters, these are removed from the raw signal by using a low pass filter with a cut-off frequency of 0.01Hz. A short excerpt of an original signal, a filtered signal and identified overtopping events is shown in Fig. 3.2. Individual volumes are computed

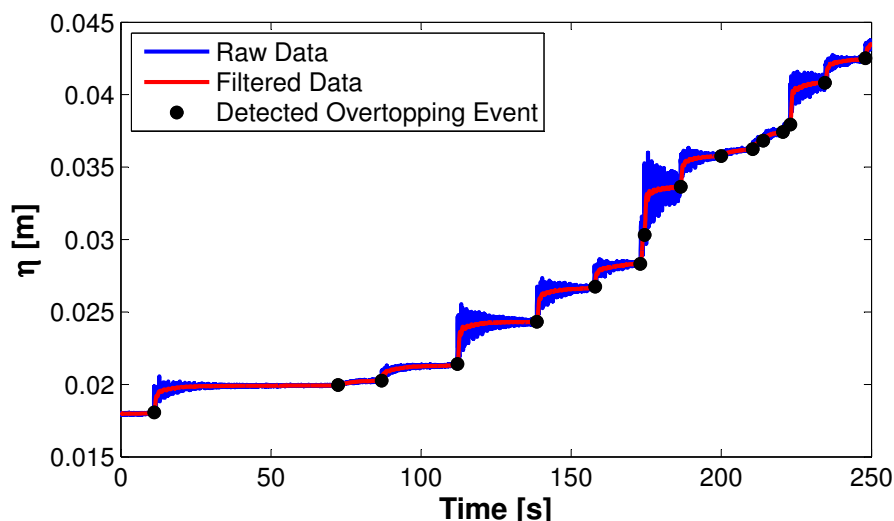


Figure 3.2: Excerpt of measured and post-processed time series of water depth in tank 2 for test 006. Blue line: raw signal. Red line: filtered signal. Black dots: visually detected overtopping events.

by calculating the difference in volume between the start of an event and the start of the next one.

The example shown is for a moderate level of overtopping where the identification of individual events was fairly clear, but it should be noted that due to the noise within this data, it is possible that very small overtopping events have not been identified, particularly in the higher magnitude overtopping tests. It is also possible in the tests with regular overtopping events that the events have merged whilst flowing down the chute. Both of these issues can affect the account of the number of overtopping waves and, in turn, the probability of overtopping. However, the overall discharge is not affected by this.

In this work, the width of the chute of tank 2 was altered for each experiment depending on whether a low or high discharge was expected based on empirical prediction. This allowed more accurate measurement of the individual events than could be obtained using tank 1. For this reason, it was decided to use the measurements only from tank 2 throughout this analysis. Pullen et al. (2007) recommends that a sea state in physical modelling can be represented by 1000 random waves, to guarantee consistent results. It is also stated numerical simulations should be carried out for a similar number of waves. Following this recommendation a test length of 1000 mean wave periods for calculating the mean overtopping discharge was chosen. This meant that although, in total, 30 irregular wave tests were carried out a number of the tests resulted in the tanks filling well before 1000 waves and therefore not being representative of the wave spectrum, or in no measurable overtopping. Those tests were excluded and it was decided

to focus on the 8 tests detailed in Table 3.1 in which representative overtopping was measured.

### 3.3 Numerical Model

A numerical solver of the NLSWE based on a finite volume scheme using a Weighted Averaged Flux (WAF) technique was used in this work. Although all the models described in Chapter 2 are suitable for studying overtopping, this model was chosen due to the low computational requirements, with only negligible losses to the underlying physics. The hydrodynamic equations are 1D conservation equations of volume and momentum,

$$\frac{\partial h}{\partial t} + \frac{\partial hU}{\partial x} = 0, \quad (3.2)$$

$$\frac{\partial hU}{\partial t} + \frac{\partial (hU^2 + \frac{1}{2}gh^2)}{\partial x} = -gh \frac{\partial z_B}{\partial x} - \frac{\tau_b}{\rho}. \quad (3.3)$$

$x$  is the spatial coordinate,  $t$  is time,  $U$  denotes the depth-averaged horizontal velocity,  $h$  is the local water depth, and  $z_B$  is the bed level as shown in Fig. 3.1, b.  $h = d + \eta$  where  $d$  is the still water depth and  $\eta$  the free surface.  $g$  is the gravitational acceleration,  $\tau_b$  the bottom shear stress,  $\rho$  is the water density.

The model was described in detail in Briganti and Dodd (2009) and Briganti et al. (2011). In Briganti et al. (2011) the original model proposed in Briganti and Dodd (2009) was equipped with the capability of computing  $\tau_b$  starting from the estimation of the bottom boundary layer thickness using the momentum integral method (Fredsoe and Deigaard, 1993). This method uses a physically based calibration parameter, the roughness factor  $K_n$ , which is defined as a function of the diameter of a uniform size sediment that generates identical flow resistance, and is therefore dependant on the material of the slope.

#### 3.3.1 Numerical set-up

The domain used in the NLSWE model is indicated in Fig. 3.1, b. The toe of the structure, which is also the position of *WG7*, was assigned as the seaward boundary in the model. The choice of the location of the offshore boundary has been chosen following the NLSWE application of Dodd (1998) and Shiach et al. (2004). Both works indicate that best results are obtained when the offshore boundary is close to the structure to be simulated in order to obtain shallow

water conditions for the incoming wave attack.

$\eta$  measured at *WG7* during the overtopping experiments provides the free surface offshore boundary conditions to the model. The corresponding  $U$  was obtained using the shallow water approximation, i.e.  $U = \eta\sqrt{g/h}$ . To allow this time series to be used, a seaward boundary condition that prescribes the total water depth and velocity is applied. This boundary condition is a reasonable approximation as shown in Dodd (1998). These results will be referred to as MOBC (Measured Offshore Boundary Conditions).

Virtual wave gauges were located at various points within the numerical domain. One of the gauges corresponds to *WG8*, allowing the comparison with the free surface measured at approximately the position of the still water level. A further virtual wave gauge was located at the crest of the structure. Here,  $h$  and  $U$  were used to measure overtopping events. Each individual overtopping event volume ( $V_{ov}$ ) was computed by integrating in time the discharge  $Q = hU$  during the duration of the event itself.

A transmissive boundary is also used at a distance behind the structure to allow waves that have overtopped to exit the domain and not influence the incoming waves.

The only parameter that needed to be calibrated in Eq. (3.3) is  $K_n$ . Since the slope is made of a smooth concrete,  $K_n = 0.001$  m, as suggested in the literature (Liu, 2001), has been used.

### 3.4 Model Validation

The purpose of carrying out the model validation is to assess how accurately the numerical model can predict reality and hence test the physical assumptions. This is achieved by directly comparing the results from the physical model with those obtained by using the numerical model. To allow a comprehensive assessment, it is therefore important to consider a number of different parameters from the experimental data. This validation will focus on the three overtopping parameters that are frequently used in engineering practice, the probability of overtopping  $P_{ov}$ , the overtopping discharge  $q$  and the maximum individual overtopping volume  $V_{max}$ .

#### 3.4.1 Physical Model Results

Firstly, the measured parameters had to be calculated from the experimental data. To calculate  $q$  from the physical model, the total depth of water collected in the tank at the end of the test is

Table 3.3: Overtopping parameters measured during laboratory wave tests

Test	$q$ (m <sup>3</sup> /s/m)	$V_{max}$ (m <sup>3</sup> /m)	$P_{ov}$ (%)	$V_{min}$ (m <sup>3</sup> /m)
001	4.10e-4	0.0041	7.4	1.2e-3
002	1.32e-6	0.0008	0.3	3.2e-5
003	4.43e-6	0.0011	1.1	1.1e-4
004	4.04e-7	0.0002	0.6	1.5e-4
005	3.99e-6	0.0017	0.9	1.6e-4
006	3.71e-5	0.0109	3.7	1.8e-4
007	1.63e-4	0.0100	7.2	2.4e-3
008	1.40e-4	0.0092	4.3	2.1e-3

measured. This is converted into a total volume by multiplying by the area of the overtopping tank. This volume is then divided by the length of the test to obtain a discharge. To convert this into a discharge per unit length, this value is then divided by the width of the overtopping chute. To calculate the  $V_{max}$  the time series of overtopping must be examined. The measured water level is converted into volumes again, by multiplying by the area of the overtopping tank, and then dividing by the chute width to obtain a volume per unit width. The individual volumes are then visually identified on the time series, with the largest being that of  $V_{max}$ . The  $P_{ov}$  is also calculated by identifying the number of overtopping events that occur in each test, and dividing by the number of waves generated by the wave paddle.

The results based on the gauge readings in tank 2 are shown in Table 3.3. It can be seen in these results that tests 001, 007 and 008 produced the higher  $q$ , and is of the order of  $10^{-4}$  m<sup>3</sup>/s/m. Test 006 produces  $q$  of the order of  $10^{-5}$  m<sup>3</sup>/s/m, but also produces the highest maximum individual volume of all the tests. This is likely due to the long wave period of this particular test condition. The remaining tests (002, 003, 004 and 005) all produce low levels of overtopping, with  $q$  in the order of magnitude of  $10^{-6}$  m<sup>3</sup>/s/m and lower. As observed by the low values for  $P_{ov}$  only a few waves actually produced overtopping in these tests.

Table 3.3 also shows the minimum overtopping volume that was possible to detect in each time series ( $V_{min}$ ). The variation in this value is due to it being easier to identify small overtopping events in the low overtopping conditions. These were lost due to the larger and more frequent overtopping events in the higher overtopping conditions. This has an effect on the value of  $P_{ov}$  and will be investigated later in this chapter.

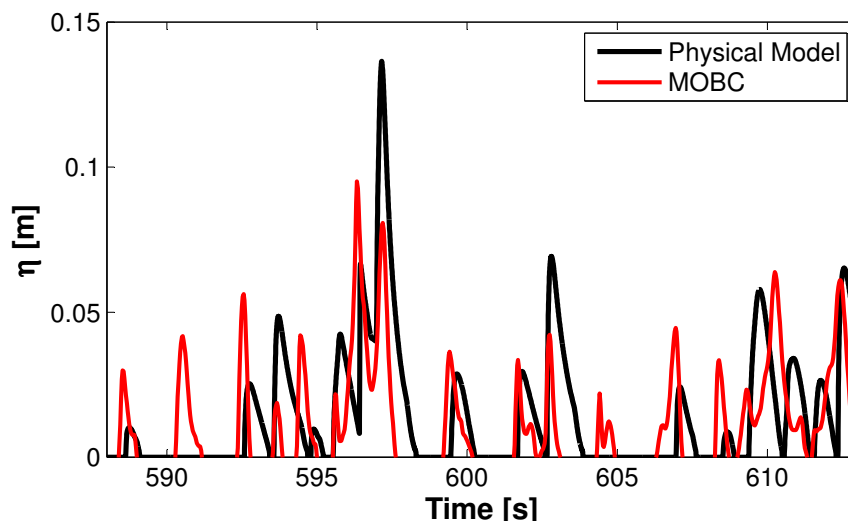


Figure 3.3: Comparison of water elevation at the same point on the slope. Black solid line:  $\eta$  for Test 006 from experimental data measured at *WG8*. Red solid line:  $\eta$  for Test 006 from MOBC results.

### 3.4.2 Run-Up Comparison

Before calculating the overtopping parameters from the numerical model, it is also possible to compare the run-up on the structure. This can be achieved by directly comparing the readings from *WG8* in the physical model, with the free surface computed at the virtual wave gauge at the same location in the numerical model. An example showing the comparison between these two can be seen in Fig. 3.3.

The two time series show a good agreement for the number of run-up events. All of the events occurring in the physical model can be observed in the numerical model. There are two additional small occurrences in the numerical model. There is more variation observed in the magnitude of the run-up events, with the numerical model both under and over-estimating the water surface level. It is not clear the source of this variation. However, overall it appears that the numerical model is computing the water surface elevation reasonably well.

### 3.4.3 Overtopping Time Series Comparison

Similar to the comparison with the run-up, it is also possible to compare the time series of the overtopping. Unfortunately, due to the additional time taken for the water to flow down the chute and into the overtopping tank, which is not modelled numerically, it is not possible to produce a time series of overtopping events from the NLSWE solver that exactly matches that of the experiment. As an example, the experimental time series of overtopping volumes for tests 003, 006 and 007 were compared with the numerically computed time series and are shown in

Fig. 3.4).

For the low overtopping (Test 003), it can be seen that a similar number of overtopping events occur in physical model and the numerical model. The overall shape of the time series are quite similar, suggesting that the events modelled in the numerical model are those occurring in the physical model. However, the numerical model generally seems to over-predict the size of the events.

For the moderate overtopping (Test 006), the similarities between the two time series are more evident. A large number of events can be observed in both of the time series, and the total volume at the end is shown to be consistent between the numerical and physical model.

For the high overtopping (Test 007), it can again be seen that a similar number of overtopping events occur in both models. Similarly to the other tests, it is also observed that the overall shape of the time series are quite similar, although like with the low overtopping test, the events are generally over-predicted resulting in a larger prediction of cumulative volume.

In all three of the tests shown here the overtopping events are more clearly defined by the numerical model. This is as expected due to the presence of noise in the experimental readings, and the flow of the overtopped water down the chute and into the tanks. It should also be noted that the test with the deeper water conditions, is the one in which the numerical model performs better. This is a test, where breaking is less likely to have already occurred at the offshore boundary of the numerical model.

#### **3.4.4 Mean Overtopping Discharge**

The numerical model is replicating the physical model with reasonable accuracy but the prediction of the overtopping parameters must be confirmed. Fig. 3.5 shows the comparison between the measured and predicted  $q$  for the MOBC tests. The overall agreement between the physical and numerical model is good; although the model has a tendency to overestimate  $q$ . This is in agreement to the earlier findings when comparing the overtopping time series.

All of the numerical model results are within the same order of magnitude as those measured in the physical model. These results are consistent with the accuracy shown by former published numerical simulations of overtopping using depth averaged models (e.g. Lynett et al., 2010, McCabe et al., 2013), confirming the suitability of the model for predicting the overtopping discharge.

Having compared the results of the numerical model with the physical model, it is also worth

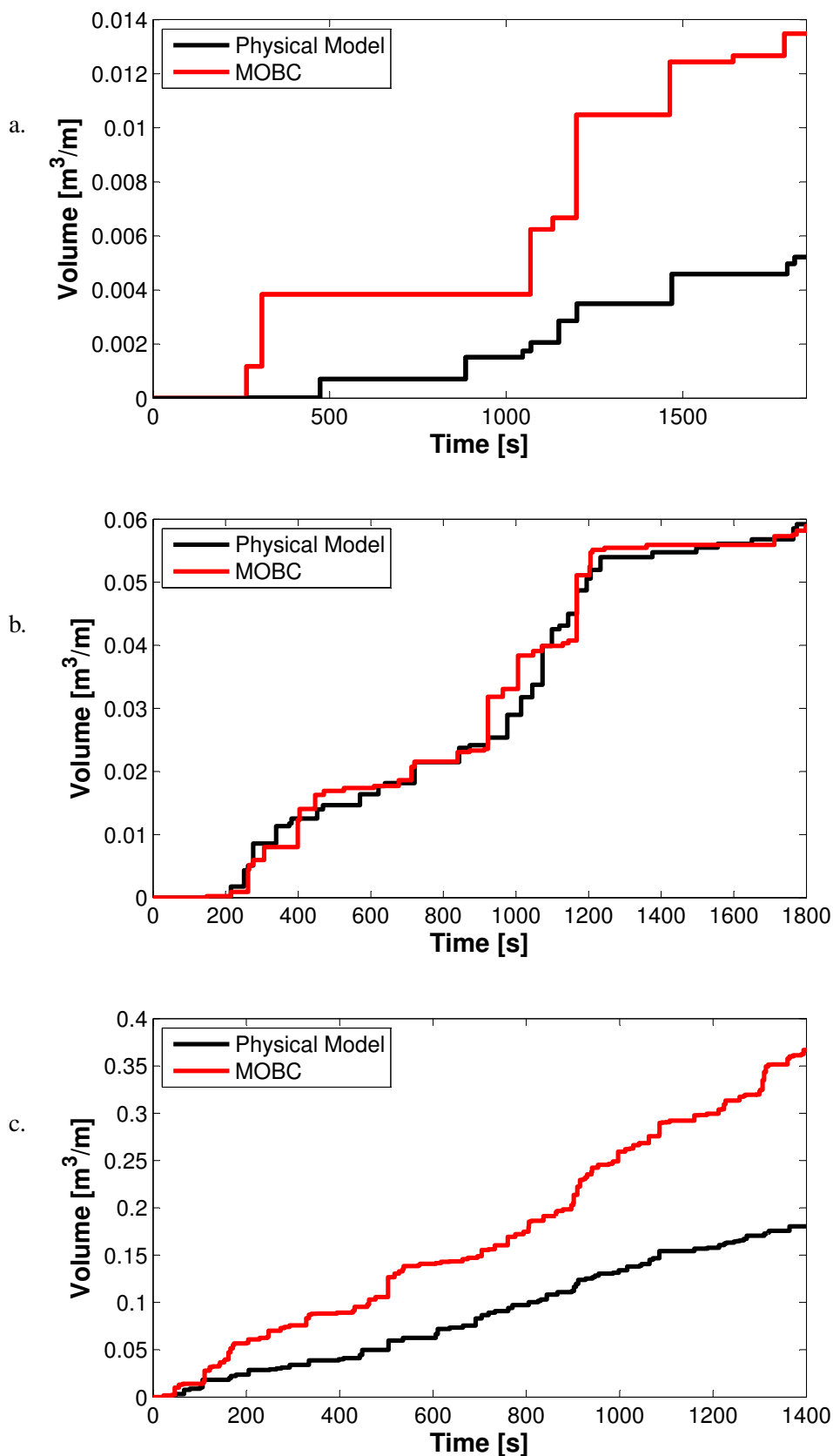


Figure 3.4: Cumulative overtopping volumes. a. Test 003. b. Test 006. c. Test 007. Black solid line: Measurement in tank for each test from experimental data. Red solid line: Volumes calculated for each test from MOBC results.

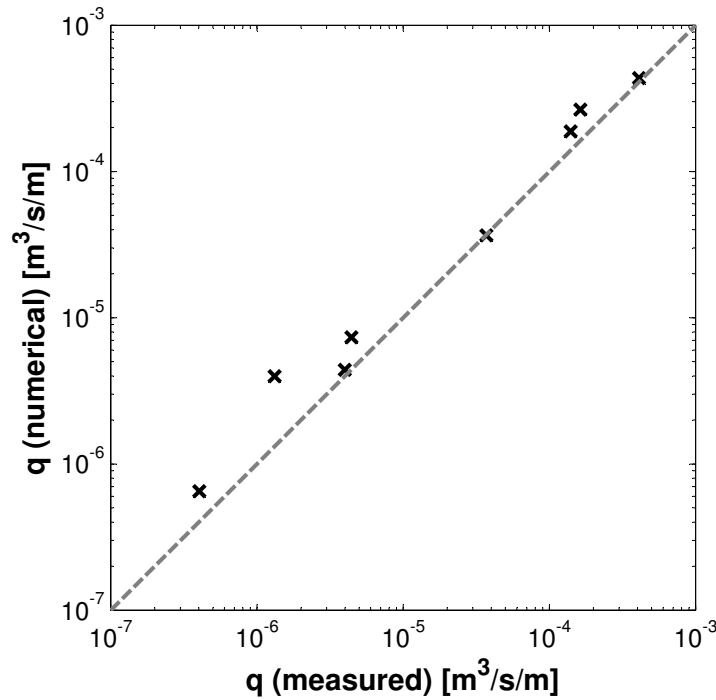


Figure 3.5: Comparison of  $q$  measured in physical model versus  $q$  calculated with the numerical model. Grey dashed line represents perfect fit.

comparing with the empirical prediction, to confirm which methods of prediction is better. In Fig. 3.6, the results from both the numerical model and the physical model have been compared with the prediction obtained from the empirical formulae specified in section 2.5 for smooth slope depending on exact wave conditions present.

Generally the empirical formulae have underestimated the overtopping, in some cases by several orders of magnitude. This magnitude of variability is expected in the low overtopping tests, but the empirical formulae should provide reasonable results for the higher overtopping tests. This does not appear to be the case in this work, with large variability occurring at all levels of overtopping. This is likely caused by a combination of using the values prescribed at the paddle in the formulae, rather than those measured, and a very smooth slope with low roughness. Overall, it can clearly be seen here the numerical models is more accurate than the empirical formulae in these tests.

### 3.4.5 Maximum Individual Overtopping Volume

Generally, the accuracy of numerical models for predicting the other overtopping parameters is not considered. However, due to the availability of the data from the physical model in this case, it is worth analysing the accuracy of the numerical model for these.

The prediction of  $V_{max}$  can be seen in Fig. 3.7 which shows more variation between the nu-

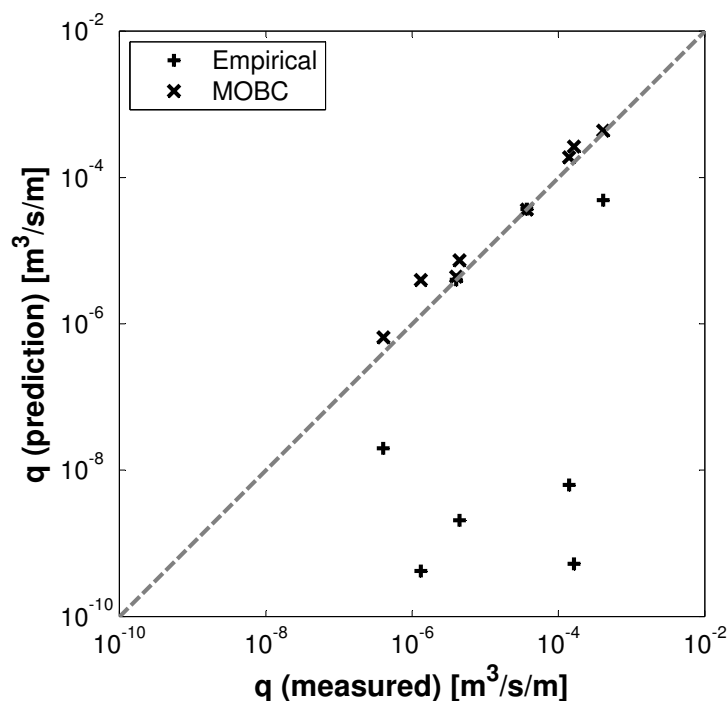


Figure 3.6: Comparison of  $q$  measured in physical model versus  $q$  calculated with the numerical model and predicted using empirical formulae. Grey dashed line represents perfect fit.

numerical model and the physical model measurements. Similar with the findings for  $q$ , there is generally a tendency of overestimating  $V_{max}$  in the numerical model. This is also in agreement with the larger individual events observed in the time series from the numerical model. One possible source of this increase is due to the detection of reflected waves at  $WG7$  in the physical model increasing the surface elevation that is read by the model.

Tests 007 and 008 showed an underestimation by the numerical model. These two tests experienced high overtopping which made it more difficult to distinguish the individual overtopping volumes in the physical model time series. The means that the  $V_{max}$  observed may have incorporated more than one overtopping event, and hence providing a false elevated measurement.

Overall the prediction of the numerical model is reasonably good with all of the results within the same order of magnitude as those measured in the physical model.

Again, in Fig. 3.8, the results from both the numerical model and the physical model have been compared with the prediction obtained from the empirical formulae specified in section 2.5. As mentioned earlier, due to the extreme nature of  $V_{max}$ , the formulae are generally understood to be less accurate than those for  $q$ . As with  $q$  the values of  $V_{max}$  are all under-predicted. In this case, the variation between the physical model and the empirical prediction is more than 3 orders of magnitude for some of the wave conditions. Even though there may be some inaccuracies in the measurement of  $V_{max}$  in the physical model, it is still clear, that the numerical model

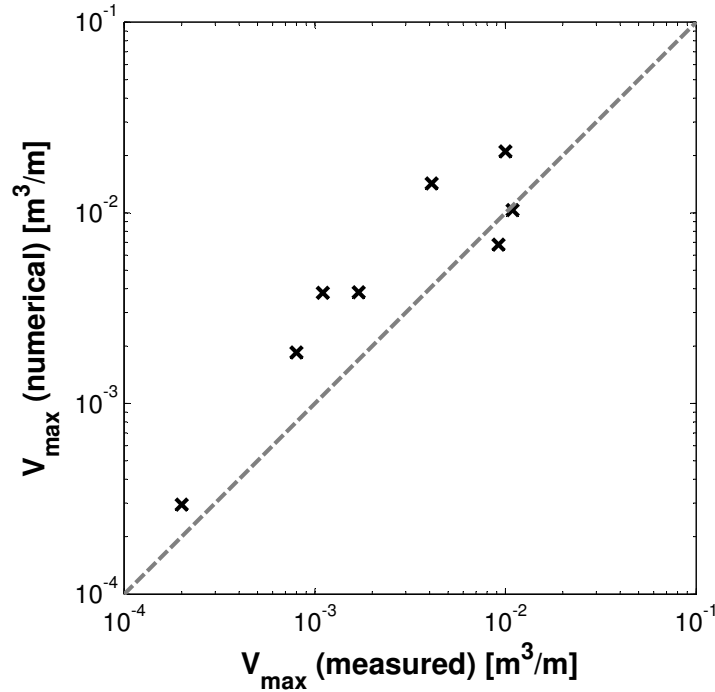


Figure 3.7: Comparison of  $V_{max}$  measured in physical model versus  $V_{max}$  calculated with the numerical model. Grey dashed line represents perfect fit.

provides much better results.

### 3.4.6 Probability of Overtopping

Even with the specific experimental data, the number of overtopping events in the physical model is still quite difficult to calculate. It is possible for events to be missed, or even additional events to be mistakenly identified. This has led to a higher variation for the prediction of  $P_{ov}$  between the numerical and physical model as shown in Fig. 3.9. It can be seen on this graph that in the higher overtopping tests the  $P_{ov}$  is generally over-predicted by the numerical model. As mentioned previously, this is probably due to the higher accuracy in identifying the individual events in the numerical model. In the lower overtopping, the  $P_{ov}$  is generally under-estimated by the numerical model.

It has already been mentioned that due to the different methods used to quantify the overtopping volumes in the two models, the number of overtopping events may diverge significantly. So in order to carry out a more meaningful comparison in terms of  $P_{ov}$ , this parameter was redefined. This was achieved by removing the events for which  $V_{ov} > V_{min}$  for each test in the numerical model, as they were not identifiable in the physical model. The redefined values are referred to as  $P_{ov,mod}$ , and are shown in Fig. 3.10.

Due to the lower value of  $V_{min}$  that was identifiable in the lower overtopping tests, there was

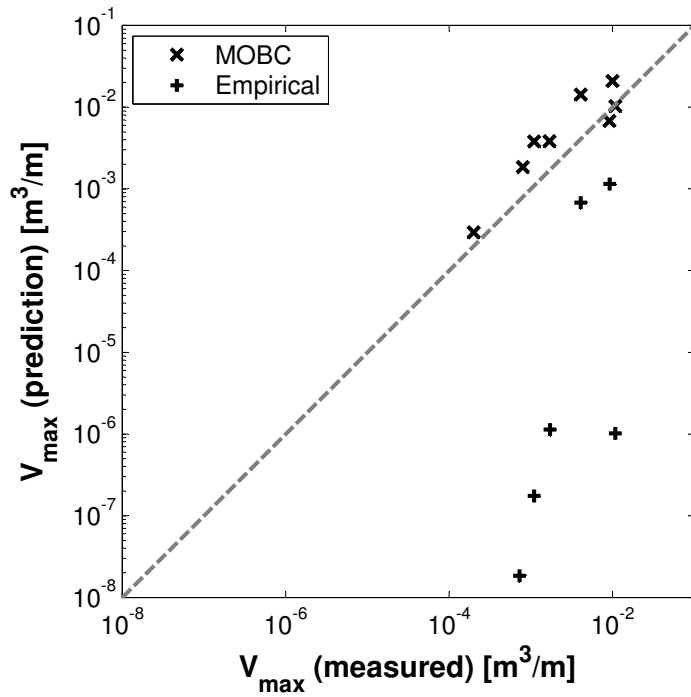


Figure 3.8: Comparison of  $V_{max}$  measured in physical model versus  $V_{max}$  calculated with the numerical model and predicted using empirical formulae. Grey dashed line represents perfect fit.

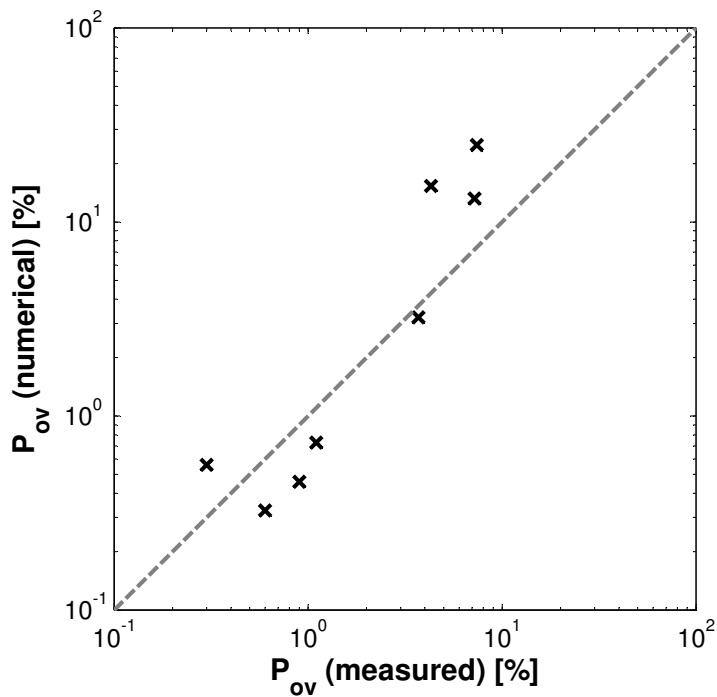


Figure 3.9: Comparison of  $P_{ov}$  measured in physical model versus  $P_{ov}$  calculated with the numerical model. Grey dashed line represents perfect fit.

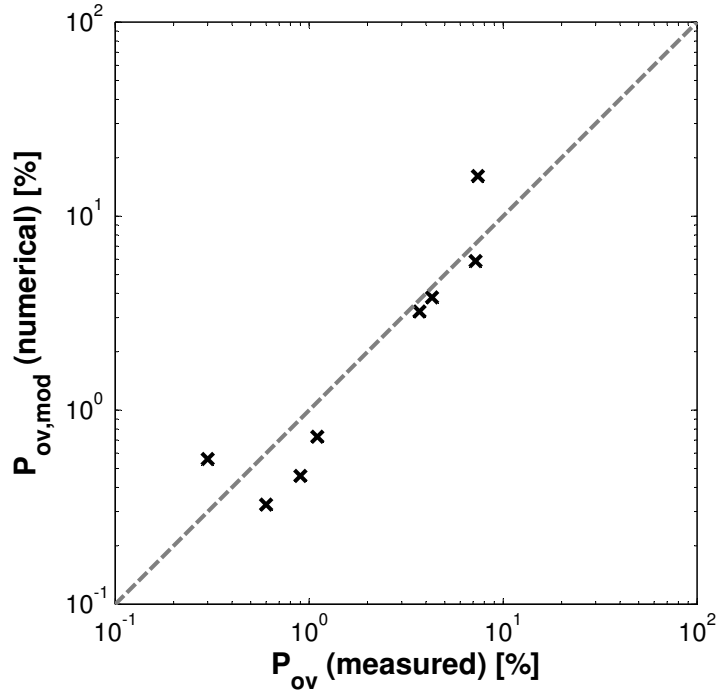


Figure 3.10: Comparison of  $P_{ov}$  measured in physical model versus modified  $P_{ov}$  calculated with the numerical model. Grey dashed line represents perfect fit.

no modification to  $P_{ov}$  in these tests. In the higher overtopping, the modification has increased the accuracy of the numerical model with comparison with the experimental results.

The results of  $P_{ov,mod}$ , and the physical model are also compared with equation 2.31. This time, the formulae generally overestimates, although the accuracy appears to be better than the empirical formulae for the other parameters. It is still clear that the numerical model provides a better prediction.

### 3.5 Summary

Validation of the ability of the NLSWE model to predict overtopping has been undertaken by simulating physical wave flume tests undertaken at HR Wallingford. Overall the comparison between the measured and predicted overtopping parameters for the MOBC tests show good agreement. The results are consistent with the accuracy shown by former published numerical simulations of overtopping using similar numerical models. When the numerical prediction and the empirical prediction is compared, it is clear that the numerical model provides a more accurate result.

This confirms that the model is suitable for this work, with the model structure, model assumptions and model domain producing minimal uncertainty.

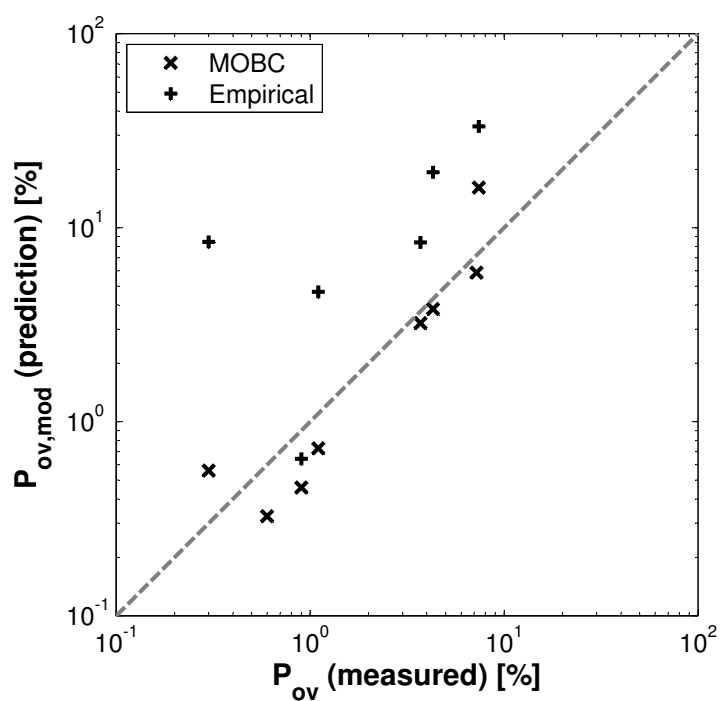


Figure 3.11: Comparison of  $P_{ov}$  measured in physical model versus modified  $P_{ov}$  calculated with the numerical model and  $P_{ov}$  predicted using empirical formulae. Grey dashed line represents perfect fit.

## Chapter 4

# Model Uncertainty due to Spectral Boundary Conditions

### 4.1 Introduction

In the previous chapter, numerical tests were carried out using the measured instantaneous water depth ( $\eta$ ) time series as offshore boundary conditions. However, in engineering practice, offshore boundary conditions for phase resolving models are often obtained from spectral models or measurements. Frequently the modeller is provided with the incident energy density spectra from which a time series will be reconstructed to be used as the boundary conditions.

Energy density spectrum provides only information on the amplitude of the components, so it is usually assumed that the phases of these components are randomly distributed. To create the randomly generated phases, an initial seed value is required which generates a population of uniformly distributed random phases. By varying this value for each simulation a different time series will be produced.

This means that from each energy density spectrum an infinite number of different wave series can be generated by changing the initial seeding of the random phase distribution. Initial evidence that this process plays an important role in the variability of the results is given in McCabe et al. (2011) for the run-up prediction and McCabe et al. (2013) for overtopping. The chapter will concentrate on the variability in the parameters under study due to this phenomenon.

## 4.2 Reconstructed Offshore Boundary Conditions

### 4.2.1 Incident Spectra

For this work the energy density spectra were obtained from the free surface elevation time series at *WG7* measured during the calibration tests (i.e. incident wave condition). Spectra can be defined in the frequency domain as shown in section 2.3.2.

Equation 2.7 states that when  $S(\omega)$  only is known, it is possible to obtain only the amplitude of the component at a given frequency. The phase  $s_n$  is undetermined, this means that from one energy density spectrum an infinite number of time series can be generated.

As mentioned earlier, the spectrum used here was obtained from the calibration tests, this was done because the separation of the incident and reflected signal would have made the reconstruction process more complex and in design practice usually the incident spectrum is provided. In contrast to the MOBC tests, an absorbing generating boundary condition using the approach in Dodd (1998) was used.

### Monte Carlo Simulation

A Monte Carlo technique was employed to quantify the effect of the different seeding used for the offshore boundary time series. In each time series the phases  $s_n$  were obtained by assuming, for each test, a different uniform distribution between 0 and  $2\pi$  across the domain. A random number generator in Matlab was used to produce these different starting phases within the defined domain of possible inputs. The phases were then combined to produce each full time series of water depth,  $\eta$ . A population of these time series was generated and the distribution of the predicted overtopping parameters was analysed. The results obtained with this approach will be referred to as ROBC (Reconstructed Offshore Boundary Conditions).

### 4.2.2 Spectral Energy Density Estimation

The purpose of spectral density estimation is to approximate the spectral density of the random time series of waves measured in the physical model. In order to generate a random wave series to correspond to each specific input spectrum, the spectrum was split into a finite number of frequencies so that Eq. 2.6 becomes:

$$\eta(t) = \sum_{n=1}^{N_{comp}} a_n \cos(\omega_n t + s_n) \quad (4.1)$$

where  $N_{comp}$  is the number of components considered.  $S(\omega_n)$  was estimated from the time series using the Welch method (Welch, 1967). This method averages the spectrum of segments of the original time series. For each segment the Fast Fourier Transform (FFT) was carried out using a number of samples referred to as  $N_{FFT}$ . The choice of  $N_{FFT}$  directly affects the length and number of segments used for the method. Once the spectral estimate was obtained, this was divided into  $N_{comp}$  and  $a_n$  is obtained using Eq. 2.7.

It is important to choose a suitable value of  $N_{comp}$ . If this is too low, waves are repeated within the time series. If  $N_{comp}$  is too high, the reconstruction takes a long computational time. In order to establish the optimum values for both  $N_{FFT}$  and  $N_{comp}$  a sensitivity analysis was carried out using test 008 incident wave conditions. Three different  $N_{FFT}$  values (512, 1024 and 2048) were considered. The resulting spectrum for each were interpolated using different  $N_{comp}$  values. For each of these values fifty ROBC runs have been generated and the resulting  $q$  was calculated. Then the relative error  $\sigma'$  of  $q$  was calculated.  $\sigma'$  is defined as

$$\sigma' = \sigma/\mu. \quad (4.2)$$

Here  $\sigma$  is the standard deviation of the parameter, and  $\mu$  is the mean value.  $\sigma'$  is useful to provide a measure of the variability of a parameter and it is often used in uncertainty analysis (see for example Pullen et al., 2007).

Fig. 4.1 shows the results of this analysis. The graph shows that, as the  $N_{comp}$  increases, the relative error in the prediction of overtopping discharge decreases converging to a plateau. This is very important to guarantee the significance of the results obtained with the ROBC tests. The three  $N_{FFT}$  values provide very similar values of  $\sigma'$ , with  $N_{FFT} = 1024$  being deemed suitable to be used in all the ROBC tests.  $N_{comp} = 32768$  has been chosen as it assures both convergence and the absence of repetitions in the time series. When such an elevated value is used, the reconstruction of the time series takes a long time to be produced. To speed up this process, the spectra were shortened to remove the values beyond  $3f_p$ , as negligible energy was found beyond this frequency.

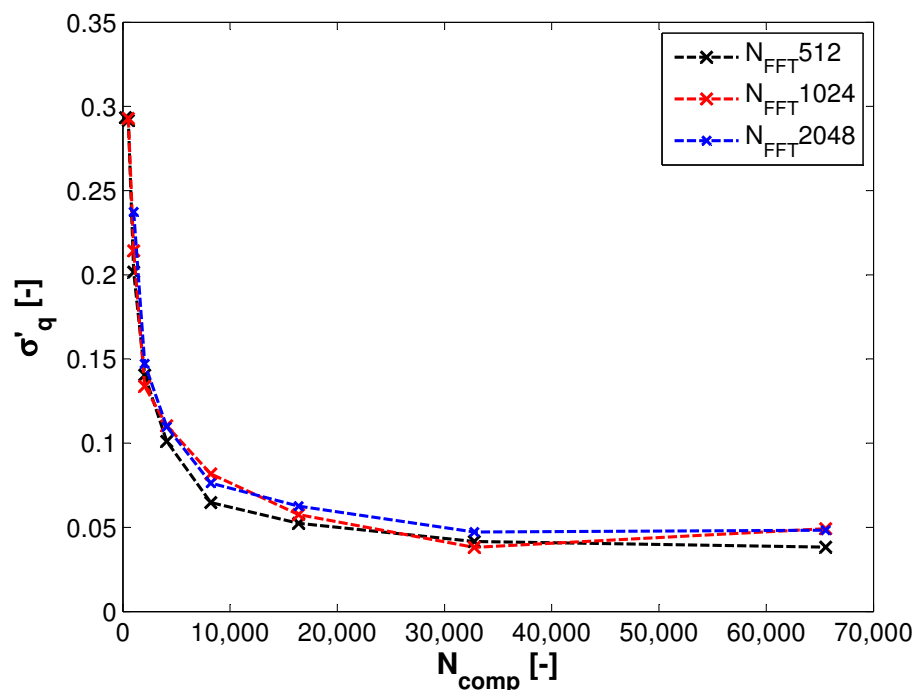


Figure 4.1: Relative error for  $q$  due to the spectral estimate and spectral components used for test 006. Red line:  $N_{FFT} = 512$ , Green line:  $N_{FFT} = 1024$  and Blue line:  $N_{FFT} = 2048$ .

### 4.2.3 Definition of the Monte Carlo Population Size

An adequate population size of ROBC tests was required to produce meaningful statistics. To establish an optimal number of tests, a further sensitivity analysis was carried out by repeating the ROBC tests for an increasing number of offshore boundary time series and for three different tests, namely 003, 006 and 007, corresponding to different levels of overtopping.  $\sigma'$  was used again to measure the convergence of the results. The relative error for  $q$  (defined as  $\sigma'_q$ ), for  $V_{max}$  ( $\sigma'_{V_{max}}$ ) and  $P_{ov}$  ( $\sigma'_{P_{ov}}$ ) were analysed separately.

Fig. 4.2 shows the quantities for the three tests. In all cases  $\sigma'$  decreases with the increasing number of ROBC tests. For medium and higher levels of overtopping  $\sigma'$  converges relatively quickly, after just 100 tests for all three of the overtopping parameters considered. However, for lower levels of overtopping  $\sigma'$  converges more slowly. It was therefore decided that a population size of 500 ROBC tests would be used to ensure convergence at all levels of overtopping.

### 4.2.4 Definition of Test Length

As already mentioned, Pullen et al. (2007) recommends that a sea state in physical modelling can be represented by 1000 random waves. This is why physical experiments are commonly carried out for a number of mean wave periods ( $N_w$ ) equal to 1000. It was important to confirm

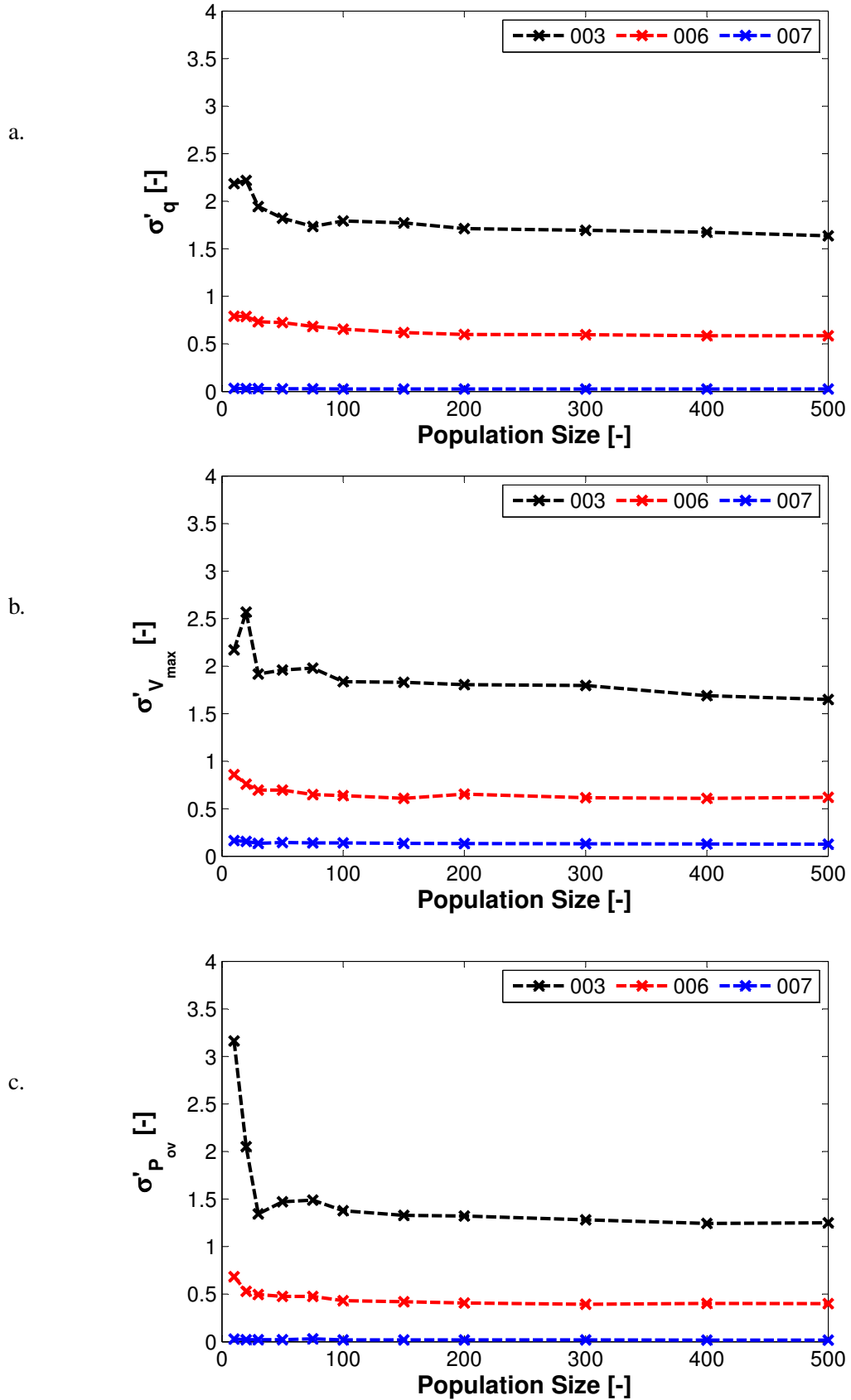


Figure 4.2: Relative error. a.  $q$ . b.  $P_{ov}$ . c.  $V_{max}$  due to the number of ROBC tests. Green line: test 003 for low overtopping. Red line: test 006 for moderate overtopping and Blue line: test 007 for high overtopping.

Table 4.1: Overtopping parameters for tests with varying number of waves

$N_w$	Test 003			Test 006			Test 007		
	$q$ (m <sup>3</sup> /m/s)	$P_{ov}$ (%)	$V_{max}$ (m <sup>3</sup> /m)	$q$ (m <sup>3</sup> /m/s)	$P_{ov}$ (%)	$V_{max}$ (m <sup>3</sup> /m)	$q$ (m <sup>3</sup> /m/s)	$P_{ov}$ (%)	$V_{max}$ (m <sup>3</sup> /m)
500	0	0	0	2.77e-6	1.00	9.77e-4	9.90e-4	98.2	0.0077
1000	8.50e-7	0.20	0.0017	1.50e-5	1.70	0.0121	9.83e-4	97.3	0.0077
2000	5.42e-7	0.10	0.0017	1.48e-5	2.10	0.0121	9.85e-4	97.5	0.0091
5000	7.57e-7	0.06	0.0054	1.45e-5	1.74	0.0121	9.68e-4	97.9	0.0091

that this number was also suitable for the generated time series in the numerical model. A test was carried out by producing a time series for a large number of waves, in this case  $N_w = 5000$ . The overtopping parameters were then calculated after an increasing number of waves for the three tests used as representative of various levels of overtopping in this work, and the results compared in Table 4.1

It can be seen in the table that for the moderate and high overtopping levels, the values of the overtopping parameters are not significantly effected by the length of the test once the 1000 wave threshold has been reached. The values for  $q$  and  $P_{ov}$  remain consistent in all of the longer tests. The  $V_{max}$  is either reached within the first 1000 waves, or a value of a similar magnitude has been reached. For the low overtopping level, there is more variation in the values of the overtopping parameters. However, the  $V_{max}$  and the  $P_{ov}$  are of the same magnitude in the different length tests. The  $q$  shows slightly more variation, however the value obtained for 1000 waves is similar to that obtained with 5000 waves.

Overall, this suggests that the 1000 waves generated in the time series is enough to achieve convergence of the parameters under study.

## 4.3 Comparison with the Validation Tests

### 4.3.1 Overtopping Time Series

The overtopping predictions of ROBC tests are dependent on the seeding used to generate the  $\eta$  time series at the boundary. Fig. 4.3 provides some examples of such variability by showing the time series of the overtopping volumes for 15, randomly selected, runs of the three different levels of overtopping test conditions.

In Fig. 4.3, a, which shows the low level of overtopping, the total overtopping volume ranged from  $0.0002\text{m}^3/\text{m}$  to  $0.005\text{m}^3/\text{m}$  over the 15 ROBC runs. This is equivalent to a variability of

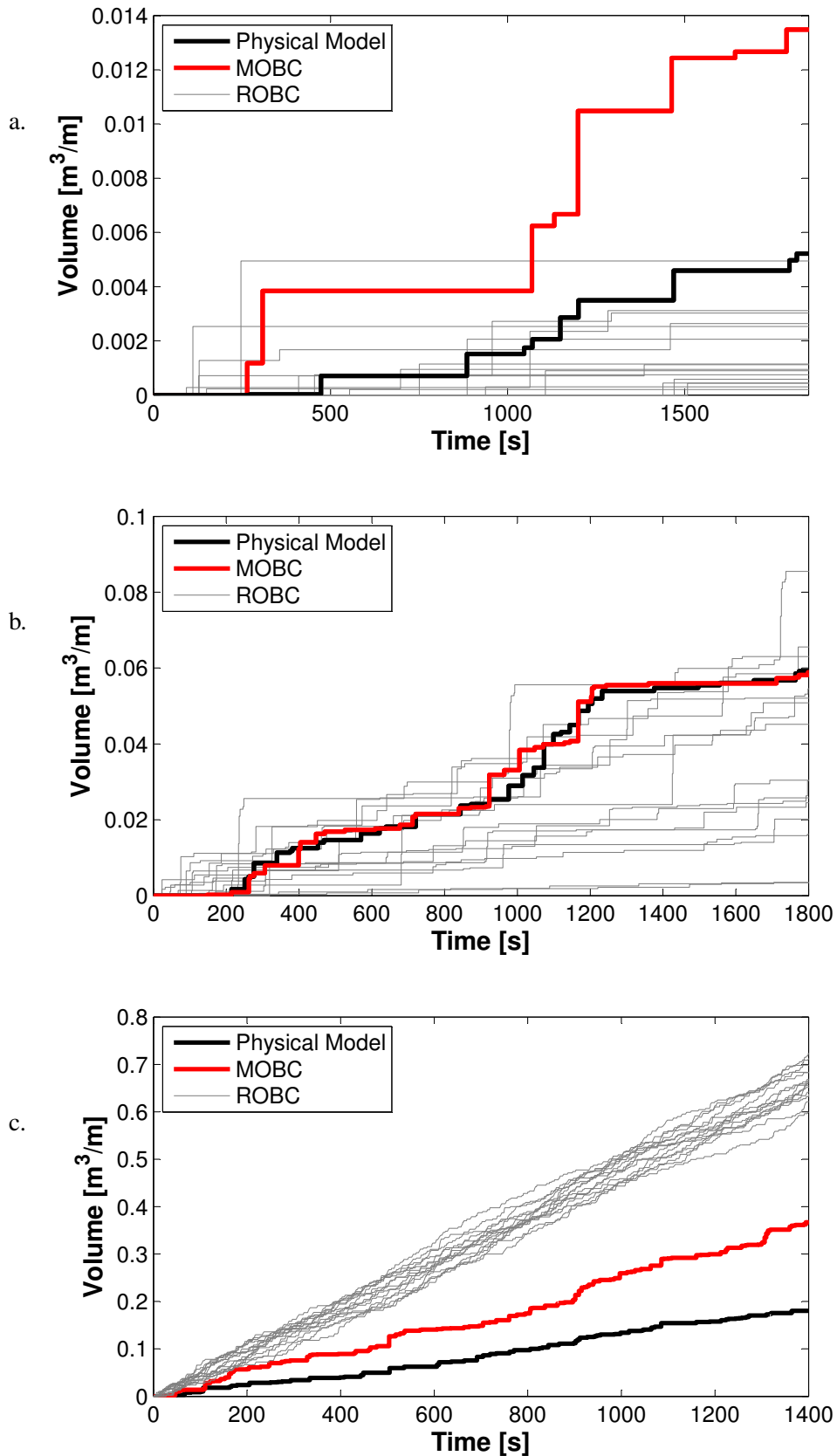


Figure 4.3: Overtopping time series for three tests. a. Test 003 (Low Overtopping). b. Test 006 (Moderate Overtopping). c. Test 007 (High Overtopping). Black line: experimental data, Red line: MOBC. Grey lines: 15 randomly selected ROBC tests.

a factor of 25 in the results. In addition the physical model and numerical records are plotted, producing values for the total volume of  $0.005\text{m}^3/\text{m}$  and  $0.013\text{m}^3/\text{m}$  respectively. The physical model results is at the top of the range from the ROBC tests, with the MOBC result being significantly higher than both set of results.

In Fig. 4.3, b, which represents a moderate level of overtopping, within the 15 runs, the total overtopping volume ranged from  $0.004\text{m}^3/\text{m}$  to  $0.085\text{m}^3/\text{m}$ , resulting in a variation of a factor of more than 20 in these results. Also, shown in this figure are the records from the experimental data and the MOBC results. These produced values for the total volume of  $0.071\text{m}^3/\text{m}$  and  $0.067\text{m}^3/\text{m}$  respectively, which is towards the top of the range predicted in the ROBC tests.

Finally, in the lower graph for high overtopping, there is less variation in the total overtopping volume with a range of  $0.62\text{m}^3/\text{m}$  to  $0.72\text{m}^3/\text{m}$ . However, it can be observed in this graph that the times series obtained from the physical model and MOBC tests are significantly smaller than the ROBC results, producing results of  $0.18\text{m}^3/\text{m}$  and  $0.37\text{m}^3/\text{m}$  respectively.

It should be noted here that only one experimental run for each test was conducted, and therefore only one MOBC test was run for each condition. The physical model could be subject to a similar level of variability due to the exact time series generated by the paddle for each wave condition, so it is possible that the results could be anywhere within the range produced from the ROBC tests.

### 4.3.2 Overtopping parameters

It is clear from the overtopping time series that variability is present in the ROBC test results, this will be analysed in depth with respect to the overtopping parameters later in this chapter. Firstly, in order to assess how accurate the average ROBC overtopping predictions are, the mean values of each overtopping parameter from the ROBC tests were compared with both the laboratory test results and those obtained with the MOBC tests. Fig. 4.4 shows both  $P_{ov}$  and  $P_{ov,mod}$  from both sets of tests.

For the smaller  $P_{ov,mod}$ , ROBC tests diverge significantly from both the measured and the MOBC tests. For tests 002 and 003,  $P_{ov}$  is significantly smaller in ROBC tests than in MOBC ones, while for tests 004 and 005 the opposite occurs. For the three tests with the highest recorded  $q$ ,  $P_{ov,mod}$  in ROBC tests is always overestimated with respect to both the MOBC tests and the laboratory experiments. When smaller volumes are retained, i.e.  $P_{ov}$  is considered (Fig. 4.4, b), this parameter is significantly larger than  $P_{ov,mod}$  in the three tests with the highest over-

topping, whilst it doesn't change significantly in other cases. This means that a large number of smaller overtopping events are generated as a result of the random phasing of the spectral components. The difference between  $P_{ov,mod}$  and  $P_{ov}$  is noticeable only for these three high overtopping tests as the comparison of Fig. 4.4, a and b, suggests.

If the values of the empirical formulae for  $P_{ov}$  that are shown in Fig. 3.11 are also compared to the ROBC results. It can be seen that a similar level of accuracy is obtained using these two methods, particularly in the tests with higher overtopping. In the lower overtopping, although the magnitude of variation between the empirical and ROBC prediction is similar, the ROBC under-predicts the results whereas the formulae over-predicts.

Differences between ROBC and MOBC tests are also evident in the analysis of both  $q$  and  $V_{max}$ . Fig. 4.5 shows the comparison between MOBC tests, the average  $q$  in ROBC tests and measurements. The average of the values obtained by the ROBC do not provide as close a match to the physical experiments as those provided by the MOBC simulations. Test 004 is largely overestimated, while tests 002 and 003 are underestimated. These tests were among those with the largest mismatch in  $P_{ov,num}$ . Tests 001, 007 and 008 appear overestimated as well but the estimate of  $q$  is within the same order of magnitude of the MOBC tests.

The mean ROBC results for  $q$  can also be compared with the values calculated using the empirical formulae which were shown in Fig. 3.6. Although not as accurate as the MOBC results, it can generally be seen that the mean ROBC results provide better prediction of  $q$  than the empirical formulae for these tests. Finally, in Fig. 4.6,  $V_{max}$  from Test 004 can be seen to be overestimated by two orders of magnitude. However in all other cases  $V_{max}$  is underestimated in the ROBC tests with respect to the MOBC one. As also seen for  $q$  the mismatch reduces for the tests with higher overtopping rates.

Again, if the ROBC results are compared with the empirical results shown in Fig. 3.8, then it is clear in this case that the ROBC provides a much better prediction in all of the tests than the empirical formulae.

#### 4.4 Variability due to ROBC

In the previous section the averaged results of the ROBC tests have been presented. Here the variability of the ROBC tests originating from the same spectrum is analysed in depth.

Fig. 4.7 shows the scatter plot of  $q$  against  $P_{ov}$  for all the ROBC tests carried out. It can be

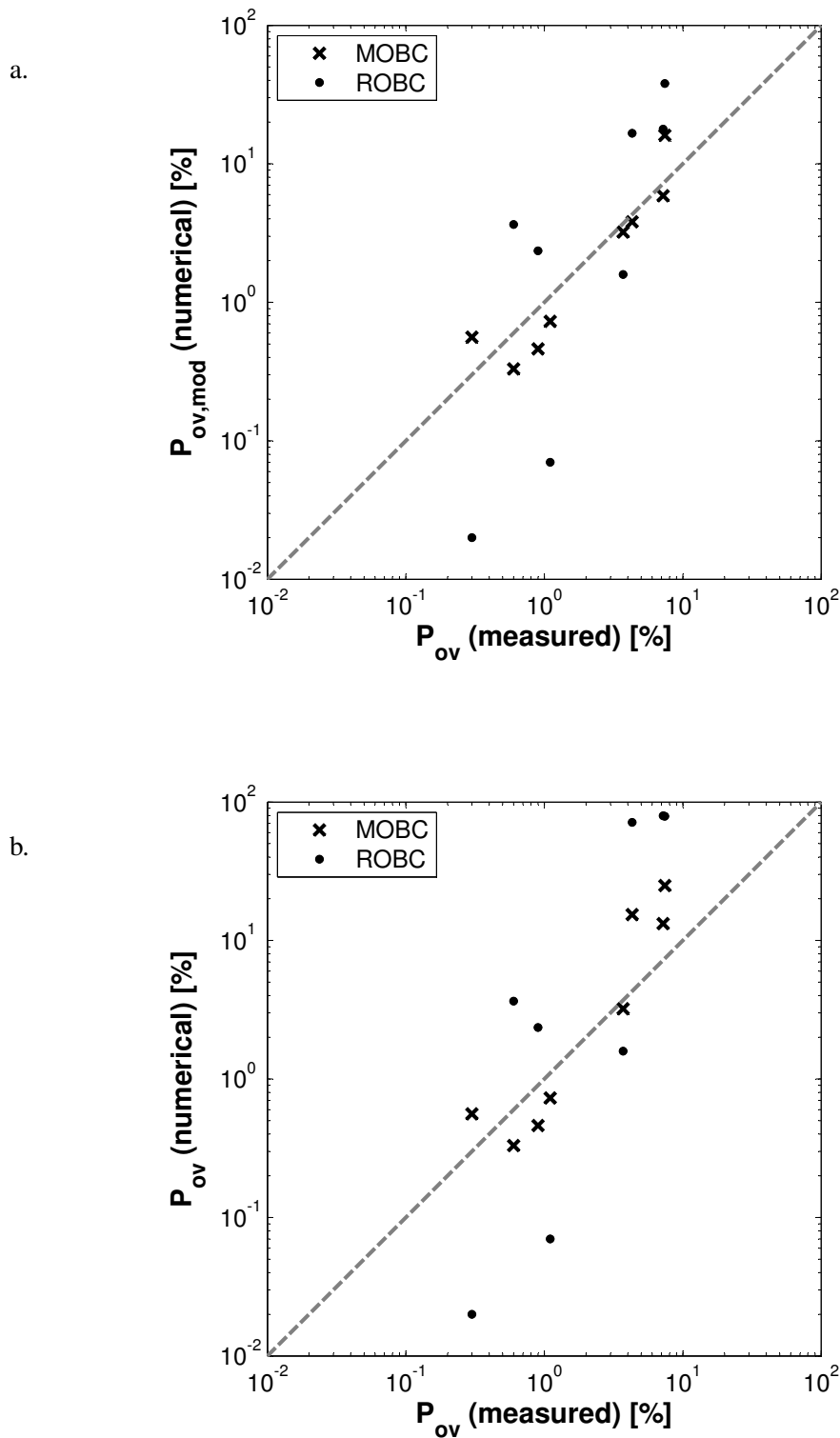


Figure 4.4: Comparison of  $P_{ov}$  measured in physical model versus both a.  $P_{ov}$  and b. modified  $P_{ov}$  calculated with the numerical model for MOBC and ROBC tests. Grey dashed line represents perfect fit.

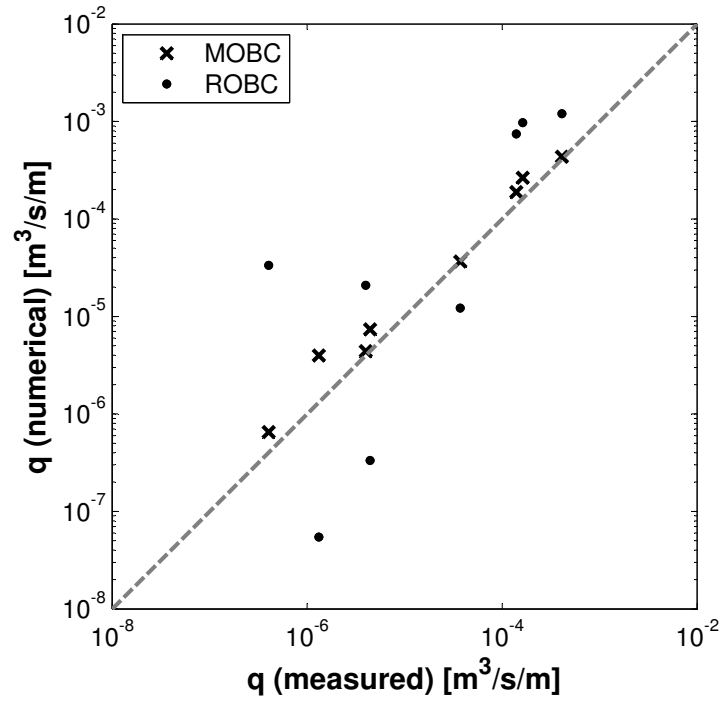


Figure 4.5: Comparison of  $q$  measured in physical model versus  $q$  calculated with the numerical model for MOBC and ROBC tests. Grey dashed line represents perfect fit.

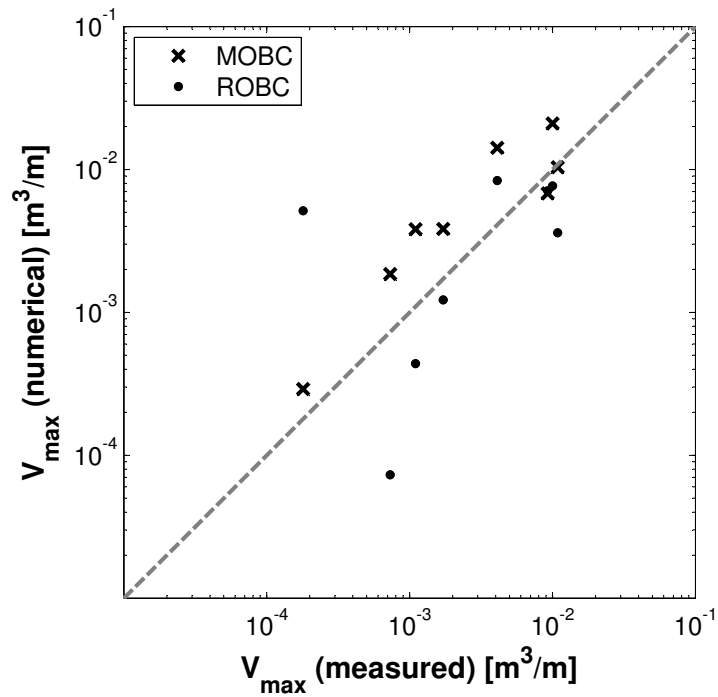


Figure 4.6: Comparison of  $V_{max}$  measured in physical model versus modified  $V_{max}$  calculated with the numerical model for MOBC and ROBC tests. Grey dashed line represents perfect fit.

observed on this figure that the variability in the predicted  $q$  is strictly related to  $P_{ov}$  in each test. Lines denoting the average ROBC results, along with the 95% confidence interval are also shown. To highlight the technical relevance of the results obtained, also reported on this figure are the scaled down overtopping limits suggested in Pullen et al. (2007).

In tests 002 and 003,  $P_{ov}$  remains lower than 1% while  $q$  varies by more than 25 times, i.e. the highest discharge is more than 25 times larger than that of the lowest discharge recorded. In these tests, few waves actually overtop, so the influence of the characteristics of the individual overtopping wave is maximised. It should be noted that many of the ROBC tests in this range of values experienced no overtopping in a number of the runs. These values are not reported in Fig. 4.7 as all  $q = 0$  would also have  $P_{ov} = 0$ . Tests 002 and 003 show the larger variability in terms of orders of magnitude of  $P_{ov}$  and  $q$ .  $P_{ov}$  varies from 0.2% to 6%. The tests with the highest  $P_{ov}$  show, in comparison, very little variability in overtopping parameters.

In addition to examining the variation in the overtopping discharge, Fig. 4.8 compares  $V_{max}$  with  $P_{ov}$ . There is no evident correlation between the variables, with variation of the same magnitude in both the low and moderate overtopping, in fact it can be seen on this graph that the maximum individual overtopping volume varies more than the overtopping discharge, particularly in the moderate overtopping levels. These are also the tests with a higher still water level. The maximum individual overtopping volume varies by more than 50 times, so the highest maximum individual volume for a particular test is more than 50 times larger than the lowest. However, across all the tests it can be observed that the overall variation is less, with even the low overtopping producing  $V_{max}$  of a similar magnitude to the high overtopping conditions.

It has been shown in the previous two graphs that  $P_{ov}$  can vary significantly in the low overtopping tests. When this is quantified, it can be shown that similarly to  $q$ , this parameter can vary by approximately 25 times. It is known that  $P_{ov}$  is directly related to the crest level, so to explore this further a graph of  $R^*$  against  $P_{ov}$  has been plotted in Fig. 4.9. This graph shows that in tests with a low dimensionless crest freeboard, the variability in the magnitude of  $P_{ov}$  is quite small. This is easily explained, by a lower value of freeboard resulting in more waves overtopping the structure.

The tests with the highest freeboard appear to show less variation than those with a slightly higher value, however this is caused by the large number of tests which resulted in a  $P_{ov} = 0$ , and are not included on the graph. There is also some variation in the values of  $R^*$  across the tests. Again, this seems to increase with the decrease in  $P_{ov}$ , caused by a decrease in the values

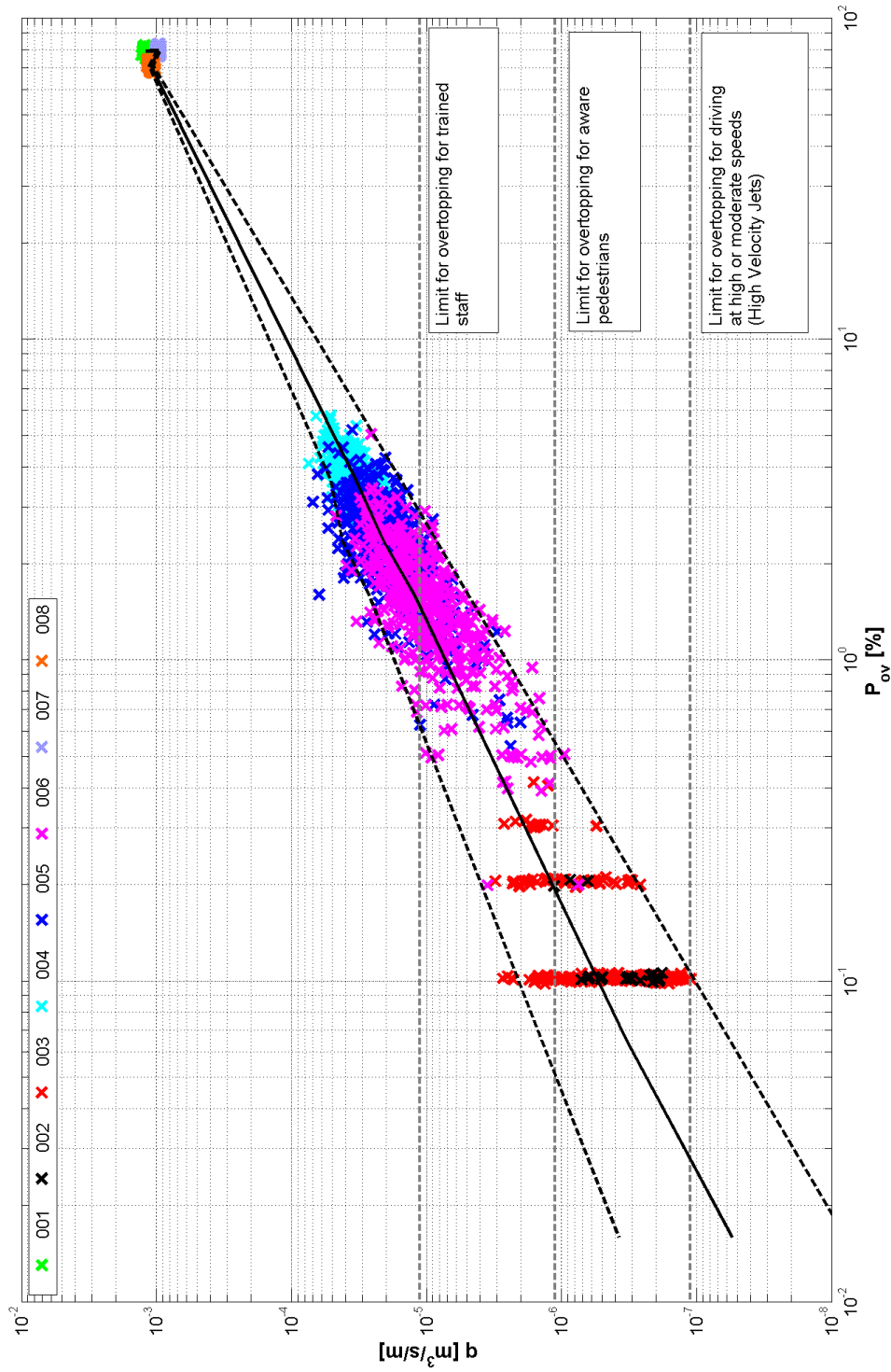


Figure 4.7: Logarithmic scatter graph showing the correlation between  $P_{ov}$  and  $q$ . Grey horizontal dashed lines: overtopping limits for  $q$  from Pullen et al. (2007). Solid black line: trend line of the average  $q$ . Black dash lines: 95% confidence interval for  $q$ .

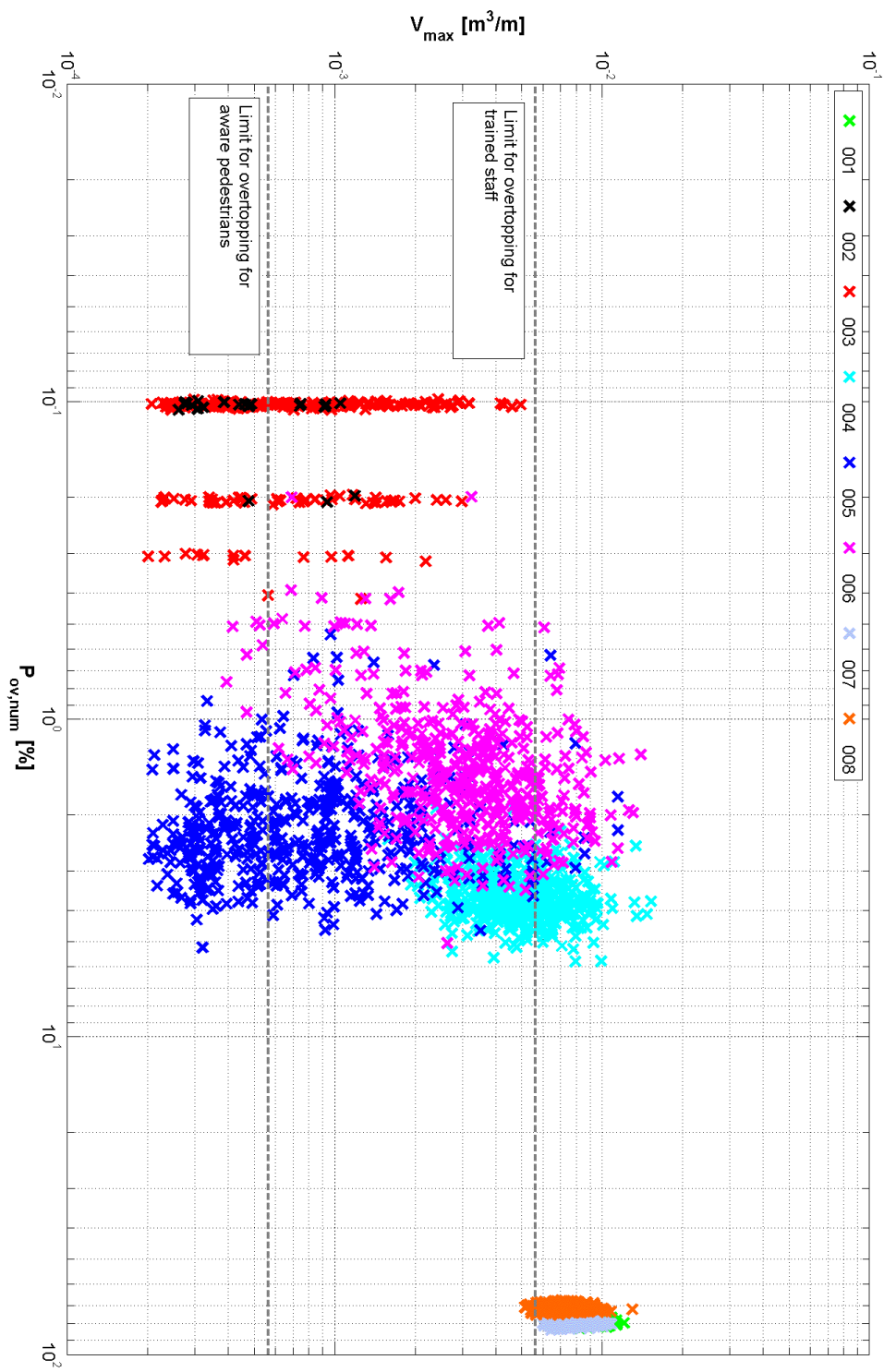


Figure 4.8: Logarithmic scatter graph showing correlation between  $P_{ov}$  and  $V_{max}$ . Grey horizontal dashed lines: overtopping limits from Pullen et al. (2007).

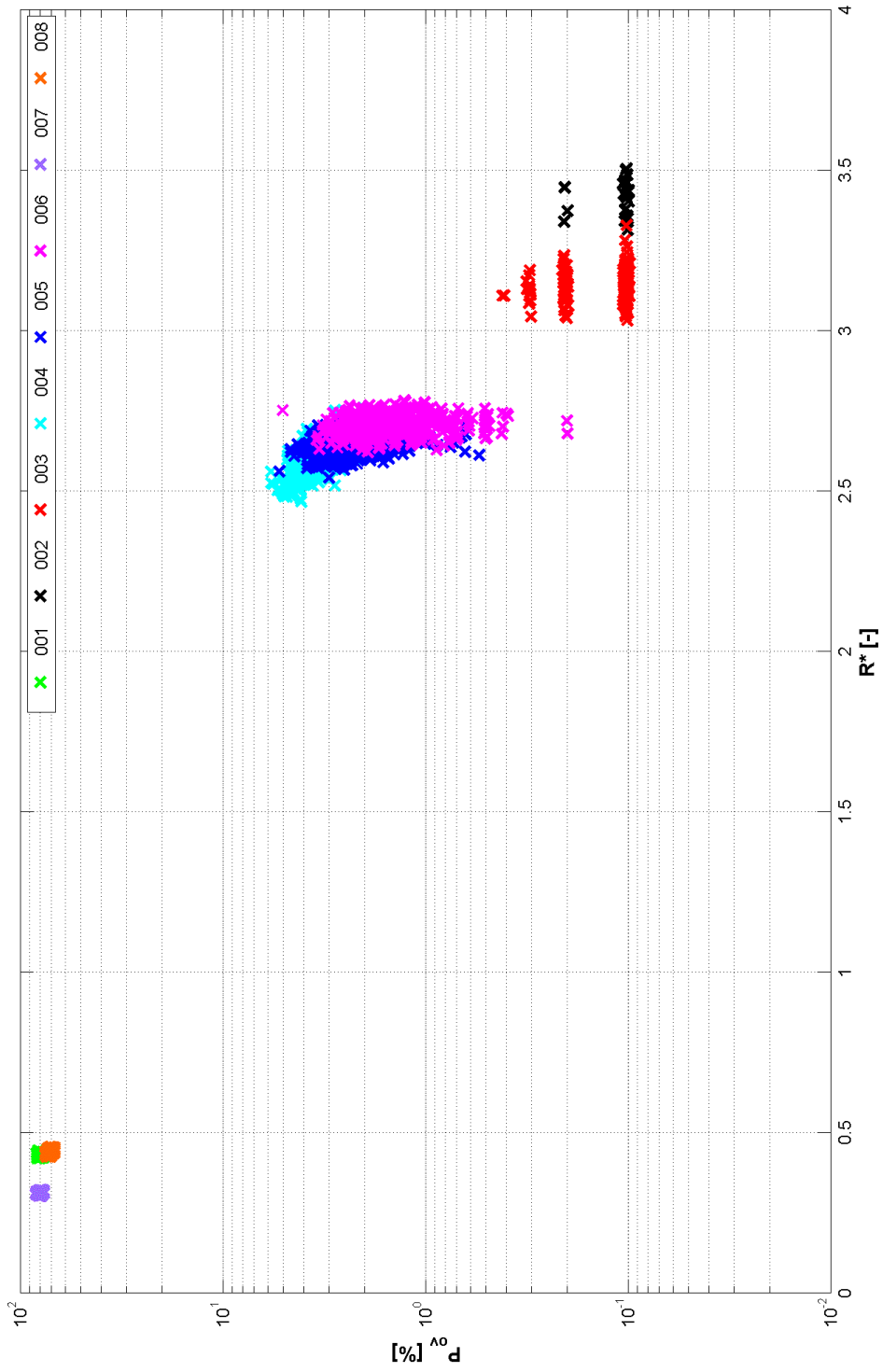


Figure 4-9: Logarithmic scatter graph showing correlation between  $R^*$  and  $P_{ov}$ .

of  $R^*$ . However, even in the tests with the highest variability this is equivalent to a variation of less than 10% across the tests.

A further graph is plotted showing  $R^*$  against  $q$ , which can be found in Fig. 4.10. Again here, it can be observed that the variation in  $q$  is significantly higher than that observed in  $R^*$ . The relationship between  $R^*$  and  $q$  is also evident which shows the magnitude of  $q$  plateauing at low values of  $R^*$ , this occurs due to the large number of waves overtopping in the numerical test, meaning that the value of  $q$  is similar in all of these tests.

Now to allow a comparison later with results from different tests, the variability needs to be assessed in terms of two non-dimensional parameters, therefore a further scatter plot showing  $R^*$  against  $Q^*$  is shown in Fig. 4.9. As previously observed, the magnitude of overtopping, in this case characterised by  $Q^*$ , directly influences the magnitude of the variation, with those experiencing lower dimensionless discharge being subject to a higher level of variability.

#### 4.4.1 Probability distribution of the overtopping parameters

The scatter plots in Figs. 4.7 and 4.8 give an overview of the variability in the results for the different overtopping parameters, without providing any further information about their distribution. This aspect is analysed in depth by focusing on tests 003, 006 and 007, as they can be considered representative of low, medium and high overtopping levels, respectively, within these numerical results. The distributions of all three overtopping parameters considered have been analysed. Fig. 4.12, Fig. 4.14 and Fig. 4.16 show the histograms of the distributions of  $q$ ,  $P_{ov}$  and  $V_{max}$  respectively. The abscissas have been normalised using the standard score  $z_\varphi$  defined as

$$z_\varphi = \frac{\varphi - \mu_\varphi}{\sigma_\varphi}, \quad (4.3)$$

where  $\varphi$  is the parameter considered, i.e.  $q$ ,  $P_{ov,num}$  or  $V_{max}$ . The advantage of normalising by using the standard score is that the results from each test can then readily be compared with standardised scores from the other tests. It also allows a good visualisation of the skewness of the distributions.

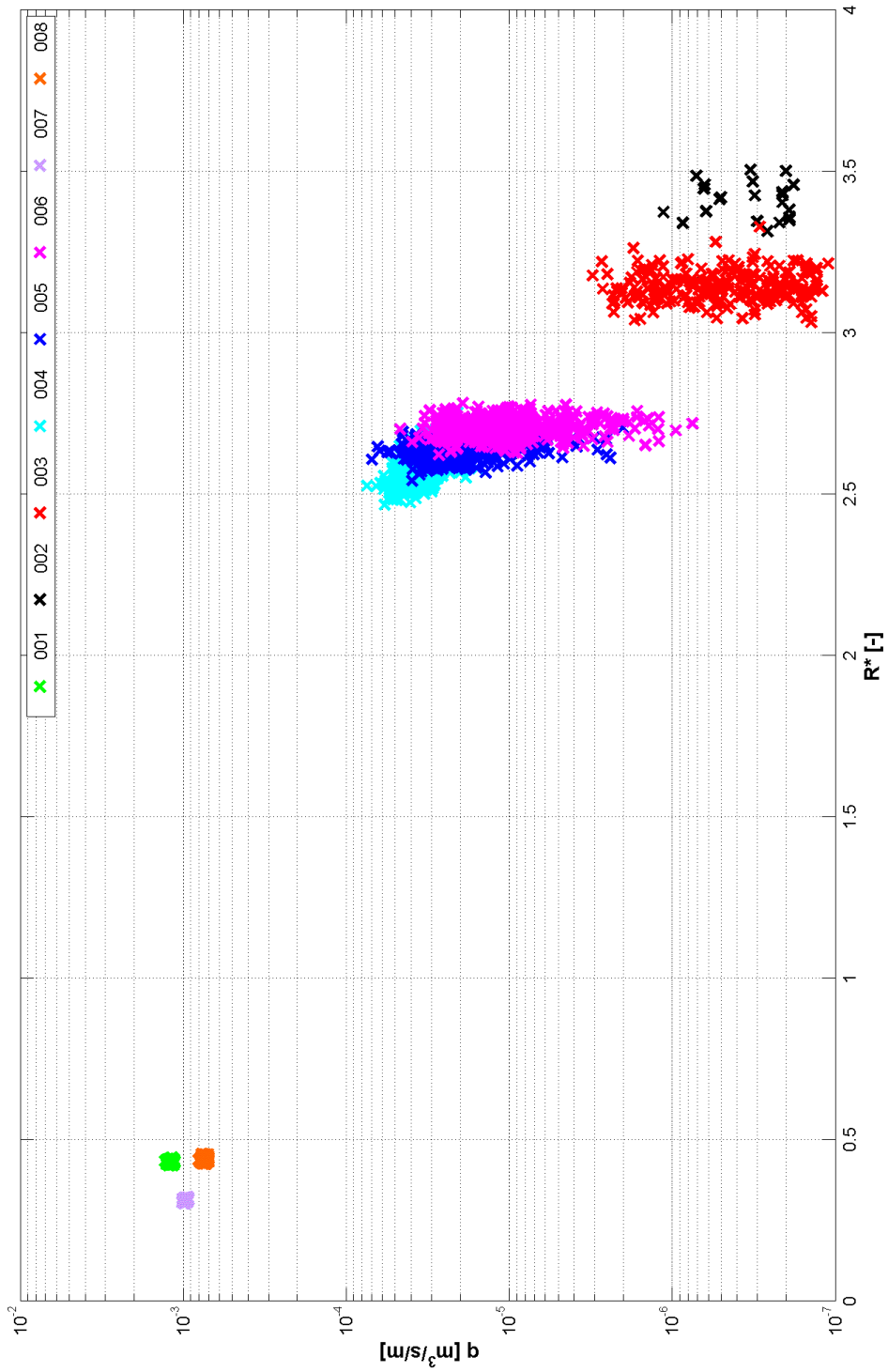


Figure 4.10: Logarithmic graph showing correlation between  $R^*$  and  $q$ .

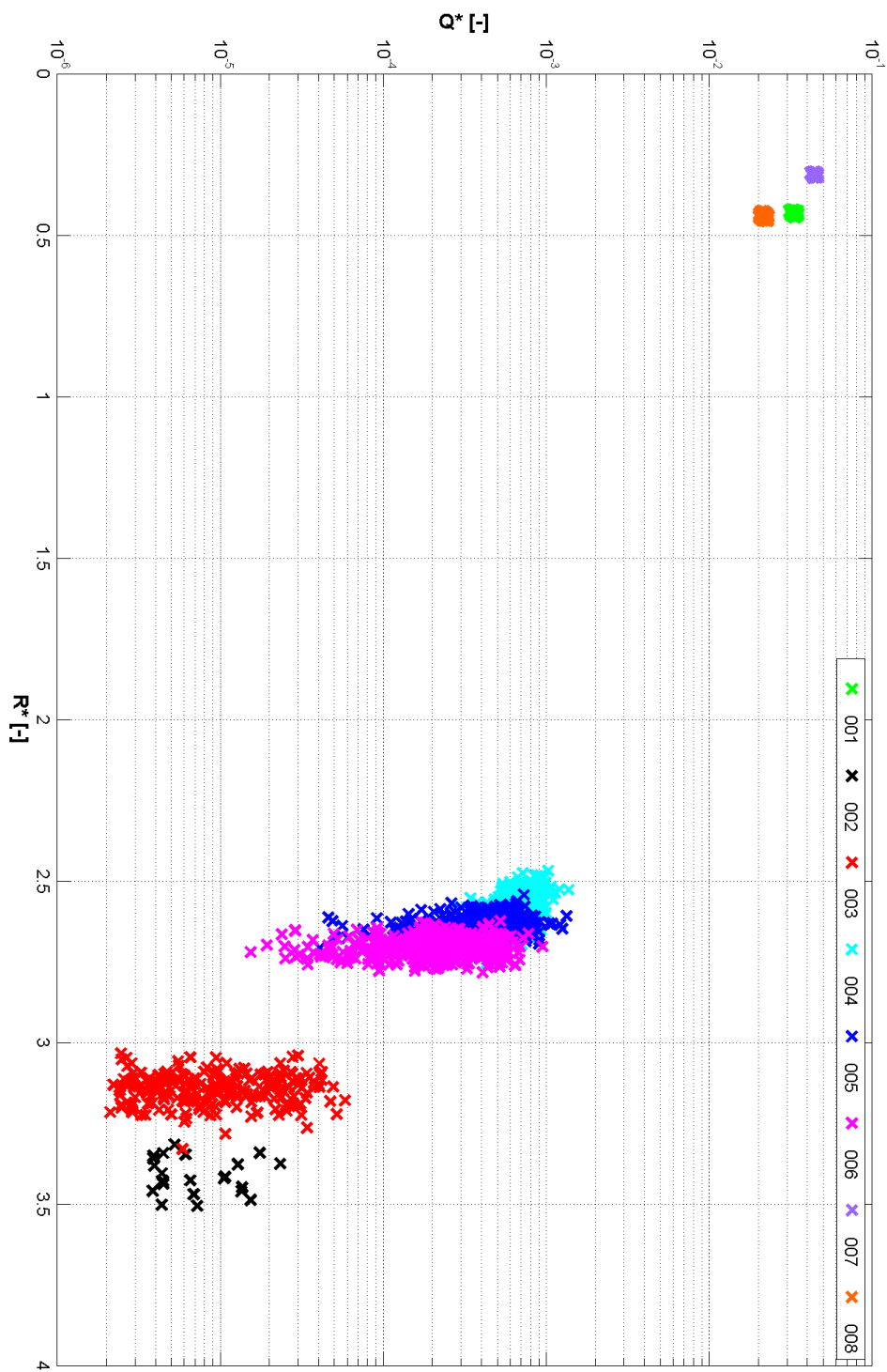


Figure 4.11 : Logarithmic scatter graph showing correlation between  $R^*$  and  $Q^*$ .

Table 4.2: CDF parameters for  $q$ 

Test	Normal		Weibull	
	$\mu$	$\sigma$	$\lambda$	$k$
003	3.32e-7	5.43e-7	N/A	N/A
006	1.22e-5	7.17e-6	1.37e-5	1.78
007	9.69e-4	1.53e-5	9.77e-4	65.4

### Mean Overtopping Discharge

Fig. 4.12 shows that for the tests that experienced a low level of overtopping a large number of them resulted in  $q_{ov} = 0$ . As the overtopping increases to a moderate level, the distribution remains positively skewed, suggesting that the majority of the results are below the mean value of  $q$ . Eventually, for high overtopping the distribution appears to be fairly symmetrical. This shape of the distributions are confirmed by plotting the cumulative distribution of  $q$  against the normal and the Weibull cumulative distribution functions (CDF). These particular distributions were chosen due to the shapes observed in the relative histograms. Fig. 4.13 shows the empirical cumulative frequency ( $F(q)$ ) against the various possible theoretical ones. The figure shows that for the lowest level of overtopping (003) only a normal distribution could be compared with the results due to the fact that the Weibull distribution cannot be used to describe distributions with occurrences of zero overtopping. It is also evident in the figure that due to the large number of tests which experience no overtopping, the normal distribution does not well describe the distribution present.

For the test with a moderate level of overtopping (006), it appears that the Weibull distribution best describes the distribution present. This is not surprising due to the positive skew observed in the histogram. Finally, for the high overtopping test (007) the normal distribution is the better fit for the ROBC results.

The parameters of the distributions are shown in Table 4.2, where  $\mu$  and  $\sigma$  are the mean and standard deviation for the normal distribution, and  $\lambda$  and  $k$  are the scale and shape factor for the Weibull distribution.

The CDF is a good way of visually comparing the empirical distribution with those produced using theoretical distribution, however to fully quantify the goodness of fit a Kolmogorov-Smirnov (K-S) test has been carried out. The test compares the empirically obtained data against the known distributions. The null hypothesis is deemed to be true if the empirical distribution follows the theoretical one. The test provides a statistic,  $D_n$ , defined as the maximum absolute difference between the two considered CDFs. Table 4.3 shows the results of the K-S test for the

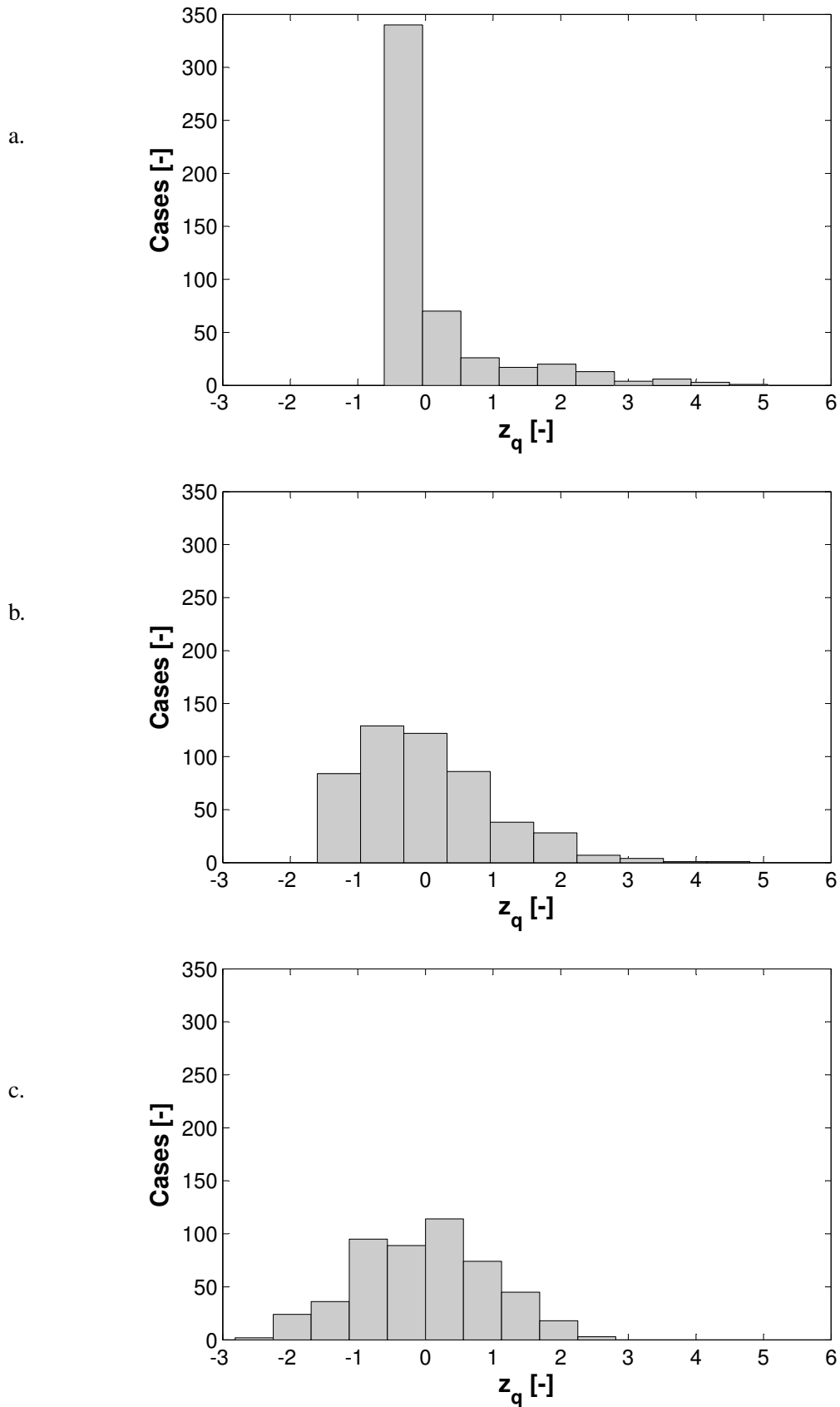


Figure 4.12: Relative histograms comparing distribution of  $q$  for different levels of overtopping. a. Test 003 (Low Overtopping). b. Test 006 (Moderate Overtopping). c. Test 007 (High Overtopping).

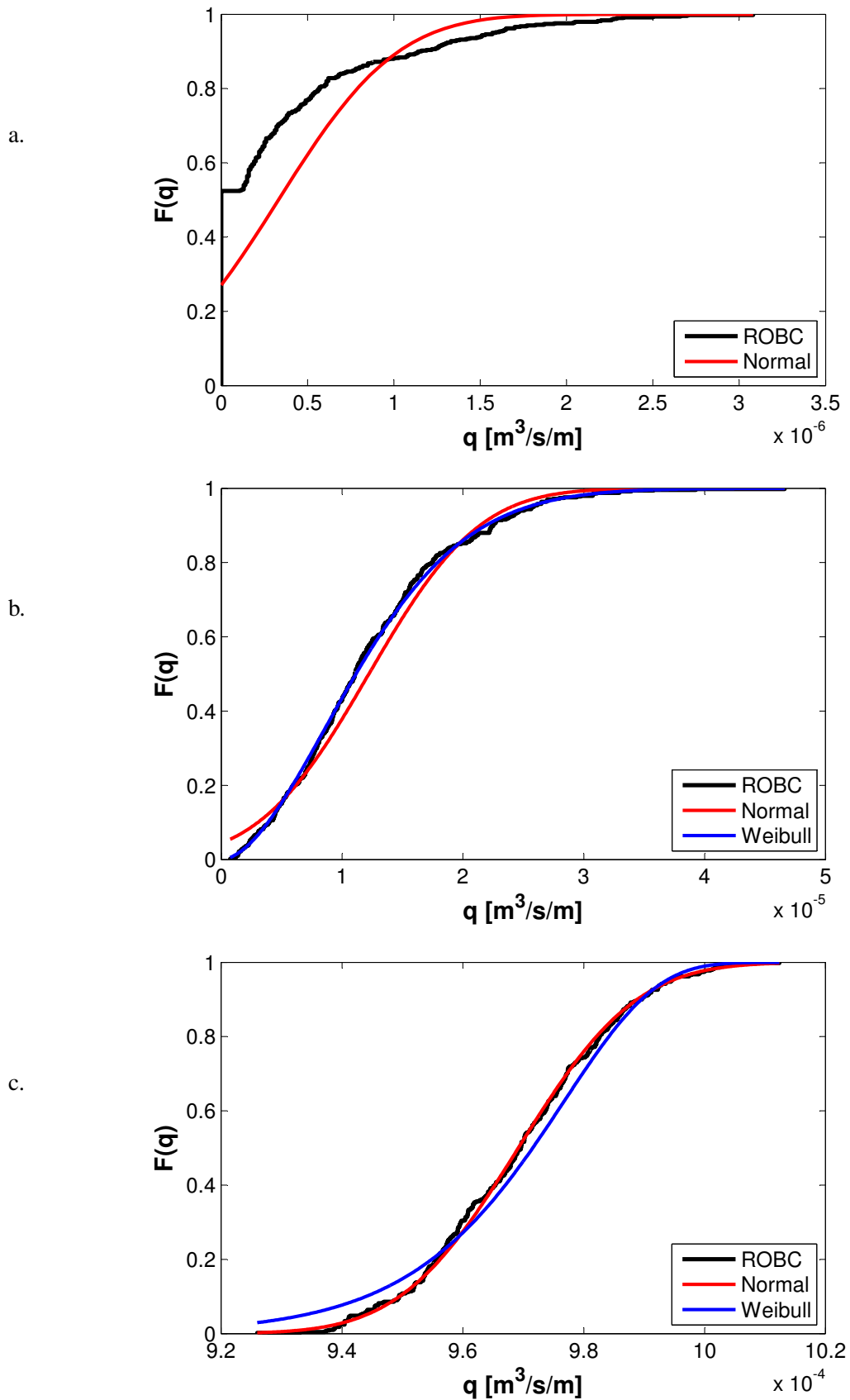


Figure 4.13: Empirical frequency curves for  $q$  from ROBC tests (black solid lines) compared with known distributions. a. Test 003 (Low Overtopping). b. Test 006 (Moderate Overtopping). c. Test 007 (High Overtopping).

Table 4.3: Results of the one sample K-S test for  $q$ 

Test	Normal		Weibull	
	$\Gamma$	$D_n$	$\Gamma$	$D_n$
003	1	0.271	N/A	N/A
006	1	0.080	0	0.030
007	0	0.037	1	0.073

Table 4.4: CDF parameters for  $P_{ov}$ 

Test	Normal	
	$\mu$	$\sigma$
003	6.55e-2	8.19e-2
006	1.59	6.39e-1
007	79.5	1.39

three ROBC distributions considered. Here  $\Gamma$  is the test decision for the null hypothesis and it is equal to 0 if the null hypothesis is accepted and 1 otherwise. This test confirms the earlier observation that the Weibull distribution better describes  $q$  at the moderate overtopping level, while the distribution tends towards normal for higher values of  $q$ .

### Probability of Overtopping

Fig. 4.14 shows the distribution of  $P_{ov}$ . For the low overtopping the distribution does not appear continuous, this is due to the small number of overtopping waves ranging between only between 0 and 5. Again, a lot of the tests here can be observed to experience no overtopping resulting in the positive skew to the histogram. This time the distribution quickly becomes symmetric at both moderate and high levels of overtopping.

As both moderate and high levels of overtopping exhibited fairly symmetric results, the Normal distribution was chosen for comparison. The CDFs are compared as done in Fig. 4.15 and it is evident that the normal distribution fits the data well. The parameters of the distributions are shown in Table 4.4.

The results of the K-S test, as shown in Table 4.5, confirm the normal distribution is appropriate for describing the variation for  $P_{ov}$ .

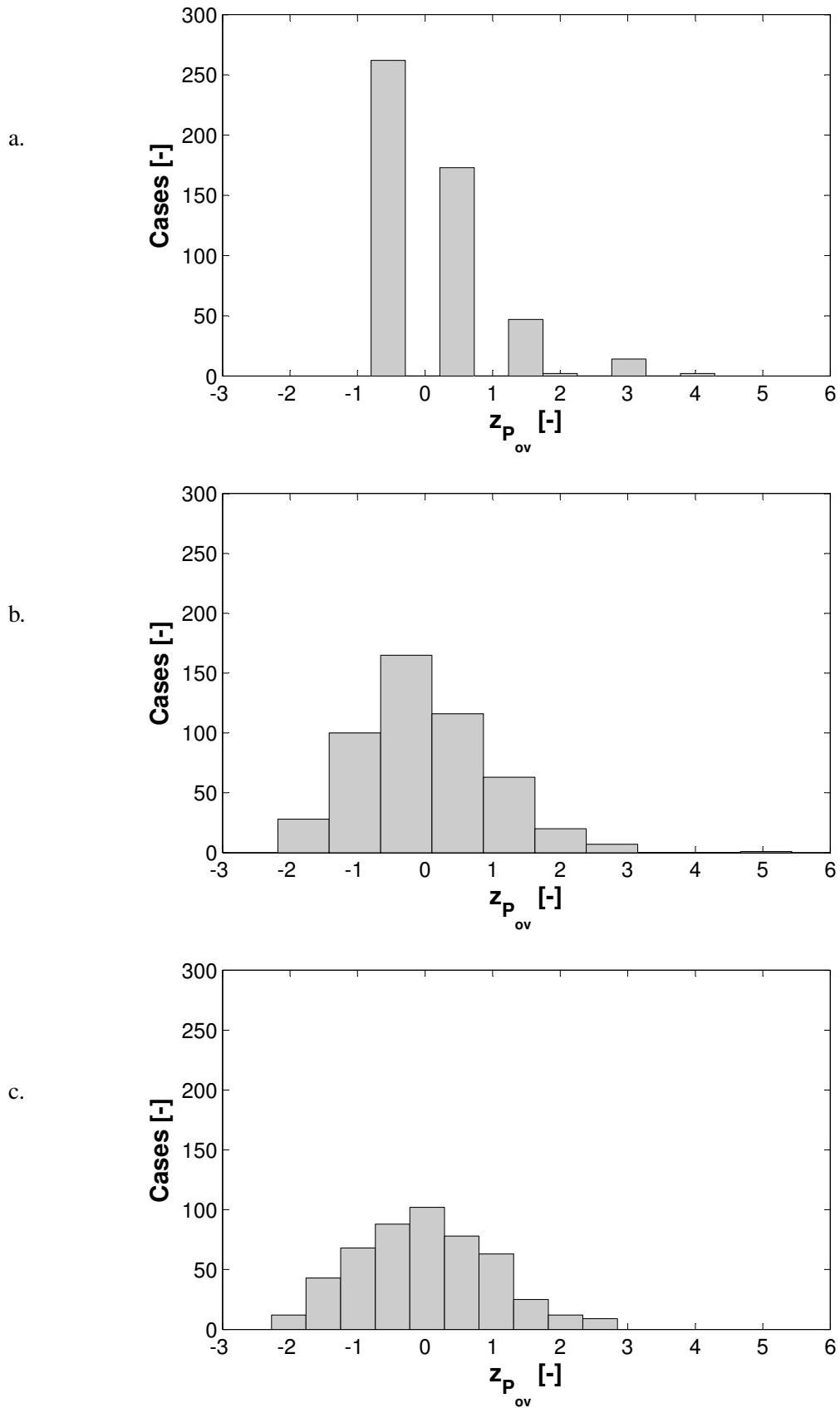


Figure 4.14: Histograms comparing distribution of  $P_{ov}$  for different levels of overtopping. a. Test 003 (Low Overtopping). b. Test 006 (Moderate Overtopping). c. Test 007 (High Overtopping).

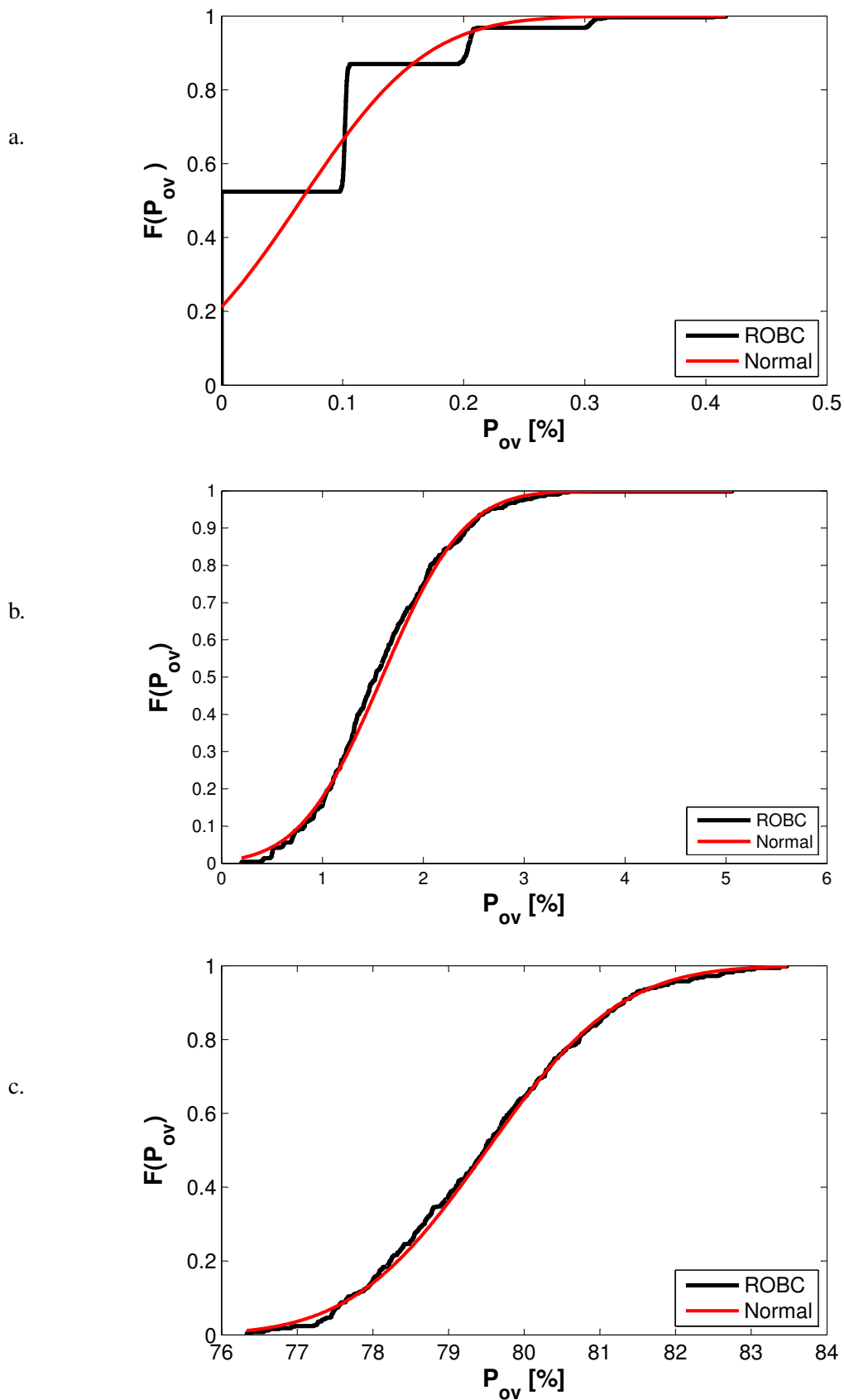


Figure 4.15: Empirical frequency curves for  $P_{ov}$  from ROBC (black solid lines) compared with known distributions. a. Test 003 (Low Overtopping). b. Test 006 (Moderate Overtopping). c. Test 007 (High Overtopping).

Table 4.5: Results of the one sample K-S test for  $P_{ov}$ 

Test	Normal	
	$\Gamma$	$D_n$
003	1	0.312
006	0	0.052
007	0	0.039

### Maximum Individual Overtopping Volume

Whereas the other two parameters are averaged across the whole of each test, the  $V_{max}$  is an extreme value, so it is anticipated that the distribution will behave in a different way.  $V_{max}$  have also been plotted as relative histograms in Fig. 4.16.

Again, the histogram for the low overtopping condition is characterised by a large number of occurrences with no value for  $V_{max}$  i.e. tests with no overtopping. However, unlike for the other parameters this time all of the histograms show a definite positive skew, even at the highest overtopping rate. This suggests that the normal distribution will not be suitable for describing the results. This has led to both the Weibull, and due to the nature of  $V_{max}$ , the Generalised Extreme Value (GEV) distributions to be considered. The parameters of the distributions are shown in Table 4.6, with  $\xi_x$ ,  $\sigma_x$  and  $\mu_x$  representing the shape, scale and location in the GEV distribution.

Fig. 4.17 shows the comparison of the CDFs. Again, for the lowest overtopping level, the Weibull distribution cannot be used, and neither of the other two appear to match the ROBC results due to the high number of tests that experience no overtopping. For the moderate level of overtopping as anticipated the normal distribution does not model well the ROBC results, however, both the Weibull and the GEV appear to provide reasonable results. In the highest overtopping level, it appears that the GEV distribution is best, with the Weibull no longer providing reasonable results. The results of the K-S test in Table 4.7 suggests that the GEV provides the best match to the results in the moderate and high overtopping. It is observed in these results, that a Weibull distribution could be used to describe the  $V_{max}$  in the moderate overtopping, but the GEV produces a lower value for  $D_n$  suggesting this is a better match.

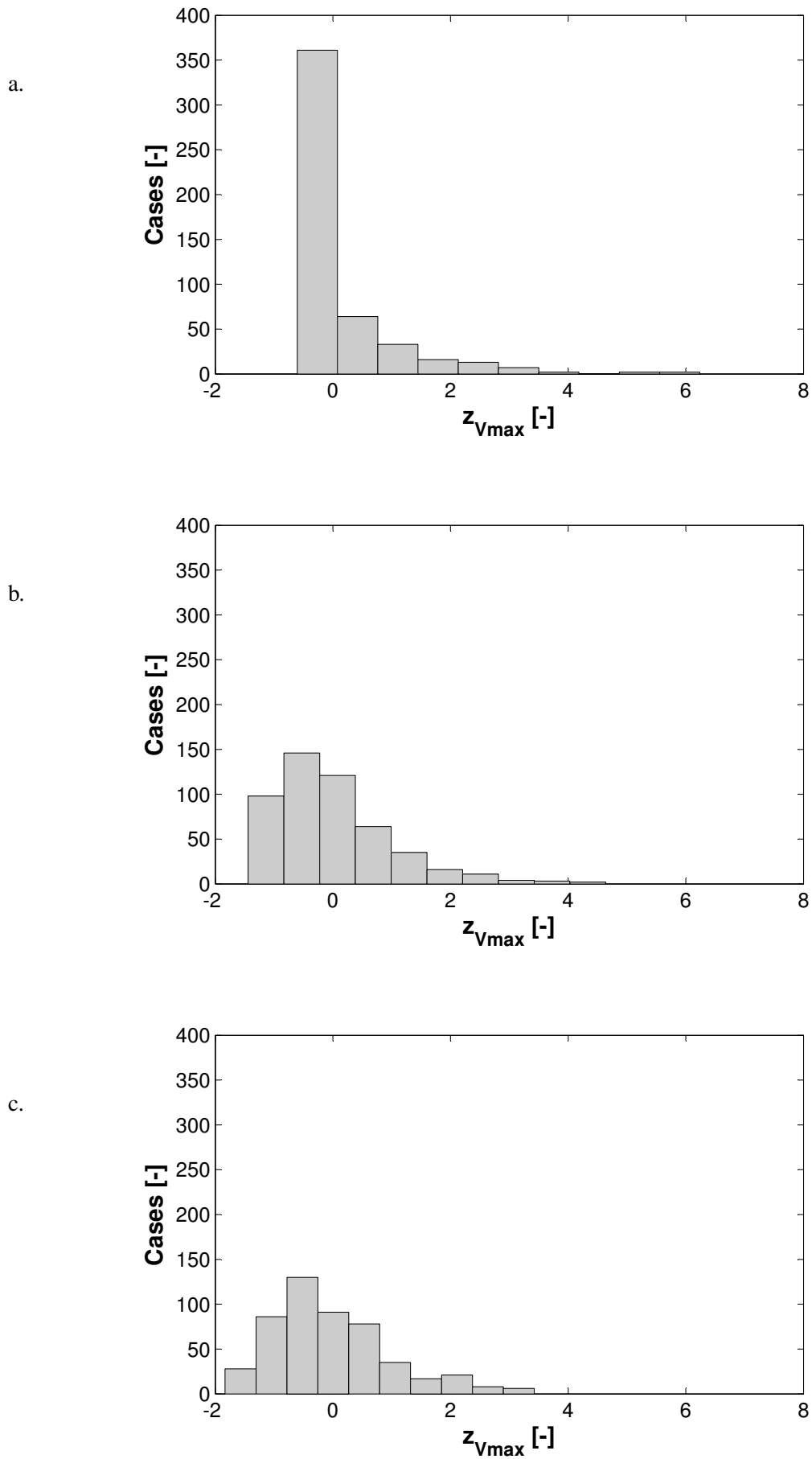


Figure 4.16: Relative histograms comparing distribution of  $V_{max}$  for different levels of overtopping. a. Test 003 (Low Overtopping). b. Test 006 (Moderate Overtopping). c. Test 007 (High Overtopping).

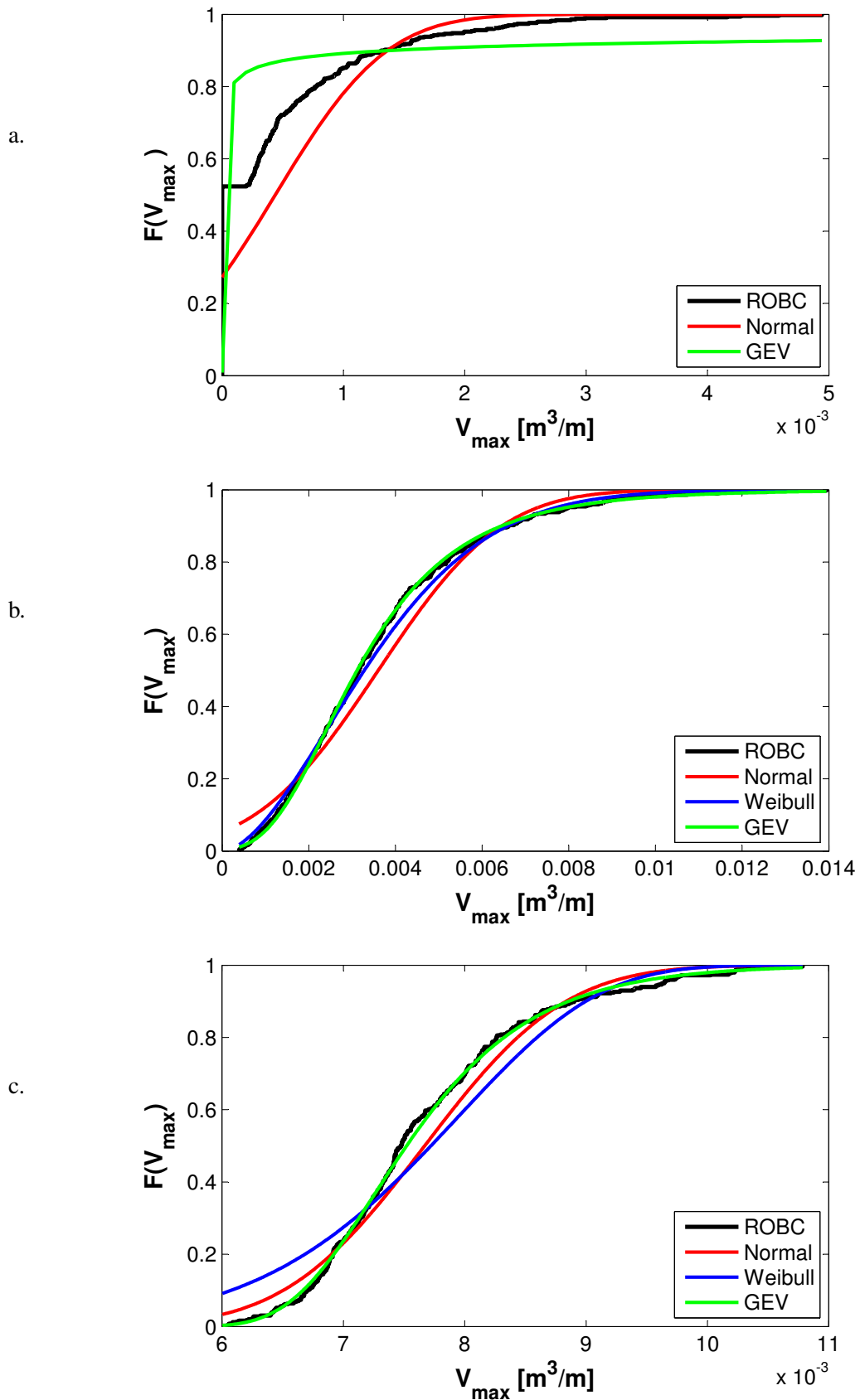


Figure 4.17: Empirical frequency curves for  $V_{max}$  from ROBC (black solid lines) compared with known distributions. a. Test 003 (Low Overtopping). b. Test 006 (Moderate Overtopping). c. Test 007 (High Overtopping).

Table 4.6: CDF parameters for  $V_{max}$ 

Test	Normal		Weibull		GEV		
	$\mu$	$\sigma$	$\lambda$	$k$	$\xi_x$	$\sigma_x$	$\mu_x$
003	4.38e-4	7.22e-4	N/A	N/A	3.83	9.46e-7	2.46e-7
006	3.60e-3	2.22e-3	4.06e-3	1.72	1.05e-1	1.54e-3	2.54e-03
007	7.67e-3	9.10e-4	8.09e-3	7.85	-2.69e-3	7.11e-4	7.26e-3

Table 4.7: Results of the one sample K-S test for  $V_{max}$ 

Test	Normal		Weibull		GEV	
	$\Gamma$	$D_n$	$\Gamma$	$D_n$	$\Gamma$	$D_n$
003	1	0.272	N/A	N/A	1	0.509
006	1	0.103	0	0.055	0	0.021
007	1	0.104	1	0.119	0	0.036

## 4.5 Summary

The variability in the overtopping prediction of the NLSWE model due to the numerical seeding used to generate the offshore boundary times series has been examined. By carrying out a Monte Carlo analysis the variability has been quantified, this information can then be used to provide guidelines on the use of numerical methods where offshore boundary conditions are generated from an energy density spectrum.

A significant variability was observed in these results. This variability decreases with the increasing level of overtopping in each of the eight laboratory tests considered in this work. This has been highlighted in Fig 4.7 by the variability in  $q$  being inversely related to the  $P_{ov}$ , so that when magnitude of  $P_{ov}$  increases the variability in  $q$  decreases. This behaviour can be straightforwardly explained: when few waves are overtopping, the relative importance of each event is large. Conversely, with an increasing number of these events, the role of each individual waves in the total amount of overtopping becomes smaller. This characteristic is consistent with the increased uncertainty in prediction of low overtopping discharges using empirical approaches. As a consequence of this variability, this means that a single ROBC test can lead to an inaccurate prediction of the overtopping as shown, for example, in Fig. 4.3. This is particularly true when a low overtopping rate is expected, which is significant due to it being a level of overtopping that a large number of structures are designed for.

The properties of the populations of ROBC tests have been studied in order to assess how the overtopping parameters are distributed. Theoretical CDFs have been found to well describe the distribution of the overtopping parameters for moderate to high levels of overtopping. Mean overtopping discharge was found to follow a Weibull distribution for moderate overtopping and

a normal one in higher levels. Probability of overtopping has been found to follow a normal distribution whilst maximum individual overtopping volume follows a GEV distribution.

The average values of the predicted overtopping parameters have also been compared with the scale tests results and the predictions of the MOBC tests. It has been shown however that, on average, the ROBC predictions are less accurate than the MOBC ones, especially for those tests with lower overtopping. However, it should be noted here that only one physical model test was run for each wave condition, and it is likely that these may also be subject to some variation if multiple runs with different time series had been conducted.

When using the average value of the ROBC tests, one has to keep in mind the uncertainty associated with the prediction, which has been measured with  $\sigma'$  (see Fig. 4.2), converges to a value that can be considered independent from the number of ROBC tests after a considerable number of tests for conditions that produce the lowest number of overtopping waves in the tested range (Test 003). For a higher number of overtopping waves, convergence is achieved much faster, within a few tens of tests.

In design practice, it is often not possible to carry out a large number of tests for the same hydraulic and structural conditions. This has led to the need to limit multiple tests to when they are really needed. Fig. 4.7 allows a preliminary recommendation based on the conditions tested. From the figure it is evident that for  $P_{ov} < 5\%$  both  $P_{ov}$  and  $q$  vary more than one order of magnitude. Therefore, this should be taken as the limit value of  $P_{ov}$  for which a sensitivity analysis should be carried out.



## **Chapter 5**

# **Distribution of Individual Overtopping Volumes**

### **5.1 Introduction**

In addition to the infinite number of time series that can be generated from a single spectrum, another issue which occurs due to reconstructing the times series is the assumption of linear superposition of wave components that is strictly valid only for linear waves, typically restricted in validity to deep water. However, the approximation is used in many existing intermediate and shallow water models proposed in the literature. Recent examples of such an assumption in the computation of run-up and overtopping are given in Zijlema et al. (2011), McCabe et al. (2011), Shi et al. (2012) and McCabe et al. (2013). When the boundary input conditions are in shallow water this results in a modification to the distribution of wave heights, which is known to directly influence the distribution of the overtopping volumes (Nørgaard et al., 2014) which needs to be investigated.

### **5.2 Incoming Waves**

This analysis will consider the same physical and numerical tests as the previous chapter with particular focus on the three conditions that were chosen as representative of the different levels of overtopping. A reminder of the wave conditions can be seen in Table 5.1.

Table 5.1: Incident wave conditions for the JONSWAP spectra random wave laboratory tests, and measured overtopping

Test	Paddle				Toe				
	$H_{m0}$ (m)	$T_p$ (s)	$s_{op}$ (-)	$\xi_{m-1,0}$ (-)	$H_{m0}$ (m)	$\frac{H_{m0}}{d_t}$ (-)	$\frac{R_c}{H_{m0}}$ (-)	$\frac{H_{m0}}{H_{1/10}}$ (-)	$\frac{d_t}{L_{m-1,0}}$ (-)
001	0.08	1.30	0.030	2.29	0.085	0.943	2.474	0.609	0.041
002	0.02	1.76	0.004	6.22	0.032	0.354	6.599	0.459	0.023
003	0.02	2.20	0.003	7.78	0.036	0.404	5.777	0.470	0.014
004	0.02	1.32	0.007	4.66	0.026	0.202	6.459	0.436	0.058
005	0.02	1.76	0.004	6.22	0.031	0.238	5.472	0.033	0.598
006	0.02	2.20	0.003	7.78	0.038	0.293	4.464	0.021	0.526
007	0.04	1.76	0.008	4.40	0.075	0.839	2.781	0.023	0.594
008	0.08	1.20	0.036	2.12	0.081	0.899	2.596	0.661	0.048

### 5.2.1 Wave Height Distribution

The short-term statistics of waves in deep water has been extensively studied, with Longuet-Higgins (1952) verifying that the heights of these types of waves obey the Rayleigh distribution,

$$F_H = P(\underline{H} \leq H) = 1 - \exp \left[ - \left( \frac{H}{H_{rms}} \right)^2 \right], \quad (5.1)$$

in which  $H$  is the individual wave height and  $H_{rms}$  is the root-mean-square of the wave height. Since the Rayleigh distribution has only one scale parameter and no shape parameter, relationships between characteristic wave heights have been established.

In shallow water the distribution of wave heights alters, due to shoaling, triad interactions and depth-induced breaking. These can therefore no longer be described by the Rayleigh distribution. Battjes and Groenendijk (2000) looked at numerous wave height distributions on shallow foreshores and found when plotted on a Rayleigh graph, a marked transition between a linear trend for the lower heights and a downward curved relation for the taller waves. This led to the development of a combination of two Weibull distributions each having a different exponent, matched at the transition wave height  $H_{tr}$ ,

$$F_H = P(\underline{H} \leq H) = \begin{cases} F_1(H) = 1 - \exp \left[ - \left( \frac{H}{H_1} \right)^{K_1} \right] & \text{for } H \leq H_{tr} \\ F_2(H) = 1 - \exp \left[ - \left( \frac{H}{H_2} \right)^{K_2} \right] & \text{for } H \geq H_{tr} \end{cases} \quad (5.2)$$

For the distribution function to be continuous, the constraint  $F_1(H_{tr}) = F_2(H_{tr})$  is imposed.

The exponents  $K_1$  and  $K_2$  are shape parameters of the distribution. They determine the curva-

ture of the corresponding part of the distribution.  $H_1$  and  $H_2$  are scale parameters. The values of  $K_1$  and  $K_2$  do not match at the transition point, meaning the the distribution is discontinuous there, which although is not physically realistic has been accepted due the well modelled statistical properties of the wave heights.

In the present tests the conditions at the toe of the structure are depth limited ( $H_{m0}/d_t > 0.2$ ) as the values of  $H_{m0}/d_t$  in Table 5.1 indicate, this means that the Battjes and Groenendijk (2000) distribution is expected to provide a better match to the wave height distribution than the Rayleigh distribution.

Three examples of measured wave height distributions are shown in Figs. 5.1, 5.2 and 5.3. These are the individual wave heights measured at the wave gauge at the location of the toe of the breakwater during the incident wave tests. The individual wave heights have been obtained by conducted a zero-crossing analysis of the incident time series. The individual wave heights,  $H$ , have been normalised with the mean wave height,  $H_m$ . In each figure the Rayleigh and Battjes and Groenendijk (2000) distributions have been included for comparison.

Fig. 5.1 shows the measured incident wave height distribution for Test 003. In this particular test,  $H_{m0}/d_t = 0.404$  and the relative depth is 0.014, which results from a relatively small wave height and long period, with a very small water depth at the structure toe. These conditions are classified as shallow water. It can be seen here that the measured wave heights follow well the Rayleigh distribution in the lower wave heights, and then a slight curvature of the distribution occurs in the larger wave heights. This results in it becoming a similar shape to the Battjes and Groenendijk (2000) distribution, although the values of the wave heights themselves are not close to those predicted. Generally the distribution appears closer to that of the Rayleigh distribution.

In addition to the measured wave height distribution from the experiments, also shown in Fig. 5.1 are the wave height distributions of 10 randomly selected generated times series from the ROBC tests. It can be observed that there is some variation across the sample in the wave height distributions, although generally they are all of a similar shape. The shapes of the distribution are also quite close to the shape obtained from the physical model measurements, and hence, they are all generally closer to the Rayleigh distribution.

Fig. 5.2 considers the wave height distribution for Test 006. For this test,  $H_{m0}/d_t = 0.293$  with a relative depth of 0.021, which although still depth-limited is closer to the deep water condition requirements than the previous test. Here, the measured wave height distribution follows rea-

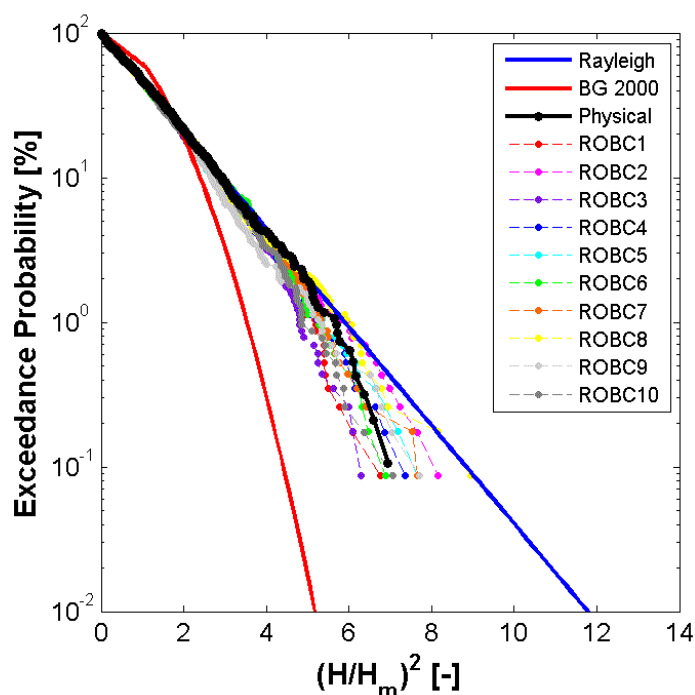


Figure 5.1: Distributions of the measured incident wave heights and the wave heights of 10 randomly selected reconstructed time series at the location of the structure toe for Test 003 (Low Overtopping). Rayleigh and Battjes and Groenendijk (2000) distributions are also shown.

sonably well that of the Battjes and Groenendijk (2000) distribution, suggesting that the wave are subjected to shallow water conditions at this point.

Again, Fig. 5.2 also considers the wave height distributions modelled in the ROBC tests, with 10 randomly selected runs presented. It is clear from this graph that there is a larger variability in the wave height distribution across these test runs, more than was observed in the previous test. Some of the distributions appears to better follow the Battjes and Groenendijk (2000) distribution, while others appear to better follow the Rayleigh distribution. Generally, the ROBC distributions fall between the two distributions, with smaller wave heights being better described where the theoretical distributions are also closer to each other.

Finally, Fig. 5.3 shows the wave height distribution for Test 007. This test had a  $H_{m0}/d_t = 0.839$  and relative depth of 0.048, making it the most depth limited of all tests considered here, and therefore subject to the shallow water conditions. It can be seen in the figure that the measured wave heights, as expected, appear to follow the Battjes and Groenendijk (2000) distribution, although surprisingly not as closely as observed in the previous test.

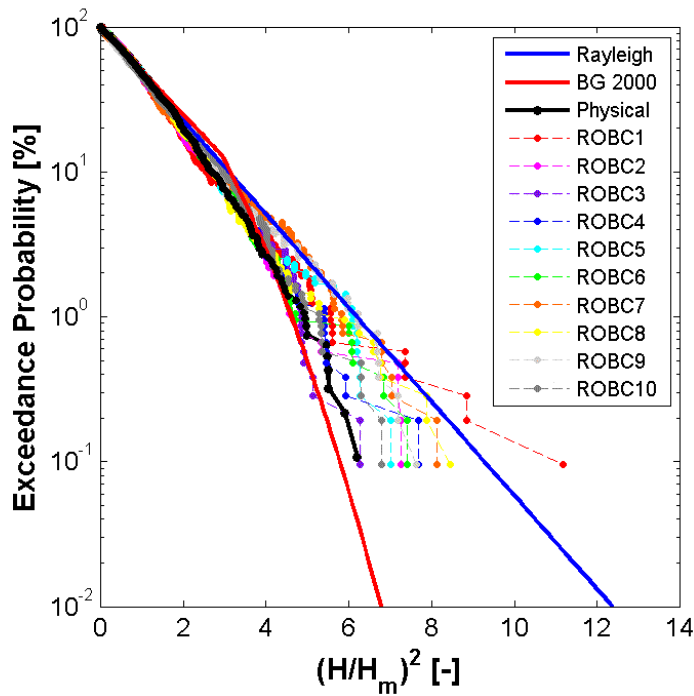


Figure 5.2: Distributions of the measured incident wave heights and the wave heights of 10 randomly selected reconstructed time series at the location of the structure toe for Test 006 (Moderate Overtopping). Rayleigh and Battjes and Groenendijk (2000) distributions are also shown.

Also shown are the 10 randomly selected ROBC runs from Test 007. These runs show a similar level of variability to Test 006. Due to the shallower nature of this test, the Battjes and Groenendijk (2000) and Rayleigh distributions are further apart than in the previous test with a deeper depth at the toe. This results in none of the reconstructed time series matching that of the Battjes and Groenendijk (2000) distribution, with all being closer to the Rayleigh distribution. It is clear though that most of the results lay between the two distributions in the higher wave heights, with none matching that measured in the physical experiments.

Overall, it has been observed that all the physical model tests are subject to the shallow water conditions as expected. It has also been seen that the reconstructed time series do not necessarily account for this, with most exhibiting a different distribution to those predicted or found in the physical model tests.

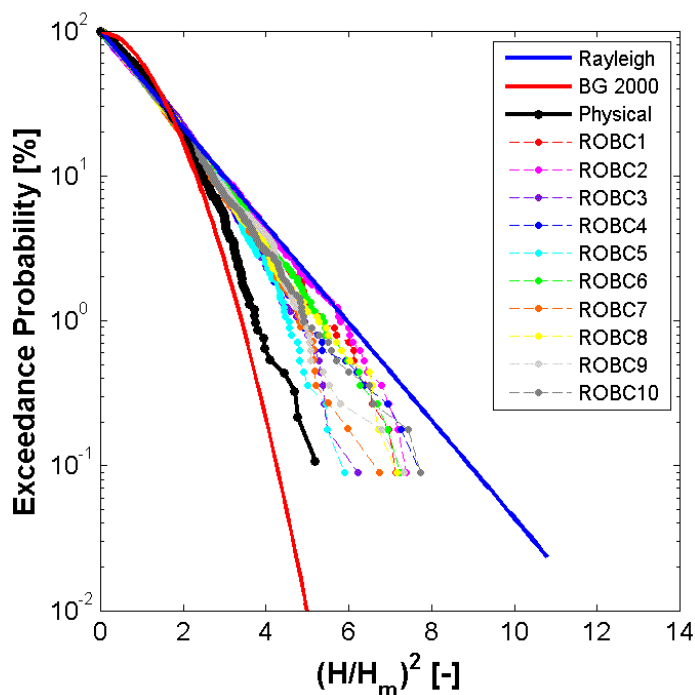


Figure 5.3: Distributions of the measured incident wave heights and the wave heights of 10 randomly selected reconstructed time series at the location of the structure toe for Test 007 (High Overtopping). Rayleigh and Battjes and Groenendijk (2000) distributions are also shown.

## 5.2.2 Measured Spectra

It is known that wave spectra in shallow water are significantly affected by cross-spectral energy transfers between various wave components due to triad interactions. These occur when three waves interact it is possible for resonance to occur, and a tertiary component can grow, with energy being transferred from the primary wave component. These can be important in shallow and intermediate water depths, and can change a single peak spectrum into a multiple peaked spectrum.

The spectra used in the physical model were single peaked at the paddle, however, it is anticipated that those at the location of the toe of the structure will have transformed. To explore this further, the spectrum for tests 003, 006 and 007 have been plotted. Firstly, in Fig. 5.4, the incident spectra from test 003 at both offshore and at the structure toe are considered. It can be seen that the peak frequency remains the same for the two spectra, but the shallow water spectrum has undergone a transformation. A secondary peak is clearly visible at the toe due to the triad interactions occurring at this water depth.

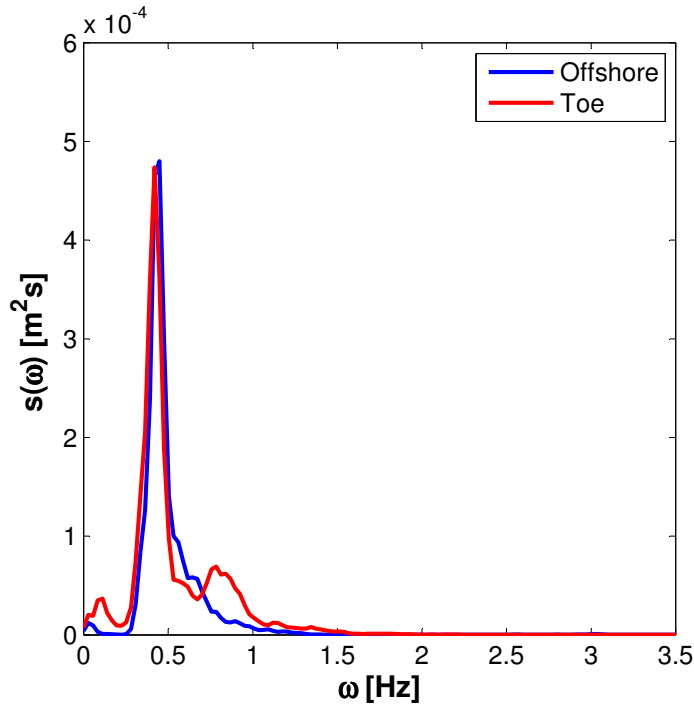


Figure 5.4: Measured incident spectrum from Test 003 ( $H_{m0}/d_t = 0.40$ ).

In Fig. 5.5, the two incident spectra from test 006 are plotted. Similarly to the previous observations, the peak frequency remains the same for the two spectra. This time a smaller secondary peak is visible at the toe. This is due to the triad interactions, and appears smaller than the previous test due to the deeper water depth at the structure toe.

Finally, in Fig. 5.6, the two incident spectra from test 007 have been plotted. These show a bigger transformation between the deep and shallow water conditions. Although the peak frequency remains approximately the same, a lot of energy has been transferred from this point on the spectrum. This loss of energy is probably due to the large number of breaking waves at this point, and has resulted in a broader spectrum at the toe of the structure.

It can clearly be seen from all of the measured spectra that non-linear interactions of the waves have effected the shapes of the wave spectra. This suggests that as anticipated the assumption of linear superposition is not really valid at the toe of the structure, and is causing a modification to the distribution of the reconstructed wave heights. An additional effect in all of the tests is the presence of long waves forming in flume. This is characterised by a peak at low frequencies. It is possible that this will have affected the magnitude of overtopping in the laboratory experiments, but without further information this affect can not be quantified.

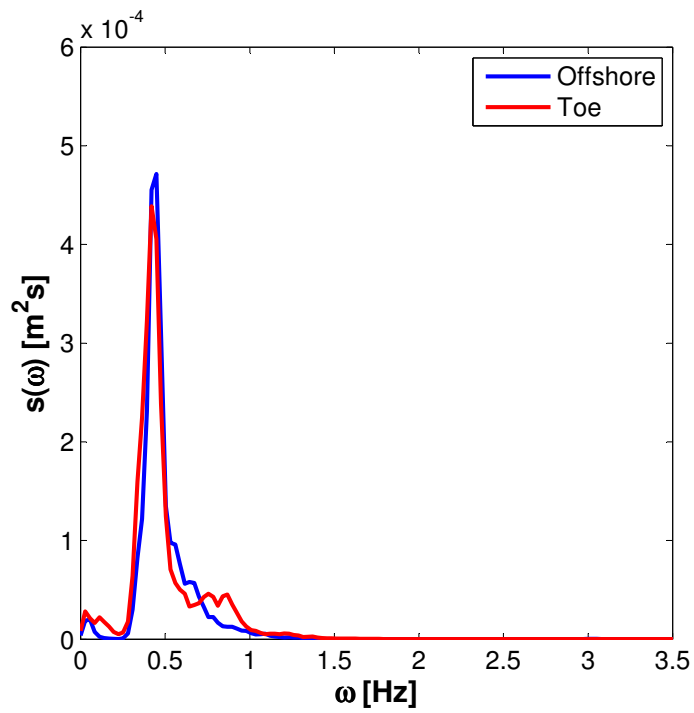


Figure 5.5: Measured incident spectra from Test 006 ( $H_{m0}/d_t = 0.29$ ).

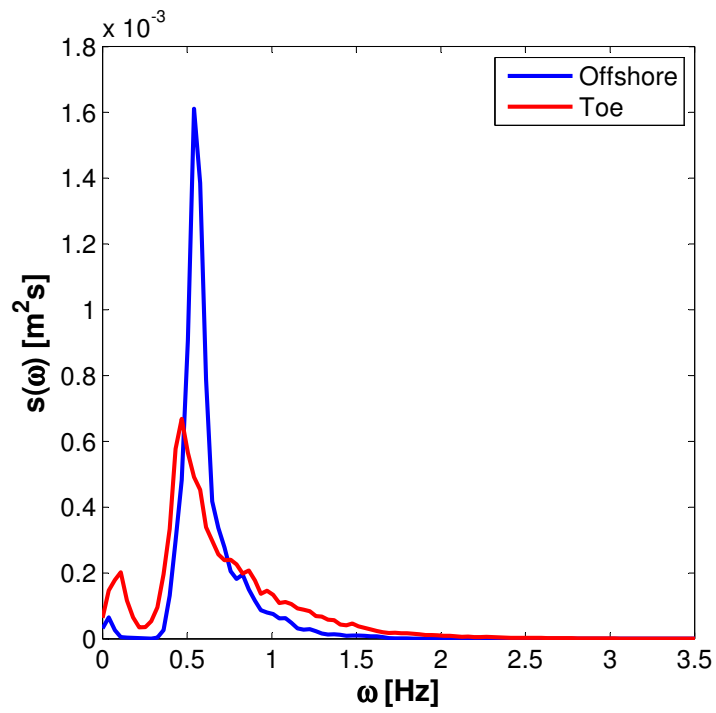


Figure 5.6: Measured incident spectra from Test 007 ( $H_{m0}/d_t = 0.84$ ).

### 5.2.3 Time Series Comparison

It has been already shown that the reconstructed time series can not replicate the shallow water conditions found in the physical model, even when the measured spectra used, are clearly subject to these conditions. To examine in more detail how well the reconstructed time series replicate those measured in the physical model, a reconstructed time series for each condition has been chosen at random and is directly compared with those measured in the experiments. These are plotted in Fig. 5.7.

It can be observed in all of the wave conditions, that the measured time series show large crest heights and shallow troughs, making the waves fairly asymmetrical about the still water level. This is due to the wave shoaling that is occurring at this location in the physical model. It is particularly evident in Test 003 and 007 which had the shallower water conditions in the experiments.

Information about the shape of the waves cannot be obtained from the spectra, and hence in contrast the ROBC time series show waves that are more symmetrical about the still water level. Although the wave heights are statistically the same as the physical experiments, it is clear that the reconstruction can not accurately reproduce the wave conditions. If the offshore boundary was in deeper water then this would not be an issue, however, it would then cause problems with the suitability of using the NLSWE.

This may explain the increase in overtopping in test 007 in the ROBC results in contrast to the physical model results. In the physical model, the waves are clearly breaking, which is not happening in the ROBC time series. This could result in less energy dissipation in the numerical model than is occurring in reality, causing more waves to run-up the structure and causing overtopping. This would explain why the  $V_{max}$  results are not that dissimilar because the amount of water contained within each overtopping wave is similar, but  $P_{ov}$  is so much higher.

## 5.3 Individual Overtopping Volumes

For irregular waves the quantity of water that overtops a structure will vary from wave to wave, this can be described by probability distributions as seen earlier in section 2.5. The various empirical prediction methods mentioned earlier will each produce a distribution of  $V_{ov}$  which will be compared with the results from the numerical tests.

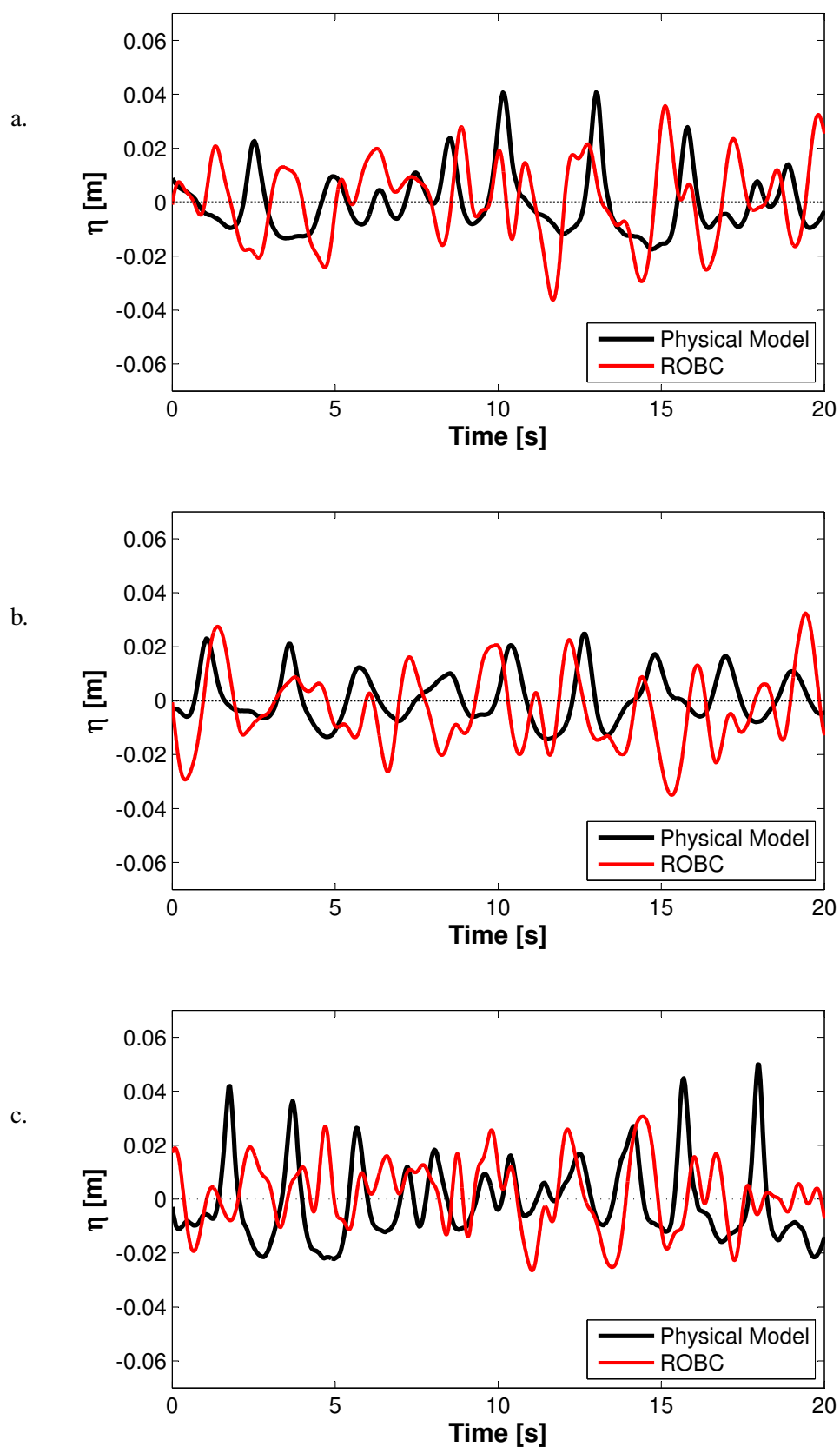


Figure 5.7: Excerpt of measured and one reconstructed time series. a. Test 003 ( $H_{m0}/d_t = 0.40$ ). b. Test 006 ( $H_{m0}/d_t = 0.29$ ). c. Test 007 ( $H_{m0}/d_t = 0.84$ ).

To quantify this similarity between prediction methods, a Kolmogorov-Smirnov (K-S) test has been carried out. Again, the null hypothesis is deemed to be true if the two distributions being compared match.

The results presented here are focussed on the moderate and high levels of overtopping. Unfortunately, in the low overtopping conditions, either they experienced no overtopping, or only one or two overtopping events. It is therefore not possible to obtain a distribution with such a small population available, so will not be considered here. Although, all of the moderate and high overtopping tests will be examined, particular focus will be on Test 006 as representative of a medium level of overtopping, characterised by waves occasionally overtopping the structure, and Test 007 as representative of the higher level of overtopping, characterised by consistent overtopping waves.

### 5.3.1 Comparison of MOBC results

Although the NLSWE solver has already been validated against the other overtopping parameters, it is still important to assess its accuracy when predicting individual overtopping volumes especially as differences in the overtopping time series were observed during the initial model validation. Therefore, first the distribution of the individual volumes from the physical model is compared with the results produced from the MOBC tests. These are plotted in the form of cumulative distribution functions in Figs. 5.8 and 5.9.

The results for Test 006 show that the distribution of individual volumes in the numerical model is similar to the results observed in the physical model. The distribution in the numerical model is slightly steeper, suggesting that more smaller events occurred than in the physical model. This may well be caused by the increased accuracy in identifying individual events in the numerical model.

Table 5.2 shows the results of the K-S test between the physical and numerical results which confirms that the distributions do match by the achievement of the null hypothesis. Also, plotted in Fig. 5.8 are the empirically predicted distributions. Although the conditions in 006 have been classified as shallow water at the toe of the structure, they do not meet both of the requirements of the Nørgaard et al. (2014) distribution (i.e.  $H_{m0}/H_{1/10} \not\geq 0.848$ ), so this distribution isn't considered here.

Both the Pullen et al. (2007) and Victor et al. (2012) prediction methods provide a reasonable approximation to the results with the latter giving the best results. The accuracy is again quan-

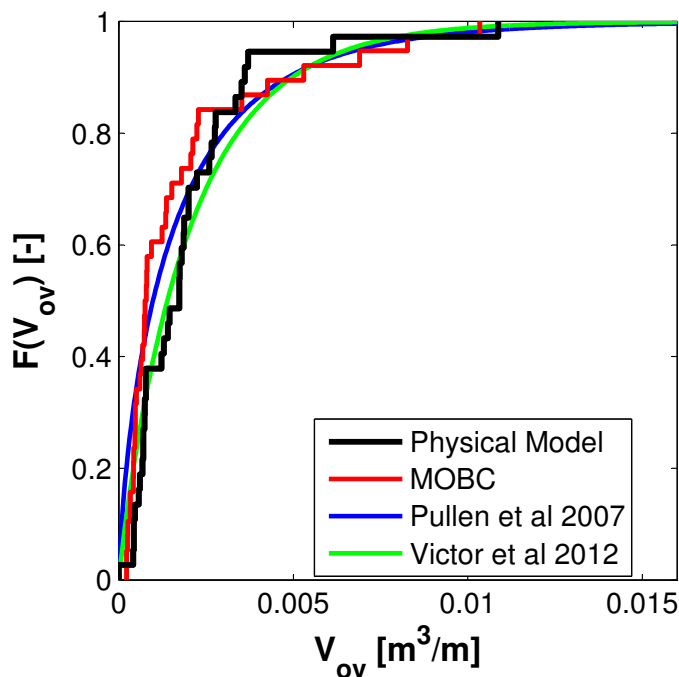


Figure 5.8: Comparison of the distribution of  $V_{ov}$  from the MOBC test of 006 with the empirical methods and the physical model

Table 5.2: Results of the K-S test for distribution of  $V_{ov}$  comparing physical model with MOBC tests and empirical formulae.

Test	Physical Model		Pullen et al. (2007)		Victor et al. (2012)	
	$\Gamma$	$D_n$	$\Gamma$	$D_n$	$\Gamma$	$D_n$
006	0	0.2368	0	0.2125	0	0.1865
007	0	0.1499	1	0.1545	0	0.0625

tified using the K-S test shown in Table 5.2, which shows that although both formulae produce the null hypothesis, the  $D_n$  value for Victor et al. (2012) is smaller, making it more suitable to describe the distribution present.

The results for Test 007 show slightly more variation in the distribution of the individual volumes in the numerical model in comparison with the physical model. This was anticipated due to a larger variation shown when examining the overtopping time series earlier in this work. The higher overtopping test shows a greater number of overtopping events in the MOBC than the physical model, this is most likely caused by the increased accuracy in the measurement of overtopping in the numerical model, which cannot be achieved with the physical model.

Table 5.2 shows the results of the K-S test between the physical and numerical results which again confirms that the distributions do match. In Fig. 5.9, the  $V_{ov}$  results from the MOBC run of Test 007 are also compared with the empirical formulae. Again, the criteria of the Nørgaard

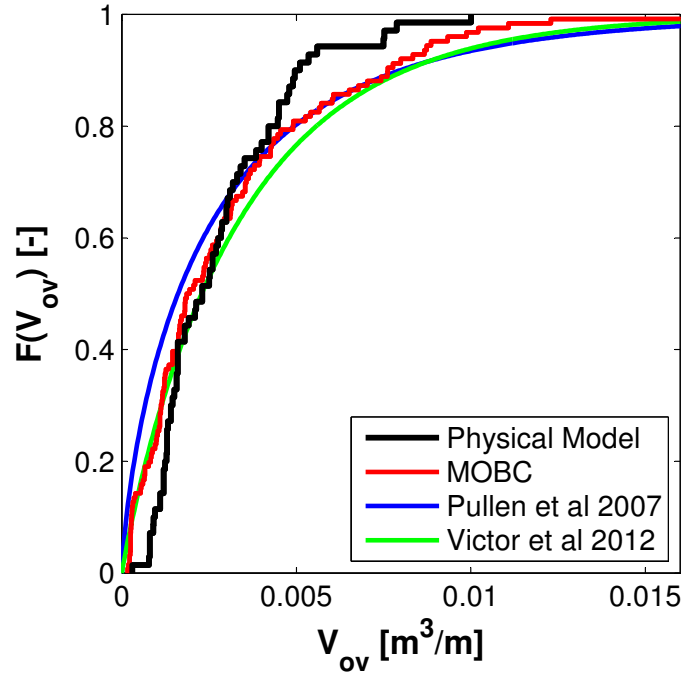


Figure 5.9: Comparison of the distribution of  $V_{ov}$  from the MOBC test of 007 with the empirical methods and the physical model

et al. (2014) distribution is not met for this test, even though there are shallow water conditions present.

Both of the formulae appear to give a reasonable approximation of the distribution of the MOBC tests with the Victor et al. (2012) method providing the closest match. However, this time the null hypothesis is not obtained for the Pullen et al. (2007). It was expected that the Victor et al. (2012) would best describe the distribution of volumes in these experiments due to similarities in the structure being tested.

### 5.3.2 Comparison of ROBC results

Now to consider the results of the ROBC tests to examine both the predicting accuracy and the variability of the  $V_{ov}$  distributions. It has already been observed that the ROBC results do not always provide good approximations of the physical model results, and that both the incident wave height distribution and the other resulting overtopping parameters showed large variability among the tests. In Fig. 5.10, the ROBC results of the three moderate overtopping tests (004, 005 and 006) are plotted as cumulative distribution functions. It can be observed as anticipated there is a large variability in the distribution of the overtopping volumes.

Table 5.3: Results showing the percentage of the K-S tests that achieved the null hypothesis by comparing empirical formulae with distribution of  $V_{ov}$  from ROBC tests. The shape factor ( $b_t$ ) of each test is also compared with the shape factor ( $b_w$ ) for each empirical method to show the percentage of over and under prediction.

Test	Pullen et al. (2007)			Victor et al. (2012)			Nørgaard et al. (2014)		
	$\Gamma = 0$	$b_t < b_w$	$b_t > b_w$	$\Gamma = 0$	$b_t < b_w$	$b_t > b_w$	$\Gamma = 0$	$b_t < b_w$	$b_t > b_w$
	%	%	%	%	%	%	%	%	%
001	0	100	0	0	100	0	0	0	100
004	51.8	73.9	26.1	98.6	43.6	56.4	72.4	25.0	75.0
005	62.0	88.6	12.4	76.4	47.8	52.2	42.8	23.2	76.8
006	74.0	83.4	16.6	80.0	59.4	40.6	46.2	23.2	76.8
007	0	100	0	0	100	0	0	0	100
008	0	100	0	0	100	0	0	0	100

The three empirical prediction methods have also been compared to these results, for this the values used have been taken from the mean values obtained from all of the ROBC tests. It can be seen that all three methods provide results approximately in the centre of those observed in the ROBC tests. To test how well the ROBC results produce an individual volume distribution, the three different empirical methods have been compared against all of the ROBC distributions using the K-S test. The percentage of the 500 ROBC tests for each condition that achieved the null hypothesis for each of the empirical methods can be seen in Table 5.3.

As with the physical model and MOBC results, it was found that the Victor et al. (2012) formula provided the best match in all three of these moderate test conditions with the highest percentages of the ROBC runs achieving the null hypothesis.

In addition the ROBC distributions have been compared to see if the shape factor for each test ( $b_t$ ) is smaller or larger than the value of  $b_w$  for the empirical prediction. The shape factor is a function of both kurtosis (peakedness) and skewness, meaning that a higher value represents a narrower distribution with positive skewness (i.e. a larger number of smaller volumes are predicted). It can be seen in Table 5.3 that compared with the Pullen et al. (2007) the shape factor for the ROBC distributions are generally larger, whilst with regard to the Victor et al. (2012) formula they are fairly evenly distributed either side, and with the Nørgaard et al. (2014) formula the ROBC distributions are generally smaller.

To examine this distribution of  $V_{ov}$  in the ROBC in more detail to establish why some of the tests follow the empirical distributions, Fig. 5.11 looks at the results from the 10 randomly selected runs of the ROBC considered earlier for test 006 (moderate overtopping). It can be seen here that a large variability is still present, although as expected some of the empirical distributions closely match the empirical formulae. This is quantified in Table 5.4 which shows the results of

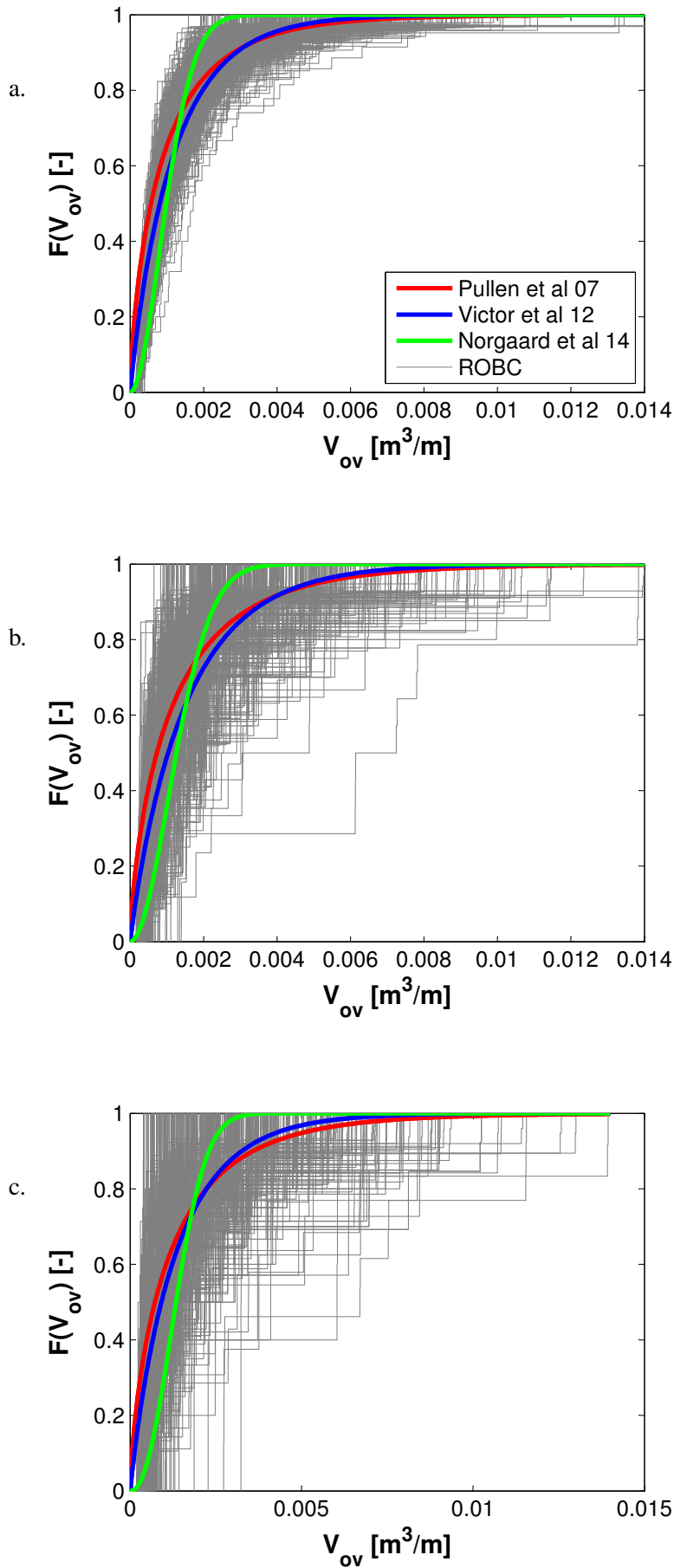


Figure 5.10: Comparison of the distribution of  $V_{ov}$  at moderate levels of overtopping from the ROBC tests and the empirical formulae. a. Test 004. b. Test 005. c. Test 006

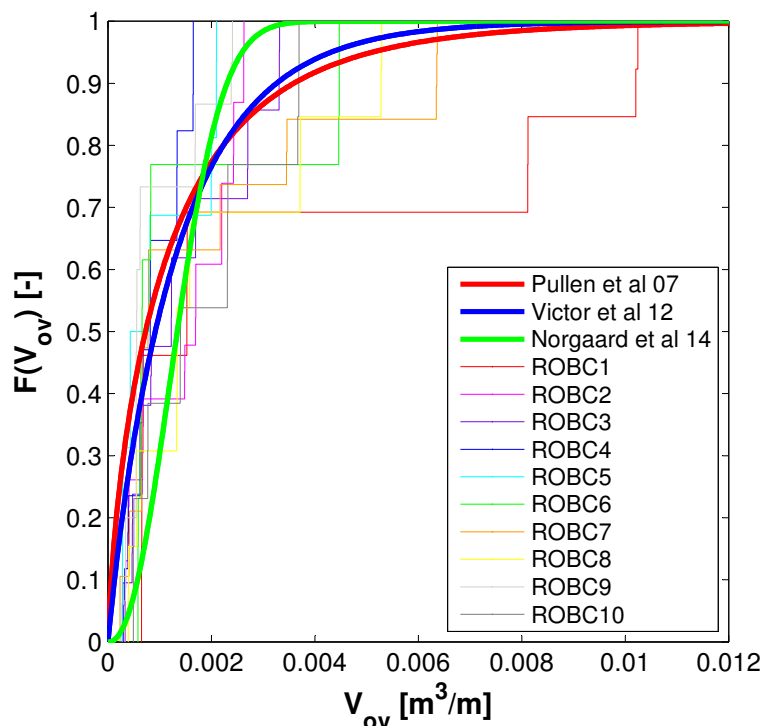


Figure 5.11: Comparison of the distribution of  $V_{ov}$  from the randomly selected ROBC tests and the empirical formulae for Test 006.

a K-S test comparing these runs with the empirical formulae. It can be seen that seven of these tests obtain the null hypothesis for the Victor et al. (2012) formula, whereas for the Nørgaard et al. (2014) tests only 3 obtain the null hypothesis. Considering the specific tests that did not achieved the null hypothesis, it can be seen these are those that did not produce a wave height distribution at the toe of the structure close to the physical model.

It can be seen in Fig. 5.12 that the overall variability between the ROBC tests in the higher level of overtopping (Tests 001, 007 and 008) is lower, with a narrower band of results shown on the graphs. This agrees with the observation earlier in this work that the variability is related to the level of overtopping.

The three prediction methods have been compared to the results using test 007 as a representative test (Fig. 5.13). This time none of the formulae provide a good match for the distribution regardless of the wave height distribution of the selected tests. In Table 5.3 it can also be seen that the shape factors for the ROBC distributions are larger than the Pullen et al. (2007) and Victor et al. (2012) formula, but smaller than that given by the Nørgaard et al. (2014) formula. The K-S tests also confirm that none of the empirical methods match the ROBC results (See Table 5.4). It should be noted here that none of the incoming wave height distributions matched that of the physical model. This resulted in a higher number of larger waves being present in the

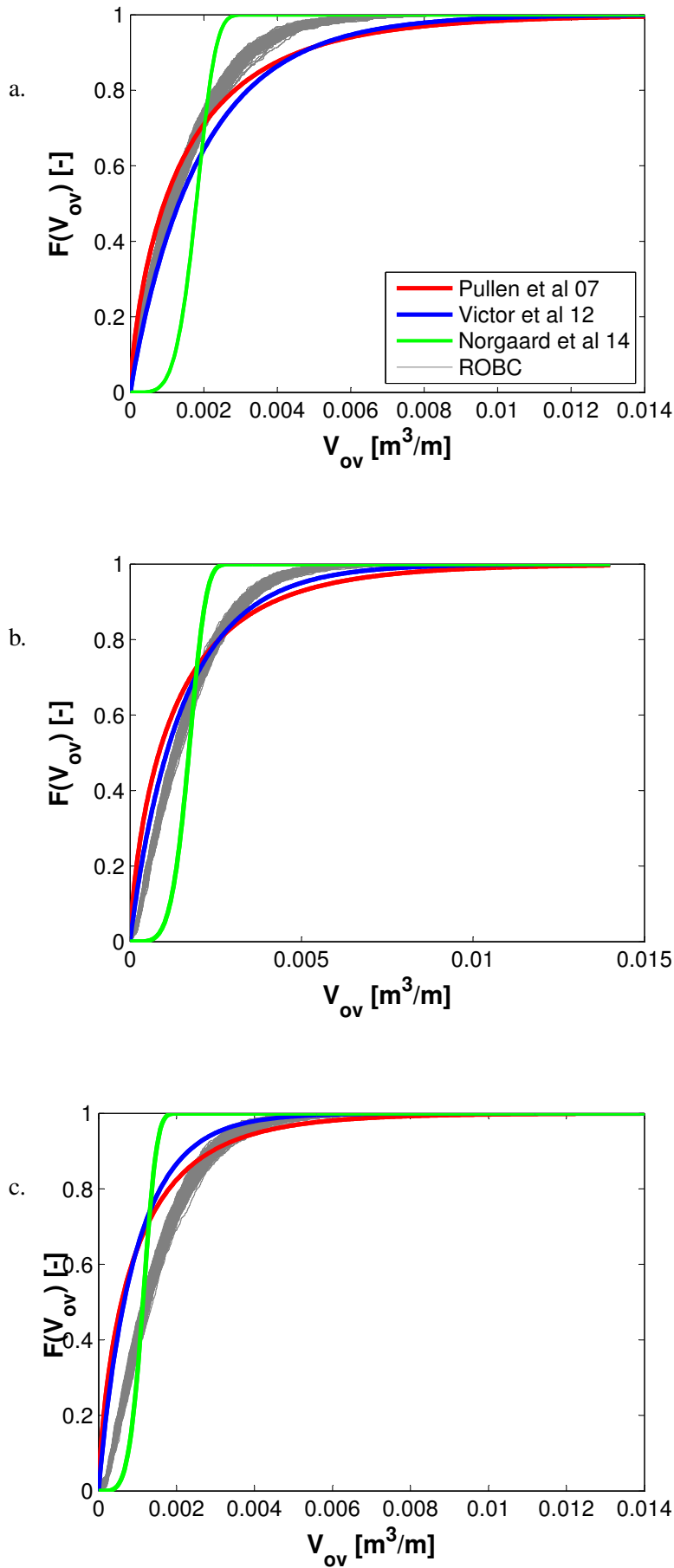


Figure 5.12: Comparison of the distribution of  $V_{ov}$  at high levels of overtopping from the ROBC tests and the empirical formulae. a. Test 001. b. Test 007. c. Test 008.

Table 5.4: Results of the K-S test for distribution of  $V_{ov}$  comparing empirical formulae with 10 randomly selected ROBC tests.

Run	Test 006				Test 007			
	Victor et al. (2012)		Nørgaard et al. (2014)		Victor et al. (2012)		Nørgaard et al. (2014)	
	$\Gamma$	$D_n$	$\Gamma$	$D_n$	$\Gamma$	$D_n$	$\Gamma$	$D_n$
1	1	0.3952	1	0.3262	1	0.1142	1	0.3476
2	0	0.2740	0	0.2657	1	0.1060	1	0.3652
3	0	0.2116	0	0.2606	1	0.1065	1	0.3593
4	0	0.2982	1	0.4394	1	0.1237	1	0.3477
5	0	0.2255	1	0.4837	1	0.1214	1	0.3343
6	1	0.3623	1	0.5585	1	0.1280	1	0.3475
7	0	0.1841	1	0.5697	1	0.1177	1	0.3601
8	0	0.3194	0	0.3064	1	0.1154	1	0.3600
9	1	0.3497	1	0.6138	1	0.0951	1	0.3855
10	0	0.3199	1	0.3622	1	0.1254	1	0.3333

reconstructed time series, which as a consequence has increased the number of larger overtopping events in the results.

## 5.4 Summary

This chapter confirms that the distribution of the volumes in the MOBC tests matches that of the physical model for both test cases, by the achievement of the null hypothesis and therefore confirms that the individual volumes can be well modelled by the NLSWE solver when MOBC are used.

The comparison between the physical model and the MOBC tests shows good agreement meaning that the NLSWE are indeed capable of producing distributions of  $V_{ov}$ . In both cases the distribution of the individual overtopping volumes can be best modelled by the Victor et al. (2012) methods for both of the levels of overtopping. This is as expected due to the steep geometry of the slope in these experiments which is similar to those used in Victor et al. (2012), although the shallow water conditions present was expected to have more of an influence.

The variability of the overtopping volume distribution in numerical models was studied; it is found that when reconstructed offshore  $\eta$  time series from energy density spectrum are used, the seeding has a significant effect on the distribution of  $V_{ov}$ . It is possible for different distributions to be produced from the same incident spectra, some of which are shown to significantly diverge from the Weibull distributions usually used for overtopping analysis. The lower level of overtopping produced more variation between the numerical model runs as expected.

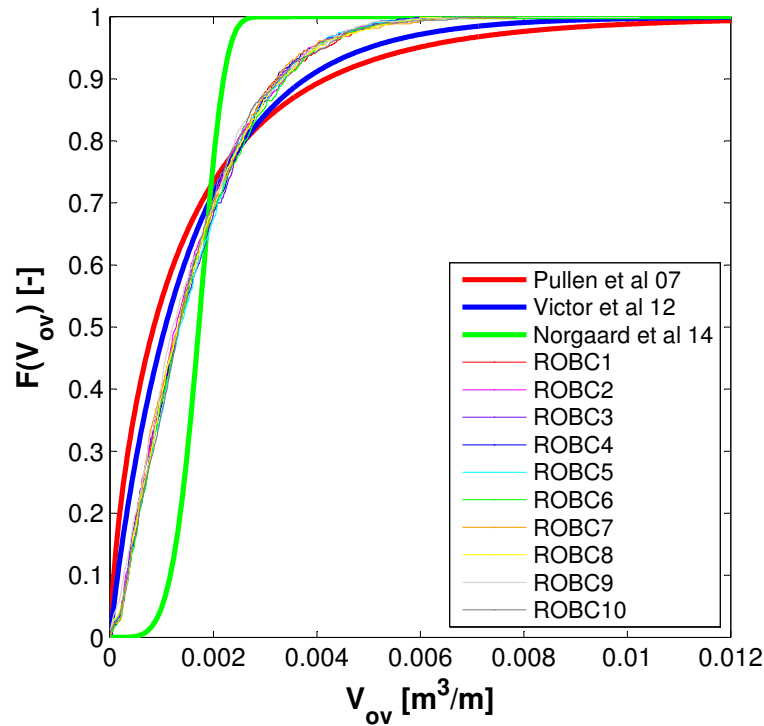


Figure 5.13: Comparison of the distribution of  $V_{ov}$  from the randomly selected ROBC tests and the empirical formulae for Test 007.

It has been shown that, if the distribution of the incident wave heights in the model does not follow that in the field, then the distribution of  $V_{ov}$  also will not be accurate. In engineering practice the distribution of  $H$  at the toe of the structure is not always known. This increases the uncertainty of the numerical estimates of the  $V_{ov}$  distribution. The results of this study suggest to preliminary analyse what type of wave height distribution is to be expected at the toe using existing wave propagation models and generate multiple time series at the boundary and chose from these only those with a distribution of wave height that is close to the expected to be used as input in an overtopping model.



## Chapter 6

# Effect of Hydraulic and Structural Parameters on Uncertainty

### 6.1 Introduction

So far this work has analysed a single steep smooth sloped structure (1:2.55) and wave conditions with relatively small wave steepness. However, it is in fact known that slope geometry and wave conditions can play an important role in overtopping and this is confirmed by existing empirical design formulas (e.g. Van der Meer (1998), Pullen et al. (2007), van Gent et al. (2007)). Therefore, in order to provide more general conclusions on the variability with offshore boundary conditions, further numerical tests have been carried out to investigate the influence of these parameters.

### 6.2 Synthetic Spectra

The numerical experiments carried out previously were based on the incident wave spectra obtained from the physical model tests. Now to allow a full analysis of the effect of the various hydraulic and geometric parameters on the variability, synthetic spectra are approximated from eq. 2.12 in section 2.3.2.

Synthetic spectra were generated based on each of the hydraulic parameters investigated. As in the previous work, to allow full assessment of the variability in the results, a Monte Carlo approach is used with each test condition being carried out using 500 different reconstructed wave time series.

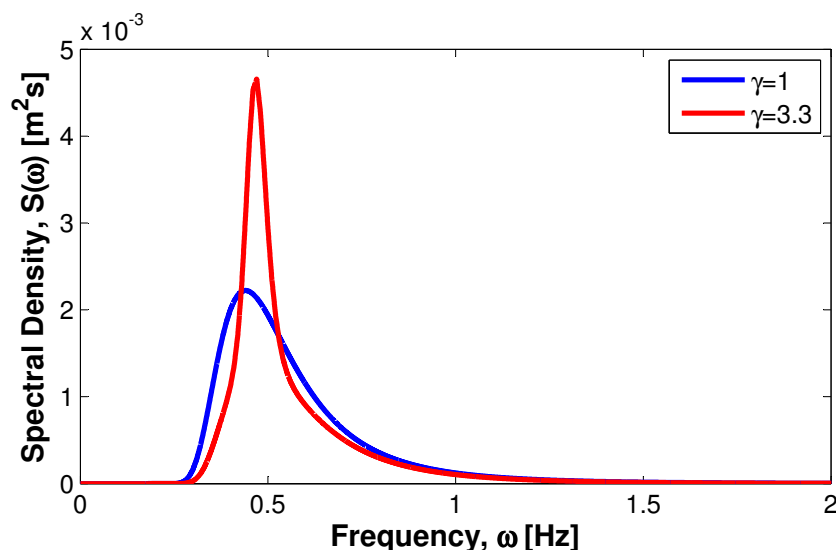


Figure 6.1: Energy density spectra used for analysis of the effect of spectral shape. Red line: JONSWAP. Blue line: Pierson-Moskovitz.

### 6.3 Influence of Spectral Shape

All the spectra used throughout the experiments were of a JONSWAP type, with a peak enhancement factor ( $\gamma$ ) of 3.3. To look at the effect that the spectral shape has on the variability of the overtopping parameters, a series of tests to compare with a broad banded Pierson-Moskovitz type spectra with a  $\gamma = 1$  were carried out and the resulting statistical distributions of the parameters compared.

Both spectra were generated using the theoretical relationships for  $S(\omega)$ ; the two spectra can be seen in Fig. 6.1. For both,  $H_{m0} = 0.04\text{m}$ , and  $T_p = 1.32\text{s}$  at the toe. The structural geometry and numerical domain were the same as in the original numerical tests.  $R_c = 0.17\text{m}$  and  $d_t = 0.13\text{m}$  were used in this case.

The empirical CDFs for both spectra for  $q$ ,  $V_{max}$  and  $P_{ov,num}$  are plotted in Fig. 6.2. This shows the similarities between the results from the two different spectra. A slight difference is observed between the two spectra for  $q$ , with the  $\gamma = 3.3$  distribution being steeper than that of the  $\gamma = 1$  distribution. This suggests a slightly narrower distribution for  $\gamma = 3.3$  which mimics the shape of the original spectra. The distribution for  $\gamma = 1.0$  appears to be a slightly wider distribution, again influenced by the shape of the original spectra. However, it does not appear to be a significant influence.

For the other two parameters the shapes of the distributions appear to be very similar. For  $P_{ov}$  the distributions has shifted slightly but overall the shapes are the same. For  $V_{max}$  the distributions are practically identical. For all of the distributions, it is the  $\gamma = 1.0$ , that always falls

Table 6.1: Distribution parameters and results of K-S test for  $q$  using a JONSWAP and PM spectra with  $H_{m0} = 0.04\text{m}$ ,  $T_p = 1.32\text{s}$  and  $R_c = 0.17\text{m}$ .

Test	Weibull			
	$\lambda$	$k$	$\Gamma$	$D_n$
$\gamma = 1.0$	3.76e-6	2.11	0	0.0420
$\gamma = 3.3$	3.44e-6	1.85	0	0.0305

 Table 6.2: Distribution Parameters and results of K-S test for  $P_{ov}$  using a JONSWAP and PM spectra with  $H_{m0} = 0.04\text{m}$ ,  $T_p = 1.32\text{s}$  and  $R_c = 0.17\text{m}$ .

Test	Normal			
	$\mu$	$\sigma$	$\Gamma$	$D_n$
$\gamma = 1.0$	0.50	0.17	0	0.0769
$\gamma = 3.3$	0.45	0.17	0	0.0760

slightly to the right of the  $\gamma = 3.3$  one. This shift does not appear to be significant.

It can be seen in Tables 6.1, 6.2 and 6.3 that when the results are fitted with the theoretical CDFs, the distribution parameters for the two shapes all appear very similar. Also included in these tables are the results of the K-S test carried out to establish which theoretical CDF describes the data more accurately. It can be seen that although there are small variations in the distribution parameters between the two spectra, the shapes of the distributions follow those observed earlier in the work. The null hypothesis has been obtained for all of the overtopping parameters against the theoretical distributions, i.e.  $q$  follows a Weibull distribution,  $P_{ov}$  a normal distribution and  $V_{max}$  follows a GEV distribution.

Overall this suggests that the variability in the overtopping parameters are only marginally dependent on the shape of the spectra. In fact, although the generated populations do have small differences they appear to still be described by the same type of distribution.

## 6.4 Influence of Surf Similarity Parameter

The seaward slope ( $\tan \alpha$ ) of a structure influences the amount of overtopping that occurs. In cases where a shallower slope is present, more persistent breaking occurs causing the waves to

 Table 6.3: Distribution Parameters and results of K-S test for  $V_{max}$  using a JONSWAP and PM spectra with  $H_{m0} = 0.04\text{m}$ ,  $T_p = 1.32\text{s}$  and  $R_c = 0.17\text{m}$ .

Test	GEV				
	$\xi_x$	$\sigma_x$	$\mu_x$	$\Gamma$	$D_n$
$\gamma = 1.0$	0.11	9.65e-4	1.86e-3	0	0.0300
$\gamma = 3.3$	0.16	9.71e-4	1.72e-3	0	0.0365

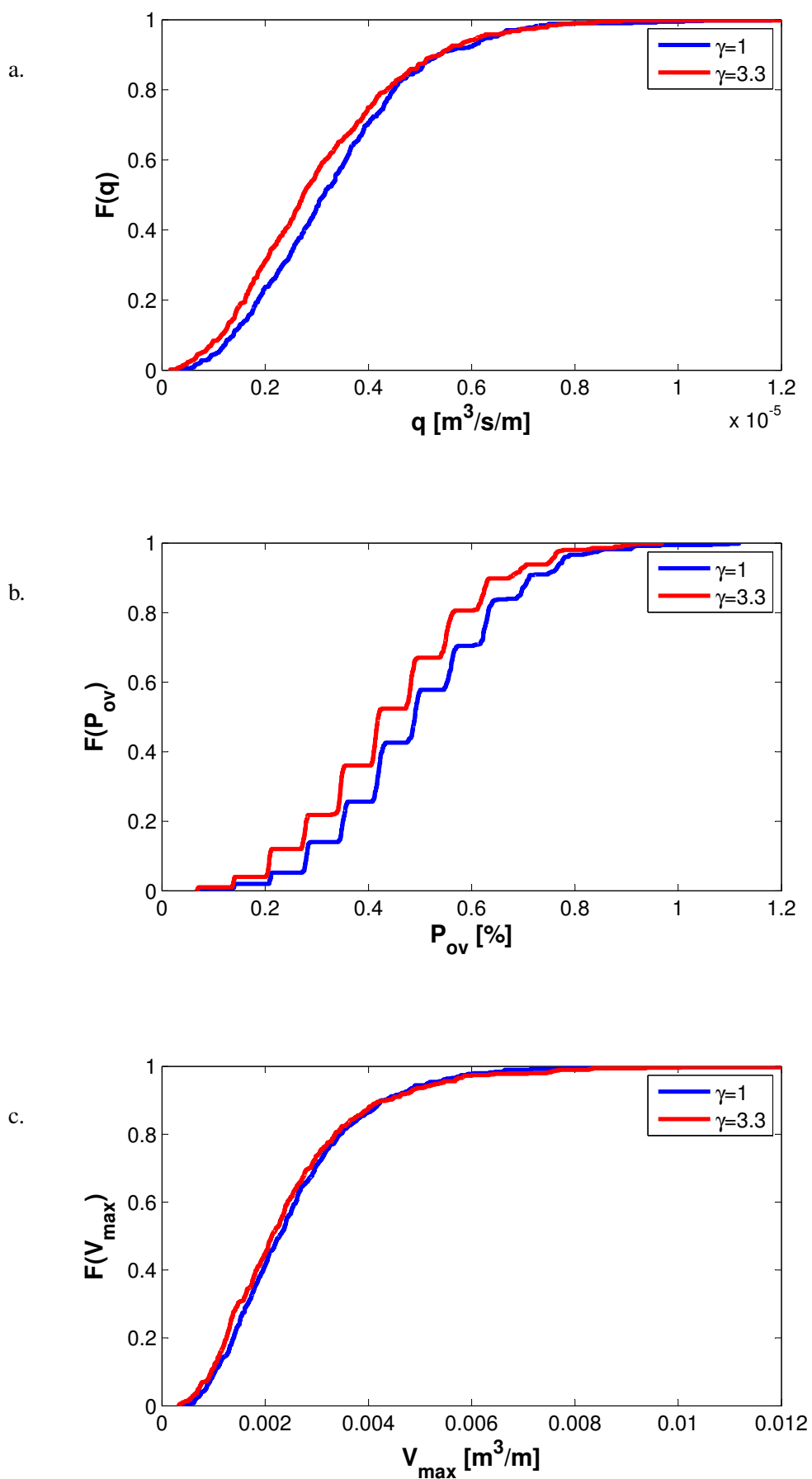


Figure 6.2: Empirical CDFs for each of the overtopping parameters for the two spectral shapes. Red line: JONSWAP and blue line: PiersonMoskovitz. a.  $q$ . b.  $P_{ov}$ . c.  $V_{max}$ .

lose energy and therefore decreasing the quantity of overtopping.

Wave steepness is defined as the ratio of wave height to wave length, and can be defined as  $s_{m-1,0} = H_{m0}/L_{m-1,0}$ , where  $H_{m0}$  is the spectral significant wave height at the toe of the structure and  $L_{m-1,0}$  is the deep water wave length defined as  $gT_{m-1,0}^2/2\pi$ .

The effect of both  $s_{m-1,0}$  and  $\tan \alpha$  on the variability will be considered separately. However, the empirical prediction formulae for discharge ( $q$ ) usually considers the surf similarity parameter which relates these two parameters, and as stated earlier can be used to distinguish the type of breaking wave present. For random waves it is given by

$$\xi_{m-1,0} = \frac{\tan \alpha}{\sqrt{(H_{m0}/L_{m-1,0})}}, \quad (6.1)$$

where  $\alpha$  is the slope of the front face of the structure,  $H_{m0}$  is the spectral significant wave height at the toe of the structure and  $L_{m-1,0}$  is the deep water wave length defined as  $gT_{m-1,0}^2/2\pi$ . The effect of this parameter on the variability will therefore also be considered in this work.

As the shape of the spectrum appears to make little difference to the results, for these numerical tests, JONSWAP type spectra were used again with a peak enhancement factor,  $\gamma = 3.3$ . In this work, the same significant wave height is considered for all the tests whilst the peak periods are modified. Three values are chosen resulting in varying wave steepness  $s_{m-1,0} = \frac{H_{m0}}{L_{m-1,0}} = 0.017 - 0.105$ .

In total, 3 different incoming wave spectra were generated. In addition to this, to allow the influence of the structure on variability to be assessed, the geometry of the numerical domain is altered to include 2 additional gradient smooth sloped structures, this results in gradients of 1:2.55, 1:4 and 1:7 being considered, as well as two different crest freeboards ( $R_c = 0.09\text{m}$  and  $0.17\text{m}$ ). The generic numerical domain can be seen in Fig. 6.3, whilst the detailed dimensions for each case can be found in Table 6.4. Overall, this resulted in a total of 18 new numerical test conditions, which are fully detailed in Table 6.5. As before, 500 ROBC tests have been conducted for each test condition.

### 6.4.1 Variability

It was found earlier in this work that the variability in the predicted  $q$  was best correlated to the probability of overtopping ( $P_{ov}$ ). To investigate if this is effected by the aforementioned wave

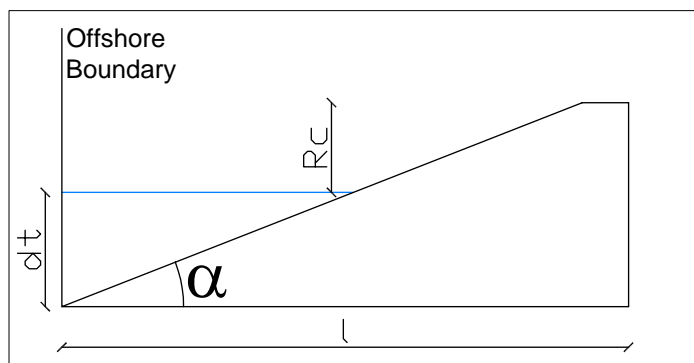


Figure 6.3: Numerical domain showing the different structural geometries. Dimensions can be found in Table 6.4

Table 6.4: Structural geometry in the numerical domain

Structure	$d_t$ (m)	$R_c$ (m)	$l$ (m)	$\tan \alpha$ (-)
101	0.12	0.09	0.54	0.40
102	0.12	0.17	0.74	0.40
103	0.12	0.09	0.84	0.25
104	0.12	0.17	1.16	0.25
105	0.12	0.09	1.47	0.14
106	0.12	0.17	2.03	0.14

Table 6.5: Incident wave conditions for the JONSWAP spectra random wave numerical tests

Test	$H_{m0}$ (m)	$T_{m-1,0}$ (s)	$T_p$ (s)	$s_{m-1,0}$ (-)	$\tan \alpha$ (-)	$\xi_{m-1,0}$ (-)	$H_{m0}/d_t$ (-)	$R_c/H_{m0}$ (-)	$H_{m0}/H_{10}$ (-)
101.0	0.067	0.63	0.69	0.105	0.40	1.21	0.52	1.34	0.837
101.1	0.067	1.10	1.21	0.034	0.40	2.12	0.52	1.34	0.824
101.2	0.067	1.58	1.74	0.017	0.40	3.04	0.52	1.34	0.827
102.0	0.067	0.63	0.69	0.105	0.40	1.21	0.52	2.52	0.837
102.1	0.067	1.10	1.21	0.034	0.40	2.12	0.52	2.52	0.824
102.2	0.067	1.58	1.74	0.017	0.40	3.04	0.52	2.52	0.827
103.0	0.067	0.63	0.69	0.105	0.25	0.77	0.52	1.34	0.837
103.1	0.067	1.10	1.21	0.034	0.25	1.35	0.52	1.34	0.824
103.2	0.067	1.58	1.74	0.017	0.25	1.94	0.52	1.34	0.827
104.0	0.067	0.63	0.69	0.105	0.25	0.77	0.52	2.52	0.837
104.1	0.067	1.10	1.21	0.034	0.25	1.35	0.52	2.52	0.824
104.2	0.067	1.58	1.74	0.017	0.25	1.94	0.52	2.52	0.827
105.0	0.067	0.63	0.69	0.105	0.14	0.44	0.52	1.34	0.837
105.1	0.067	1.10	1.21	0.034	0.14	0.77	0.52	1.34	0.824
105.2	0.067	1.58	1.74	0.017	0.14	1.10	0.52	1.34	0.827
106.0	0.067	0.63	0.69	0.105	0.14	0.44	0.52	2.52	0.837
106.1	0.067	1.10	1.21	0.034	0.14	0.77	0.52	2.52	0.824
106.2	0.067	1.58	1.74	0.017	0.14	1.10	0.52	2.52	0.827

parameters, a number of new scatter plots of  $q$  against  $P_{ov}$  have been produced for these tests. Firstly, Fig. 6.4 considers the overtopping with respect to the slope of the structure. According to Pullen et al. (2007), the overtopping on a smooth slope will decrease as the value of  $\tan \alpha$  decreases. It can be seen in this figure, that the numerical tests are behaving in this way, with those tests with a lower value of  $\tan \alpha$  resulting in lower values of  $q$ . Consequently the variability is generally greater in the shallower slopes due to these lower values of  $q$  obtained. It can also be seen that tests with identical values of  $\tan \alpha$  do not show the same levels of variability, suggesting that this parameter only has an indirect effect on the variability caused by the resulting lower overtopping.

Unusually at the top of the range for  $q$ , it is the middle steepness slope that produces the highest overtopping. It is anticipated that this is caused by the wave conditions present in these particular tests. In fact, in all of these tests it is not always the steepest slope that produces the highest overtopping in each set of wave conditions.

In Fig. 6.5, the overtopping is examined with respect to  $s_{m-1,0}$ . The steeper waves are expected to break, with the plunging waves resulting in lower overtopping (Pullen et al., 2007). Again the numerical results behave in the expected manner, with those tests with a higher value of  $s_{m-1,0}$  producing the lowest values of  $q$ . This results in the variability generally being higher in the tests with higher values of wave steepness, and consequently lower  $q$ . It can again be seen that tests with the same values of  $s_{m-1,0}$  do not have the same magnitude of variability, so once more no direct effect on the variability is observed.

This time, as expected, it is one of the tests with the lowest wave steepness that produces the highest overtopping, and it appears that this is consistent throughout the various results based on different structural geometries.

Finally these two parameters are considered together as  $\xi_{m-1,0}$ , obtaining the graph found in Fig. 6.6. Based on the previous findings and knowledge of the relationship between  $\xi_{m-1,0}$ ,  $s_{m-1,0}$ , and  $\tan \alpha$ , the results are expected to show lower  $q$  for lower values of  $\xi_{m-1,0}$ . The numerical model results appears to agree with this theory. As with the previous panels it can be seen that higher variability is generally found for the lower values of  $\xi_{m-1,0}$ , but again this is due to the resulting lower overtopping rather than the parameter itself, as tests in the same range of  $\xi_{m-1,0}$  produce results with different variability.

Overall, the results appear to behave in a very similar manner to those observed previously. There is clearly more variation in the mean values for each test condition here across all of

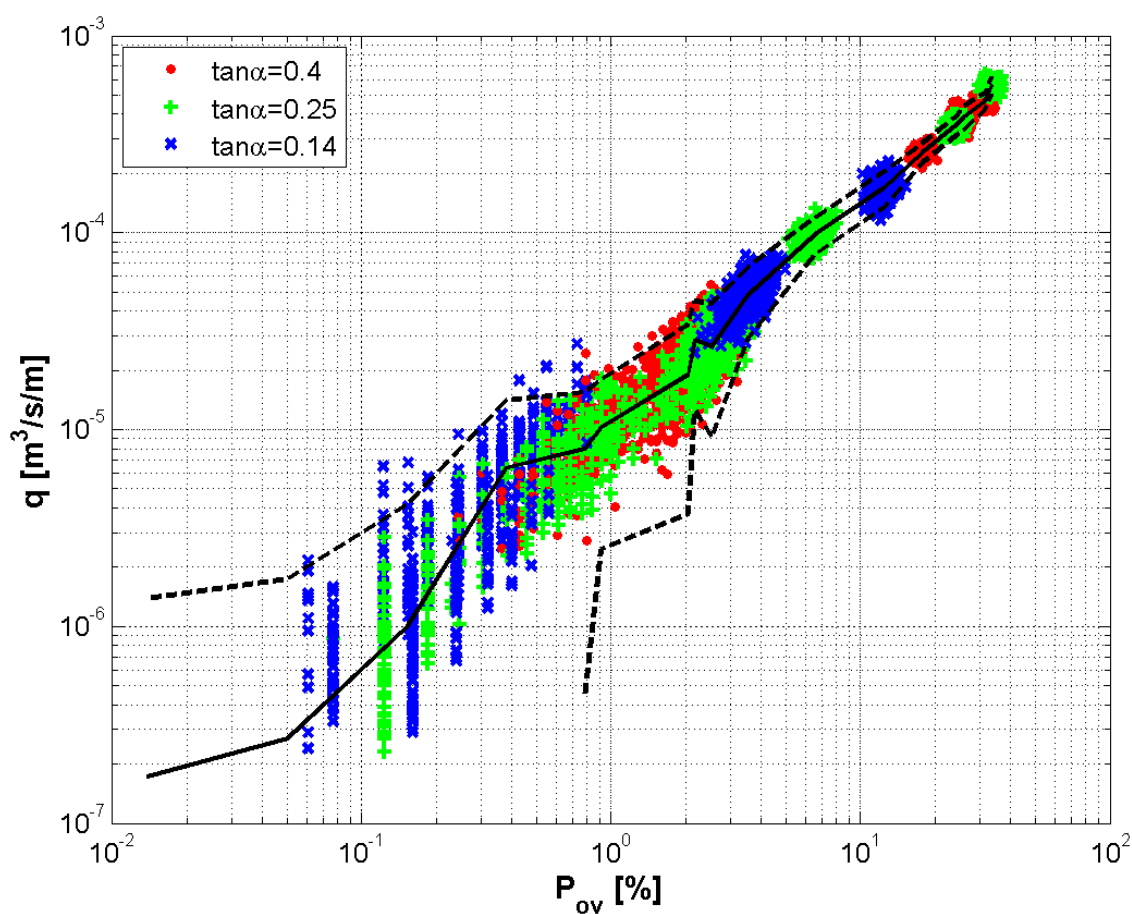


Figure 6.4: Logarithmic scatter graph showing  $q$  plotted against  $P_{ov}$  classified in terms of slope angle. Solid lines represent the mean values of  $q$ . Dashed lines represent the 95% confidence limits of  $q$ .

the tests, which is caused by the variation in the gradients of the structure slopes which wasn't present in the original numerical tests. These results suggest that neither the incoming wave conditions or the slope of the structure appear to have a significant effect on the variability of the results.

## 6.4.2 Comparison with Empirical Methods

From the graphs in the previous section it appears that the main factors influencing the variability are  $q$  or  $P_{ov}$  themselves, both of which are related to the relative freeboard ( $R_c/H_{m0}$ ). To examine this in more detail, Fig. 6.7 shows the dimensionless discharge ( $Q^* = q/\sqrt{(gH_{m0}^3)}$ ) plotted as a function of  $\xi_{m-1,0}$ . In this graph, the results have been classified based on the  $\tan \alpha$  of each particular test. As there are no physical model results for these tests, the empirical prediction curves from Pullen et al. (2007) have been plotted based on the two different values of  $R_c/H_{m0}$ .

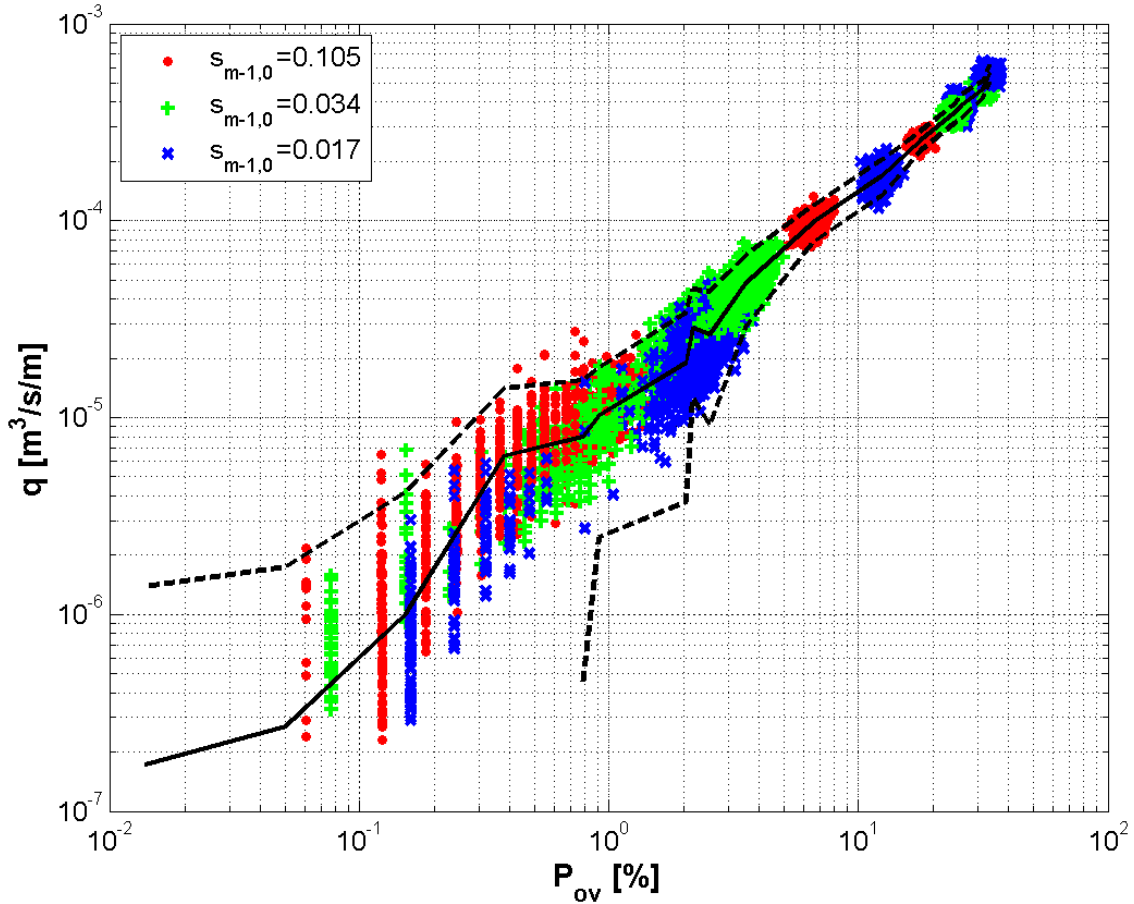


Figure 6.5: Logarithmic scatter graph showing  $q$  plotted against  $P_{ov}$  classified in terms of wave steepness. Solid lines represent the mean values of  $q$ . Dashed lines represent the 95% confidence limits of  $q$ .

It can be seen in this graph that the numerical model follows a similar pattern to the empirical prediction, although generally the empirical prediction under predicts the results of the numerical model in the tests with lower  $\xi_{m-1,0}$ . For both values of  $R_c/H_{m0}$  it can be observed that as the value of  $\xi_{m-1,0} \simeq 2$  from the numerical model, the dimensionless overtopping reaches a maximum, in agreement with the empirical predictions.

In Fig. 6.8, the same results are plotted but this time they have been classified based on the values of  $s_{m-1,0}$ . In both plots it is clear that the earlier findings are confirmed with  $\xi_{m-1,0}$ ,  $\tan \alpha$  and  $s_{m-1,0}$  not showing any direct effect on the magnitude of the variation. Tests with the same values of these parameters do not produce the same magnitude of variability.

From these two graphs it can be seen that the variability is influenced by the  $R_c/H_{m0}$ . The tests with the higher value of  $R_c/H_{m0}$  clearly show a greater variation in the resulting  $Q^*$ . Although, this is due to the value of  $R_c/H_{m0}$  being the major contributor to the quantity of overtopping, so tests with high  $R_c/H_{m0}$  produce lower overtopping which in turn is subject to greater vari-

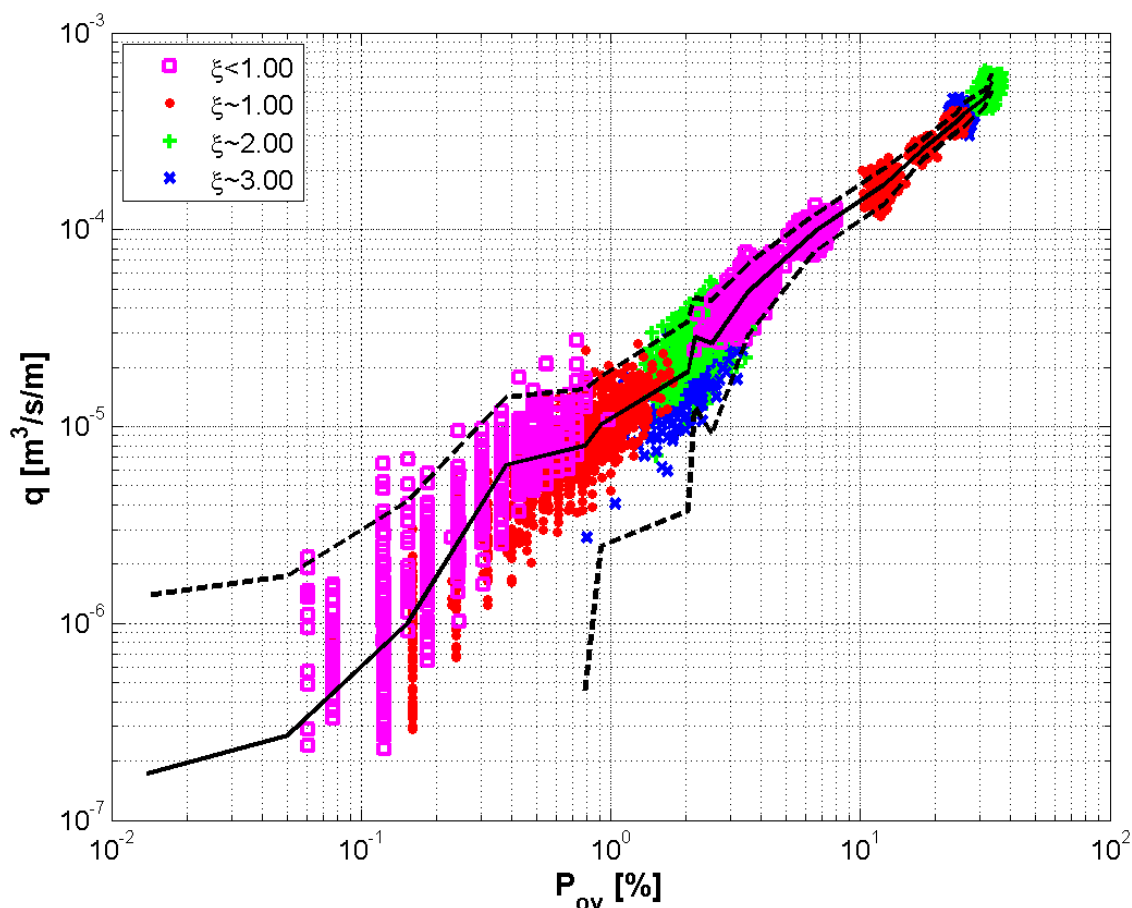


Figure 6.6: Logarithmic scatter graph showing  $q$  plotted against  $P_{ov}$  classified in terms of surf similarity. Solid lines represent the mean values of  $q$ . Dashed lines represent the 95% confidence limits of  $q$ .

ability.

When comparing the ROBC results with the empirical formulae, it is also important to compare the uncertainty in the two types of results. Fig. 6.9 shows the numerical results plotted with relation to dimensionless freeboard and dimensionless overtopping discharge. Also, included on this graph are the formula (eq. 2.19) specified in section 2.5 for each of the structure gradients considered.

Overall, the empirical formula agrees reasonably well with the numerical results. A slight mismatch occurs due to the empirical formula being dependent on both the slope gradient and the surf similarity parameter. Unfortunately it is only really possible to consider one of these variables changing in this graph. It can also be observed here, that the variability in the numerical model is of a similar magnitude as that occurring in the empirical formulae.

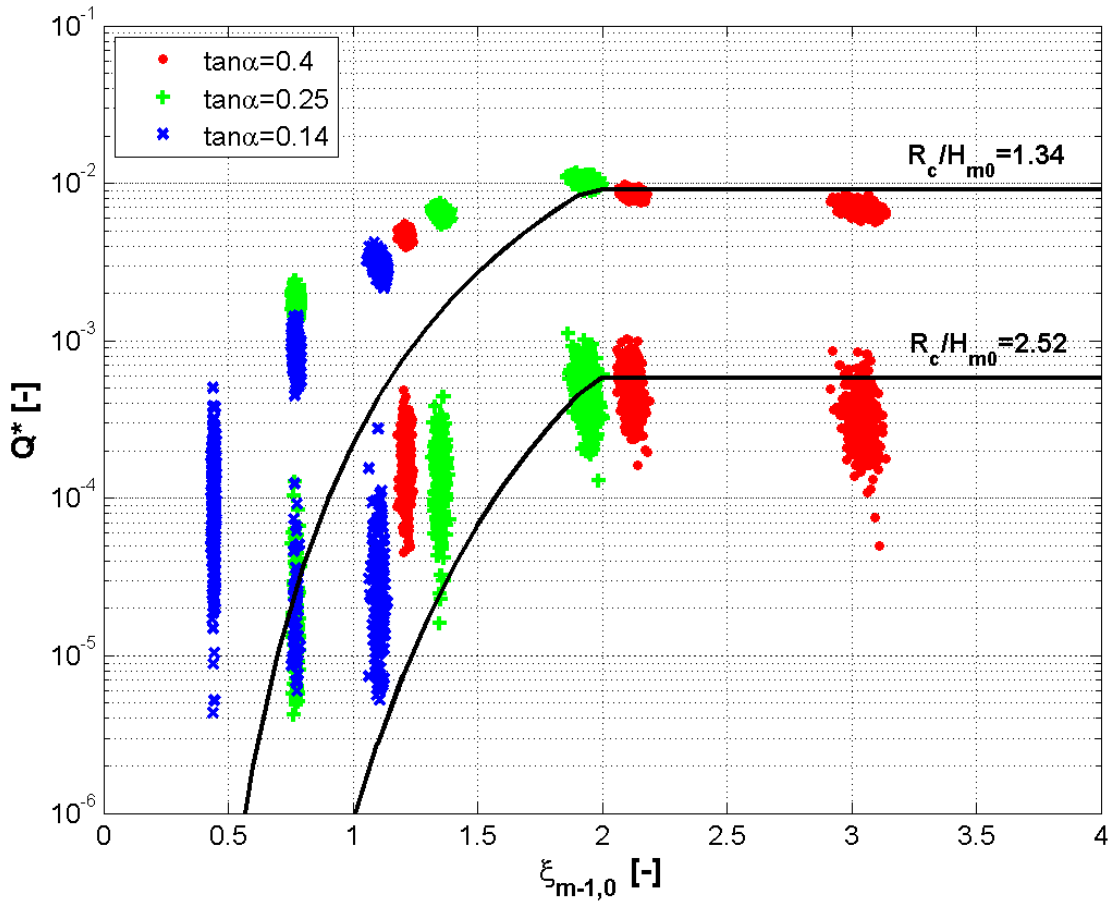


Figure 6.7: Scatter graph showing  $\xi_{m-1,0}$  plotted against  $Q^*$  classified in terms of slope angle. Solid lines represent the empirical predictions based on each  $R_c/H_{m0}$  present.

### 6.4.3 Distributions

It has been established that the variability due to reconstructed boundary conditions in these tests is of a similar magnitude to that observed earlier, regardless of the hydraulic and structural parameters. It is now important to consider if the distributions of the overtopping parameters match those found in the earlier tests. These will be considered by choosing 4 different values of  $\xi_{m-1,0}$  from these new tests.

In Fig. 6.10, the distributions of  $q$  have been considered. Earlier it was found that in lower overtopping this followed a Weibull distribution, tending to Normal distribution in the higher tests. It was therefore decided to compare the  $q$  found here against these two distributions. It can clearly be seen that a similar trend is evident. In the test with a lower  $\xi_{m-1,0} < 1$ , the distribution clearly follows a Weibull distribution. For the remaining three tests conditions considered it appears that the distributions are more suitably modelled by the Normal distribution. This is in agreement with the earlier findings.

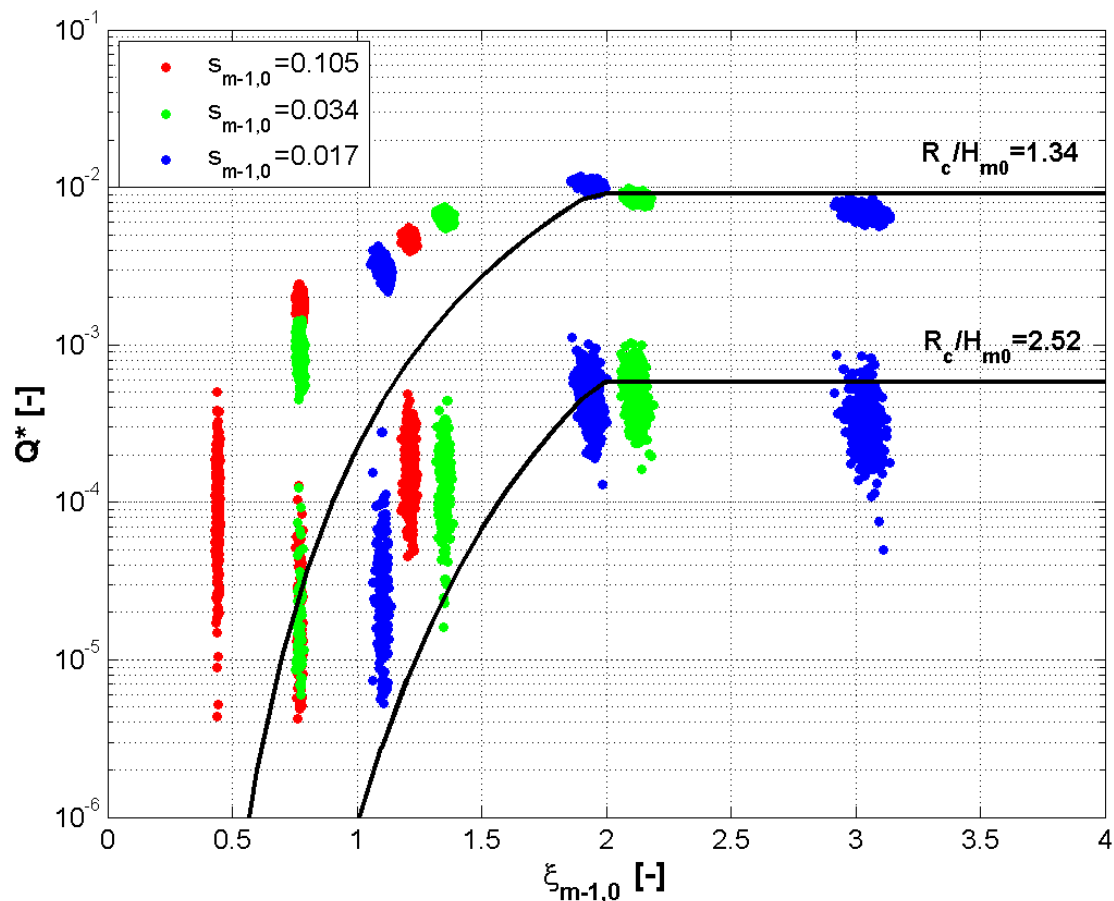


Figure 6.8: Scatter graph showing  $\xi_{m-1,0}$  plotted against  $Q^*$  classified in terms of wave steepness. Solid lines represent the empirical predictions based on each  $R_c/H_{m0}$  present.

To confirm these findings, a K-S test has been performed. The results can be seen in Table 6.6. It is clear from these that the lowest value of  $\xi_{m-1,0}$ , which also corresponds to the lowest value of  $q$ , is indeed a match for only the Weibull distribution. The two highest values of  $\xi_{m-1,0}$ , which do correspond to the higher values of  $q$  are a match for only the Normal distribution. The test with  $\xi_{m-1,0} = 1.21$ , appears to be modelled by both distributions but the value of  $D_n$  suggests that the Normal distribution is a better match.

Now to consider the distribution of  $P_{ov}$ , which was earlier found to follow a Normal distribu-

Table 6.6: Results of the one sample K-S test based on  $q$  for various values of  $\xi_{m-1,0}$

$\xi_{m-1,0}$	$q$							
	Normal		K-S		Weibull		K-S	
	$\mu$	$\sigma$	$\Gamma$	$D_n$	$\gamma$	$k$	$\Gamma$	$D_n$
0.44	6.37e-6	3.86e-6	1	0.0663	7.24e-6	1.77	0	0.0293
1.21	2.57e-4	1.48e-5	0	0.0215	2.63e-4	17.98	0	0.0570
1.94	5.61e-4	2.88e-5	0	0.0354	5.75e-4	19.92	1	0.0841
3.04	3.81e-4	2.63e-5	0	0.0308	3.93e-4	14.68	1	0.0677

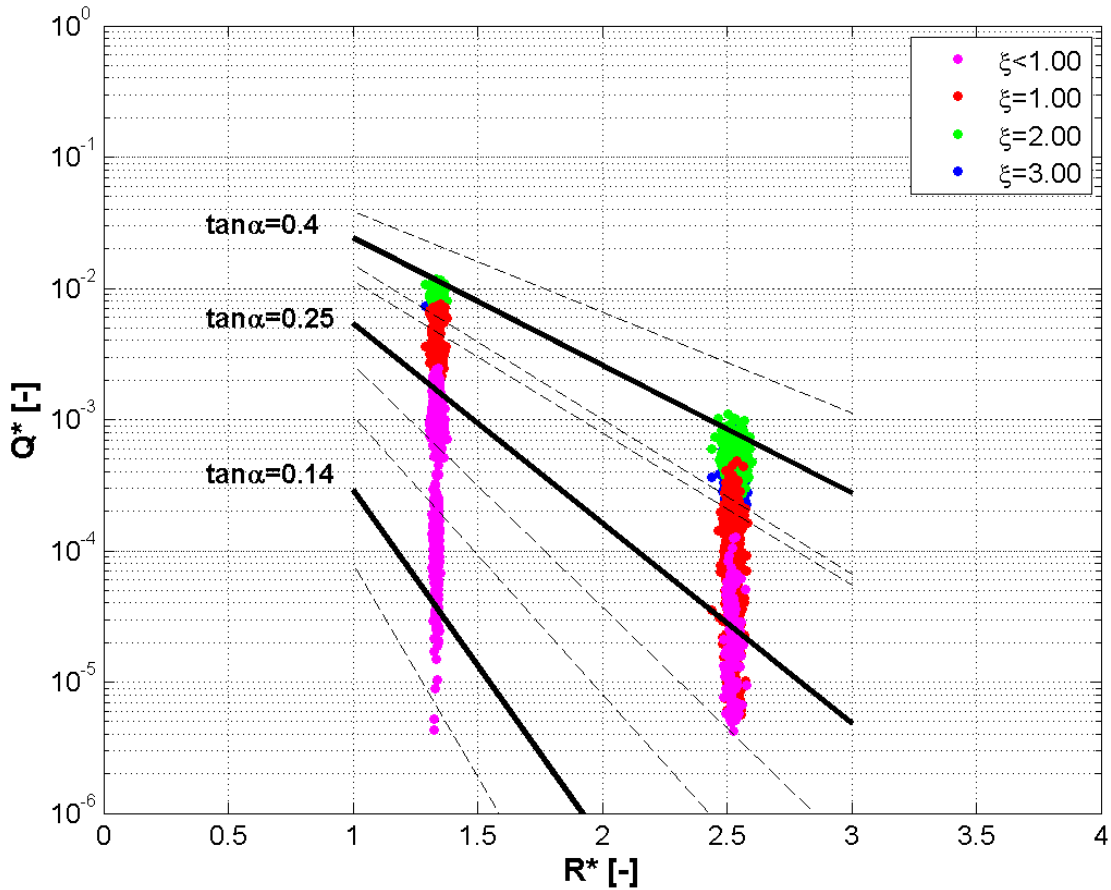


Figure 6.9: Scatter graphs showing  $R^*$  plotted against  $Q^*$  classified in terms of  $\xi_{m-1,0}$ . Solid lines represent empirical predictions.

tion at all levels of overtopping. Fig. 6.11 therefore shows the empirical distribution for this parameter plotted alongside the theoretical Normal distribution. It appears that the Normal distribution provides a good match at all levels of overtopping, agreeing with the earlier findings.

Again, to confirm these findings, a K-S test has been performed with the results shown in Table 6.7. It can therefore be seen that the Normal distribution is suitable for modelling the variability in all of the tests here.

Finally, the distribution of  $V_{max}$  must be considered. Earlier it was found that the GEV dis-

Table 6.7: Results of the one sample K-S test based on  $P_{ov}$  for various values of  $\xi_{m-1,0}$

$\xi_{m-1,0}$	$P_{ov}$			
	Normal		K-S	
	$\mu$	$\sigma$	$\Gamma$	$D_n$
0.44	0.39	0.18	0	0.0790
1.21	18.35	0.81	0	0.0335
1.94	35.04	1.62	0	0.0408
3.04	26.64	1.28	0	0.0354

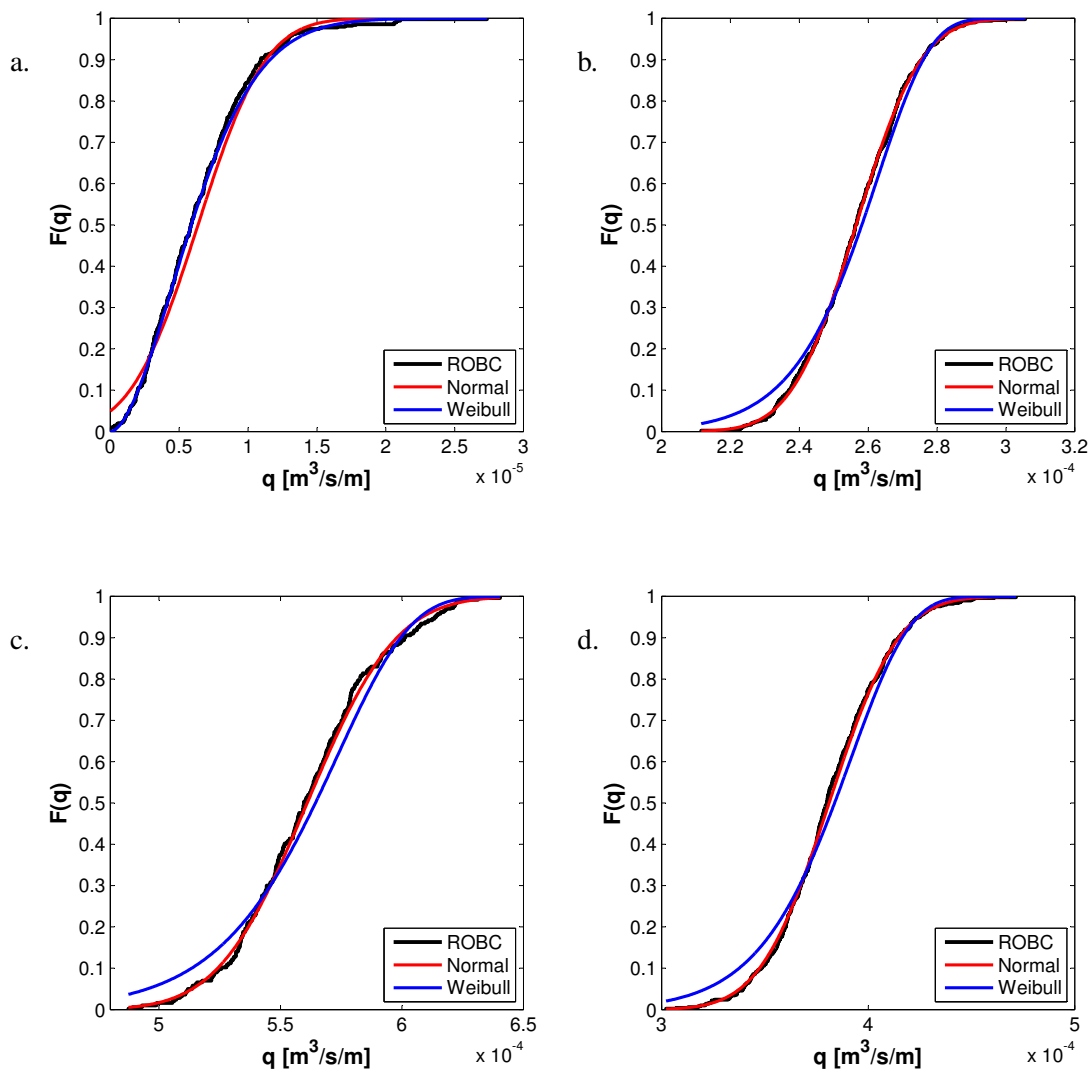


Figure 6.10: Empirical frequency curves for  $q$  from ROBC (black solid lines) compared with expected distributions for different levels of overtopping. a.  $\xi_{m-1,0} = 0.44$ . b.  $\xi_{m-1,0} = 1.21$ . c.  $\xi_{m-1,0} = 1.94$ . d.  $\xi_{m-1,0} = 3.04$

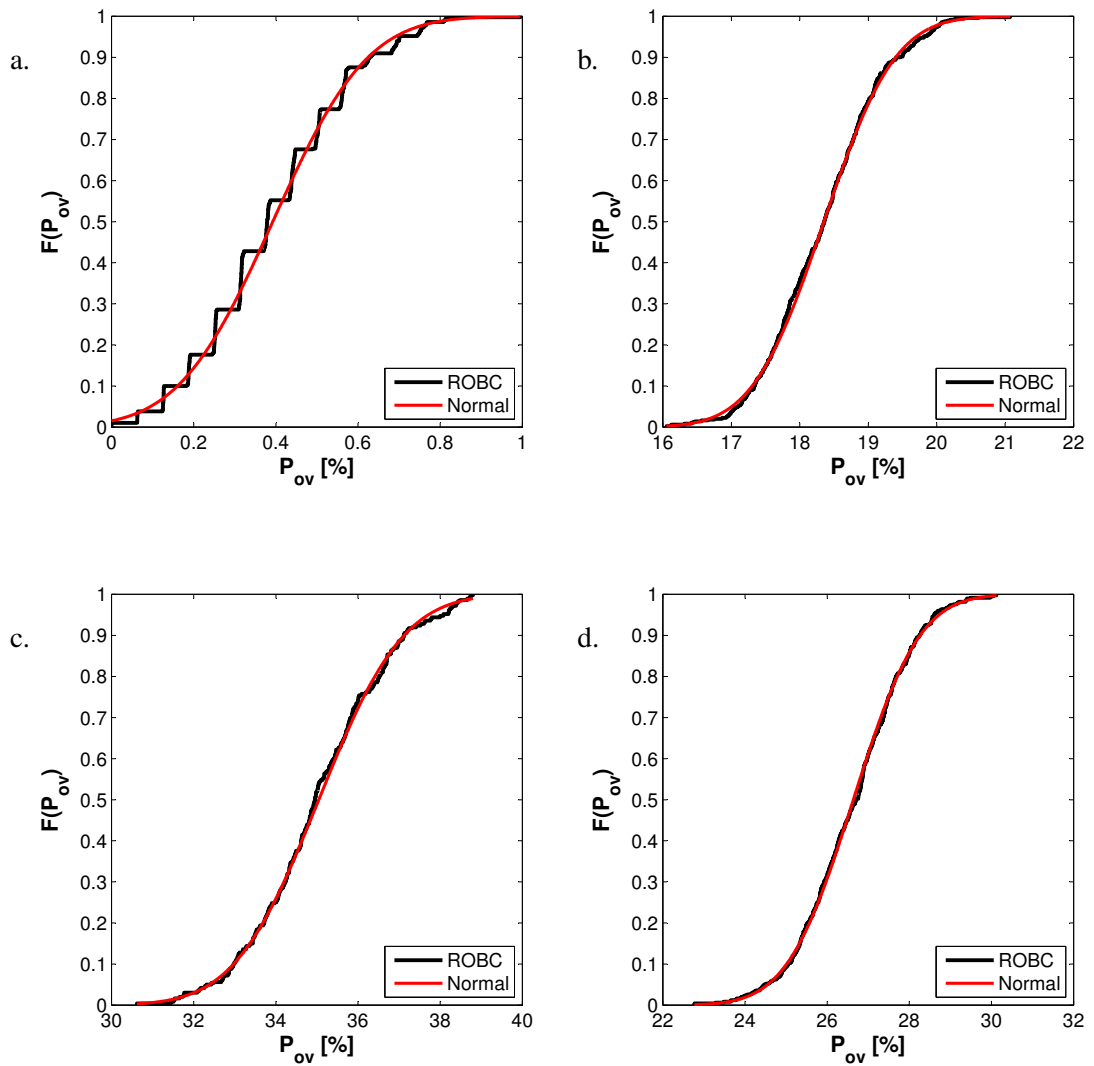


Figure 6.11: Empirical frequency curves for  $P_{ov}$  from ROBC (black solid lines) compared with expected distributions for different levels of overtopping. a.  $\xi_{m-1,0} = 0.44$ . b.  $\xi_{m-1,0} = 1.21$ . c.  $\xi_{m-1,0} = 1.94$ . d.  $\xi_{m-1,0} = 3.04$

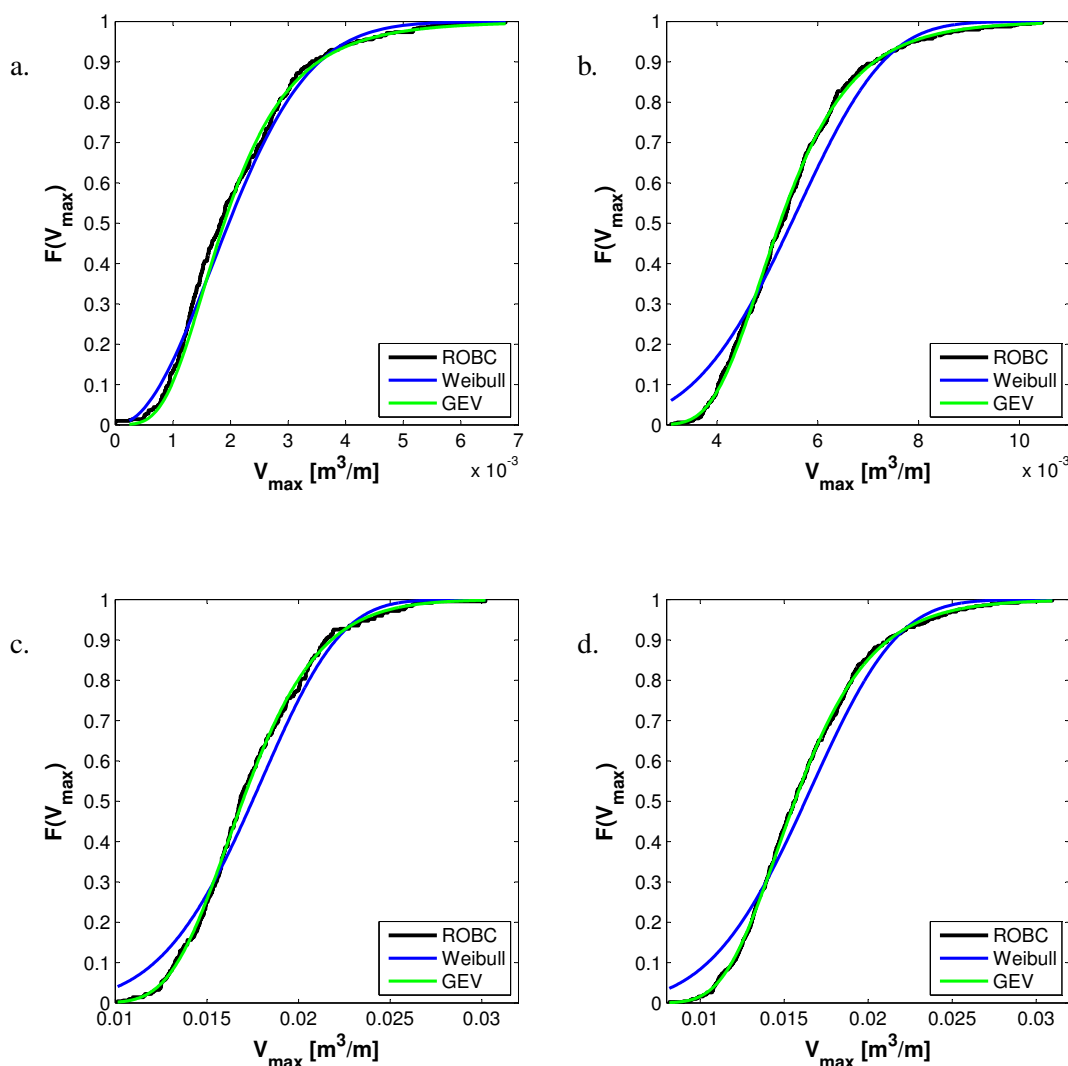


Figure 6.12: Empirical frequency curves for  $V_{max}$  from ROBC (black solid lines) compared with expected distributions for different levels of overtopping. a.  $\xi_{m-1,0} = 0.44$ . b.  $\xi_{m-1,0} = 1.21$ . c.  $\xi_{m-1,0} = 1.94$ . d.  $\xi_{m-1,0} = 3.04$

tribution was the closest match although in the moderate overtopping the Weibull distribution also provided a reasonable match. The distributions are plotted in Fig. 6.12. For the lowest value of  $\xi_{m-1,0}$ , again which corresponds to the lowest values of  $V_{max}$ , both the Weibull and GEV distributions provide a reasonable match to the empirical distribution. For the remaining three tests, with higher values of  $V_{max}$ , the GEV is clearly the better match to the empirical distributions.

If the results from the K-S test found in Table 6.8 are considered it is clear that in all cases the GEV provides the closest match to the empirical results. In the lowest value of  $\xi_{m-1,0}$ , the Weibull distribution does achieve the null hypothesis but the values of  $D_n$  shows that the GEV is more suitable.

Overall, the results from this set of tests suggest that the hydraulic and structural parameters do

Table 6.8: Results of the one sample K-S test based on  $V_{max}$  for various values of  $\xi_{m-1,0}$ 

$\xi_{m-1,0}$	$V_{max}$								
	Weibull		K-S		GEV			K-S	
	$\gamma$	$k$	$\Gamma$	$D_n$	$\xi_x$	$\mu_x$	$\sigma_x$	$\Gamma$	$D_n$
0.44	2.35e-3	2.04	0	0.0728	8.88e-2	7.72e-4	1.56e-3	0	0.0629
1.21	5.97e-3	4.21	1	0.1028	1.56e-2	9.75e-4	4.90e-3	0	0.0507
1.94	1.88e-2	5.18	1	0.0804	-9.35e-2	2.92e-3	1.59e-2	0	0.0272
3.04	1.77e-2	4.27	1	0.0840	-3.34e-2	3.10e-3	1.45e-2	0	0.0189

not have a direct effect on the variability of any of the overtopping parameters. However, it is observed that an indirect effect on the magnitude of the variability occurs due to the subsequent decrease or increase in overtopping due to the exact conditions present.

## 6.5 Influence of Surface Roughness

Coastal structures can be constructed from a variety of different materials. As well as concrete structures like that used in the laboratory experiments, the surface of seawalls can be covered in grass, or even rocks. This introduces an increased surface roughness to the structure which can reduce the amount of overtopping experienced. This is taken into account in the empirical formulae by the introduction of a roughness factor. In the numerical model this can be changed by altering the value of the roughness coefficient,  $K_n$ .

To investigate the effect that  $K_n$  has on the variability, three of the tests from the previous section were chosen. These were those with the medium value of  $s_{m-1,0} = 0.034$ , with each of the three slopes considered. The lower value of  $R_c/H_{m0}$  was used, to ensure that even with a high value of  $K_n$ , enough overtopping would occur to allow analysis.

As the original numerical tests were based on the laboratory experiments, a  $K_n$  value was chosen to match the smooth concrete used ( $K_n = 0.001$ ). However, this would be unlikely to be used in the construction of a real coastal defence due to the high resultant overtopping. It was therefore decided to investigate the effect that other types of material would have on the variability of overtopping. A normal short grass covered structure, like those common along the coast of northern Europe, would according to literature produce a  $K_n = 0.030$  (Liu, 2001). Small rocks or block revetment are also common dyke surfaces, and would increase the friction on the surface producing a  $K_n = 0.070$ . Finally a very high value of  $K_n = 0.200$  will be considered. This is not necessarily representative of a real structure, but was chosen as an extreme values in these tests to allow a full assessment of the effect of the surface roughness.

Table 6.9: Incident wave conditions for the JONSWAP spectra random wave numerical tests based on  $K_n$ 

Test	$H_{m0}$ (m)	$T_{m-1,0}$ (s)	$T_p$ (s)	$s_{m-1,0}$ (-)	$\tan\alpha$ (-)	$\xi_{m-1,0}$ (-)	$K_n$ (m)	$H_{m0}/d_t$ (-)	$H_{m0}/H_{10}$ (-)
101.1.0	0.067	1.10	1.21	0.034	0.40	2.12	0.001	0.52	0.824
101.1.1	0.067	1.10	1.21	0.034	0.40	2.12	0.030	0.52	0.824
101.1.2	0.067	1.10	1.21	0.034	0.40	2.12	0.070	0.52	0.824
101.1.3	0.067	1.10	1.21	0.034	0.40	2.12	0.200	0.52	0.824
103.1.0	0.067	1.10	1.21	0.034	0.25	1.35	0.001	0.52	0.824
103.1.1	0.067	1.10	1.21	0.034	0.25	1.35	0.030	0.52	0.824
103.1.2	0.067	1.10	1.21	0.034	0.25	1.35	0.070	0.52	0.824
103.1.3	0.067	1.10	1.21	0.034	0.25	1.35	0.200	0.52	0.824
105.1.0	0.067	1.10	1.21	0.034	0.14	0.77	0.001	0.52	0.824
105.1.1	0.067	1.10	1.21	0.034	0.14	0.77	0.030	0.52	0.824
105.1.2	0.067	1.10	1.21	0.034	0.14	0.77	0.070	0.52	0.824
105.1.3	0.067	1.10	1.21	0.034	0.14	0.77	0.200	0.52	0.824

Overall, this results in 9 additional tests plus 3 taken from the last section, details of all of the numerical tests carried out here are included in Table 6.9.

### 6.5.1 Influence on Magnitude of Run-up

Before the variability caused by the roughness coefficient is investigated, the direct effect that altering this value has on the run-up is examined. In Fig. 6.13 the depth of water measured at various virtual wave gauges situated on the front face of the 1:2.55 structure is plotted. This is repeated using a single incoming wave time series chosen at random with the varying values of  $K_n$ .

The first plot shows the incident wave conditions at the toe of the structure. The second plot is a wave gauge located on the slope at the mean water level. The third plot shows a location part way up the front face of the structure, and the finally the last plot shows the wave gauge at the crest of the structure used to detect overtopping. A trace has also been included on all the graphs to show which of the incident waves result in overtopping at the crest.

The effect of increasing the value of  $K_n$  on the overtopping generally seems to either very slightly decrease the depth of the water measured by that gauge, or in the case of small events removes it entirely. It can be seen that 8 overtopping events occur when the surface roughness is lowest, this reduces to 6 for the test with  $K_n = 0.030\text{m}$ . There are then 5 events occurred in the two higher  $K_n$  conditions. For the other two gauges located on the structure, the increase in surface roughness does not appear to have any significant effect on either the magnitude or

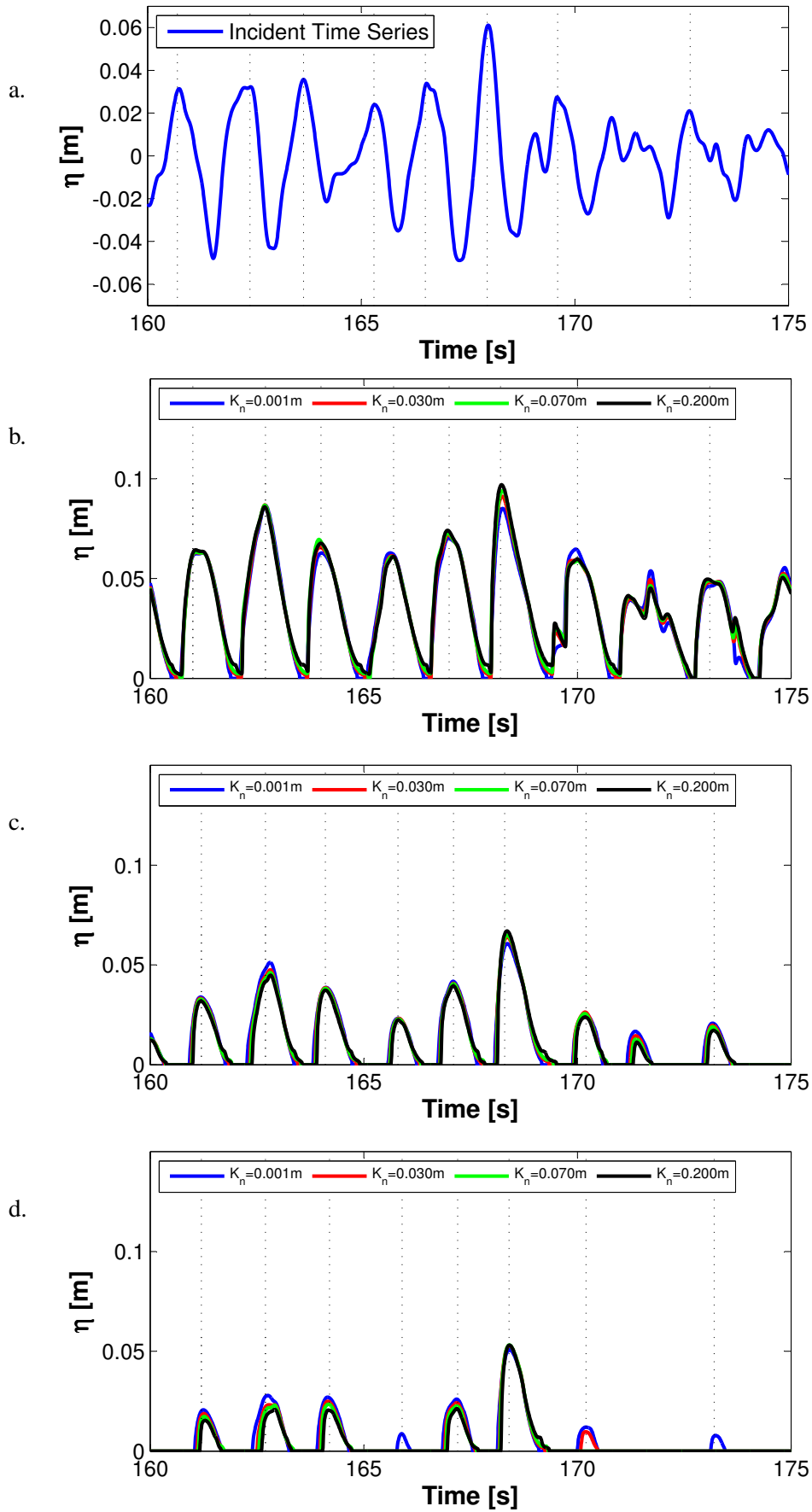


Figure 6.13: Water depth detected at various points in numerical domain of 1:2.55 slope for different surface roughness. a. Toe. b. Still water level. c. Front slope. d. Structure crest.

number of events.

The same time series was also used to investigate the effect on the other gradient slopes. Firstly, Fig. 6.14 shows the effect altering  $K_n$  has for the 1:4 structure. Again, the second gauge is located at the still water level, and the third one part way up the structure, at the same vertical height as in the previous tests.

This time it can be observed that only 6 of the waves overtop on this structure, when the lowest value of  $K_n$  is used. As expected, these events match the larger ones observed in the previous tests. Only 3 events are observed in the tests with higher values of  $K_n$ . It should also be noted that the overtopping event that occurs at approximately 168s, appears to be larger in the tests with higher surface roughness. This suggests the roughness may have an additional effect on the interaction of the run-up waves on the shallower slopes. It can already be seen by comparing the two different slopes that the water on the slope increases more rapidly and then recedes at a slower rate on the shallower slope. This, along with the increase in surface roughness could cause some of the waves to merge together increasing the magnitude of particular events, although decreasing the number overall.

On the 1:4 slope, it can also be seen that the surface roughness has more of an effect at the virtual wave gauges located part way up the structure, with run-up events not occurring for the higher values of  $K_n$ .

Finally, the same time series have been used for the 1:7 structure, with the results being plotted in Fig. 6.15. This time only one overtopping event occurs, which corresponds to the largest wave in the incident time series. This event does occur for all of the different values of  $K_n$ . At the gauge located part way up the structure only 4 run-up events are observed, and as observed previously some of these are only present in the tests with lower values of  $K_n$ .

At the location of the still water level on the structure, it can again be seen that the water depth increases suddenly, and then recedes at a slower rate. This causes all of the waves to merge and interact with each other more, than on the shallower slopes. This has again resulted in events with the higher values of  $K_n$  being larger than those with smaller values.

Overall, it has been observed that the surface roughness does have an effect on the overtopping. By increasing the value of  $K_n$ , it can be seen that generally the magnitude of the events does not alter that much, but a number of small events disappear completely. This leads to a slight decrease in the value of  $q$  but a greater decrease in the value of  $P_{ov}$  as  $K_n$  is increased.

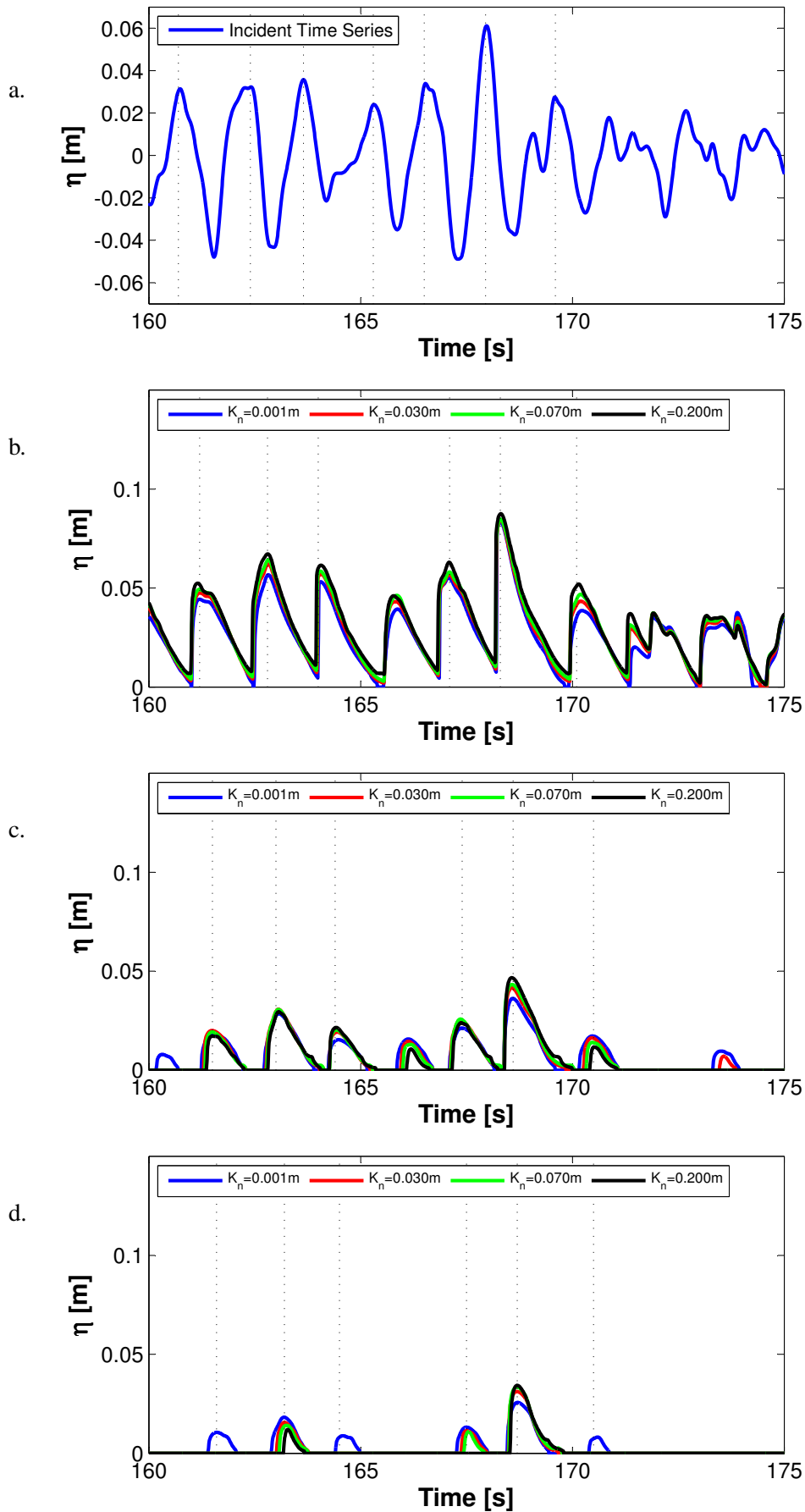


Figure 6.14: Water depth detected at various points in numerical domain of 1:4 slope for different surface roughness. a. Toe. b. Still water level. c. Front slope. d. Structure crest

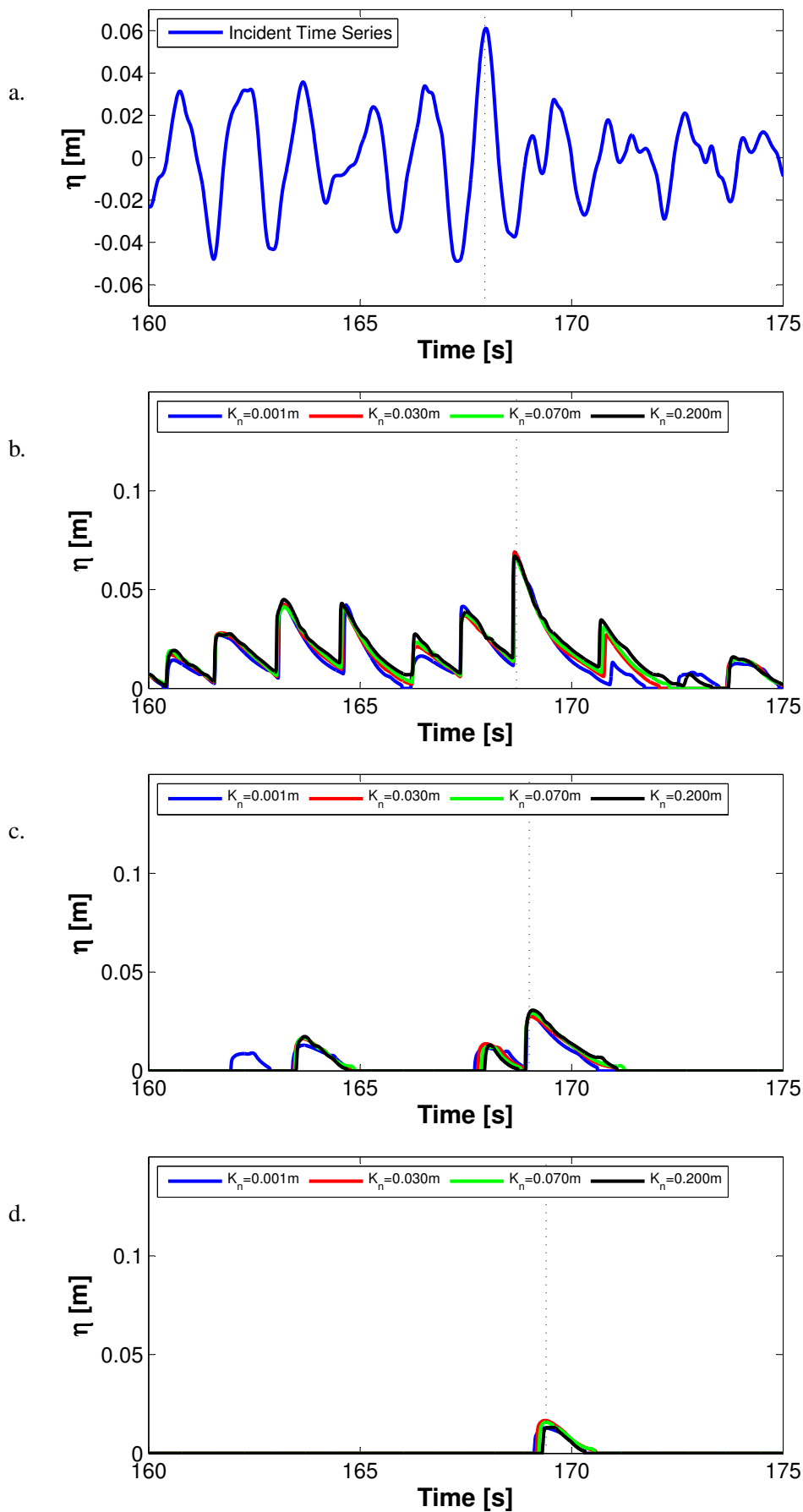


Figure 6.15: Water depth detected at various points in numerical domain of 1:7 slope for different surface roughness. a. Toe. b. Still water level. c. Front slope. d. Structure crest

### 6.5.2 Variability

As before, to first examine the variability due to the surface roughness, a scatter plot (See Fig. 6.16) has been produced showing the correlation between  $P_{ov}$  and  $q$ . The results are classified into three separate regions dependent on the slope of the structure in each test. It can be observed in this figure, that the roughness of the slope appears to have more influence on  $q$  than on  $P_{ov}$ , although this is less evident in the lower overtopping conditions.

This is in agreement with the results shown in the previous section, where although the variation in the magnitude of the larger events was small, due to the large numbers of events experiencing a decrease, there was a cumulative effect on the overall  $q$ . The number smaller events that no longer occur in the tests with higher values of  $K_n$  also decreases the value of  $q$ , but do not alter the value of  $P_{ov}$  as much, except in the lower overtopping where more smaller events were initially occurring, and subsequently removed.

In the shallower slope tests which experience lower overtopping, the individual volumes are generally smaller, so the loss of events here is more significant to the overall overtopping. This results in a larger variation in the value of  $q$  than for the steeper slopes.

Overall, the magnitude of the variation in the results, appears to be of a similar level to that which was previously observed in the other numerical tests.

### 6.5.3 Distributions

The distributions are now examined to see if the values of  $K_n$  have influenced their shape. Firstly the distributions of  $q$  are considered in Fig. 6.17. The four tests on the 1:4 slope are chosen as representative of the four different values of  $K_n$ . Due to the magnitude of the overtopping in these tests, only the Normal distribution has been compared. It appears from the graph, that as anticipated all of the distributions of  $q$  are well modelled by the Normal distribution.

The parameters of the theoretical distribution and the results of the K-S test are shown in Table 6.10. It is confirmed here that all of the empirical distributions for  $q$  can be modelled by the Normal distribution.

Fig. 6.18 compares the empirical distributions for  $P_{ov}$  with the Normal distribution. It can be seen here that all of the tests appear well modelled by this distribution. This is confirmed by the results of the K-S test shown in Table 6.11. The parameters of the theoretical distributions are also found in this table.

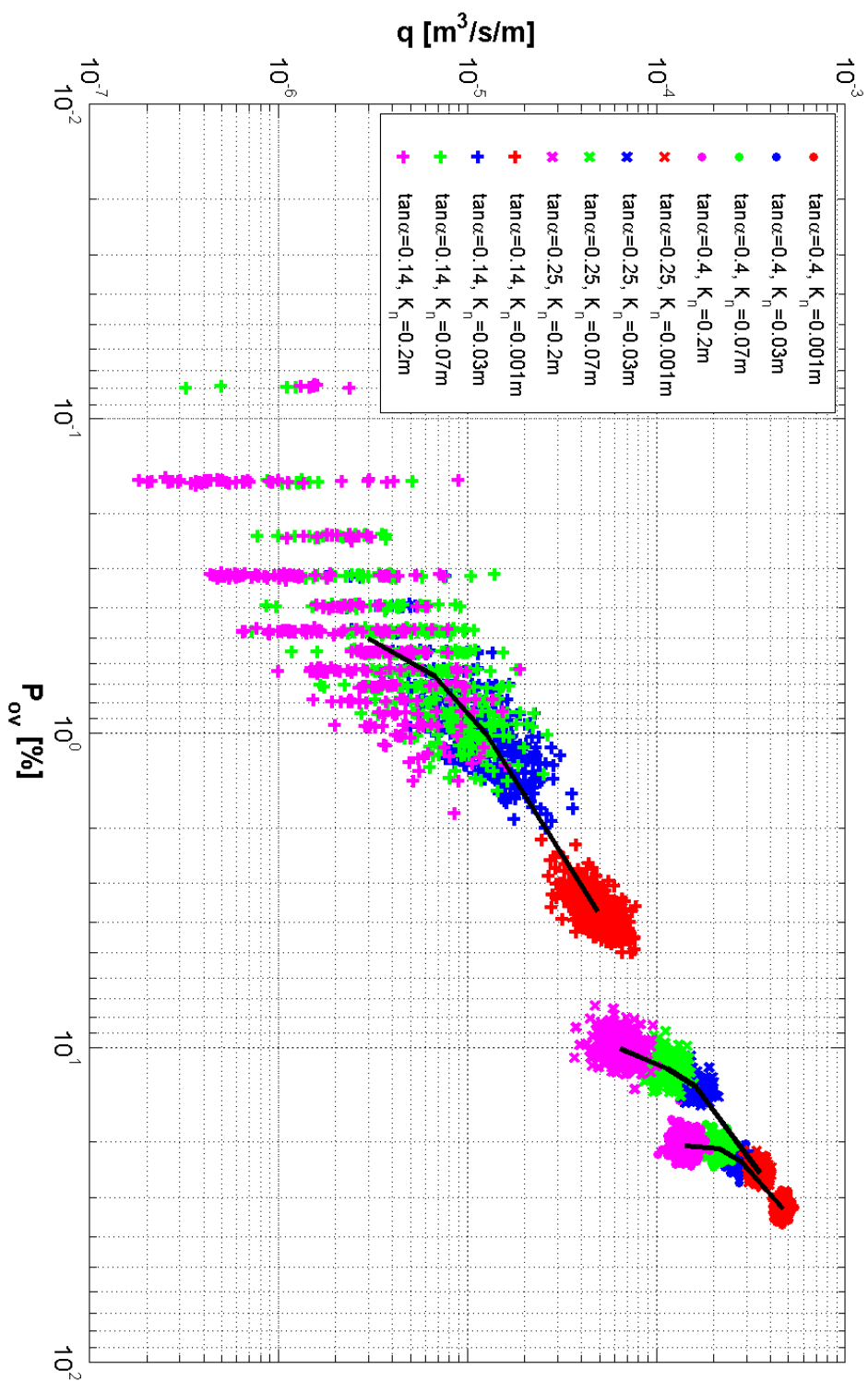


Figure 6. 16: Logarithmic scatter graph showing the correlation between  $P_{ov}$  and  $q$  for different slope angles and values of  $K_n$ .

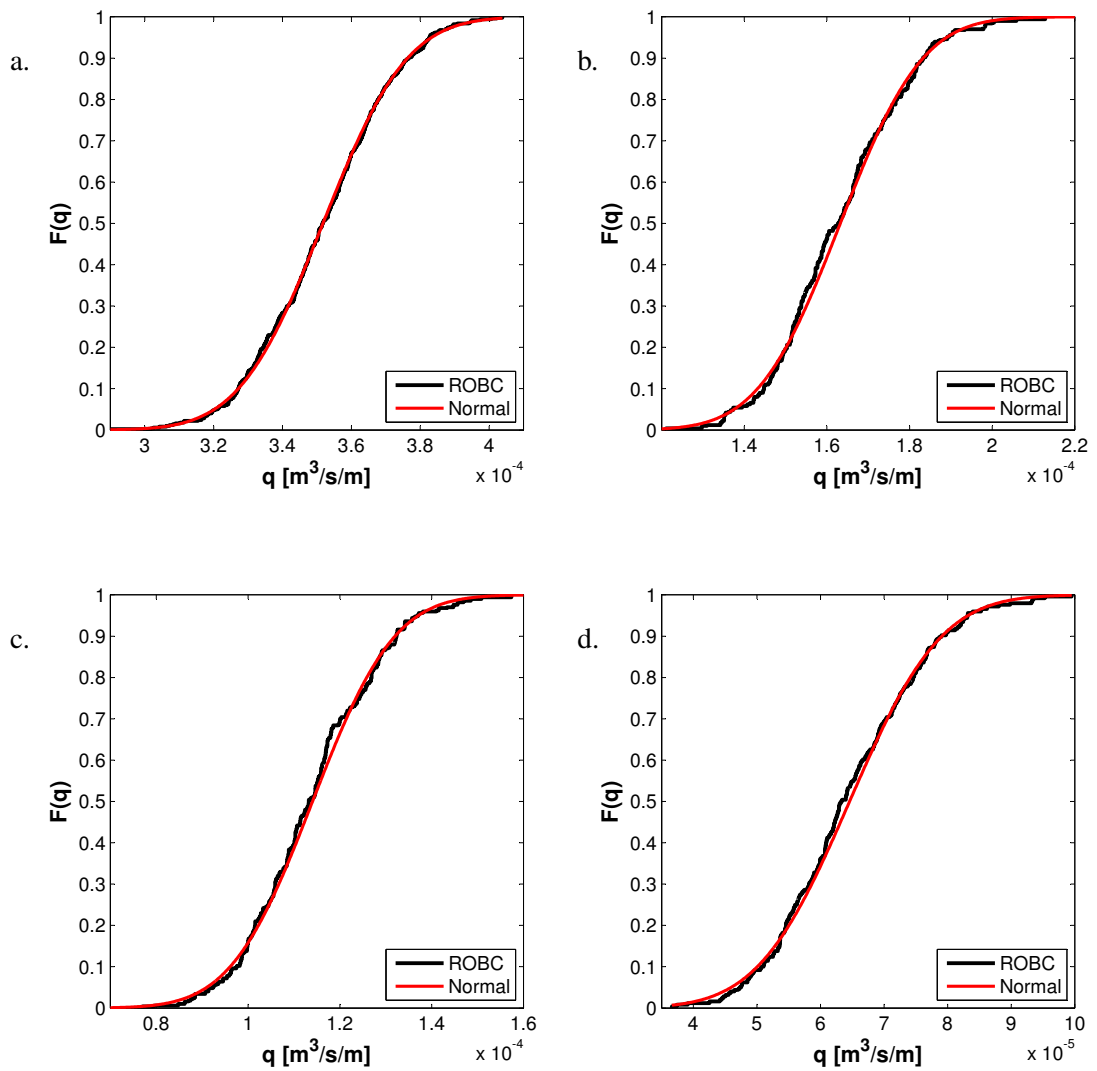


Figure 6.17: Empirical frequency curves for  $q$  from ROBC (black solid lines) compared with expected distributions for different levels of overtopping. a.  $K_n=0.001\text{m}$ . b.  $K_n=0.030\text{m}$ . c.  $K_n=0.070\text{m}$ . d.  $K_n=0.200\text{m}$ .

Table 6.10: Results of the one sample K-S test based on  $q$  for various values of  $K_n$

$K_n$	$q$			
	Normal		K-S	
	$\mu$	$\sigma$	$\Gamma$	$D_n$
0.001	3.53e-4	1.92e-5	0	0.0253
0.030	1.63e-4	1.56e-5	0	0.0521
0.070	1.14e-4	1.40e-5	0	0.0608
0.200	6.46e-5	1.33e-5	0	0.0505

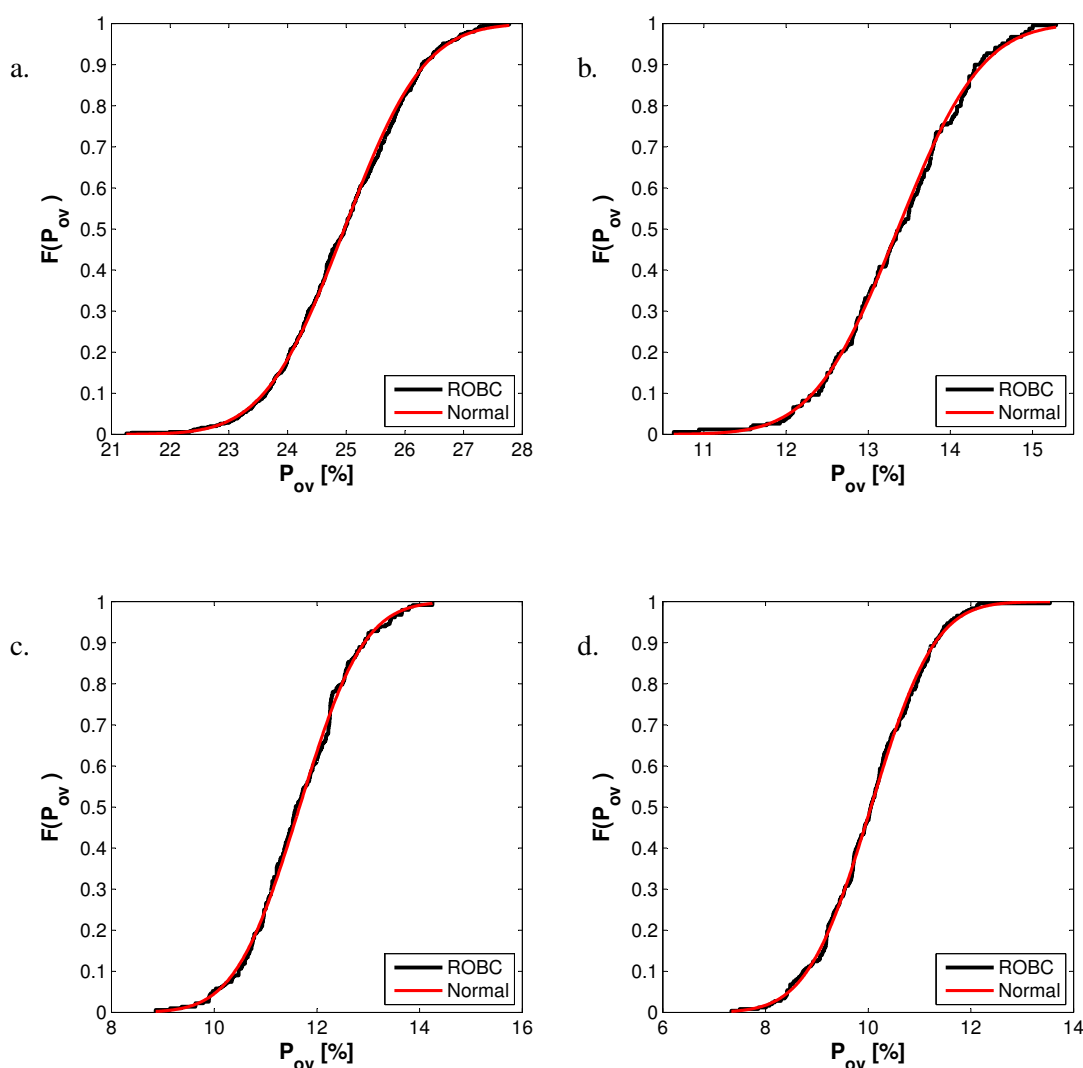


Figure 6.18: Empirical frequency curves for  $P_{ov}$  from ROBC (black solid lines) compared with expected distributions for different levels of overtopping. a.  $K_n=0.001\text{m}$ . b.  $K_n=0.030\text{m}$ . c.  $K_n=0.070\text{m}$ . d.  $K_n=0.200\text{m}$

The final overtopping parameter to consider here is  $V_{max}$ . The empirical distributions are shown in Fig. 6.19. As with  $q$ , due to the relatively high magnitude of the overtopping in all of the tests here, only a single theoretical distribution has been considered, in this case the GEV distribution.

The parameters of the theoretical distribution and the results of the K-S tests can be found in Table 6.12, which confirms the suitability of the GEV distribution for all of the values of  $K_n$ .

Overall, it appears that the value of  $K_n$  does not have a significant effect on the variability of the overtopping prediction other than the subsequent alteration to the magnitude of the overtopping.

Table 6.11: Results of the one sample K-S test based on  $P_{ov}$  for various values of  $K_n$ 

$K_n$	$P_{ov}$			
	Normal		K-S	
	$\mu$	$\sigma$	$\Gamma$	$D_n$
0.001	24.97	1.07	0	0.0272
0.030	13.36	0.81	0	0.0400
0.070	11.66	0.98	0	0.0366
0.200	10.05	0.97	0	0.0264

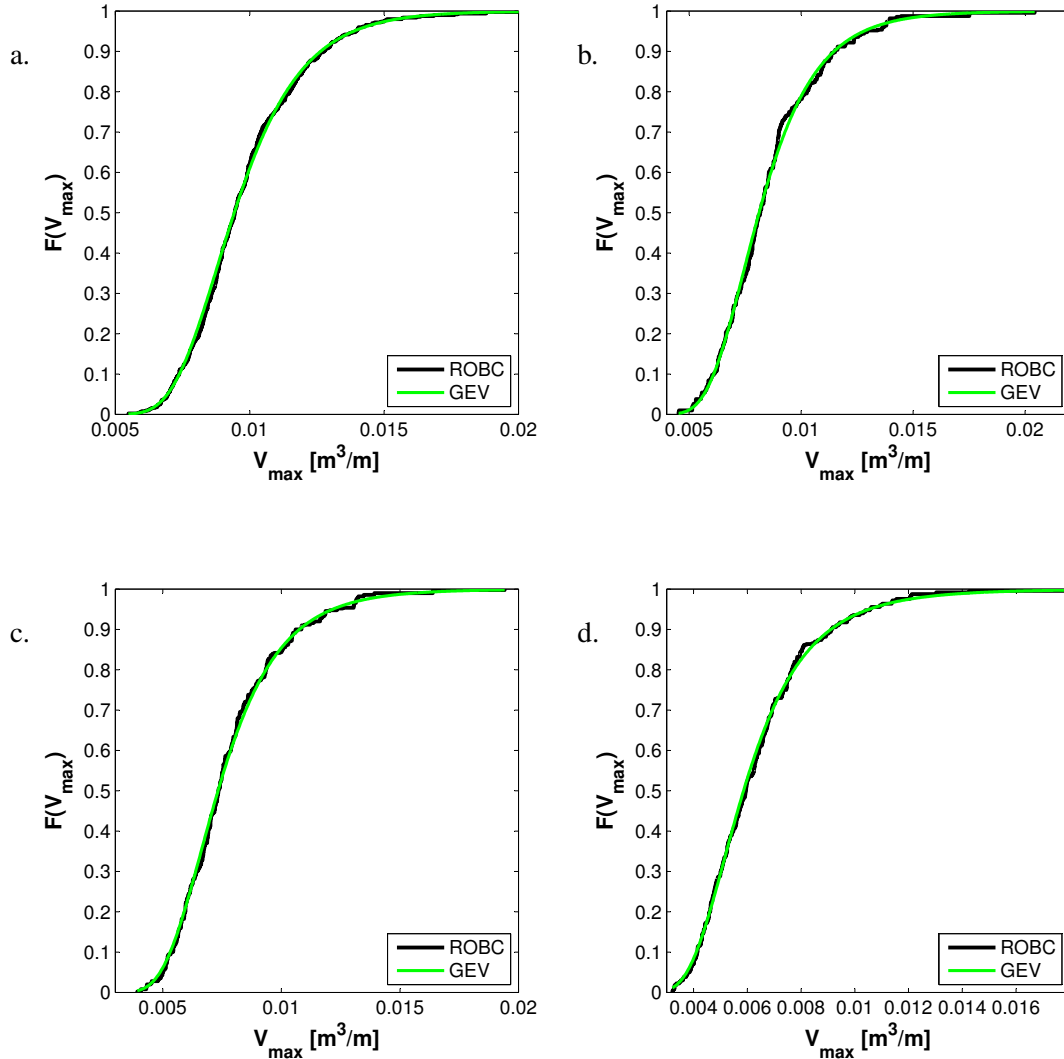

 Figure 6.19: Empirical frequency curves for  $V_{max}$  from ROBC (black solid lines) compared with expected distributions for different levels of overtopping. a.  $K_n=0.001$ m. b.  $K_n=0.030$ m. c.  $K_n=0.070$ m. d.  $K_n=0.200$ m.

 Table 6.12: Results of the one sample K-S test based on  $V_{max}$  for various values of  $K_n$ 

$K_n$	$V_{max}$				
	GEV			K-S	
	$\xi_x$	$\mu_x$	$\sigma_x$	$\Gamma$	$D_n$
0.001	9.89e-4	1.70e-3	8.83e-3	0	0.0318
0.030	3.14e-2	1.73e-3	7.50e-3	0	0.0460
0.070	5.11e-2	1.65e-3	6.72e-3	0	0.0344
0.200	0.11	1.50e-3	5.30e-3	0	0.0349

## 6.6 Summary

To generalise the initial findings with the numerical model, the influence of various structural and hydraulic parameters on the variability of ROBC tests has been investigated. Firstly, this involved looking at the effect of spectral shape by using a narrow banded and wide banded spectra. It was found that this had minimal effect on the variability of the overtopping parameters, with all distributions remaining the same.

The effect of the surf similarity parameter was then investigated. Again, this appeared to have no direct effect on the variability. An indirect effect was observed due to resulting increase or decrease in overtopping that occurred due to the change in conditions. The distributions of each of the overtopping parameters was again found to be the same as those observed earlier.

Finally, the effect of the surface roughness was investigated. Initially the direct effect this had on the overtopping phenomenon was examined. It was found that generally, increasing the surface roughness decreased the magnitude of overtopping events slightly which cumulatively had a larger effect of  $q$ , with a few of the smaller events being removed completely adding to this. This resulted in a larger reduction in the  $q$  than  $P_{ov}$ . As with the other tests, it was found that the distribution of the overtopping parameters were not directly effected by the increase in surface roughness other than the resulting decrease in the total overtopping.

Overall, the structural and hydraulic parameters do not appear to have a significant effect on the variability of the overtopping parameters, meaning that the conclusions found earlier in the work can be generalised for other conditions.

## **Chapter 7**

# **Uncertainty in Physical Modelling**

### **7.1 Introduction**

When discussing the accuracy of the MOBC and average ROBC in predicting the overtopping from the initial experiments, it was observed that the MOBC generally provided better results. However, it was also acknowledged that only one test was run for each of the wave conditions and that the experiments may be subject to the same uncertainty due to the exact time series of each test. This means that potentially the physical experiments could have been on the extremes of the distribution, and hence not well modelled by the average of the ROBC tests. The purpose of this next chapter is to examine whether this uncertainty is present in physical modelling.

### **7.2 Experimental set-up**

This time the experiments were carried out in the wave flume at the University of Nottingham. The flume is approximately 16m long and 0.23m wide with an operating depth of up to 0.22m, as shown in Fig. 7.1. The waves are generated using an absorbing piston type wave generator similar to that used previously. The bottom of the flume is flat along the entire length.

The intention of these experiments was to make them as similar as possible to those carried out at HR Wallingford, given the facilities available. The first major difference was the scale of the experiments, due to the smaller equipment, the scale had to be decreased to 1:50. An additional issue was the flat bottom in the new flume, which would have resulting in little wave transformation between the paddle and the structure. This was rectified by the construction of a foreshore out of stainless steel. This foreshore was 4 metres long in total, with a steeper 1m

Table 7.1: Incident wave conditions prescribed at the paddle for the JONSWAP spectra random wave laboratory tests

Test	$H_{m0}$ (m)	$T_{m-1,0}$ (s)	$T_p$ (m)	$d_p$ (-)	$H_{m0}/d_p$ (-)	$s_{m-1,0}$ (-)	$R_c/H_{m0}$ (-)
TS01.SS	0.06	0.92	1.01	0.22	0.27	0.045	1.00
TS02.SS	0.04	0.78	0.86	0.22	0.18	0.042	1.50
TS03.SS	0.03	0.64	0.70	0.22	0.14	0.047	2.00
TS05.SS	0.05	0.85	0.93	0.22	0.22	0.044	1.20
TS01.VW	0.06	0.92	1.01	0.22	0.27	0.045	1.00
TS02.VW	0.04	0.78	0.86	0.22	0.18	0.042	1.50
TS05.VW	0.05	0.85	0.70	0.22	0.22	0.044	1.20
TS07.VW	0.05	1.13	1.24	0.22	0.22	0.025	1.20

section, followed by a 3m section with a gradient of 1:50. This foreshore then met the toe of structures. In this case, two different structures were tested. Firstly a impermeable smooth slope with a gradient of 1:2.55, that was an exact scaled down version of the slope previously used, except constructed from stainless steel. The second structure was a vertical wall with the same crest height as the smooth slope. The full set-up of both experiments is shown in Fig. 7.1. Photographs showing the structures *in situ* are also shown in Fig. 7.2.

### 7.2.1 Wave Conditions

A summary of the wave conditions that were prescribed at the paddle for these tests are shown in Table 7.1. Here  $H_{m0}$  is the spectral significant wave height,  $T_{m-1,0}$  is the mean spectral period,  $T_p$  is the peak period,  $d_p$  is the water depth at the paddle and  $R_c/H_{m0}$  is the relative freeboard. Also, SS denotes those tests carried out on the Smooth Slope structure, whilst VW denotes those using the Vertical Wall structure.

To be able to examine the variability of each wave condition, a large number of tests was required. In each test, the seeding was altered to produce a different wave time series. The random number sequence used in the random wave generation of the paddle is a pseudo random sequence. This means it is repeatable if the same initial seed is used. In the software to control the paddle in the flume, the initial seed value must be a positive integer between 0 and 2,147,483,647. To obtain the initial seed values, a random number generator was used to choose values within this range.

In the numerical results, it was decided to run 500 tests of each wave condition, but due to the length of time the physical model takes to run this was not possible. It was therefore decided

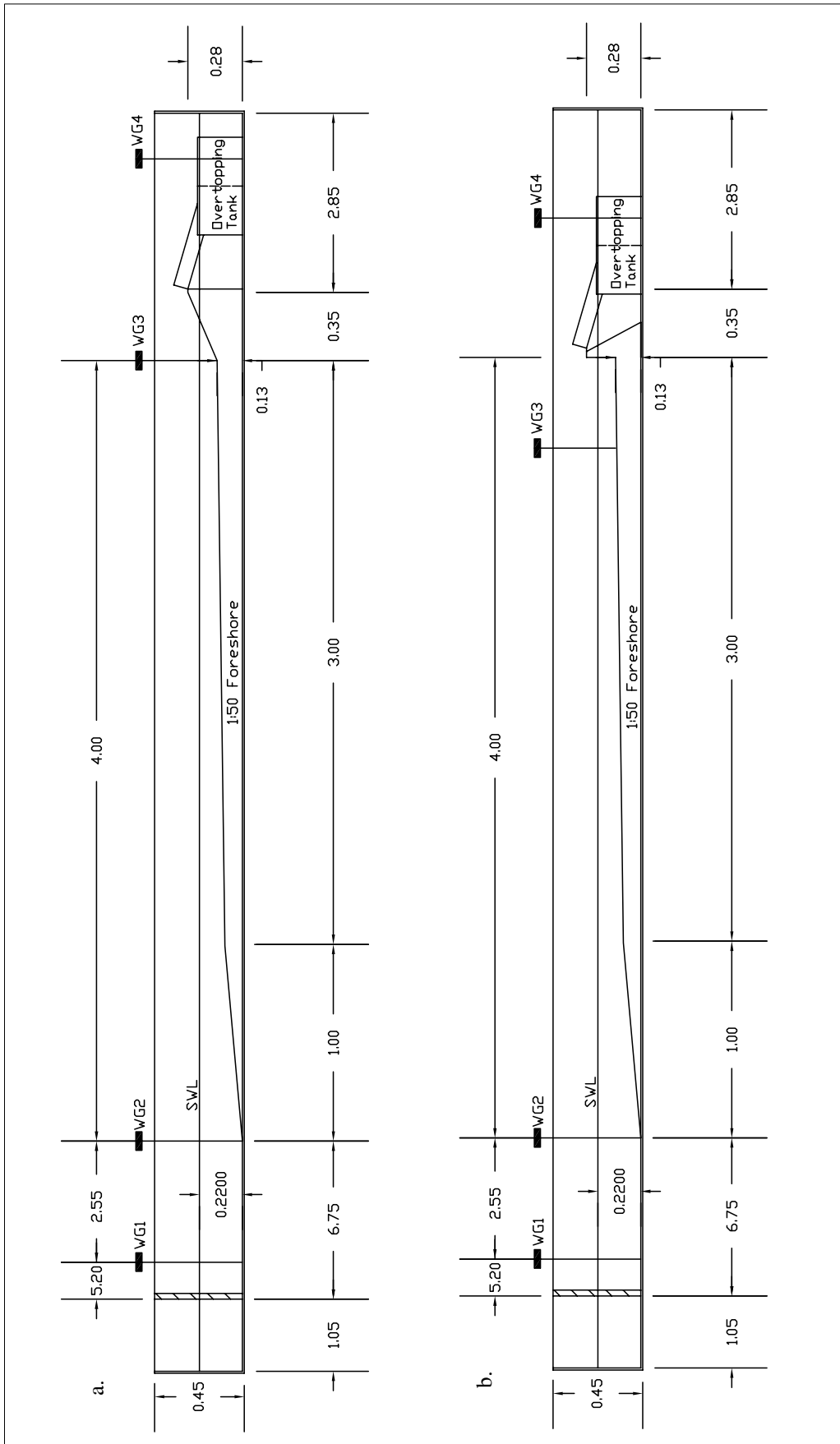


Figure 7.1: a. Layout of the physical model with smooth sloped structure. b. Layout of the physical model with vertical wall structure

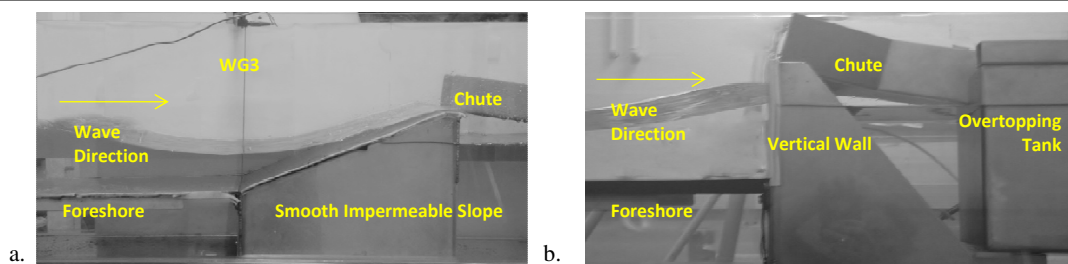


Figure 7.2: Photographs of University of Nottingham experimental set-up. a. Smooth Impermeable Slope. b. Vertical Wall.

that 100 different time series would be generated for each wave condition, as this was previously found to be a suitable number for establishing the variability in  $q$  in the numerical model. This means that in total, 800 physical model tests were conducted.

In addition, it has previously been observed that repeatability of two nominally identical flume experiments may only be within 25% (McCabe et al., 2013). It was therefore also important to carry out a number of experiments repeating the same seeding to examine this issue. This meant for each wave condition, an additional 20 runs were carried out, resulting in a further 160 tests.

## 7.2.2 Measurement

As before, the water free surface ( $\eta$ ) was measured at various points along the flume, this time using three wave gauges ( $WG1 - 3$ , see Fig. 7.1 for their positions) including one at the toe of the structure ( $WG3$ ) during the smooth sloped experiments, which was repositioned approximately 0.20m away from the structure toe for the vertical wall experiments.

Again the wave gauges used were resistance type wave gauges, and due to the sensitivity of these they were calibrated twice everyday, once in the morning, and once in the afternoon.

The incident wave conditions were retrieved by running the wave conditions in the empty flume, so that there was no reflection from the structure. During these tests, the foreshore remained in the flume, and a porous beach was placed at the end of the flume to absorb the waves, as active absorption wasn't used. During the overtopping tests, the paddle was operated with active absorption to absorb any reflected waves present.

A summary of the incident wave conditions measured at the location of the toe of the structure is shown in Table 7.2. As the structures were not in place, the results are the same for both sets of tests. Here  $H_{m0}$  is the measured spectral significant wave height,  $H_{m0}/d_t$  is the local wave height to local water depth ratio, where  $d_t$  is the water depth at the structure toe and  $R_c/H_{m0}$  is relative freeboard, where  $R_c$  is the structure freeboard.

Table 7.2: Incident wave conditions measured at the toe for the JONSWAP spectra random wave laboratory tests

Test	$H_{m0}$ (m)	$T_{m-1,0}$ (s)	$R_c$ (m)	$d_t$ (m)	$H_{m0}/d_t$ (-)	$R_c/H_{m0}$ (-)
TS01	0.043	0.98	0.06	0.09	0.48	1.40
TS02	0.032	0.78	0.06	0.09	0.36	1.88
TS03	0.020	0.77	0.06	0.09	0.22	3.00
TS05	0.038	0.89	0.06	0.09	0.42	1.58
TS07	0.040	1.33	0.06	0.09	0.44	1.50

The standard procedure used for measuring overtopping volumes that was used in the HR Wallingford experiments, was also implemented here. In this case, only a single chute could be placed on the crest of the structures each time. The water that entered the chute could then flow into a single overtopping tank situated at a distance behind the structure. The tank was constructed in a similar manner to those used previously, with the false wall to dampen oscillations. Again, a gauge (*WG4*) was placed in the rear section of the overtopping tank to detect the change in water depth. The width of chute and size of the tank was again altered depending on the expected level of overtopping.

Due to the smaller scale used for these experiments, it was decided to mainly concentrate on the overtopping discharge. This was because of the difficulty in identifying the individual overtopping volumes from the measured time series at this scale, however the other overtopping parameters have been investigated in terms of variability later in this chapter.

### 7.3 Influence of Laboratory Effects

To accurately quantify the uncertainty in the physical model results due to the different seeding of the time series, it is important to consider the other sources of uncertainty present.

#### 7.3.1 Wave Height Distribution

Earlier in this work, the sources of laboratory effects during physical modelling were highlighted. The first one of these was the generation of unwanted non-linear effects due to the mechanical method of wave generation. This will now be investigated in these experiments. Firstly, it is important to classify the relative depth of the different conditions at the wave paddle to establish if non-linear effects are expected. The relative depths in each of the wave conditions are given in Table 7.3. It can be seen that all of the tests are clarified as intermediate depth at

Table 7.3: Relative depths at the paddle

Test	Relative Depth (-)
TS01	0.14
TS02	0.19
TS03	0.28
TS05	0.16
TS07	0.09

the paddle, with *TS07* being the closest to the shallow water conditions.

The distribution of wave heights being produced by the paddle that are analysed here, are those from the incident wave tests. When the active absorption is employed during the overtopping tests, the resultant wave height distribution should be the same. The paddle itself is equipped with a wave gauge on the front, to give an accurate measurement of the wave heights produced. A zero-crossing analysis was carried out on this data to obtain the full series of wave heights.

In Fig. 7.3 the distribution of the wave heights for all the incident wave conditions are considered. As previously with the numerical model, the wave heights have been normalised with the mean wave height of each sample. Also included in this figure is the predicted Rayleigh distribution of wave heights for deep water. Firstly, the waves in *TS01* are considered in the top left plot. It can be seen here that although the conditions present are intermediate, the measured wave heights follow the Rayleigh distribution reasonably well. Surprisingly, in fact if anything they are slightly under-predicted.

In the top right plot, the distribution of the wave heights for *TS02* are considered. Here the relative depth is slightly further away from the shallow water condition than the previous test. This is demonstrated clearly in the results with the measured wave heights closely matching the prediction of the Rayleigh distribution this time.

In the middle left plot, the distribution of the wave heights for *TS03* are considered. This test is the furthest away from shallow water conditions of all of the tests conducted, however, it is still classified as intermediate depth rather than deep water. Again, generally the results from the experiments match fairly closely the Rayleigh distribution, although there is some variation in the highest wave heights. Although these conditions are the closest to deep water, they are also the steepest waves tested and it is possible this deviation is caused by some wave breaking at the paddle.

In the middle right plot, the distribution of wave heights for *TS05* are considered. This test shows the largest variation of the measured wave heights from the Rayleigh distribution predic-

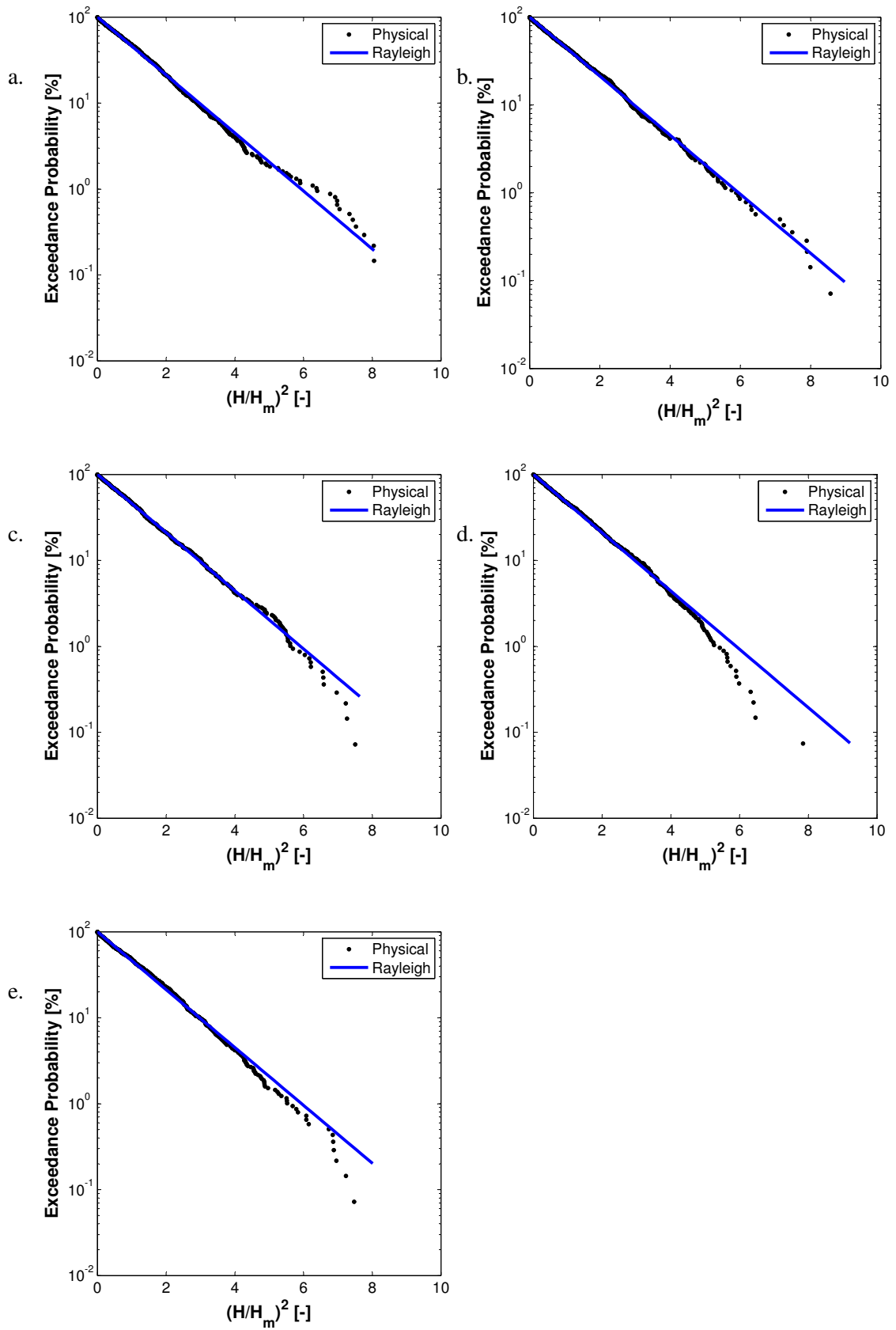


Figure 7.3: Distributions of the measured incident wave heights at paddle compared with expected Rayleigh distributions. a. TS01. b. TS02. c. TS03. d. TS05. e. TS07.

tion, although it is not the shallowest condition tested. As previously observed, the smaller wave heights are well modelled by the Rayleigh distribution with only the larger ones being smaller than predicted. Again, this is likely to be caused by the occurrence of some wave breaking at the paddle.

Finally, the plot in the bottom left shows the distribution of wave heights for *TS07*. This test is the most depth-limited of all the conditions tested. The results show a fairly good match with the Rayleigh distribution, although some of the larger waves are less than the prediction, again suggesting that some breaking is occurring at the paddle caused by the shallow water depth present.

Overall, the wave paddle appears to be doing a reasonable job of producing the appropriate wave height distribution. It is observed that all of the tests show distributions that are fairly similar to the Rayleigh distribution, and the slight variation from this is likely caused by the intermediate depth present rather than any additional unwanted non-linear effects.

### 7.3.2 Presence of Long Waves

One of the most common laboratory effects that can affect the performance of physical model experiments is the reflection of wave energy from boundaries or structures, and dealing with this wave reflection is an important aspect of laboratory experiments. The wave generator used here had the capability to absorb this type of energy that might form in the flume. However, as it is known that overtopping is sensitive to long wave energy, it is therefore important to investigate if there is any long wave activity due to the resonance of certain frequencies. The natural frequencies of the wave flume were therefore calculated using Eq. 7.1, and included in Table 7.4.

$$T = \frac{2L}{\sqrt{gd}} \quad (7.1)$$

where  $T$  is the longest natural period,  $L$  is the wavelength,  $g$  is the gravitational acceleration and  $d$  is the depth of the water in the flume. The longest natural period of this wave is the period associated with the fundamental resonance of the water in the flume corresponding to the longest standing wave. The period of the second harmonic will be half the natural period, the period of the third harmonic will be a third of the natural period, and so forth.

To investigate this issue, the spectra will be calculated from the wave measurements at each of the wave gauges for each of the test conditions. For each condition, all 100 time series have

Table 7.4: Natural Periods of the Experimental Setup

Harmonic	Period (s)	Frequency (Hz)
1st	16.0	0.0625
2nd	8.0	0.1250
3rd	4.0	0.2500
4th	2.0	0.5000

been analysed, and then an average spectra obtained. Firstly, the results based on the smooth slope tests are considered in Fig. 7.4. For each test condition, the spectra from the three wave gauges have been plotted.

In all of the smooth slope test conditions it can be observed that the offshore spectra and the one located at the toe of the foreshore are very similar. This is expected as both gauges are at the same water depth due to the flat bottom present in the flume. In all the test conditions, no additional energy is observed at either lower or higher frequencies at these gauges.

In TS01.SS, it is clear that at the toe of the structure the spectra has undergone a transformation. The main peak of the spectra still occurs at  $f_p$ , but an additional peak also appears at  $2f_p$ . This is expected due to the influence of triad interactions in the shallow water present at the structure toe. It is known that energy spectra of shoaling waves often show the appearance of harmonics of the spectral peak (Young and Eldeberky, 1998).

A third peak can also be observed in the spectra, at a frequency of 0.1250Hz. As this corresponds to the 2<sup>nd</sup> harmonic of the flume, it is assumed that this energy is caused by the presence of a long wave that has formed in the flume. For this particular condition this accounts for nearly 20% of the energy present, and therefore could be an influence on the variability of the overtopping. It is also observed that there is energy present at 0Hz, this would suggest the presence of an infinitely long wave, which is not possible in the wave flume, so it is anticipated that this energy is erroneously caused by the decrease in the water level throughout the tests.

For TS02.SS, the spectra at the structure toe, again undergoes a transformation, with the spectra peak still occurring at  $f_p$ , and a second peak occurring at  $2f_p$ . This time the second peak is smaller than previously, due to the slightly less shallow water conditions present in this test. Again in this test, a third peak is observed in the spectra and this occurs around the 2<sup>nd</sup> and 3<sup>rd</sup> harmonics of the flume. This time the energy present here equates to approximately 4% of the total energy present. This suggests that a long wave is still present in the flume although is smaller than previously measured.

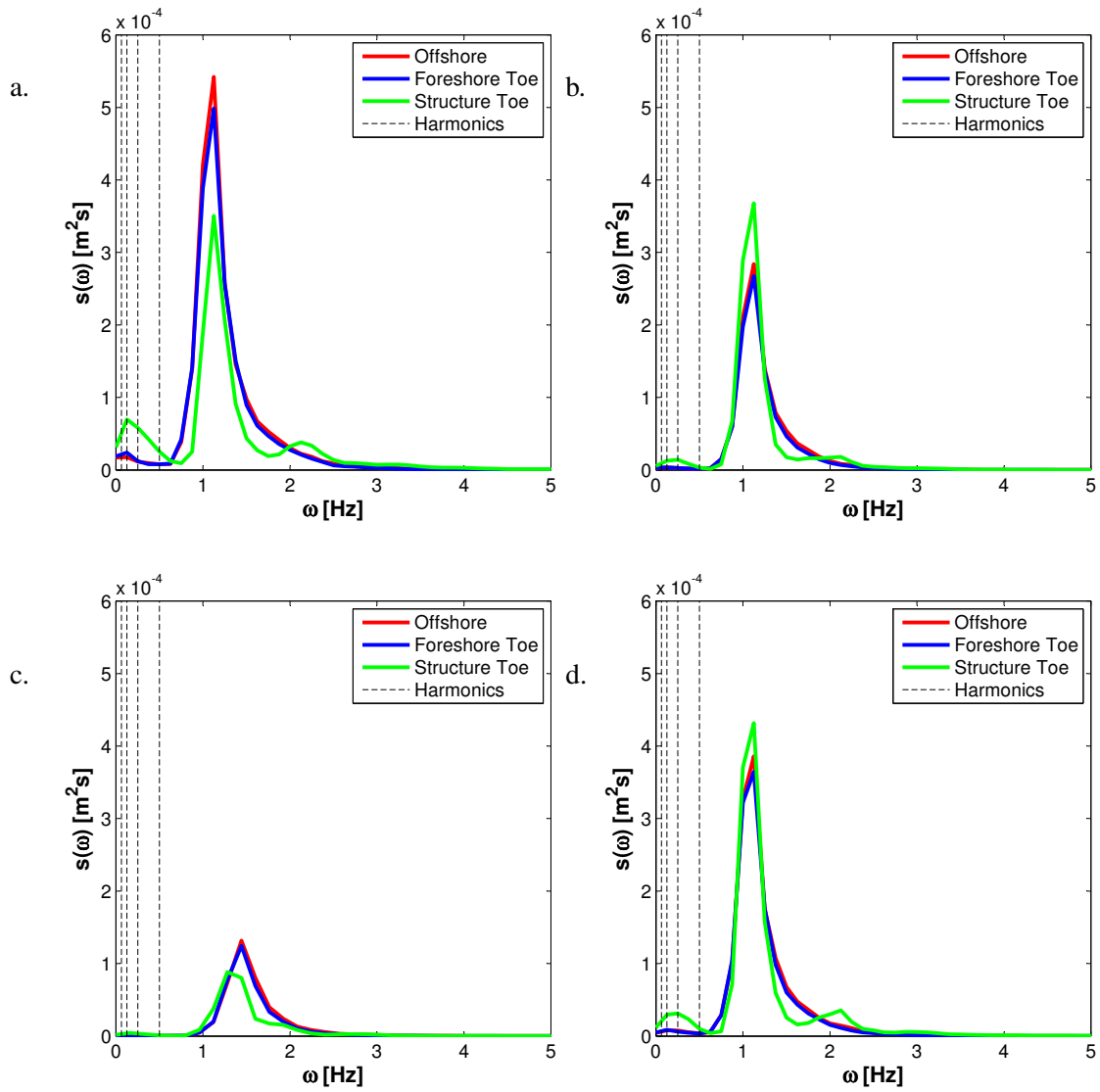


Figure 7.4: Measured spectra at different locations in the wave flume for smooth slope tests. a. TS01. b. TS02. c. TS03. d. TS05

In TS03.SS, the spectra at the toe of the structure appears to undergo less transformation than observed previously, this is due to the smaller wave heights present resulting in the least shallow water conditions tested. A slight peak can still be observed at  $2f_p$  in this test. A small peak is also observed around the 2<sup>nd</sup> harmonic of the flume. Similarly to the last test, it is equivalent to only about 4% of the total energy present.

Finally, TS05.SS is considered. The spectra at the toe also undergoes the expected transformation, and the additional peak at  $2f_p$  can be clearly observed here. A peak is also observed between the 2<sup>nd</sup> and 3<sup>rd</sup> harmonics of the flume due to long waves forming, although this again only equates to approximately 7% of the total energy present. It is also observed that a small amount of energy is present at 0Hz, as acknowledged earlier this is due to the decrease in water depth throughout the test. This is only really noticeable on TS01.SS and TS05.SS where the quantity of overtopping is quite large, resulting in a significant amount of water being removed from the flume into the overtopping tank.

Now to consider the tests with the vertical wall in place. Due to the nature of this type of structure it wasn't possible to place a wave gauge right at the structure toe, instead it is placed approximately 200mm from the structure. As before, all 100 time series have been analysed, and then an average spectra at each of the three wave gauges have been obtained. The results of all the vertical wall tests is shown in Fig. 7.5.

As observed in the smooth slope tests, the spectra offshore and at the foreshore toe remain very similar in all of the vertical wall test conditions, with little additional energy at frequencies other than the peak frequency.

The first condition examined is that of TS01.VW, the spectrum closest to the toe shows a lot more transformation than previously observed. The main peak remains at  $f_p$ , and a small peak can be seen at  $2f_p$  as before. However, there are a couple of additional peaks, one just before the main peak and one just afterwards. It is expected that these are present due to the large amount of reflected waves so close to the vertical wall. In addition, a final peak can be observed at around the 1<sup>st</sup> and 2<sup>nd</sup> harmonics of the flume. This equates to around 6% of the total energy present. Also, consistent with the previous high overtopping tests, energy is found at 0Hz due to the decrease in water level throughout the tests.

For TS02.VW, the spectrum at the toe of the structure shows a narrower peak at  $f_p$ , and then a small secondary peak at  $2f_p$ . A third peak is situated between these two, which is again likely caused by the reflected waves. This test shows very little energy (< 1%) at the harmonics of the

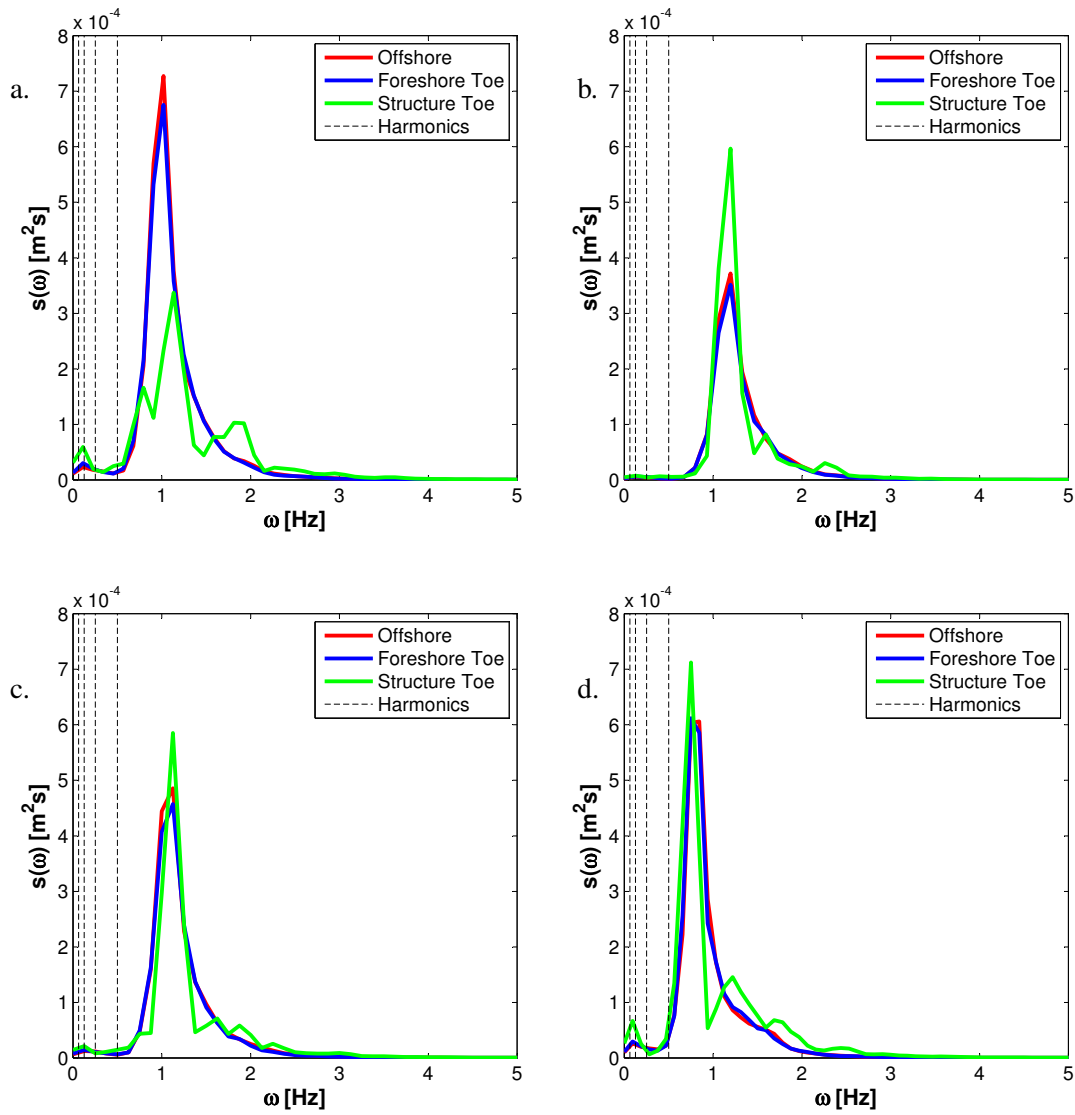


Figure 7.5: Measured spectra at different locations in the wave flume for vertical wall tests. a. TS01. b. TS02. c. TS05. d. TS07

flume suggesting that long waves were not an issue for these conditions.

TS05.VW behaves in a similar way to the previous test with the structure toe spectra showing a narrower peak at  $f_p$ , with a small secondary peak at  $2f_p$ . Again there are some additional peaks caused by the reflected waves. In this test a small amount of energy can be seen around the 1<sup>st</sup> and 2<sup>nd</sup> harmonics, which equates to approximately 1% of the total energy present.

Finally, for TS07.VW the spectra at the structure toe again shows a slightly narrow peak at  $f_p$  with the secondary peak at  $2f_p$ . An additional peak is also seen due to the reflected waves. A small peak is also seen around the 1<sup>st</sup> and 2<sup>nd</sup> harmonics of the flume. This is approximately 3% of the total energy in this test. It can also be seen that the issue of the drop in water level is present here, with energy appearing at 0Hz.

Overall, the results suggest that the active absorption is effective in the tests. This is observed in the wave spectra measurements at the offshore locations which do not show any energy at additional frequencies. It is also clear that the presence of long waves is less in the smaller wave heights. The effect that these long waves have on the variability in overtopping will be examined in the tests where the same seeding is considered, as according to the results, these long waves form in all the tests for each condition.

## **7.4 Tests with Same Seeding**

McCabe et al. (2013) observed considerable variation in experimental results. They found that even when repeating the exact same test, a 25% variation could be observed in the cumulative overtopping volumes. This was attributed to the sensitivity of overtopping to very small changes in conditions. To be able to quantify the variation due to the offshore boundary condition, the sensitivity of the physical model to minor condition changes must first be examined.

### **7.4.1 Still Water Level Control**

The main influence on the repeatability of the experiments was the control of the still water level. Due to the small scale used in these experiments, even tiny differences in the water level at the beginning of a test can significantly effect the overtopping quantities. It was therefore important to maintain an accurate still water level throughout the experiments.

During the experiments there was a small loss of water within the flume over a period of time. This was due to leaking at joints in the flume, and evaporation. These issues made it very dif-

difficult to maintain a constant level at the start of each test, so a methodology was developed to minimise the problem.

Firstly, a manual point gauge was placed on the wave flume to establish an initial water level. This consisted of a small point which is manually adjusted to touch the water surface and then a reading is taken using a graduated scale. This measurement was then recorded to ensure that subsequent tests produced the same reading when measuring the water surface.

At the start of each test, if the point gauge was not touching the water surface then water would be added to the flume, until this was achieved. The water was then allowed to settle completely to confirm this was successful. At this point, the wave gauges were used to measure the water surface for approximately 20 seconds, to establish the baseline for that set of tests.

A test was then carried out which had known overtopping, i.e. it had the same time series and wave conditions as a test previously carried out. The measurements from this new test were then compared with those obtained previously. If the new test produced an overtopping depth measured in the tank using the electronic wave gauge within 0.5mm of the previous one, then it was concluded that the water level was correct in the flume.

The water that entered the overtopping tank during the test would then be returned to the main flume. The point gauge was again placed on the flume to get the water level. Once the water had settled down, the electronic wave gauges were used to measure the water surface again. These results were then compared with the original measurements at the start of that particular testing regime. If the results produced a variation in the water level of more than 0.5mm then the test could not be run. Water was either added or removed from the flume until a variation of less than 0.5mm was achieved.

#### **7.4.2 Overtopping Measurement**

To examine the issue of the repeatability of the experiments, a number of tests were carried out with exactly the same wave conditions and wave time series generated at the paddle. As mentioned earlier, this could be achieved by using the same initial seed number, which was randomly chosen from the selection of seeding values for each test. In total, for each condition, 20 repeat tests were carried out, this does not include those tests that were repeated to ensure the initial still water level. The overtopping discharge was then calculated for each test, with the results plotted as dimensionless parameters in Fig. 7.6.

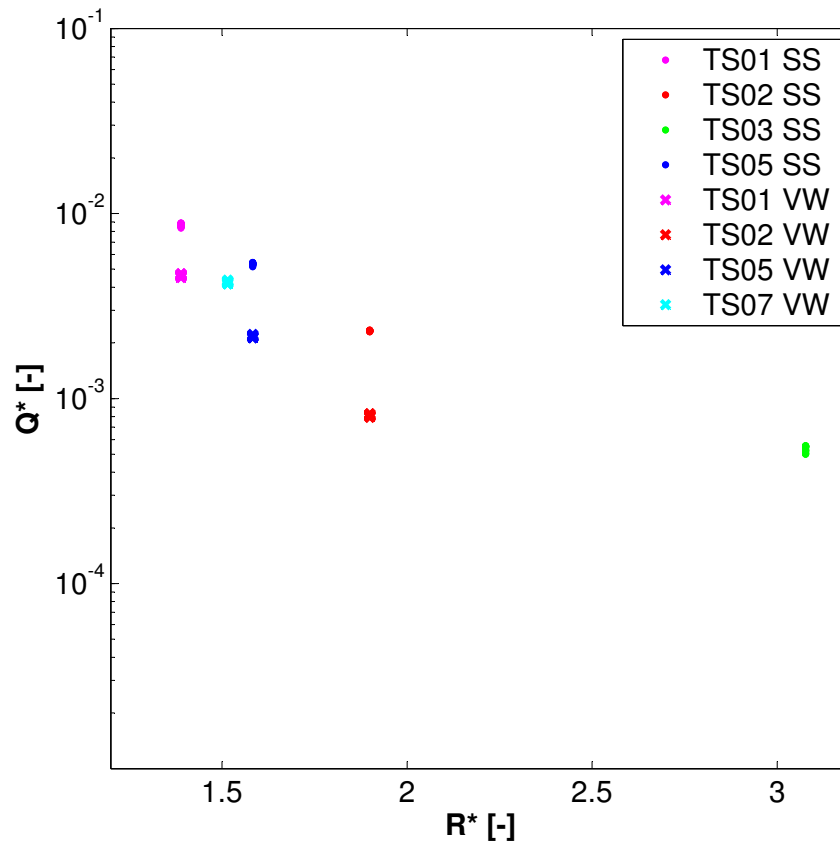


Figure 7.6: Graph showing  $R^*$  plotted against  $Q^*$  for tests with the same offshore wave time series for each condition

It can be observed here that there is some variation present in the identical test runs, which appears to be fairly consistent throughout the different levels of overtopping. This is quantified by considering the percentage variation in each of the test conditions, with the results shown in Table 7.5.

It can clearly be seen here that these results show a lot less variation than those mentioned in McCabe et al. (2013), where as much as 25% variation was observed. At this scale, this level of variation is the equivalent to differences of less than a few millimetres in the depth detected

Table 7.5: Percentage variation in  $Q^*$  for same seeding tests

Test	Variation (%)
TS01.SS	< 7.0
TS02.SS	< 3.0
TS03.SS	< 10.0
TS05.SS	< 6.0
TS01.VW	< 6.0
TS02.VW	< 5.0
TS05.VW	< 5.0
TS07.VW	< 5.0

Table 7.6: Percentage variation in  $H_{m0}$  for same seeding tests

Test	Variation (%)
TS01.SS	< 2.0
TS02.SS	< 4.0
TS03.SS	< 6.0
TS05.SS	< 2.0
TS01.VW	< 2.0
TS02.VW	< 2.0
TS05.VW	< 2.0
TS07.VW	< 2.0

in the tank. It is quite possible that this variation is caused by inaccuracies in the measurement technique. Although the wave gauges were calibrated twice a day, it is still possible for this to vary during the experiments, and is very difficult to remove the effect completely.

Overall, it appears that when the methodology for ensuring the still water level at the beginning of each test is followed, the variation due these laboratory effects is minimal.

### 7.4.3 Wave Heights

It has been observed that a small variation in the overtopping for the same seeding is present. It is important to investigate if this could be caused directly by a variation in the wave heights produced by the paddle. The spectral wave height measured at the offshore wave gauge has been calculated for each of the same seeding tests. The variation across the tests has then been calculated and can be found in Table 7.6.

It is clear from this table that the variation in measured wave heights is less than that observed in the overtopping discharge. This is further confirmed in Fig. 7.7 which compares the relative error in the results for both parameters. This suggests that slight variations in the wave height produced are not the only factor influencing the variation in the overtopping discharge. This suggests that the water depth is an influencing factor, and hence it is important to follow the procedure for ensuring this remains constant between tests.

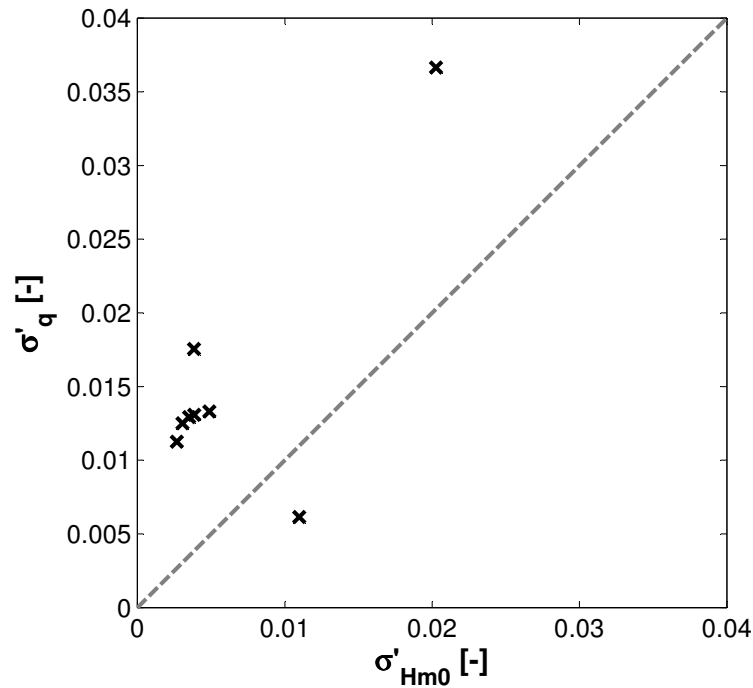


Figure 7.7: Comparison of Relative error of  $H_{m0}$  versus  $q$  for same seeding tests. Grey dashed line represents the perfect fit.

## 7.5 Tests with Different Seeding

### 7.5.1 Overtopping Time Series

As with the ROBC tests, the measured time series of overtopping have been plotted. In this case, instead of randomly selecting 15 runs, all of the experimental time series are plotted after they have been filtered. The filtering allows more clarity of the variation in these results. These can be found in Fig. 7.8 for the smooth sloped tests, with the extremes plotted in black. It should also be noted, that these have been plotted in terms of depth change in the tank rather than volume per metre, so are dependant on the both the size of the chute used and the size of the overtopping tank used in each condition.

In the top graph, which shows the highest level of overtopping in these experiments, the total depth of overtopping ranged from 0.128m and 0.090m over all of the runs. This is equivalent to a variability of a factor of approximately 1.4 in the results.

The second graph shows one of the moderate levels of overtopping. This time the total depth ranged from 0.068m and 0.042m across all of the runs which equates to a variation of a factor of approximately 1.7 in the results, only slightly higher than that observed in the highest overtopping level.

The third graph shows the lowest level of overtopping recorded in all of the experimental re-

sults. As anticipated, this shows the largest variability of all of the tests. The overtopping depth ranged from 0.005m and 0.001m, resulting in a variability of a factor of 4.5.

The final graph here shows the second highest level of overtopping for the smooth slope. The depth here varies between 0.078m and 0.051m, which produces a variability of a factor of 1.5.

Overall, the variability in these results are of a similar magnitude to those observed in the highest overtopping in the ROBC tests carried out earlier in this work. The lowest overtopping shows slightly more variability but still lower than that observed in the ROBC tests for the low and moderate levels of overtopping. Now the time series of overtopping for the vertical wall experiments are compared in Fig. 7.9. The top graph shows the highest level of overtopping for the vertical wall, although not the highest overall. The total depth ranged between 0.085m and 0.054m, which is the equivalent of a variability of a factor of approximately 1.6.

The second graph here, shows the lowest level of overtopping for the vertical wall. This time the total depth detected ranges between 0.019 *m* and 0.006 *m*. This is the highest variation in the vertical wall tests, and has a magnitude of approximately 3.5.

The third graph is that of TS05.VW, which is the second lowest overtopping condition in these tests. The depth varies between 0.085 *m* and 0.050 *m* for this condition, which is a variability with a magnitude of 1.7.

Finally the bottom graph examines the second highest overtopping conditions in the vertical wall tests. Here the overtopping depth detected ranged between 0.086 *m* and 0.053 *m*, which is equivalent to a variability of magnitude of approximately 1.6.

Again, the magnitude of the variation in the three higher overtopping tests is similar to that observed in the high ROBC overtopping tests. The lowest test here shows slightly higher variability although lower than both the moderate and lower levels of overtopping in the ROBC tests, and lower than found in the smooth slope conditions.

So far it has been observed that the variability in overtopping is less in the physical model than in the ROBC numerical tests. It is now important to compare these results with the empirical predictions that can be found in section 2.5. Firstly the smooth sloped results are investigated as shown in Fig. 7.10. All of the results of the smooth slope tests have been plotted here, along with the empirical prediction and its 95% confidence interval.

It can be seen here, that generally the empirical method using either Eq. 2.17 or Eq. 2.19 depending on conditions, over predicts the overtopping present, with most of the experimental results being below that of the lower 95% confidence limit. This is contrary to the findings with

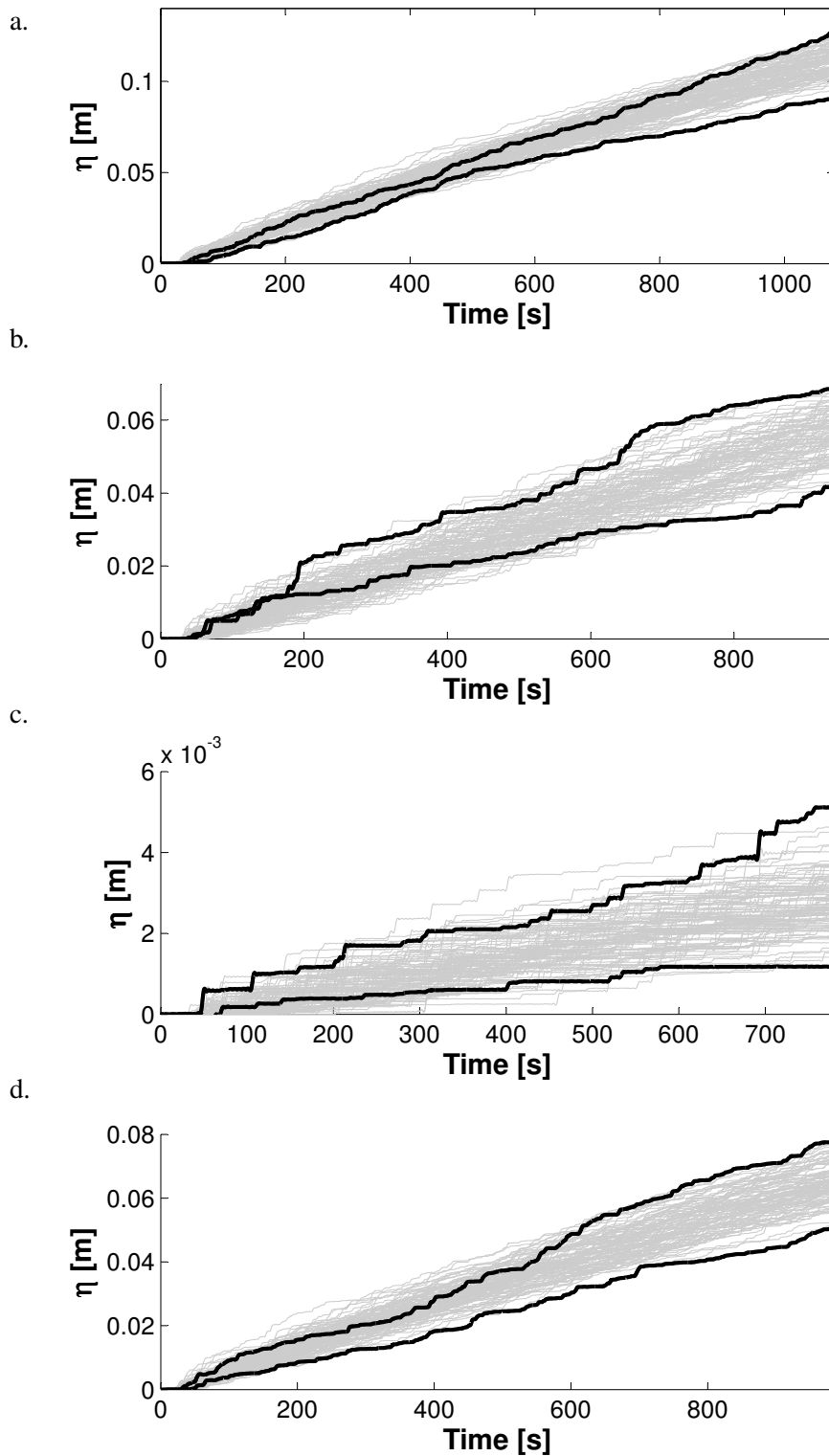


Figure 7.8: Measured filtered overtopping time series for all tests in each condition for smooth slope. Black lines: Minimum and Maximum measurements. a. TS01. b. TS02. c. TS03. d. TS05.

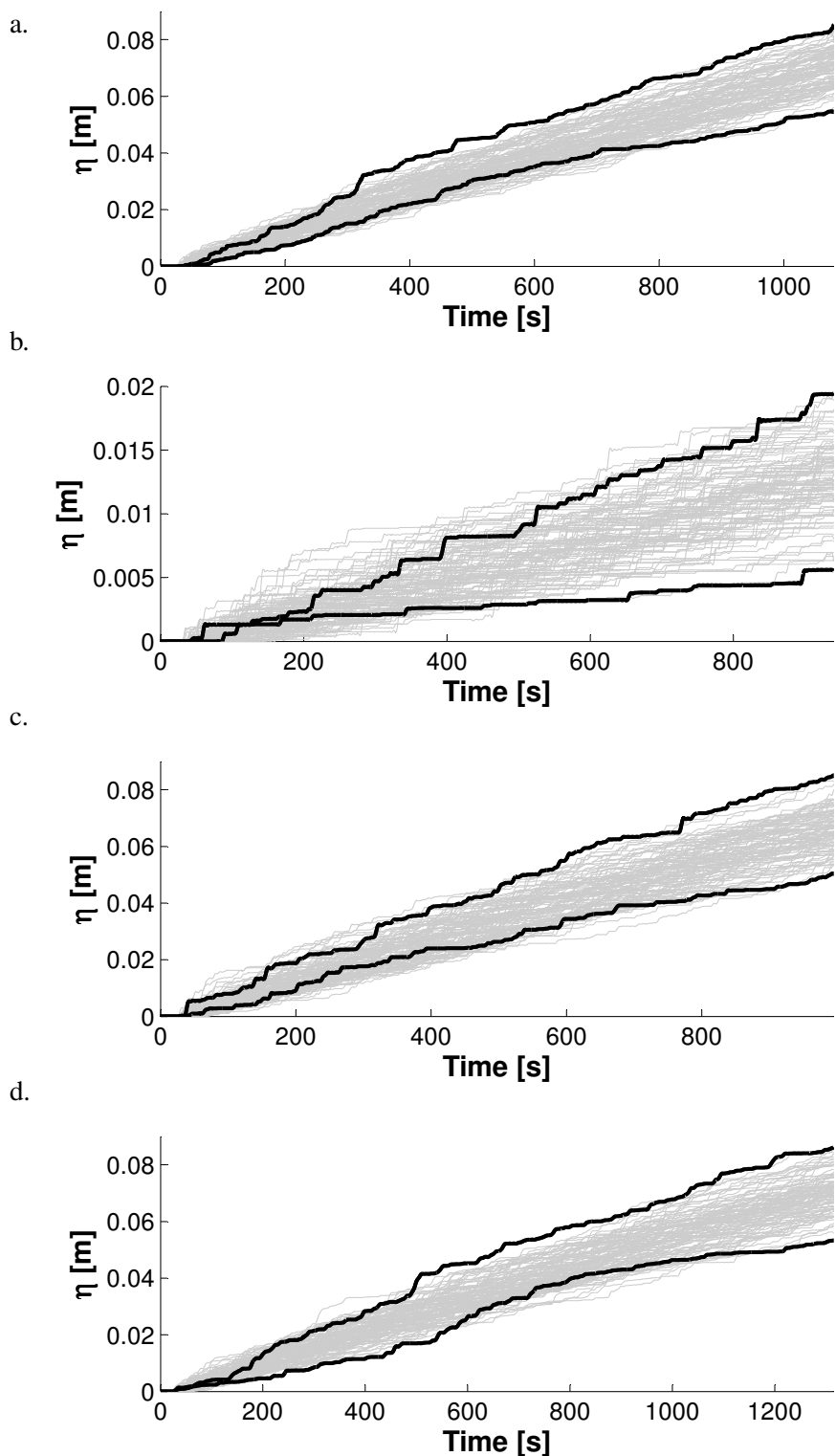


Figure 7.9: Measured filtered overtopping time series for all tests in each condition for vertical wall. Black lines: Minimum and Maximum measurements. a. TS01. b. TS02. c. TS05. d. TS07.

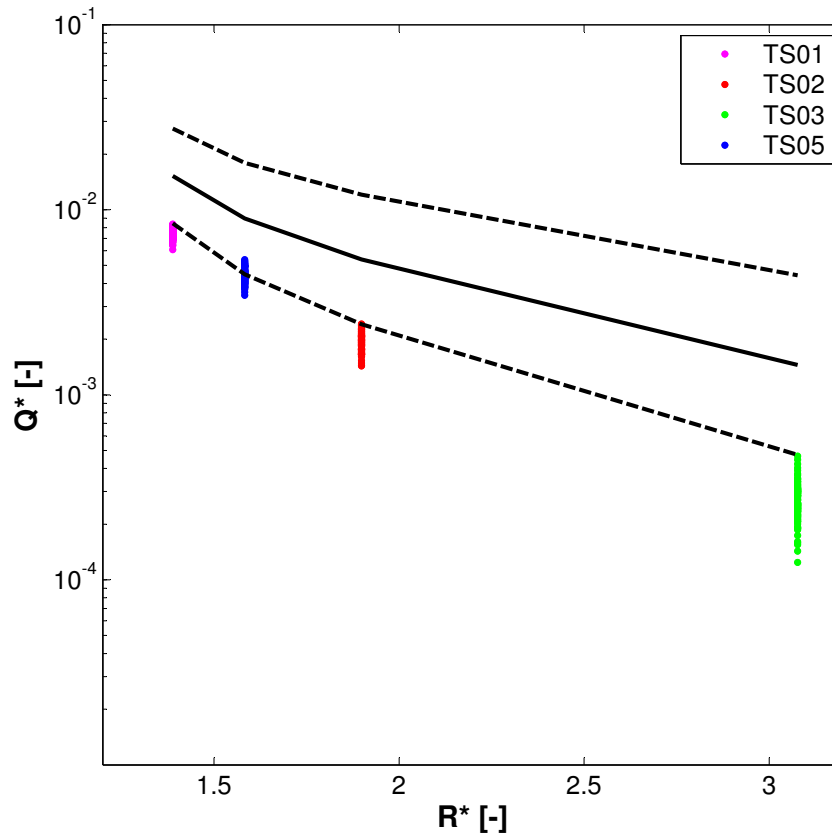


Figure 7.10: Graph showing  $R^*$  plotted against  $Q^*$  for random seeding test with smooth slope structure. Solid line: Empirical prediction. Dash line: 95% confidence interval.

the HR Wallingford tests, where the empirical method generally under predicted the results of the experiments.

It is also evident that the empirical prediction appears to show higher variability than the physical model in these conditions. In this case, the empirical method is subject to a variation of up to approximately one order of magnitude, whereas even in the low overtopping, the physical model results do not display such a high level of variability.

Now the results of the vertical wall tests are plotted in Fig. 7.11. Again, the empirical prediction of Eq. 2.21 or Eq. 2.22 depending on the conditions and the 95% confidence interval are shown on this graph. This time the physical model results are reasonably well predicted by the empirical formulae. Most of the results lie between the prediction and the upper 95% confidence limit.

It can also clearly be seen by these results that the physical models shows much less variability compared with the empirical prediction. The empirical prediction here shows variation of up to 2 orders of magnitude. As with the smooth slope, the variability in the physical model results are equivalent to less than 1 order of magnitude even at the lowest level of overtopping. Overall,

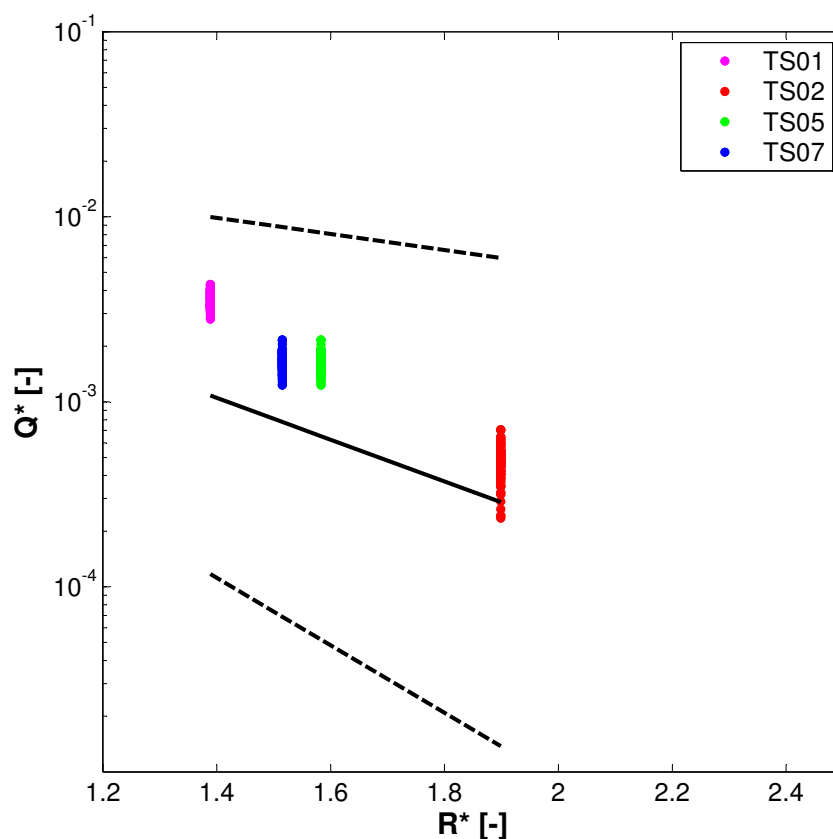


Figure 7.11: Graph showing  $R^*$  plotted against  $Q^*$  for random seeding test with vertical wall structure. Solid line: Empirical prediction. Dash line: 95% confidence interval.

the physical model shows less variation than that expected using the empirical methods.

The dimensionless crest level appears to show less variation in the physical model, however, it should be noted that this is based solely on the value obtained in the incident wave condition tests, and therefore remains constant for these results. Unfortunately, with the equipment available, it was not possible to determine the exact individual incident wave conditions for each of the different seeding tests.

Now these physical model results are compared with those obtained for the various ROBC tests in Chapter 4 and 6. Whilst the different sets of ROBC tests showed very similar magnitudes of variation for dimensionless discharge (See Fig. 4.11 and 6.9), of upto two orders of magnitude, it can be seen here again that the physical model shows variation of less than one order of magnitude.

It was found in the numerical modelling that the magnitude of variation in the discharge and maximum individual overtopping volume were directly related to the probability of overtopping, it was therefore important to investigate this for the physical model. Firstly, the proba-

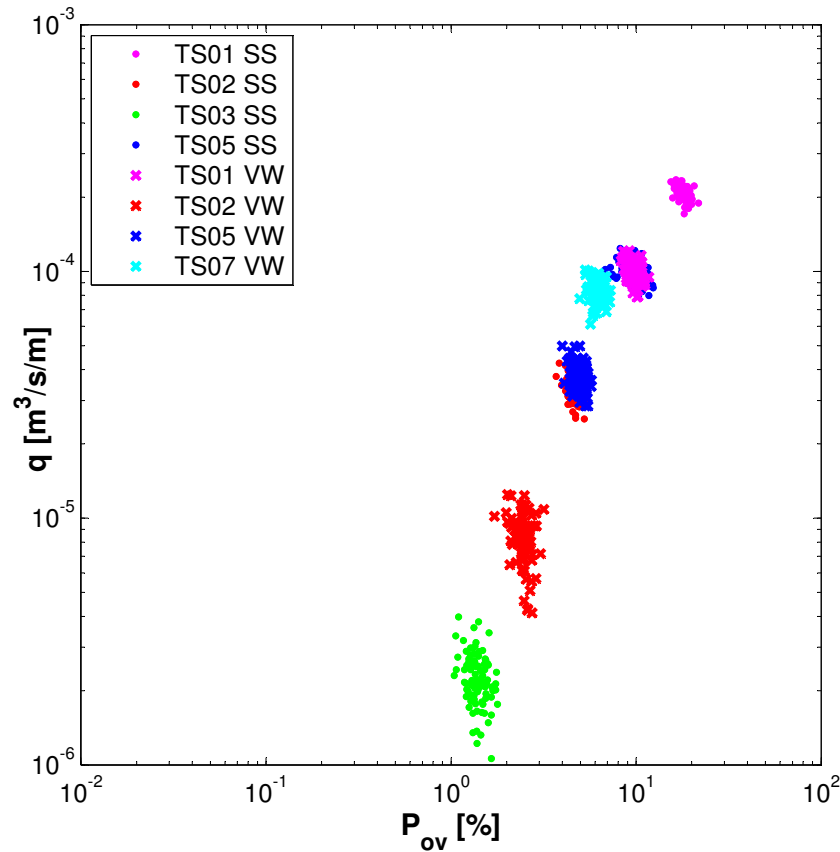


Figure 7.12: Graph showing  $P_{ov}$  plotted against  $q$  for random seeding test with both structures.

bility of overtopping and maximum individual volume had to be obtained from the measured overtopping time series. Due to the noise within this data, the accuracy with which this could be carried out is reasonably low. The values were obtained by filtering the time series with a low pass filter as done in the previous experiments. A peak detection method was then used to detect each overtopping event, the volumes were then calculated by working out the difference between each subsequent peak. Due to the filtering, it is quite possible that overtopping events were lost, particularly in the high overtopping conditions, limiting the accuracy of the results. The results from both sets of physical model tests can be seen in Fig. 7.12, where the probability of overtopping is plotted against the overtopping discharge. As with the dimensionless parameters it can be seen here that  $q$  varies by less than one magnitude in all of the test conditions. Whilst the variability in terms of  $P_{ov}$  is significantly less than one order of magnitude in all of the tests. In fact, this remains fairly constant throughout all of the tests carried out regardless of the magnitude of overtopping.

It can also be seen that tests on the different structures which result in the same levels of overtopping, vary by the same amount, suggesting as found in the numerical tests, that the shape of

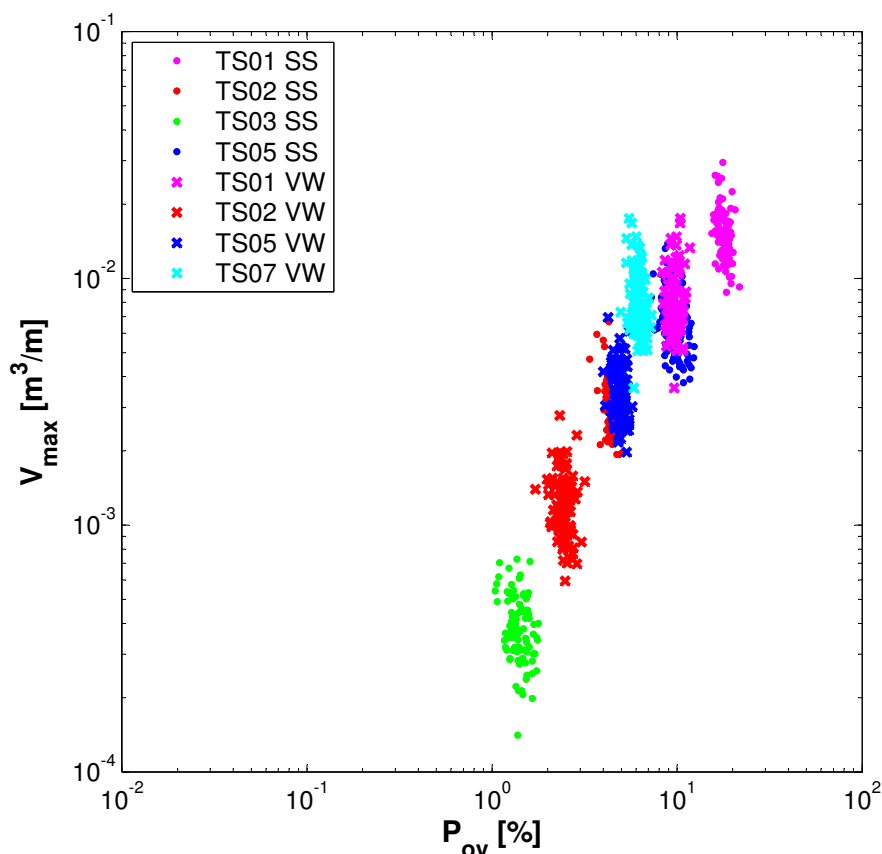


Figure 7.13: Graph showing  $P_{ov}$  plotted against  $V_{max}$  for random seeding test with both structures.

the structure or incoming wave parameters do not have an effect on the variability in overtopping.

These physical model results should also be compared with those obtained with the numerical model earlier in the work. It can again clearly be seen that the variability in  $q$  is less in the physical model than that obtained by the numerical model, even at similar values of  $P_{ov}$ . The variation in  $P_{ov}$  is also seen to vary significantly less in the physical model than in the numerical model tests. This could be an issue with the detection of overtopping events in the physical model that was not present in the numerical model. In particular, the smaller events could be missed, which would have great effect on the  $P_{ov}$  and hence less variation would be present.

Now to look at the comparison of  $V_{max}$  with  $P_{ov}$ , which has been plotted in Fig. 7.13. Again here, it can be seen that  $V_{max}$  does show variation, but only within one order of magnitude. It does appear to show slightly larger variation than found for  $q$ . It can also be seen that the value of  $P_{ov}$  has less influence on this variability with all the tests showing a similar level of variation for all the levels of overtopping.

When comparing the results of the physical model with the numerical model in terms of  $V_{max}$ ,

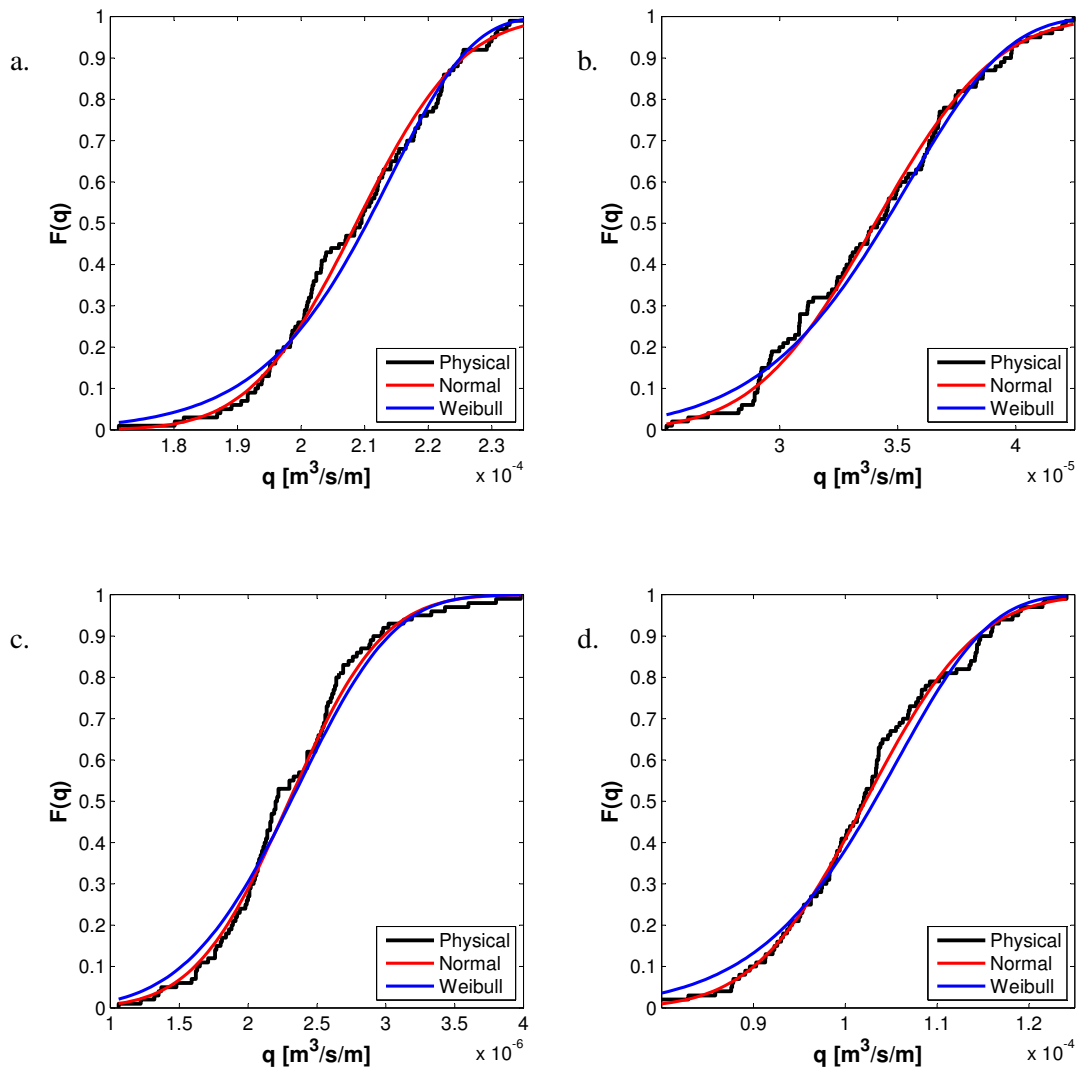


Figure 7.14: Empirical frequency curves for  $q$  from physical model tests (black solid lines) compared with expected distributions for different levels of overtopping. a. TS01. b. TS02. c. TS03. d. TS05

it is clear that within each test the variability in  $V_{max}$  is again lower. However, comparing all of the test conditions at once, the physical model does show more variability overall, this is likely due to more variation in the incident wave conditions. There also appears to be more correlation between  $P_{ov}$  and  $V_{max}$  that was not observed in the ROBC tests earlier.

## 7.5.2 Distributions

It has already been observed that generally the physical model tests show less variability due to random seeding than the numerical model. However, it is important to investigate whether the variability that is present behaves in the same manner as that found earlier. To begin this, the distribution of  $q$  for the smooth slope is assessed, and shown in Fig. 7.14.

As before, the empirical distribution of the results of  $q$  has been plotted against a number of

Table 7.7: Distribution parameters and results of the one sample K-S test for  $q$  for smooth slope

Test	$q$							
	Normal				Weibull			
	$\mu$	$\sigma$	$\Gamma$	$D_n$	$\lambda$	$k$	$\Gamma$	$D_n$
TS01	7.43e-3	4.66e-4	0	0.0717	7.65e-3	17.78	0	0.1015
TS02	1.94e-3	2.30e-4	0	0.0683	2.05e-3	9.35	0	0.0690
TS03	7.29e-4	1.70e-4	0	0.0877	7.96e-4	4.47	0	0.0897
TS05	5.91e-3	5.50e-4	0	0.0716	6.17e-3	11.56	0	0.1159

theoretical distributions to see if they match. It was found in the numerical model that the distribution of  $q$  was best modelled by the Weibull distribution in low-moderate overtopping and the Normal distribution in higher levels of overtopping, so these are the distributions considered here.

From the graphs it appears that the Normal distribution provides the closest match to the empirical distribution. In the lowest level of overtopping measured (TS03.SS), the Weibull also looks like a reasonable match. As in the previous work, a K-S test was carried out to confirm the most suitable distribution. The results of this, along with the parameters of the theoretical distributions are shown in Table 7.7. It can be seen here, that the null hypothesis is obtained for both distributions, but the value of  $D_n$  is smaller for the Normal distribution, so this is more suitable for describing the empirical distribution in all the smooth slope test conditions.

Now the distributions of  $q$  for the vertical wall tests are considered. Again, the empirical distributions are plotted along with the most likely theoretical distribution in Fig. 7.15. In the three highest overtopping levels, the empirical distribution appears to be modelled best by the Normal distribution, however, in the lowest overtopping (TS02.VW), both the Weibull and Normal distribution appear to match well the physical model results.

To confirm which distributions best model the physical results, the K-S test has been carried out again. The results of this, and the distribution parameters can be found in Table 7.8. As with the smooth slope, it can be seen that both theoretical distributions produce the null hypothesis. This time, in the three highest overtopping, as anticipated the Normal distribution is the most suitable according to the values of  $D_n$ . However, for the lowest overtopping (TS02.VW), the Weibull distribution produces the lower value of  $D_n$  meaning this provides a better match. This finding is the same as that obtained using the numerical model, for moderate levels the Weibull produces the closest match but this tends towards normal as overtopping increases.

As it has already been observed that variability is significantly lower in the physical model than the numerical model, it is now important to consider the distribution of  $P_{ov}$  for the physical

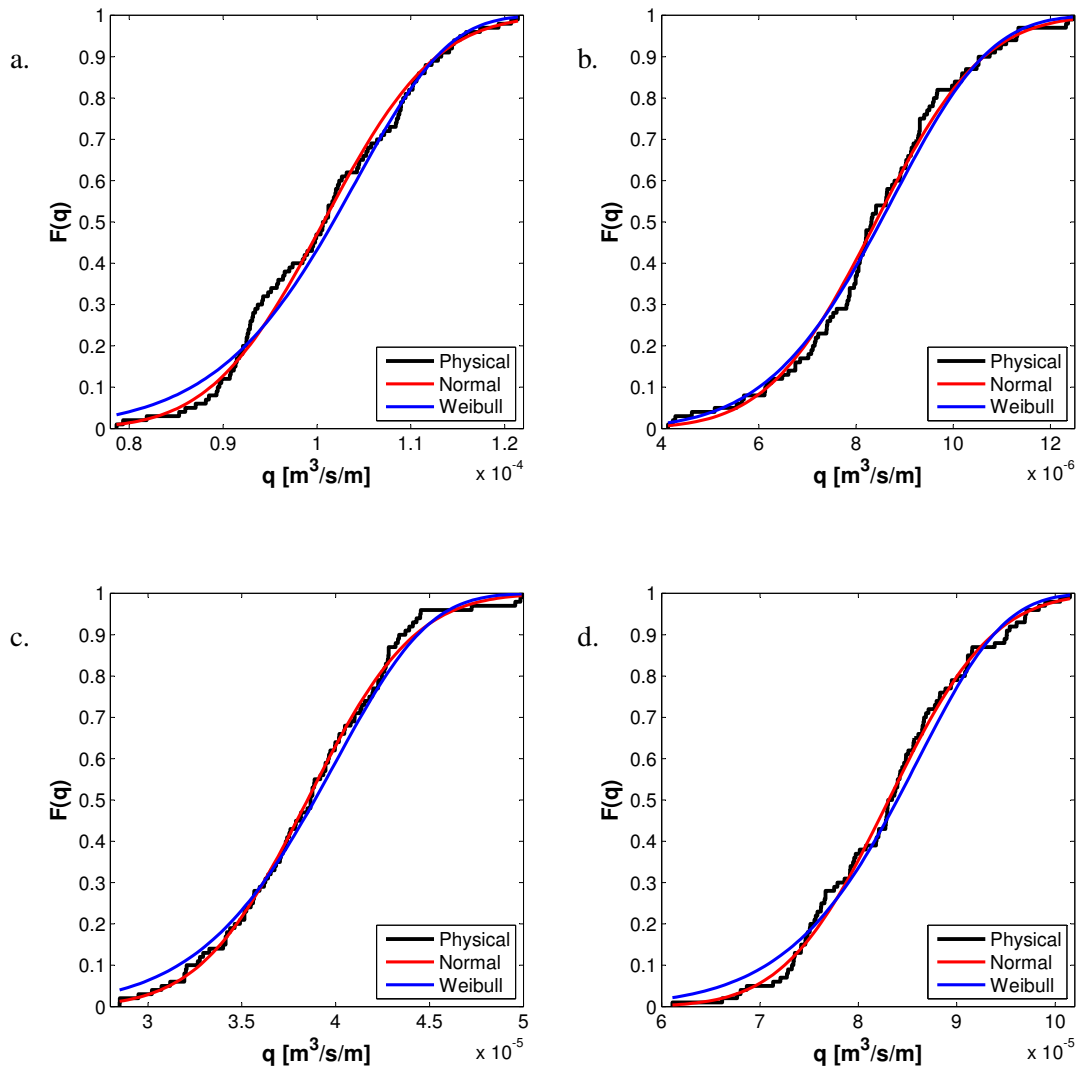


Figure 7.15: Empirical frequency curves for  $q$  from physical model tests (black solid lines) compared with expected distributions for different levels of overtopping. a. TS01. b. TS02. c. TS05. d. TS07

Table 7.8: Results of the one sample K-S test for  $q$  for vertical wall

Test	$q$							
	Normal				Weibull			
	$\mu$	$\sigma$	$\Gamma$	$D_n$	$\lambda$	$k$	$\Gamma$	$D_n$
TS01	4.73e-3	4.42e-4	0	0.0727	4.94e-3	11.71	0	0.0749
TS02	4.80e-4	9.92e-5	0	0.0741	5.19e-4	5.41	0	0.0719
TS05	2.22e-3	2.58e-4	0	0.0487	2.33e-3	9.10	0	0.0588
TS07	3.36e-3	3.35e-4	0	0.0716	3.52e-3	10.90	0	0.0759

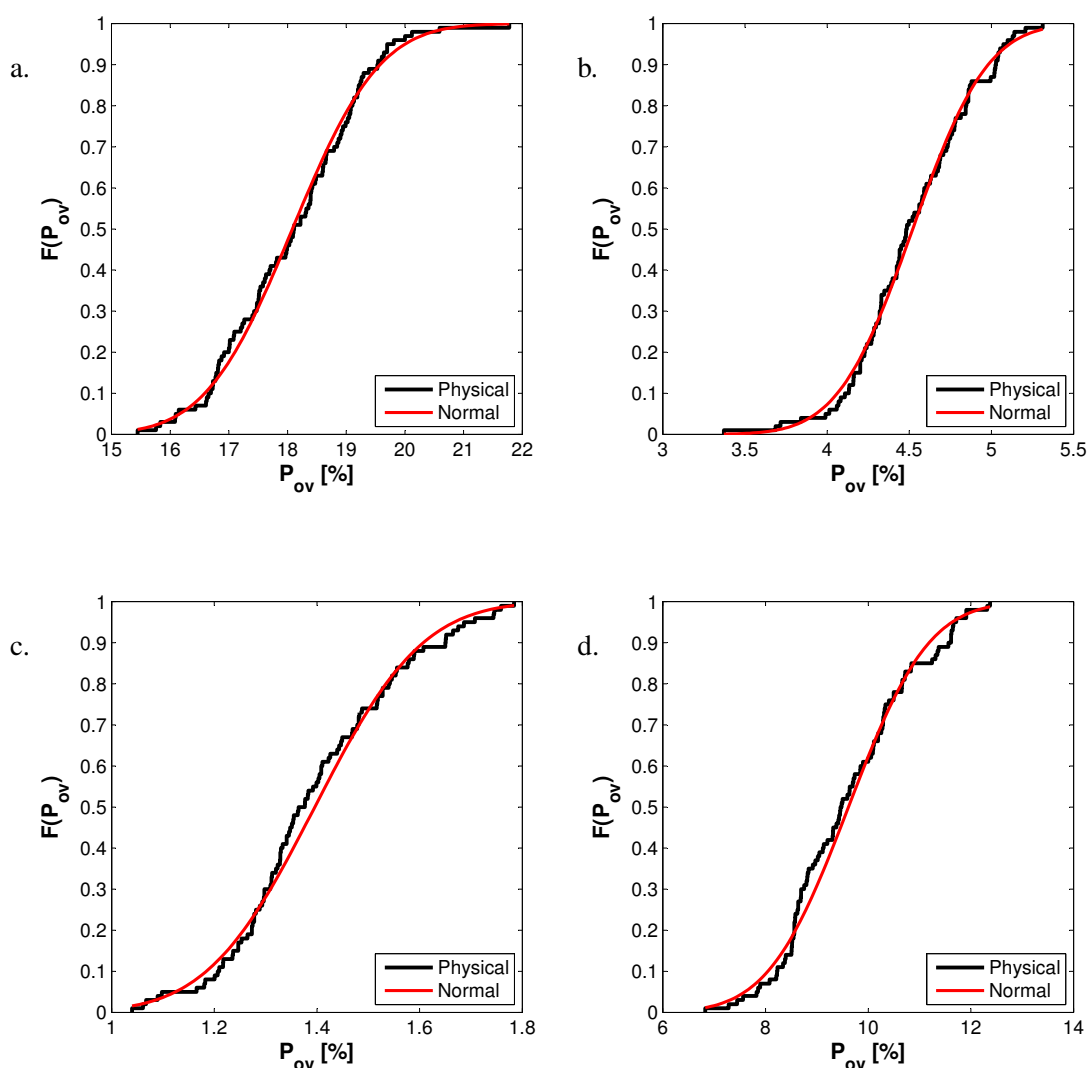


Figure 7.16: Empirical frequency curves for  $P_{ov}$  from physical model tests (black solid lines) compared with expected distributions for different levels of overtopping. a. TS01. b. TS02. c. TS03. d. TS05

tests. Firstly, the distribution of  $P_{ov}$  for the smooth slope tests are considered in Fig. 7.16.

In the numerical tests, it was found that the Normal distribution was the most suitable for modelling the distribution of  $P_{ov}$ , so this is the distribution considered here. It can be seen in the graphs, that the Normal distribution does indeed appear to model well the  $P_{ov}$ . This is confirmed by the results of the K-S test which are shown in Table 7.9, along with the theoretical distribution parameters. This confirms that the Normal distribution is suitable.

Now to consider the the distributions of  $P_{ov}$  for the vertical walls, which are shown in Fig. 7.17. Again, here the Normal distribution has also been plotted which appears to show a reasonable approximation to the empirical distribution. To confirm this, the results of the K-S test are included in Table 7.10.

Finally, the distribution on  $V_{max}$  is considered. As with  $P_{ov}$  there is slightly less confidence in the measured quantities than with  $q$  due to noise within the data. It is quite possible that some

Table 7.9: Distribution parameters and results of the one sample K-S test for  $P_{ov}$  on smooth slope

Test	$P_{ov}$			
	Normal			
	$\mu$	$\sigma$	$\Gamma$	$D_n$
TS01	18.08	1.166	0	0.0521
TS02	4.521	0.352	0	0.0501
TS03	1.396	0.165	0	0.0783
TS05	9.616	1.226	0	0.0868

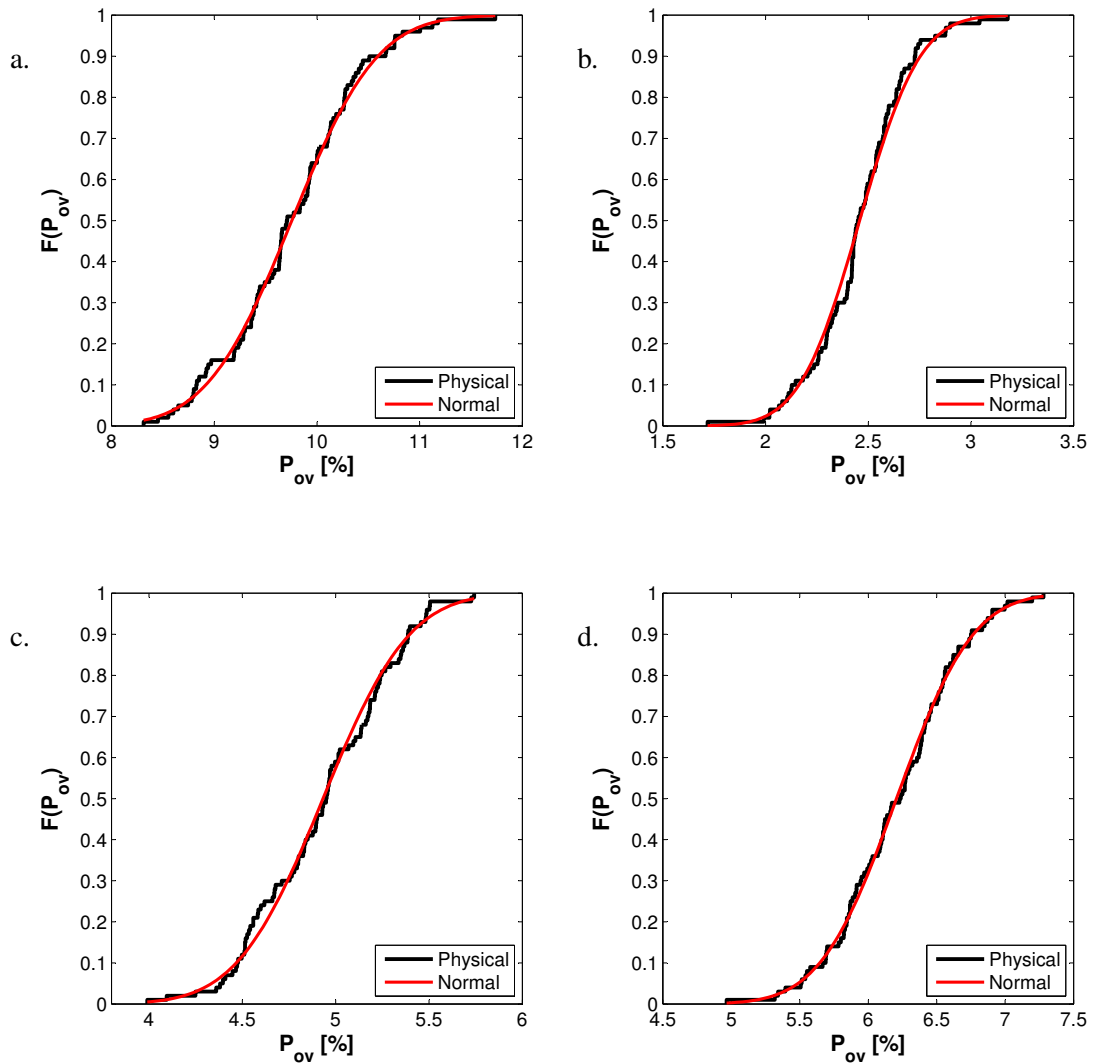

 Figure 7.17: Empirical frequency curves for  $P_{ov}$  from physical model tests (black solid lines) compared with expected distributions for different levels of overtopping. a. TS01. b. TS02. c. TS05. d. TS07

 Table 7.10: Results of the one sample K-S test for  $P_{ov}$  on vertical wall

Test	$P_{ov}$			
	Normal			
	$\mu$	$\sigma$	$\Gamma$	$D_n$
TS01	9.755	0.653	0	0.0448
TS02	2.458	0.231	0	0.0832
TS05	4.933	0.363	0	0.0607
TS07	6.207	0.438	0	0.0453

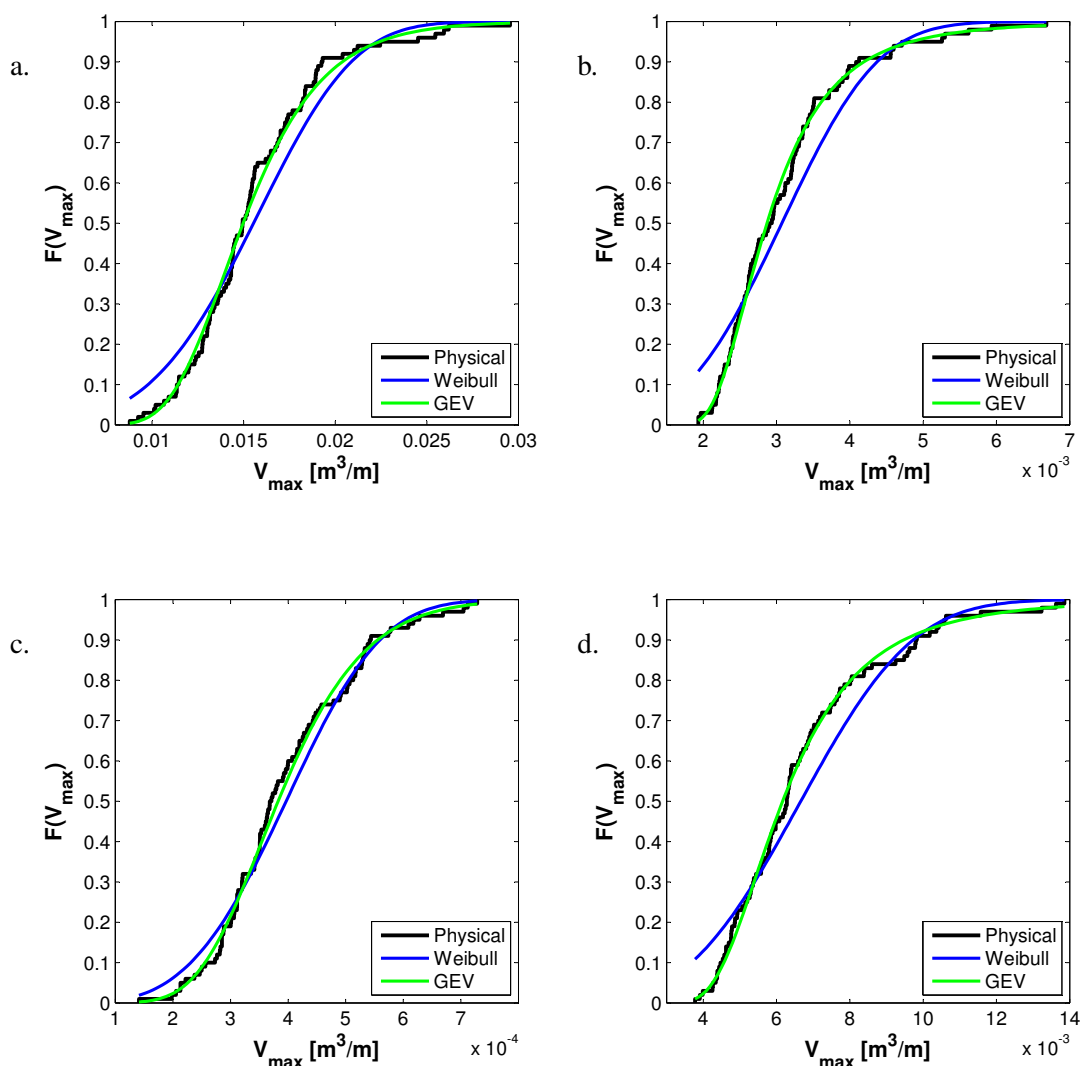


Figure 7.18: Empirical frequency curves for  $V_{max}$  from physical model tests (black solid lines) compared with expected distributions for different levels of overtopping. a. TS01. b. TS02. c. TS03. d. TS05

of the  $V_{max}$  values may include smaller overtopping events that could not be identified. In the numerical work, the distribution with  $V_{max}$  was compared with both the Weibull and the GEV distribution, so these have been included in Fig. 7.18 which shows the empirical distributions for the smooth slope structure.

The graphs show that as with the numerical model, the GEV does appear to model the empirical distribution best, particularly in the three higher overtopping levels. The two theoretical distributions are both fairly close for the lowest level of overtopping. To confirm the results, the K-S test has been carried out. These along with the parameters of the theoretical distributions can be found in Table 7.11. This shows that although both theoretical distributions match, the GEV does indeed provide a closer match.

Now the distribution for  $V_{max}$  for the vertical tests are considered. They are plotted in Fig. 7.19 along with the theoretical distributions. Again, it can be seen from these graphs that the

Table 7.11: Results of the one sample K-S test for  $V_{max}$  on smooth slope

Test	$V_{max}$								
	Weibull				GEV				
	$\lambda$	$k$	$\Gamma$	$D_n$	$\xi_x$	$\mu_x$	$\sigma_x$	$\Gamma$	$D_n$
TS01	0.0170	4.073	0	0.1322	-0.0189	0.0029	0.0139	0	0.0654
TS02	0.0034	3.408	0	0.1474	0.1843	5.49e-4	0.0027	0	0.0553
TS03	4.40e-4	3.487	0	0.0939	-0.0930	1.03e-4	3.45e-4	0	0.0529
TS05	0.0075	3.171	0	0.1313	0.1755	0.0014	0.0056	0	0.0507

Table 7.12: Results of the one sample K-S test for  $V_{max}$  on vertical wall

Test	$V_{max}$								
	Weibull				GEV				
	$\lambda$	$k$	$\Gamma$	$D_n$	$\xi_x$	$\mu_x$	$\sigma_x$	$\Gamma$	$D_n$
TS01	0.0669	3.909	0	0.1371	0.0751	0.0012	0.0056	0	0.0524
TS02	0.0014	5.408	0	0.0925	-0.0186	3.01e-4	0.0011	0	0.0438
TS05	0.0039	3.691	0	0.1317	0.0909	6.76e-4	0.0030	0	0.0647
TS07	0.0094	3.298	0	0.1247	0.0479	0.0019	0.0073	0	0.0667

GEV provides the best match, which is confirmed by the K-S test results shown in Table 7.12.

Overall, the physical model shows less variability than both the numerical model and the empirical methods. It has also been seen that the distributions of the various parameters follow those established in the numerical model.

### 7.5.3 Comparison with Same Seeding Results

The variability in the physical model due to different seeding has been established, however, it was earlier found that even with the same seeding the results for  $q$  showed some variation when repeated. It is therefore important to compare these two sets of results, so that the variability due to laboratory effects can be separated from the variability caused by the random seeding.

This is carried out by calculating the relative error in  $q$  for each of the tests. These are then plotted in Fig. 7.20. It can be seen on these graphs, that the relative error for the same seedings remains fairly consistent throughout all the different tests, whereas the relative error for the random seeding tests increases significantly as  $R^*$  increases.

If the total relative error found in  $q$  across the two sets of test on the smooth slope is considered, it can be seen that approximately 6% could be due to laboratory effects that cannot be removed in the lowest levels of overtopping, in the higher levels this could be equal to as much as 29%, this is mainly due to the lower variability in the different seeding tests due to high number of overtopping waves. This does mean however, that there is a significant amount of variability due to the random seeding.

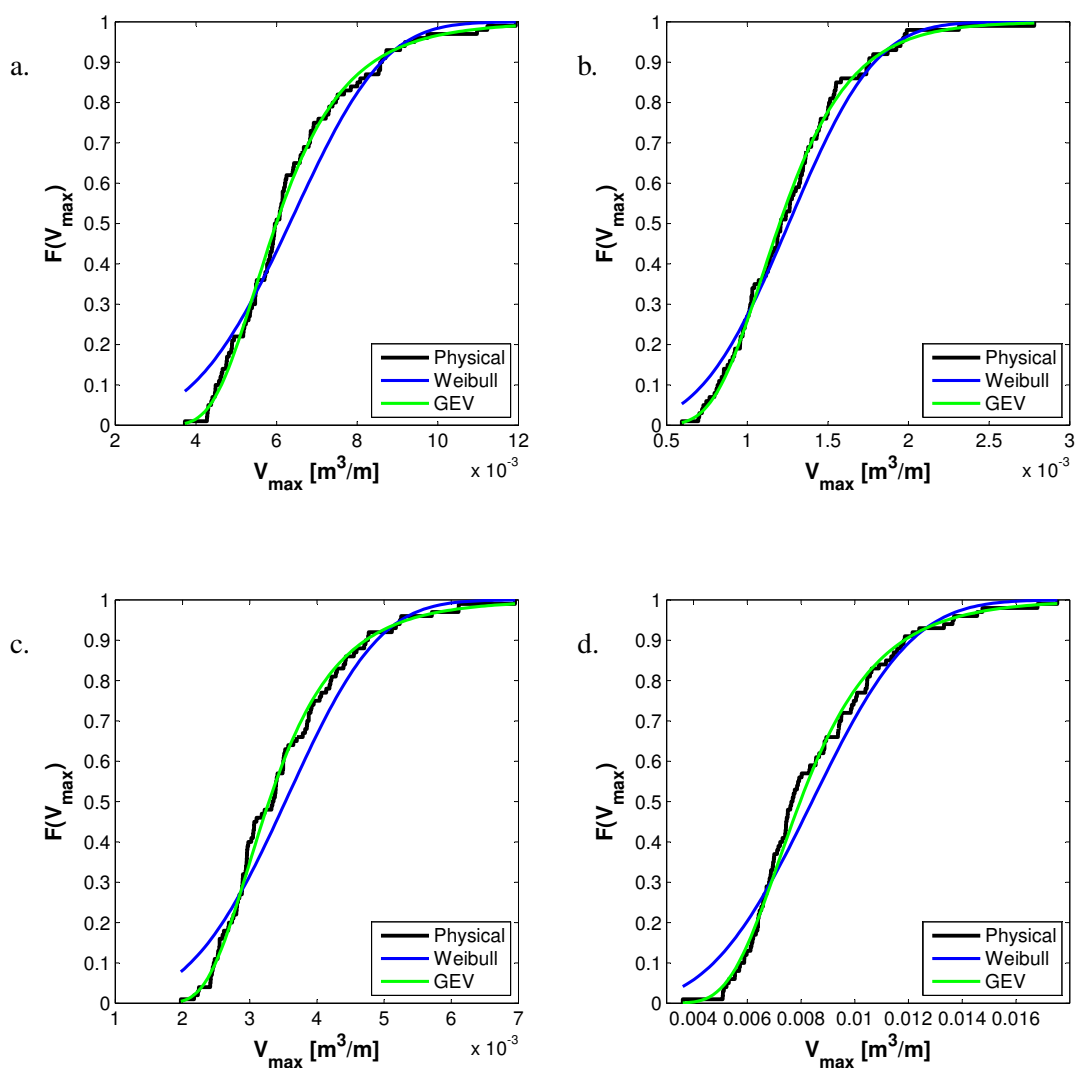


Figure 7.19: Empirical frequency curves for  $V_{max}$  from physical model tests (black solid lines) compared with expected distributions for different levels of overtopping. a. TS01. b. TS02. c. TS05. d. TS07

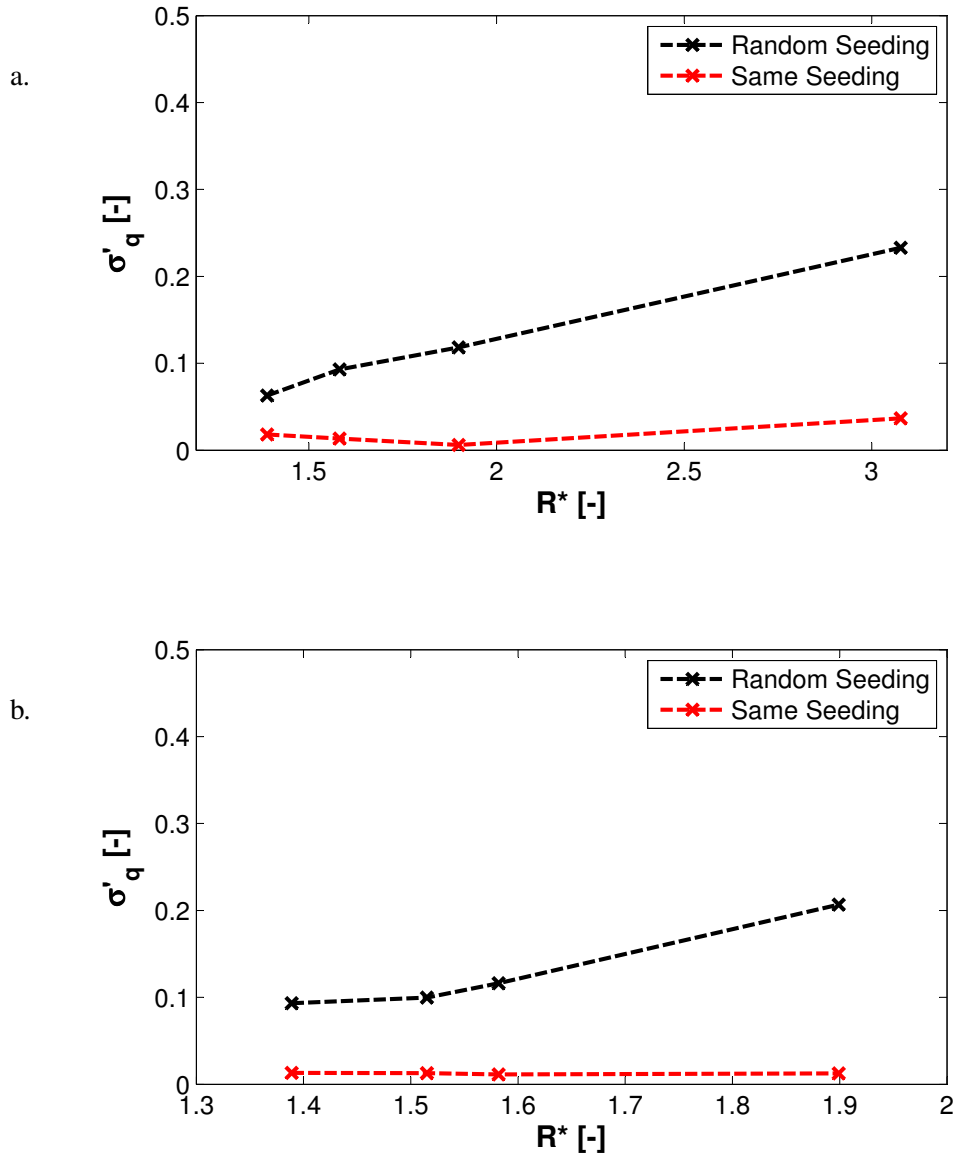


Figure 7.20: Relative error of  $q$  for Random Seeding and Same Seeding tests. a. Smooth Slope. b. Vertical Wall.

For the vertical wall, the laboratory effects seem to have less influence on the overall variability, with the same seeding tests equating to approximately 6% again in the lower overtopping, but only 15% in the higher overtopping tests. Again, this suggests that there is variability due to the random seeding that is greater than that caused simply by laboratory effects.

## 7.6 Summary

Physical models tests have been carried out to investigate the effect that the seeding of the waves at the paddle has on the variability in the overtopping parameters. Two different structures have been constructed, and a total of 8 different test conditions have been used. Calibration tests have also been conducted to obtain the incident waves conditions for each test.

The influence of laboratory effects was investigated first so the variability caused by this could be separated from that caused by the random seeding. It was found that the wave paddle produced an accurate wave height distribution without any additional non-linear effects occurring. The presence of long waves forming in the flume were also investigated and were found to not have a significant effect on the total wave energy present in the flume.

A methodology was produced to control the still water level in the experiments to limit the effect this had on the variability of the results.

The variability in  $q$  was investigated and as with the numerical models was found to decrease with increase in  $P_{ov}$ . The distributions of the variability of each of the overtopping parameters was also investigated, and again found to match those established in the numerical tests. Overall, it was found that the variability in the physical model was less than that found in the numerical model.

# Chapter 8

## Conclusions

### 8.1 Summary of this Work

This work has presented the validation of the ability of a NLSWE model to predict overtopping. This was achieved by carrying out a comparison between physical model test results and those obtained from the numerical model results when a measured time series of waves was used as input. This comparison between the two methods of prediction showed good agreement, with the results showing accuracy consistent with other similar numerical simulations of overtopping in terms of overtopping discharge.

Due to specific experimental data being available, accuracy in the prediction of the parameters of maximum individual overtopping volume and probability of overtopping were also considered. The numerical results were again compared with those obtained in the physical modelling, and showed reasonable agreement, however as little previous research has been carried out in terms of these parameters it was not possible to compare the accuracy with similar numerical simulations. The numerical model was generally shown to be more accurate than the empirical prediction methods.

Another parameter that has had little previous research in terms of numerical modelling is the individual overtopping volumes which are usually expressed as a distribution. It was found that the numerical model showed good agreement with the physical model, and the distributions were also found to be well modelled by the existing empirical methods.

The variability in the overtopping prediction of the NLSWE model due to the seeding used to generate the offshore boundary times series from energy density spectra has then been examined. By carrying out a Monte Carlo analysis this variability has been quantified, initially using

the incident spectra obtained from the physical model. A significant variability was observed in these results, which can lead to an inaccurate prediction of overtopping if only a single test is carried out. The variability was found to decrease with increasing levels of overtopping. This behaviour can be straightforwardly explained: when only a few waves overtop a structure, the relative importance of each event is large, whereas when the number of overtopping events increases, the role of each individual event in the total overtopping becomes smaller. This is consistent with the increased uncertainty in prediction of low overtopping discharges using empirical approaches.

The properties of the populations of each of the overtopping parameters in the variability tests have been studied in order to assess how they are distributed. Theoretical distributions have been found to well describe the empirical distributions from the tests for moderate to high levels of overtopping. The low overtopping tests could not have theoretical distributions fitted due to the large number of tests that experienced no overtopping. It was found that  $q$  follows a Weibull distribution at moderate levels of overtopping, and tends towards the Normal distribution for higher levels.  $P_{ov}$  was found to follow a Normal distribution at moderate and high levels of overtopping.  $V_{max}$  was found to follow the Generalised Extreme Value distribution at both the moderate and high levels of overtopping.

The average values of the predicted overtopping parameters in the variability tests have also been compared with the both the physical model results, and the predictions of the numerical model when the measured offshore boundary condition was used. It was found that generally these are less accurate. It was also found that when using the average value of the reconstructed offshore boundary tests, there is an uncertainty associated with the prediction, which is dependent on the number of tests for the test condition. In low overtopping, a large number of tests is required for the value to converge, in high overtopping this is achieved much faster.

The variability of the individual overtopping volume distribution in numerical models was studied. It was found that it is possible for different distributions to be produced from the same incident spectra; some of these were shown to significantly diverge from the Weibull distributions expected. As with the other overtopping parameters, the lower levels of overtopping produced more variation than those that experienced higher overtopping. It was also shown however, that overall the lower levels of overtopping produced a distribution closer to that expected.

It was also shown that, when the distribution of the incident wave heights, and the shape of the incoming waves in the reconstructed time series do not match those observed in reality, then the

distribution of the individual volumes will not be accurate. This was particularly evident in the very shallow water conditions.

The initial set of results were based on the physical experiments where the wave and structural conditions were specifically chosen to be suitably modelled by the NLSWE. To extend this study, the influence of both the hydraulic and geometric conditions needed to be explored. Firstly, the influence of the spectral shape was examined, and found to have little effect on the variability, with all of the parameters being appropriately modelled by the distributions established in the earlier work.

The influence of wave steepness, slope geometry and their combined effect as the surf similarity parameter on the variability was studied. Again, it was found that these did not have a significant direct impact on the variability, although some indirect influence was observed due to the resultant changes to the level of overtopping. Again, the distributions of the parameters matched those found in the earlier work.

The influence of the roughness of the slope on the variability was also examined. Increasing the roughness on the slope surface was found to decrease the overtopping discharge, more than the probability of overtopping, but did not have a significant influence on the magnitude of the variability. The distributions of the individual parameters were still found to match the earlier observations.

The variability due to reconstructing the time series from an energy density spectra was also examined in terms of physical modelling. Similarly to the numerical experiments, this involved carrying out a Monte Carlo analysis, by changing the seeding at the wave paddle. In total, 8, different test conditions were chosen, with 4 based on a smooth slope structure and 4 using a vertical wall structure. 100 different seedings were used for each condition, and the measured overtopping discharge calculated.

A significant variability was observed in these tests. As with the numerical experiments this was observed to be related to the level of overtopping, with tests experiencing high levels resulting in lower variability. Although, in all tests the variability was generally found to be less than that observed in the numerical modelling. The influence of laboratory effects on this variability was also examined, and found to have a small effect on the total variability.

The other two parameters were also calculated from the time series although due to the noise in the data and the small scale used their accuracy is considerably less. However, the distributions of the variability of the various overtopping parameters were examined and were found to gen-

erally agree with the earlier numerical findings.

Overall, the work presented in this thesis has shown that the offshore boundary conditions for both NLSWE solvers and physical models derived from energy density spectra play an important role in the simulation of overtopping at coastal structures. This is particularly true when a low overtopping rate is expected, which is significant as coastal structures are often designed for this level of overtopping. This information can now be used to provide some recommendations on the use of both numerical and physical models where the offshore boundary conditions are generated in this way.

Often, in design practice it is not possible to carry out a large number of tests for the same hydraulic and structural conditions, so there is a need to limit the conditions where multiple tests are necessary. It has been concluded that when  $P_{ov} < 5\%$  both  $P_{ov}$  and  $q$  can vary by more than one order of magnitude, and therefore, this should be taken as the limit value of  $P_{ov}$  for which a sensitivity analysis should be carried out. In addition, in the numerical model it is suggested to carry out preliminary analysis to establish the distribution of wave heights at the offshore boundary. This should then be used to compare generated time series, with those providing the closest match being chosen as the input.

## 8.2 Recommendations for Future Work

Overall this work has provided a comprehensive investigation into the effect of the offshore boundary conditions on the uncertainty in both physical and numerical modelling, with over 23,000 numerical tests and over 1,000 physical model tests being carried out and subjected to a full analysis. However, there are a number of areas that could still be investigated as follows;

- Different numerical schemes. This work has concentrated solely on a NLSWE model for the numerical tests, however, the issue of spectral offshore boundary conditions is likely to be present in the other types of model mentioned in Chapter 2. As the numerical and physical model were found to behave in a similar manner, it is anticipated that other numerical schemes would yield similar results but to confirm this, the issue should be investigated.
- Alternative methods of time series reconstruction. As part of this work, it was found that the wave height distribution was not always well modelled in the reconstructed time

series. Alternative methods for the reconstruction should be examined to see if this can be improved upon for example the filtered white noise method for generation is generally accepted to better represent natural waves than the random phase used here. This is the method that the wave paddle uses, and it is possible that some of the decrease in variability found in the physical model is due to this.

- Location of offshore boundary conditions. The location of the offshore boundary was chosen to be suitably modelled by the NLSWE equations, however, it was found that depending on the wave conditions and depth present, the time series generated did not take account of the wave shoaling occurring at this location, with waves appearing too symmetrical about the still water level. In the shallower water conditions this was seen to limit the wave breaking, and hence there was less of a decrease in wave energy and more overtopping occurred than expected. This issue could be investigated by looking at the previous two recommendations, and by incorporating a deeper water model with the NLSWE model where the waves have not begun to shoal.



# Bibliography

- Airy, G., 1845. On tides and waves: Encyclopaedia Metropolitana, vol. 5 (mixed sciences). London.
- Allsop, W., Franco, L., Bellotti, G., Bruce, T., Geeraerts, J., 2005. Hazards to people and property from wave overtopping at coastal structures. In: Int. Conf. on Coastlines, Structures and Breakwaters. pp. 153–165.
- Battjes, J., Groenendijk, H., 2000. Wave height distributions on shallow foreshores. Coastal Engineering 40 (3), 161 – 182.
- BBC, 2014a. Dawlish rail line: Closure 'costs economy up to 1.2bn'.  
URL <http://www.bbc.co.uk/news/uk-england-devon-31140192>
- BBC, 2014b. Uk storms destroy railway line and leave thousands without power.  
URL <http://www.bbc.co.uk/news/uk-26042990>
- BBC, 2014c. Winter storm hits uk.  
URL <http://www.bbc.co.uk/news/uk-scotland-25231224>
- Besley, P., March 1999. Overtopping of seawalls: Design and assessment manual. R&D Report W 178, Environment Agency, North East Region.
- Booij, N., Ris, R. C., Holthuijsen, 1999. A third-generation wave model for coastal regions. 1. Model description and validation. J. Geophys. Res. 104(C4), 7649–7666.
- Briganti, R., Bellotti, G., Franco, L., De Rouck, J., Geeraerts, J., 2005. Field measurements of wave overtopping at the rubble mound breakwater of RomeOstia yacht harbour. Coastal Eng. 52(12), 1155–1174.
- Briganti, R., Dodd, N. and Pokrajac, D., T., O., 2011. Non linear shallow water modelling of bore-driven swash: Description of the bottom boundary layer. Coastal Eng. 58(6) (<http://dx.doi.org/10.1016/j.coastaleng.2011.01.004>), 463–477.
- Briganti, R., Dodd, N., 2009. Shoreline motion in nonlinear shallow water coastal models. Coastal Eng. 56(5-6) (doi:101016/j.coastaleng.2008.10.008), 495–505.
- Brocchini, M., Dodd, N., 2008. Nonlinear shallow water equation modeling for coastal engineering. ASCE J. Water. Port Coast. Ocean Eng. 134(2), 104–120.
- Chen, Q., Kirby, J. T., Dalrymple, R. A., Kennedy, A. B., Chawla, A., 2000. Boussinesq modeling of wave transformation, breaking and run-up 2: 2D. ASCE J. Water. Port Coast. Ocean Eng. 126(1), 48–56.
- Dalrymple, R., Rogers, B., 2006. Numerical modeling of water waves with the sph method. Coastal Engineering 53 (23), 141 – 147.

- Dodd, N., 1998. A numerical model of wave run-up, overtopping and regeneration. *ASCE J. Water. Port Coast. Ocean Eng.* 124(2), 73–81.
- Ferson, S., Hajagos, J., 2006. Varying correlation coefficients can underestimate uncertainty in probabilistic models. *Reliability Engineering and System Safety* 91, 1461 – 1467.
- Franco, L., Geeraerts, J., Briganti, R., Willems, M., Bellotti, G., De Rouck, J., 2009. Prototype measurements and small-scale model tests of wave overtopping at shallow rubble-mound breakwaters: the Ostia-Rome yacht harbour case. *Coastal Eng.* 56(2) (doi:10.1016/j.coastaleng.2008.03.009), 154–165.
- Fredsøe, J., Deigaard, R., 1993. *Mechanics of Coastal Sediment Transport*. Vol. 3 of *Advanced Series on Ocean Engineering*. World Scientific, Singapore.
- Geeraerts, J., Kortenhaus, A., Gonzalez-Escriv, J., Rouck, J. D., Troch, P., 2009. Effects of new variables on the overtopping discharge at steep rubble mound breakwaters the zeebrugge case. *Coastal Engineering* 56 (2), 141 – 153.
- Goda, Y., 1985. *Random Seas and Maritime Structures*. University of Tokyo Press.
- Guardian, 2014. Stormy weather batters europe's atlantic coast.  
URL <http://www.theguardian.com/world/gallery/2014/jan/08/stormy-weather-europe-atlantic-coast-in-pictures>
- Hall, J., Boyce, S., Wang, Y., Dawson, R., Tarantola, S., Saltelli, A., 2009. Sensitivity analysis for hydraulic models. *Journal of Hydraulic Engineering* 135 (11), 959–969.
- Hasselmann, K., Barnett, T., Bouws, E., Carlson, H., Cartwright, D., Enke, K., Ewing, J., Gienapp, H., Hasselmann, D., Kruseman, P., Meerburg, A., Miller, P., Olbers, D., Richter, K., Sell, W., Walden, D., 1973. Measurements of wind-wave growth and swell decay during the joint north sea wave project (JONSWAP). *Ergänzungsheft zur Deutschen Hydrographischen Zeitschrift Reihe A(8) (95)*.
- Hibberd, S., Peregrine, D. H., 1979. Surf and run-up on a beach: A uniform bore. *J. Fluid Mech.* 95, 323–345.
- Hu, K., Mingham, C. G., Causon, D. M., 2000. Numerical simulation of wave overtopping of coastal structures using the non-linear shallow water equations. *Coastal Eng.* 41, 433–465.
- Hughes, S., 1993. *Physical models and laboratory techniques in coastal engineering*. World Scientific, New York.
- Kamphuis, J., 1991. Wave transformation. *Coastal Eng.* 15, 173–184.
- Kobayashi, N., Otta, A. K., Roy, I., 1987. Wave reflection and run-up on rough slopes. *ASCE J. Water. Port Coast. Ocean Eng.* 113(3), 282–298.
- Kobayashi, N., Wurjanto, A., 1989. Wave overtopping on coastal structures. *ASCE J. Water. Port Coast. Ocean Eng.* 115(2), 235–251.
- Lin, P., Liu, P., 1998. A numerical study of breaking waves in the surf zone. *Journal of Fluid Mechanics* 359, 239 – 264.
- Liu, Z., 2001. *Sediment Transport*. Laboratoriet for Hydraulik og Havnebygning Institut for Vand, Jord og Miljøteknik. Aalborg Universitet. Denmark.
- Longuet-Higgins, M., 1952. On the statistical distribution of the heights of sea waves. *Journal of Marine Research* 9, 245–266.

- Lynett, P. J., Melby, J. A., Kim, D.-H., 2010. An application of boussinesq modeling to hurricane wave overtopping and inundation. *Ocean Engineering* 37 (1), 135 – 153.
- McCabe, M., Stansby, P., Apsley, D., 2011. Coupled wave action and shallow-water modelling for random wave runup on a slope. *J. Hydraulic Res.* 49(4), 515–522.
- McCabe, M., Stansby, P., Apsley, D., 2013. Random wave runup and overtopping a steep sea wall: Shallow-water and boussinesq modelling with generalised breaking and wall impact algorithms validated against laboratory and field measurements. *Coastal Engineering* 74 (0), 33 – 49.
- Network Rail, U., 2014. Dawlish.  
URL <http://www.networkrail.co.uk/timetables-and-travel/storm-damage/dawlish/>
- Nørgaard, J., Lykke Andersen, T., Burcharth, H., 2014. Distribution of individual wave overtopping volumes in shallow water wave conditions. *Coastal Engineering* 83 (0), 15 – 23.
- Peregrine, D. H., 1967. Long waves on beaches. *J. Fluid Mech.* 27, 815–827.
- Phillips, O., 1958. The equilibrium range in the spectrum of wind-generated waves. *Journal of Fluid Mechanics* 4 (4), 426 – 434.
- Pierson, W., Moskowitz, L., 1964. A proposed spectral form for fully developed wind seas based on the similarity theory of s. a. kitaigorodskii. *Journal of Geophysical Research* 69 (24), 5181 – 5190.
- Pu, J., Shao, S. Pu, J. H., 2012. Smoothed particle hydrodynamics simulation of wave overtopping characteristics for different coastal structure. *The Scientific World Journal* 2012.
- Pullen, T., Allsop, N., Bruce, T., Kortenhaus, A., Schüttrumpf, H., van der Meer, J., 2007. *EurOtop - Wave Overtopping of Sea Defences and Related Structures Assessment Manual*. Environment Agency, UK.
- Raosa, N., Zanuttigh, B., Lara, J., Hughes, S., 2012. 2DV RANS-VOF modelling of depths and velocities of overtopping waves at overwashed dikes. *Coastal Engineering Proceedings* 1 (33).
- Reeve, D., Chadwick, A., Fleming, C., 2004. *Coastal engineering: process, theory and design practice*. London:Spon Press.
- Reeve, D., Soliman, A., Lin, P., 2008. Numerical study of combined overflow and wave overtopping over a smooth impermeable seawall. *Coastal Engineering* 55 (2), 155 – 166.
- Roy, C., Oberkampf, W., 2011. A comprehensive framework for verification, validation, and uncertainty quantification in scientific computing. *Computer Methods in Applied Mechanics and Engineering* 200, 2131–2144.
- Shankar, N., Jayaratne, M., 2003. Wave run-up and overtopping on smooth and rough slopes of coastal structures. *Ocean Engineering* 30, 221 – 238.
- Shao, S., Ji, C., Graham, D. I., Reeve, D. E., James, P. W., Chadwick, A. J., 2006. Simulation of wave overtopping by an incompressible SPH model. *Coastal Engineering* 53 (9), 723 – 735.
- Shi, F., Kirby, J. T., Harris, J. C., Geiman, J. D., Grilli, S. T., 2012. A high-order adaptive time-stepping TVD solver for boussinesq modeling of breaking waves and coastal inundation. *Ocean Modelling* 4344 (0), 36 – 51.

- Shiach, J., Mingham, C., Ingram, D., Bruce, T., 2004. The applicability of the shallow water equations for modelling violent wave overtopping. *Coastal Engineering* 51 (1), 1 – 15.
- St-Germain, P., Nistor, I., Readshaw, J., Lamont, G., 2014. Numerical modeling of coastal dike overtopping using sph and non-hydrostatic nlsw equations. *Coastal Engineering Proceedings* 1 (34).
- Stansby, P. K., 2003. Solitary wave run-up and overtopping by a semi-implicit finite-volume shallow water Boussinesq model. *J. Hydraulic Res.* 41(6), 639–647.
- Suzuki, T., Shibaki, H., Suzuyama, K., 2014. The numerical analysis of wave overtopping and water overflow over the coastal levee in the storm condition. *Coastal Engineering Proceedings* 1 (34).
- Trucano, T., Swiler, L., Igusa, T., Oberkampf, W., Pilch, M., 2006. Calibration, validation, and sensitivity analysis: What's what. *Reliability Engineering & System Safety* 91, 1331–1357.
- USACE, 2002. *Coastal Engineering Manual*, 1110-2-1100. Washington, D.C.
- Van der Meer, J., 1998. *Seawalls, dikes and revetments*, Chapter 8 : Wave run-up and overtopping. Balkema.
- van der Meer, J., Janssen, J., 1994. Wave run-up and wave overtopping at dikes and revetments. R&D Report 454, Delft Hydraulics.
- van Gent, M. R., van den Boogaard, H. F., Pozueta, B., Medina, J. R., 2007. Neural network modelling of wave overtopping at coastal structures. *Coastal Engineering* 54 (8), 586 – 593.
- Van Gent, M. R. A., 1994. The modelling of wave action on and in coastal structures. *Coastal Eng.* 22, 311–339.
- Verhaeghe, H., 2005. Neural network prediction of wave overtopping at coastal structures. Ph.D. thesis, Universiteit Gent.
- Verhaeghe, H., van der Meer, J., Steendam, G., Besley, P., Franco, L., van Gent, M., 2003. Wave overtopping database as the starting point for a neural network prediction method. In: *Coastal Structures*. pp. 418–430.
- Victor, L., van der Meer, J., Troch, P., 2012. Probability distribution of individual wave overtopping volumes for smooth impermeable steep slopes with low crest freeboards. *Coastal Engineering* 64 (0), 87 – 101.
- WalesOnline, 2014. Wales storms: 22 pictures that show the ferocious power of the latest storm to pummel the welsh coastline.  
URL <http://www.walesonline.co.uk/news/wales-news/wales-storms-22-pictures-show-6472623>
- Welch, P., 1967. The use of fast fourier transform for the estimation of power spectra: A method based on time averaging over short, modified periodograms. *IEEE transactions on Audio and Electroacoustics* AU-15 (2), 70–73.
- Young, I., Eldeberky, Y., 1998. Observations of triad coupling of finite depth wind waves. *Coastal Eng.* 32, 137–154.
- Zijlema, M., Stelling, G., Smit, P., 2011. Swash: An operational public domain code for simulating wave fields and rapidly varied flows in coastal waters. *Coastal Engineering* 58 (10), 992 – 1012.